CaF Tweezer Arrays in the Quantum Many-Body Regime

Connor Martin Holland

A Dissertation
Presented to the Faculty
of Princeton University
in Candidacy for the Degree
of Doctor of Philosophy

Recommended for Acceptance
by the Department of
Physics
Adviser: Lawrence W. Cheuk

May 2026

© Copyright by Connor Martin Holland, 2026.

All rights reserved.

Abstract

Ultracold molecules trapped in reconfigurable optical tweezer arrays are a versatile platform for exploring quantum science. Molecules have rich internal structure useful for attaining quantum control; laser cooling and fluorescence imaging utilize electronic transitions, quantum information can be processed in rotational states, and hyperfine states provide highly-coherent and non-interacting storage qubits. Complementing these capabilities, reconfigurable optical tweezer arrays enable single-site detection and control, which enable generating arbitrary trapping geometries and measuring quantum correlations functions.

This thesis presents 1) the design and construction of a new CaF molecular tweezer array apparatus, and 2) subsequent quantum science investigations advancing molecular quantum control, information processing, and quantum-enhanced metrology.

On apparatus design and construction, we report several advances in molecular laser-cooling and detection. First, we describe a novel imaging alignment and characterization procedure utilizing an in-situ and in-vacuum target. Second, we report an efficient approach to synthesize optical spectra which leverages algorithms in optical holography. Third, we report a novel background-free fluorescence detection protocol utilizing two distinct electronic transitions in CaF. Fourth, we develop and characterize a Λ-enhanced blue-detuned molecular MOT enabling robust optical tweezer loading.

Regarding quantum science, we describe several advances in quantum control, quantum information processing, and quantum-enhanced metrology. First, we report observations of coherent dipolar spin-exchange between individually trapped CaF molecules; we use these interactions to realize a molecular iSWAP gate and deterministically entangle molecules for the first time. Second, we describe a new rapid fluorescence detection scheme enabling measurement-enhanced internal state preparation. The latter enables preparing internally pure and defect-free molecular arrays with record fidelity, opening the door to quantum many-body physics with molecular tweezer arrays. We also demonstrate mid-circuit erasure conversion of single-qubit errors, and coherent transduction of quantum information

between a rotational and hyperfine molecular qubit. Lastly, we generate and characterize metrologically useful many-body entangled spin-squeezed states of molecules. Microscopic measurements of these states reveal long-range spatial correlations, bi-partite entanglement, and bidirectional Einstein-Podolsky-Rosen steering.

The work in this thesis establishes molecular tweezer arrays as a promising platform for exploring quantum information processing, and quantum many-body physics both in the context of quantum spin models and quantum-enhanced metrology.

Acknowledgements

First and foremost, I'd like to thank my advisor **Lawrence Cheuk**, who set the lab up for success from the very early days. Lawrence is an expert in everything AMO, and it's been an amazing opportunity to learn and work alongside him. I'd also like to thank **Waseem Bakr** for both being on my committee and for lending some of his lab space to us during the first year or so. Sorry we flooded the prelab that one time... I'd also like to thank **David Huse** for being on my committee, and **Jeff Thompson** for being the second reader of my thesis (even though no Yb was involved).

Our lab has certainly grown a lot over the years. For the first few years, it was just Lawrence, **Yukai Lu**, and me. Yukai, I had a lot of fun building the lab with you (and almost burning it down during that one ODT scan). It was awe-inspiring seeing you become the go-to computer-interface and MW expert. Our late night (sometimes into early morning) data campaigns were certainly type-II fun,[1] to say the least. I count myself lucky to have benefited from your dedication and diligence along the way. When **Samuel Li** joined the lab, it was clear we were in for a huge boost to the team. It was incredible watching Sam essentially do all the theory for RSC as a first year grad student. It was great having you around, thank you for the Plutonium paper weight, and I wish you continued success at Samsung. I had the distinct pleasure of mentoring **Callum Welsh** during his first year. It has been fantastic seeing Callum come into his own in the lab, leaving me in the dust as the "old man in lab". Although I have only overlapped with **Chris Tong** for a year, he has picked up the reins very quickly and has brought a great attitude to the lab. If your fiber laser project ever runs Precilasers out of business, I will be a dedicated customer. Lastly, the lab is truly lucky to have the one and only **Xingyan Chen** as our postdoc. Your chill demeanor, but amazing knowledge and exacting expertise, has really allowed the lab to flourish over the last few years. Between Callum, Chis, and Xingyan, the lab is well-positioned to have a productive and successful future.

[1] Fun' $\leq$ Fun

The staff and administrators in the Physics Department at Princeton are truly one-of-a-kind. There have been countless instances where so many people offered help or guidance when we ran into trouble – allowing us to just focus on the physics. I don't think that can be said for every department; our lab should count ourselves lucky. In particular, I'd like to thank **Darryl Johnson**, the "Mayor of Jadwin", for always keeping his eye on me, and encouraging me to keep spending Lawrence's money. Alongside Darryl, **Corbe Pale** and **Marlin Alverado** have run a tight ship in the shipping department. I'd also like to thank **Julio Lopez** and **Ryan McGann** for running a top-notch physics supply store, and never batting an eye when I asked for help cutting raw materials. In the machine shop, **Steve Lowe** is an absolute legend. In the early days of the lab, you probably saw Yukai and me in the machine shop on a daily basis. Thank you for always being extremely patient and willing to assist when those last "couple thou" could make or break the part. Recently, **Pat Bradshaw** has continued Steve's legacy of patience and helpfulness; I really appreciate all your help. **Geoff Gettelfinger** has always been a great resource to ensure all Jadwin facilities continue to run smoothly. I'd especially like to thank **Tim Phelan** for his constant willingness to be of assistance, and for his extremely friendly demeanor.

A tremendous shout-out goes to **Lauren Callahan** and **Ted Lewis** for being a fantastic and extremely responsive purchasing department team. I would especially like to thank them for submitting *multiple* buy-it-now bids on eBay requesting 90% discounts.[2] Although I only overlapped with **Catherine Borowsky** for my first year, she was my introduction to Princeton and how amazing the physics department is during the welcome visit those many years ago. Kate was an amazing Grad Program Administrator, and made sure us first years always felt at home; she really made it a priority to have everything go as smoothly as possible. **Katherine Lamos** soon took over as Grad Program Administrator; I enjoyed being part of the team to run the physics open house with you. Now, the department is lucky to have **Leanne Grundel** as Grad Program Administrator; thank you for answering all my

[2]For those interested, this led to my somewhat-infamous corollary to Cicero's 50-50-90 rule: there's a 50-50 shot of sellers accepting 90%-off bids on eBay.

panicked emails about deadlines for this thesis! To **Lisa Scalice**, thank you for providing your watchful eye over all things Jadwin, and saving us physicists from ourselves more times than not. Last but not least, a big thank you to **Dale O'Brien**. I'm pretty sure Dale first thought I was an intruder to Jadwin after seeing me in my 2nd floor coffee lounge "office" during my first year. Since then, she has been relieved to know I am not an intruder, and she has been a great person to see every day, and never gives me too many grumbles when asking her to open the Chair's Conference Room for PSAMORI.

Over the last seven years, it has been great to be part of and grow a great AMO community here at Princeton. Thank you to all the members of the Cheuk, Bakr, Thompson, and Romalis labs for making that happen. In particular, the Cheuk and Bakr labs are very close (sometimes indistinguishable); I'd like to thank all the past and current grad students and postdocs of the Bakr Lab: **Youssef Aziz Alaoui**, **Zengli Ba**, **Lysander Christakis**, **Laura Futamura**, **Elmer Guardado-Sanchez**, **Junlan Jin**, **Jongheum Jung**, **Sanjay Kumar**, **Max Prichard**, **Ravin Raj**, **Jason Rosenberg**, **Donghyuk Seo**, **Yue (Fred) Shi**, **Ben Spar**, and **Zoe Yan**. In particular, **Ben Spar** and I have known each other since late 2014; I believe we first met sitting one row from each other in Physics 61 at Stanford, and I seemed to follow him wherever he went next. **Lysander Christakis** provided a great deal of casual mentorship and support during the first years of my PhD. It was great to chat with you about dipolar physics when our two labs were first seeing signatures of coherent interactions between molecules for the first time. I'd also like to thank **Laura Futamura** for taking up the reins of the Princeton Student AMO Reading Initiative (PSAMORI).[3] Last but certainly not least, I am really grateful to have become best friends with **Max Prichard**. Whether it's sharing my latest crazy idea with you at 10pm on a Saturday, chilling in the coffee lounge to procrastinate re-aligning our optics, de-breifing after the latest round of crazy papers on arXiv last night, or just getting a casual lunch – I'm really gonna miss hanging out with you every day!

[3]Pronounced as you would the professional warrior class in pre-industrial Japan.

I'm also extremely grateful to the friends[4] I've made in the physics department, especially in my cohort. In particular, I'd like to thank all the members of "Liftin' Humans": **Ross Dempsey**, **Sophie Dvali**, **Adri Dropulic**, **Michael Scheer**, **Chase Goddard**, **Hichem Bouchamaoui**, **Bennett Greenberg**, **Suren Gourapura**, and **Zach Atkins**. We've kept each other sane in otherwise insane times, whether it was organizing Zoom trivia nights during Covid, irreligious nondenominational secret santa gift exchanges, or trips to the beach to celebrate Adri's birthday. In particular, I'd like to thank **Suren Gourapura** for keeping me sane during the pandemic by agreeing to go on evening walks with me. It was great looking at all the expensive houses in the suburbs of Princeton – especially those with a lot of copper. Thanks for helping me get swol when I probably should have been writing this thesis. To **Sophie Dvali** – my Jadwin buddy during Covid. It was great commiserating about lasers and molecules with you. You helped expose me to the brethren field to AMO – Biophysics. Larry the Mantis Shrimp[5] has kept a watchful eye over our office ever since you croche'd him. C. Elegans is the Rubidium of Biophysics! **Michael (Jean-Michel) Sheer** – thanks for being my roommate for like 3 months and helping me assemble my IKEA furniture. Your house parties were always poppin. I still think the TBG high-five will catch on.[6] **Bennett (BPG13BallinFollowOnTwitter) Greenberg**, thank you for being my roommate after Michael realized Princeton was super boring during Covid and left. I have truly come to appreciate the wonders of central-central New Jersey! The Garden State has never had a more low-key hype-man. To **Matthew Ai** – it's been great to have a San Diego friend doing quantum science at Princeton. I enjoyed acting on our mutual obsession for Szechuan peppercorn when we made mapo tofu at my apartment.

[4] "fiends", before Adri caught the typo. At times, equally valid descriptor though...

[5] I've come to imagine that Mantis Shrimps would be excellent AMO grad students. For starters, all the different lasers in a molecule lab would probably look like a psychedelic rainbow to the 16 different color receptors in their eyes. That, combined their eyes' ability to detect circularly polarized light, would make it very easy for a Mantis Shrimp to set up a MOT.

[6] For the un-initiated, a TBG high-five is like a normal high-five, but the participant's hands slightly twist after contact revealing a moire pattern. See Michael's thesis for more details on its low-temperature phase diagram.

I'd next like to thank the friends, mentors, and figures who have encouraged me and provided invaluable advice and support along the way. To **Bill Nye (The Science Guy)** – thank you for encouraging my curiosity, love for science, and perhaps slightly irreverent behavior at an early age. I shall always remember that "inertia is a property of matter". The first science teacher I remember was **Nancy Swanberg**. Thank you for continuing to encourage and support my love for science in elementary school. Towards the end of high school, I was stuck in an existential crisis of whether I should pursue Physics or Biology, largely thanks to two amazing teachers: **Tony (Doc) Pelletier** and **Marcus Milling**. **Doc** introduced me to the wonders and excitement of open-ended research questions, and the joys of working in a research lab in his renegade Advanced Honors Biology course (more lovingly known as "Special Bio"). **Marcus Milling** was an absolutely fantastic physics teacher, who concocted a stellar physics curriculum, producing several students who have gone on to obtain PhDs in physics. I still think about "Eric the Halibut" whenever a kinetmatic equation comes up! My physics career arguably started when **Kathryn (Kam) Moler** took a chance on a random freshman from her mechanics class and welcomed me into her lab in the summer of 2015. After two summers of experience in her lab, I was hooked on physics. She continues to be an inspiration to me of excellence in both teaching and research. My first introduction to AMO physics was with **Jason Hogan**, whose lab I worked in for three years. Jason and I still reminisce about that one memorable office hour I attended, where the discussion quickly derailed into an hour-long back-and-forth over whether we could engineer a dispersion relation enabling faster-than-light communication.[7] I am very thankful to have kept chatting with you over Zoom throughout the ups and downs of my PhD. Your constant enthusiasm and gentle guidance were indispensable. I've also had the pleasure of keeping in touch with my high school and college physics friend **Lark Wang**. It was great hearing about all the life updates during our sporadic Zoom calls over the last seven years.

[7]We actually did find one, but the margins of this thesis are too small to provide details.

Although many people have supported and encouraged my choice to pursue science as a "day job", no one has supported me more than my family. To **Mom**, you've always been around to chat or call when I needed some perspective. I'm really lucky to always have your support, even if I drive you crazy sometimes. To **Dad**, thank you for all the time you dedicated to supporting me, especially throughout Boy Scouts. A PhD is basically a very long Eagle Scout Project, but with more lasers. To **Ashley**, thanks for being a great sister; I enjoyed escaping the lab on the weekends to watch your Equestrian matches in random Pennsylvania towns with mom. To **Effie (F-E-Z) Trinket**, thanks for being the best and most goofy dog, and for always stealing my socks when I come home to visit. To **Grandma**, thank you for your exuberant love, and for asking the toughest questions, like how exactly quantum computers would make Barley (her dog) happier. To **Grandpa**, you've always been the greatest role-model, and are a living example of never ceasing to be curious, learn new things, and seek out new experiences. Thanks for teaching Ashley and me guitar during the pandemic, and for allowing us to be yet another band that you couldn't keep together. Last but certainly not least, to **Andrea Wynn**. I am so happy to have been your swimming buddy at Princeton, and now your everything buddy. I love you so much (more than Bean loves coffee[8]), and am so lucky to have you in my life.

Finally, to all the **frustrated grammarians** out there, I apologize for switching between tense and person so often throughout these acknowledgments. Although they are frustrated, I know you will forgive me.

[8]To those who have not met Bean, she is a caffeine-addicted stuffed animal kitty. She will stop at nothing to get more coffee. She would also make a good grad student, come to think of it.

To my family.

Contents

Abstract iii

Acknowledgements v

List of Tables xix

List of Figures xx

Publications xxiii

1 Introduction **1**

1.1 Molecular Tweezer Arrays for Quantum Science 2

1.2 Outline 4

2 CaF Molecular Structure **7**

2.1 Diatomic Molecules 8

2.1.1 Born-Oppenheimer Approximation 9

2.1.2 Angular Momentum 11

2.1.3 Nomenclature 13

2.2 CaF Structure 14

2.2.1 Low-Lying Electronic States 15

2.2.2 Considerations for Closed Optical Cycling 16

2.3 Interactions with Electric & Magnetic Fields 18

2.3.1 Magnetic Fields 19

2.3.2 Electric Fields 19

2.3.3 Off-Resonant Optical Fields 20
2.3.4 Vibrational State Transitions 21
2.4 Dipolar Interactions Between Polar Molecules 22
2.4.1 General Formulation 22
2.4.2 Resonant Exchange Interaction 24
2.4.3 Mapping to a Spin Model 25
2.4.4 Role of Motional Degrees of Freedom 25

3 Experimental Apparatus **26**
3.1 Cryogenic Beambox 27
3.2 Vacuum System 30
3.3 Lasers 32
3.3.1 Laser Locking 33
3.3.2 Slowing ($X - B$) Laser 33
3.3.3 Main 606 nm ($X - A$) Laser 34
3.3.4 Vibrational Repumping Lasers 34
3.3.5 Rotational Repumping Lasers 36
3.3.6 Coherent Two-Photon Raman (605 nm) Laser 37
3.4 Microscope Objective Paths 39
3.4.1 Tweezer Path 41
3.4.2 Fluoresence Imaging Path 45
3.4.3 MOT Top Path 45
3.5 In-Situ Interferometric Alignment of a High-NA Microscope Objective 47
3.5.1 Principle of Operation 48
3.5.2 Mounting and Installation 49
3.5.3 Preliminary Alignment 50
3.5.4 Interferometric Alignment 52
3.5.5 Alignment of Other Beams 56

3.6 Computer-Experiment Interface 57
3.7 Microwave and Raman Pulse Control 58

4 Preparing Tweezer-Trapped CaF 59

4.1 Producing a CBGB 60
4.2 Chirped Slowing 60
4.3 MOT 62
4.4 Lambda-Cooling 64
4.5 ODT & Tweezer Loading 66
4.6 5-Beam Λ-Imaging 67
4.7 Optical Pumping 67
4.8 Tweezer Parameters and Molecular Temperature 70
4.8.1 Tweezer Parameters 70
4.8.2 Molecular Temperatures 71

5 Generating Arbitrary Optical Spectra using High-Bandwith EOMs 73

5.1 A Need for Sidebands 74
5.2 Spectral Engineering is Holography 75
5.2.1 Spectral Engineering with Computer Holography Solutions 77
5.2.2 Creating a Single Frequency 78
5.2.3 Creating Multiple Frequencies 79
5.3 Technical Considerations 79
5.3.1 Compatibility with Non-Linear Frequency Generation 80
5.3.2 Chromatic Dispersion in Long Fibers 81
5.3.3 Linear Electronic Effects 82
5.3.4 Minimizing RF Non-linearities 82
5.4 Experimental Realization and Characterization 82
5.4.1 Calibrating the Amplitude Response 84

5.4.2 Calibrating the Phase Response . . . 85
5.4.3 Compensated Signal Comparison . . . 87
5.4.4 Proof-of-Principle Demonstration . . . 88
5.4.5 GSA vs Concantenated Serrodynes . . . 90
5.5 Simulation of Optical Scattering . . . 90
5.5.1 Optical Bloch Equation Simulations . . . 92
5.6 Outlook . . . 94
5.6.1 Adoption in Molecular Laser-Cooling Platforms . . . 95
5.6.2 CGH Variants and Waveform Modifications . . . 97

6 Background-Free Detection via Bichromatic Imaging 99
6.1 Dual-Frequency Background-Free Detection . . . 100
6.2 Bichromatic Imaging in CaF . . . 101
6.2.1 Imaging Scheme . . . 101
6.3 Evaluating Imaging Performance . . . 103
6.3.1 Performance Summary . . . 103
6.3.2 Model-Free Estimation of Imaging Identification Errors . . . 105
6.4 Imaging Loss Mechanisms . . . 110
6.4.1 Loss Due to Heating . . . 110
6.4.2 Loss Due to Rotational Branching . . . 110
6.4.3 Loss Due to Admixtures of Excited States . . . 113
6.5 The $B - C$ Transition Dipole Moment . . . 115
6.5.1 Measurement Procedure . . . 115
6.5.2 Extracting Transition Dipole Moment from Lineshape . . . 115
6.5.3 Comparison of Measured and Predicted Differential ac Stark Shifts . 117
6.6 Outlook . . . 117

7 Λ-Enhanced Blue-Detuned MOT **119**

7.1 Operating Principle of a (Λ-Enhanced) BDM 120

7.2 Integration into the Existing Sequence 121

7.3 Optimizing the BDM 123

7.3.1 Measuring Cloud Size 126

7.3.2 Measuring (Phase Space) Density 127

7.4 Characterizing Loss in the BDM 128

7.4.1 Loss and Temperature 128

7.4.2 Force, Damping, Effective Depth 129

7.5 Robust Tweezer Loading 132

7.6 Upgraded BDM & Outlook 133

8 Coherent Interactions and Entanglement Between CaF Molecules **134**

8.1 Preparing Defect-Free Arrays 135

8.2 Long Coherence Times in a Rotational Qubit 138

8.3 Observing $1/r^3$ Dipolar Interactions 140

8.4 Entangled States of Molecules 142

8.4.1 Entangling Protocol 142

8.4.2 Entanglement Witness 142

8.4.3 Bell State & iSWAP Gate Fidelity 143

8.4.4 State Preparation & Measurement Correction 145

8.4.5 Coherent Transport 151

8.5 Contributions to Bell State Infidelity 151

8.6 Singlet-Triplet Rotations 154

8.6.1 Implementing Site-Dependent S_z Shifts 155

8.6.2 Decoherence-Free Subspace 157

8.7 Outlook 157

9 Enhancing State Preparation and Erasing Errors **159**

9.1 Related Protocols 162

9.2 Leveraging Molecular Structure for Error Detection 164

9.3 Rapid Resonant Imaging 165

9.3.1 Imaging Performance Characterization 166

9.3.2 Off-Resonant Scattering Rate Estimation 167

9.4 Improving State Preparation via Error Detection 168

9.5 Coherent Control of a New Hyperfine Qubit 171

9.6 Composite Erasure Detection 174

9.7 Correcting Hyperfine Leakage Errors 176

9.7.1 Leakage Errors Induced by Black-Body Radiation 176

9.7.2 Lifetimes Affecting Erasure Conversion and Detection 179

9.7.3 Modeling BBR Erasure Conversion Efficiencies 182

9.8 Coherent Transduction Between Qubit Encodings 187

9.9 Measurement-Enhanced Cooling Protocols 188

9.9.1 Measurement-Enhanced Sideband Cooling 189

9.9.2 Measurement-Enhanced Suppression of Thermal Tunneling 190

9.10 Discussion and Outlook 193

10 Generating Metrologically Useful Spin-Squeezed States **196**

10.1 Introduction to Quantum-Enhanced Metrology 199

10.2 Floquet Engineering XXZ Models 204

10.2.1 Pulse Sequence to Engineer XYZ Models 204

10.2.2 Characterizing Floquet-Engineered XXZ Models 206

10.3 Spin-Resolved Imaging 207

10.3.1 Implementation of SRI 208

10.3.2 Correcting for Errors During SRI 210

10.3.3 Post-selection and Expectation Values 212

10.4 Realizing Spin-Squeezing with XX Interactions 213
10.5 Probing Spatial Structure of XX Squeezed States 215
10.5.1 EPR Steering and Many-Body Entanglement 218
10.6 Spin Squeezing Towards the Heisenberg Point 220
10.7 Transduction to Non-Interacting States 223
10.8 Outlook 225

11 Outlook **227**

Bibliography **229**

List of Tables

6.1 Contributions to $X - B$ Differential Stark Shift 118

9.1 Erasure-corrected $N = 0$ population lifetime 184

10.1 EPR Witness Parameters vs XXZ Ising Anisotropy 219

List of Figures

2.1 Diatomic Vibrational and Rotational States 10

2.2 Hund's Cases 12

2.3 CaF Level Structure 15

3.1 Cryogenic Beambox and Cell 28

3.2 UHV System 30

3.3 Light Generation and Locking Schematic 32

3.4 Rotational Repumper Lasers 35

3.5 605 Laser System and Associated Components 37

3.6 Optical Paths Through Objective 40

3.7 Nonlinearities in High-Bandwidth AODs 42

3.8 Tweezer and Fluoresence Optical Paths 44

3.9 MOT Top Path 46

3.10 Operating Principle of Bead Measurement 49

3.11 Bead and Associated Components Pictures 51

3.12 Optics for Spherical Bead Interferometry 53

3.13 Interference Fringe Pictures 54

4.1 Beambox Rotational Temperature 61

4.2 Molecular Beam Doppler Spectroscopy 62

4.3 Type I and II MOTs 63

4.4 GMC and Λ-Cooling Mechanism 65
4.5 Single-Beam m_F Pumping 68
4.6 Tweezer Trapping Frequencies 71

5.1 The Gerchberg-Saxton Algorithm 78
5.2 Experimental Setup to Measure GSA-Generated Spectra 83
5.3 EOM Amplitude Response 84
5.4 EOM Phase Response 86
5.5 Compensated and Uncompensated Serrodyne Spectra 88
5.6 Proof-of-Principle $X - B$ Spectrum Generation 89
5.7 Comparison of Concatenated Serrodynes and GSA Solutions 91
5.8 Optical Bloch Equation Simulations using GSA Spectra 93

6.1 CaF Levels and Transitions in Bichromatic Imaging 102
6.2 Error Probabilities Versus Classification Threshold θ 104
6.3 Inferring Loaded-Tweezer Fluoresence Histogram 108
6.4 Imaging Configuration Thermometry 110
6.5 Loss and Scattering During Bichromatic Imaging 111
6.6 Loss and Dispersive Shifts vs Tweezer Wavelength 112
6.7 Differential ac Stark shifts Δ_{XB} 116

7.1 MOT Laser Configurations and Λ-BDM Loading Dynamics 121
7.2 Λ-BDM Temperature and Lifetime 124
7.3 Λ-BDM Properties versus Axial Magnetic Gradient B'_z 125
7.4 Λ-BDM Density and PSD 128
7.5 Exemplary Velocity Damping Curves 129
7.6 Velocity Damping, Restoring Force, and Enhanced Tweezer Loading 131

8.1 Laser-cooled Molecules in a Reconfigurable Optical Tweezer Array 136

8.2 Tweezer Rearrangement and Internal State Initialization 137
8.3 Single Particle Coherence and Spin-Exchange Oscillations 138
8.4 Creating and Probing Bell Pairs 144
8.5 Reconstructed Two-Tweezer Occupation Probabilities 150
8.6 A Decoherence Free Subspace Qubit 156

9.1 Rapid Resonant Imaging Scheme 165
9.2 Characterizing Errors during Rapid Resonant Imaging 166
9.3 Robust and Enhanced State Preparation Using Error Detection 169
9.4 A New Hyperfine Qubit 172
9.5 Composite Erasure Detection 174
9.6 Erasure Conversion of Blackbody Errors 177
9.7 Population of $X^2\Sigma(v = 0, N = 1)$ Molecules Under BBR 180
9.8 Raman π-Pulse Quality Factor 181
9.9 Long-time $N = 0$ population survival 186
9.10 Rotational to Hyperfine Qubit Transduction 187
9.11 Suppressing Thermal Tunneling via Mid-Sequence Measurement 191

10.1 XY8-XYZ Floquet Sequence 205
10.2 XY8-XYZ Coherence Times and Global Fields 207
10.3 SRI Sequence and Histograms 209
10.4 Spin Squeezing Protocol 214
10.5 XX Squeezing Dynamics 215
10.6 Spatial Structure of XX Squeezed State 217
10.7 Temporal Dynamics of Squeezing at $\Delta \neq 0$ 221
10.8 Squeezing, Correlations, and Witnesses vs Δ 222
10.9 Transduction of Spin-Squeezed States 223

Publications

Work in this thesis has led to the following publications:

1. Connor M. Holland, Yukai Lu, Lawrence W. Cheuk. Synthesizing optical spectra using computer-generated holography techniques. *New J. Phys.* **23**, 033028 (2021) [1].

2. Yukai Lu*, Connor M. Holland*, Lawrence W. Cheuk. Molecular Laser-Cooling in a Dynamically Tunable Repulsive Optical Trap. *Phys. Rev. Lett.* **128**, 213201 (2022) [2].

3. Connor M. Holland, Yukai Lu, Lawrence W. Cheuk. Bichromatic Imaging of Single Molecules in an Optical Tweezer Array. *Phys. Rev. Lett.* **131**, 053202 (2023) [3].

4. Connor M. Holland*, Yukai Lu*, Lawrence W. Cheuk. On-Demand Entanglement of Molecules in a Reconfigurable Optical Tweezer Array. *Science* **382**, 1143 (2023) [4].

5. Yukai Lu*, Samuel J. Li*, Connor M. Holland*, Lawrence W. Cheuk. Raman Sideband Cooling of Molecules in an Optical Tweezer Array. *Nat. Phys.* **20**, 389 (2024) [5].

6. Samuel J. Li*, Connor M. Holland*, Yukai Lu, Lawrence W. Cheuk. Blue-Detuned Magneto-optical Trap of CaF Molecules. *Phys. Rev. Lett.* **132** 233402 (2024) [6].

7. Connor M. Holland, Yukai Lu, Samuel J. Li, Callum L. Welsh, Lawrence W. Cheuk. Demonstration of Erasure Conversion in a Molecular Tweezer Array. *Phys. Rev. X* (2025) [7].

8. Yukai Lu, Connor M. Holland, Callum L. Welsh, Xingyan Chen, Lawrence W. Cheuk. Probing Coherent Many-Body Spin Dynamics in a Molecular Tweezer Array Quantum Simulator. *arXiv*: 2603.19090 (2026) [8].

Work in this thesis has led to the following manuscripts in preparation:

1. Connor M. Holland, Callum L. Welsh, Yukai Lu, David Wellnitz, Xingyan Chen, Ana-Maria Rey, Lawrence W. Cheuk. Spin Squeezing in a Molecular Tweezer Array (In Preparation)

Parts of this thesis have appeared in the following presentations:

1. Yukai Lu, Connor M. Holland, Lawrence W. Cheuk. Towards a Quantum Gas Microscope for Laser-Cooled Molecules. APS DAMOP 2020.
2. Connor M. Holland, Yukai Lu, Lawrence W. Cheuk. Synthesizing Optical Spectra Using Computer-Generated Holography Techniques. APS DAMOP 2021.
3. Connor M. Holland, Yukai Lu, Lawrence W. Cheuk. A Novel Imaging Technique for Optical Tweezer Arrays of CaF Molecules. APS DAMOP 2022.
4. Connor M. Holland, Yukai Lu, Samuel J. Li, Lawrence W. Cheuk. Coherent Interactions and Entanglement Between CaF Molecules in a Reconfigurable Tweezer Array. APS DAMOP 2023.
5. Connor M. Holland, Yukai Lu, Samuel J. Li, Callum L. Welsh, Lawrence W. Cheuk. Erasure Conversion in a Molecular Tweezer Array. APS DAMOP 2024.
6. Connor M. Holland, Yukai Lu, Callum L. Welsh, Xingyan Chen, Lawrence W. Cheuk. Quantum Science With Optical Tweezer Arrays of CaF Molecules. Gordon Research Conference: Atomic Physics 2025.
7. Connor M. Holland. Exploring Many-Body Spin Physics in a CaF Molecular Tweezer Array. Boeing Quantum Creators Prize Symposium 2025.

Chapter 1

Introduction

Molecules are cool, and you can do cool things with them.

– Albert Einstein, probably

Quantum mechanics was originally developed to explain the peculiar and often counter-intuitive ways in which light interacts with matter, particularly atoms and molecules. More than a century after its formulation, this relationship has in many ways been reversed: rather than merely using quantum theory to understand natural systems, we now engineer and control photons, atoms, and molecules to probe quantum mechanics in regimes far removed from those found in nature.

Beyond its foundational importance, quantum mechanics has also driven technological advances. The so-called first quantum revolution gave rise to devices such as the laser, which is an indispensable tool in atomic, molecular, and optical (AMO) physics. These developments harnessed quantum effects to enhance otherwise classical technologies, enabling unprecedented precision in measurement and control.

We are now in the midst of a second quantum revolution, in which quantum systems are no longer simply tools for improving classical devices, but instead are used to generate intrinsically non-classical resources. Entanglement and coherence, once regarded as fragile curiosities, are now key ingredients for quantum computation, simulation, and sensing. AMO

platforms, with their exceptional levels of isolation and control, have emerged as leading candidates for realizing these new technologies.

Despite their role in some of the earliest studies of light-matter interactions [9] and precision spectroscopy [10], molecules were gradually set aside in favor of atoms, whose simpler internal structure made them easier to cool, trap, and control. Over the past two decades, however, there has been a resurgence of interest in molecular systems – the second molecular revolution. Molecules' rich internal structure and spatially-anisotropic, long-range interactions offer new opportunities that are more difficult to achieve with atoms alone. This thesis contributes to this second revolution by developing tools to prepare, control, and study individual molecules in highly controlled environments. Building on these capabilities, this thesis presents some of the first explorations of quantum many-body physics using molecules.

1.1 Molecular Tweezer Arrays for Quantum Science

The use of ultracold molecules as a platform for quantum computation [11] and quantum simulation [12] was proposed more than two decades ago. In contrast to atoms, molecules host additional vibrational and rotational degrees of freedom, resulting in rich internal structure [13, 14]. The internal structure and complexity of molecules enable a range of capabilities that are difficult to access in atomic systems. For example, certain molecular states exhibit enhanced sensitivity to physics beyond the Standard Model, which is utilized in searches for an electron electric dipole moment [15, 16]. Molecules also undergo chemical reactions, and can be used to study ultracold collisions and chemical reactions with quantum-level control [17, 18]. In the context of quantum science, polar molecules possess permanent electric dipole moments, which give rise to long-range, anisotropic interactions between molecules prepared in long-lived rotational states. These interactions form the basis of molecule-based platforms for quantum simulation [12, 19] and quantum computation [20].

The same internal structure that underpins these advantages also makes molecules more difficult to cool, trap, and manipulate. Two experimental pathways have emerged for producing ultracold molecular samples.

One route begins with ultracold atoms, which are associated into weakly bound molecules and then coherently transferred to their rovibrational ground state. Following the first demonstration in KRb [21], this approach has been extended to many bialkali species [22–28]. Subsequent advances have enabled the creation of degenerate molecular gases, including both degenerate Fermi gases [29] and Bose-Einstein condensates [30]. In parallel, the incorporation of high-resolution imaging has improved control and detection, leading to a molecular quantum gas microscope [31] and optical tweezer arrays of bialkali molecules [32, 33].

A complementary strategy, which we employ in this work, involves direct laser slowing and cooling of molecules. In this approach, molecules are first produced, often in a cryogenic buffer gas beam [34], and are then slowed and cooled using laser light. This technique was first demonstrated using SrF [35], and soon after was applied other molecular species [36–38]. Next, magneto-optical trapping [39–42], and sub-Doppler cooling [40, 43–45] can produce cold, dense molecular samples. The cold gas of molecules are transferred into conservative optical traps [45–48], including optical tweezers, enabling control and readout at the single-molecule level. These techniques have been applied to several other molecular species [49–53], including polyatomic ones [54–58], opening new directions in precision measurement [59, 60].

For applications in quantum science, it is essential to achieve long single-particle coherence times between two molecular states (forming a molecular qubit) and to control interactions between particles. Considerable progress has been made toward realizing molecular qubits [31, 61–67]. In addition, dipolar interactions between molecules have been observed in optical lattices, both in bulk systems [68, 69] and at the single-particle level [31].

Optical tweezer arrays provide a complementary set of capabilities that are well suited to advancing molecular quantum science, including deterministic initialization of defect-free samples, site-resolved control, and high-fidelity detection. Originally developed for neutral atoms, these systems enable the assembly of defect-free arrays through rearrangement [70, 71], programmable geometries [72], and dynamic reconfiguration during experiments [73]. Such capabilities have driven rapid advances in quantum simulation [74, 75], quantum computation [76, 77], and metrology [78, 79], and have been extended across a wide range of atomic species [80–85].

Motivated by these developments, reconfigurable molecular tweezer arrays have recently emerged as a promising platform for quantum science [4, 32, 33, 86–88]. By combining the rich internal structure and long-range interactions of molecules with the precise, bottom-up control of optical tweezers, this approach enables deterministic assembly, individual state preparation and readout, and engineered interactions between molecules. In recent years, this platform has opened the door to exploring quantum simulation and quantum information processing with ultracold molecules.

1.2 Outline

The chapters of this thesis can be grouped into three sections, corresponding to the three epochs of my PhD. Chapters 2, 3, 4 summarize the *construction epoch*, in which we built a CaF molecular tweezer array and implemented the, by now, "day-to-day" standard protocols to cool, trap, and initialize individual tweezer-trapped CaF molecules. Chapters 5, 6, 7 highlight the *technical development epoch*, in which we made major contributions to cooling, trapping, and imaging CaF. Finally, Chapters 8, 9, 10 summarize the *science epoch*, which established CaF tweezer arrays as a leading platform for quantum information processing and quantum simulation using laser-cooled molecules.

In detail, we provide brief summaries of these chapters, highlighting novel and important content which may be of interest to the reader.

- Chapter 2 provides an introduction to molecular structure, with an emphasis on CaF energy levels, interactions with EM fields, and inter-molecular interactions.

- Chapter 3 highlights the CaF tweezer array apparatus itself, with an emphasis on the optics and laser systems. In particular, I present extensive details on the development, characterization, and realization of an in-situ interferometric alignment target consisting of an in-vacuum spherical bead. This system is used to measure optical aberrations in our imaging and tweezer optics paths, enabling diffraction-limited performance to be achieved independently for each path. In addition, the in-vacuum bead substantially simplifies aligning ∼mm-waist beams to the focal point of the objective.

- Chapter 4 details the "day-to-day" experimental sequence, which begins with chemical precursors to CaF and ends with preparing individually trapped CaF molecules in a molecular tweezer array.

- Chapter 5 presents the theoretical underpinnings for and experimental realization of a powerful and versatile technique to generate arbitrary spectral content on a laser using commercially available arbitrary waveform generators and high-bandwidth EOMs. This technique has been used extensively in our group and other direct molecular laser cooling groups to reduce the cost and complexity of achieving high optical scattering rates along multiple optical transitions and across many molecular species.

- Chapter 6 explores the development of a novel, high-fidelity, background-free fluorescence imaging protocol for CaF tweezer arrays. This investigation led to practical insights about how CaF's electronic and vibration structure impacts high-fidelity imaging in a tweezer array. We also developed a technique to characterize imaging identification infidelities. On the molecular Hamiltonian front, these investigations suggest the need for a substantial revision to the $B - C$ transition dipole moment in CaF.

- Chapter 7 presents our development and characterization of a blue-detuned MOT of CaF which utilizes two-photon coherent dark states. We also explore the limitations of this MOT, concluding that shallow trap depths ultimately limit molecular density enhancement via magnetic-field-gradient ramps.

- Chapter 8 details deterministically entangling molecules into a two-particle Bell state, constituting the first implementation of an entangling two-qubit molecular gate. We provide details on how we achieve long single-particle coherence times, the characterization of long-range dipolar interactions between molecules, and several sources of noise limiting the two-qubit gate fidelity.

- Chapter 9 highlights a substantial shift in perspective concerning how high-fidelity many-body quantum state initialization can be achieved in CaF tweezer arrays. In particular, we developed measurement-based error mitigation and correction protocols, which enabled achieving record-level single-particle and many-body initialization fidelities. In conjunction with the development of a novel hyperfine-qubit, these techniques enabled population leakage from the hyperfine-qubit to be flagged while preserving the delicate quantum information stored in error-free tweezers. This investigation led to new insights about how room-temperature black body radiation environments may limit next-generation CaF-based molecular quantum simulators.

- Chapter 10 presents investigations into generating metrologically useful spin-squeezed states in a 1D CaF array. The squeezed states are generated via one-axis-twisting (OAT)-like dynamics arising from dipolar XXZ models, which we generate via Floquet Hamiltonian engineering. The local-nature of dipolar interactions give rise to spatially inhomogeneous correlations and entanglement between the molecules, which depend strongly on parameters of the XXZ Hamiltonian. Using protocols developed in Chapter 9, we coherently transduce a squeezed state into the non-interacting hyperfine-qubit manifold, where the state remains metrologically useful.

Chapter 2

CaF Molecular Structure

CaF is the Rb of molecules.

– 2022 ITAMP workshop

In this chapter, we provide an introduction to the structure of polar diatomic molecules and their interactions with optical, electric, and magnetic fields. Our goal is to establish the theoretical framework necessary to understand both the internal structure of these molecules and their dynamics in experimental settings.

We begin with a general overview of the structure of polar diatomic molecules. This includes a discussion of the Born-Oppenheimer approximation, its underlying assumptions, and its consequences for separating electronic and nuclear degrees of freedom.

We then turn to the specific case of CaF, highlighting the low-lying electronic states relevant for optical control. We describe the rovibrational structure within each electronic manifold and discuss the requirements for achieving closed optical cycling transitions in polar diatomic molecules, which are essential for efficient laser cooling and state detection. We also discuss the structure of Franck-Condon factors, which play a central role in enabling direct laser cooling of molecules.

Next, we examine the interactions of CaF with electromagnetic fields. These interactions underpin the techniques used for laser cooling, trapping, state preparation, and readout in our optical tweezer array apparatus.

Finally, we introduce the framework for understanding interactions between two polar molecules. In this regime, dipolar interactions give rise to an effective spin-exchange Hamiltonian. The strength and dynamics of this interaction are central to the experiments presented in Chapter 8.

2.1 Diatomic Molecules

A neutral diatomic molecule consists of two nuclei with charges $Z_1 e$ and $Z_2 e$ and $N_e = Z_1 + Z_2$ electrons. Neglecting spin degrees of freedom for the moment, the full molecular Hamiltonian is given by the kinetic energy of the nuclei and electrons together with the Coulomb interactions between all charged particles,

$$H_{\mathrm{Mol}} = \frac{\mathbf{p}_{1,n}^2}{2M_1} + \frac{\mathbf{p}_{2,n}^2}{2M_2} + \sum_{i=1}^{N_e} \frac{\mathbf{p}_{i,e}^2}{2m_e} + V, \tag{2.1}$$

where the Coulomb potential is

$$V = \frac{e^2}{4\pi\epsilon_0}\left[\frac{Z_1 Z_2}{|\mathbf{r}_{1,n} - \mathbf{r}_{2,n}|} - \sum_{i=1}^{N_e} \frac{Z_1}{|\mathbf{r}_{1,n} - \mathbf{r}_{i,e}|} - \sum_{i=1}^{N_e} \frac{Z_2}{|\mathbf{r}_{2,n} - \mathbf{r}_{i,e}|} + \sum_{i<j}^{N_e} \frac{1}{|\mathbf{r}_{i,e} - \mathbf{r}_{j,e|}}\right]. \tag{2.2}$$

Here, $\mathbf{r}_{1,n}$ and $\mathbf{r}_{2,n}$ denote the nuclear coordinates and $\mathbf{r}_{i,e}$ the electronic coordinates. This Hamiltonian cannot, in general, be solved exactly, and a sequence of controlled approximations is required to arrive at a useful description of molecular structure [89].

2.1.1 Born-Oppenheimer Approximation

The first key simplification arises from the large mass ratio between the nuclei and electrons, $M \gg m_e$. As a result, the nuclei move more slowly than the electrons, allowing a separation of electronic and nuclear degrees of freedom. This is formalized in the Born-Oppenheimer approximation by expressing the total wavefunction as

$$\Psi(\mathbf{r}_e, \mathbf{r}_n) = \psi_e(\mathbf{r}_e; \mathbf{r}_n)\, \chi(\mathbf{r}_n), \tag{2.3}$$

where $\mathbf{r}_e$ ($\mathbf{r}_n$) collectively denotes all electronic (nuclear) coordinates.

One first solves the electronic Schrödinger equation for fixed nuclear positions,

$$H_e(\mathbf{r}_n)\, \psi_e(\mathbf{r}_i; \mathbf{r}_n) = E_e(\mathbf{r}_n)\, \psi_e(\mathbf{r}_i; \mathbf{r}_n), \tag{2.4}$$

where H_e contains the electronic kinetic energy and all Coulomb interactions. The resulting electronic energy $E_e(\mathbf{r}_n)$ defines a potential energy surface (PES) on which the nuclei subsequently evolve.

Substituting this ansatz back into the full Hamiltonian yields an effective Schrödinger equation for the nuclear wavefunction $\chi(\mathbf{r}_n)$. Additional terms arise from derivatives of ψ_e with respect to $\mathbf{r}_n$, which can couple different electronic states. The Born-Oppenheimer approximation neglects these non-adiabatic coupling terms, which is justified when they are small compared to the energy separation between electronic states. In this regime, the nuclei evolve on a single PES with the electronic state adiabatically following the nuclear motion.

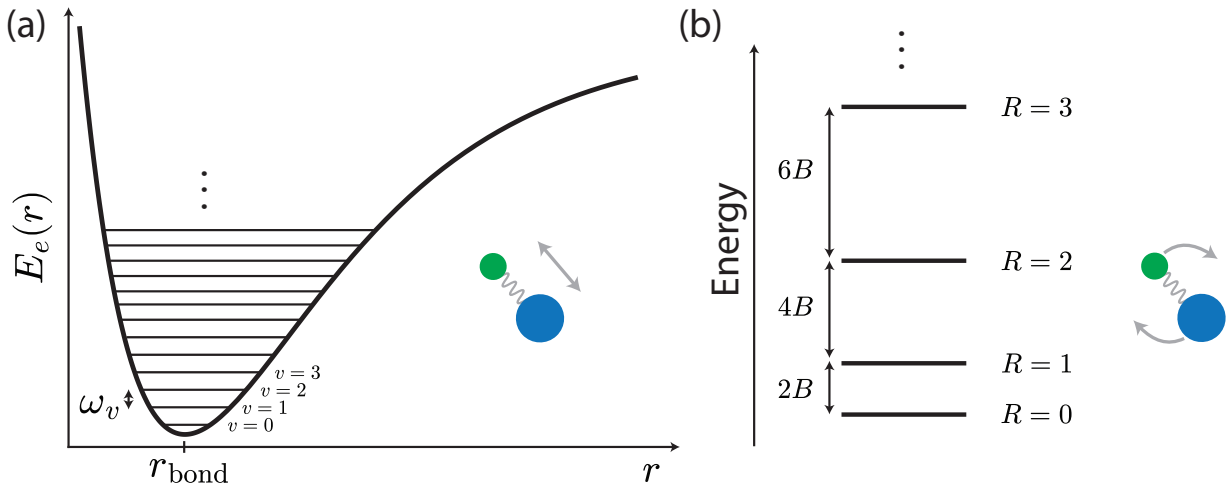


Figure 2.1: Diatomic Vibrational and Rotational States: (a) Vibrational states (v) are equally spaced near the bottom of the PESs. (b) For each vibrational state, there is a ladder of rotational states (R) spaced roughly by multiples of the rotational constant.

Nuclear Motion

For a diatomic molecule, the nuclear motion can be simplified by introducing center-of-mass and relative coordinates,

$$\mathbf{r}_{\text{cm}} = \frac{M_1\mathbf{r}_{1,n} + M_2\mathbf{r}_{2,n}}{M_1 + M_2}, \qquad \mathbf{r} = \mathbf{r}_{1,n} - \mathbf{r}_{2,n}. \tag{2.5}$$

The center-of-mass motion Hamiltonian does not depend on the relative coordinate, and simply describes the kinetic energy of the molecule's center of mass. This leaves a Hamiltonian for the relative nuclear coordinate $\mathbf{r}$ with reduced mass $\mu = \frac{M_1 M_2}{M_1+M_2}$,

$$H_{\text{rel}} = \frac{\mathbf{p}^2}{2\mu} + E_e(\mathbf{r}). \tag{2.6}$$

The motion associated with $\mathbf{r}$ can be further decomposed into radial and angular degrees of freedom. The angular motion is well described by a rigid rotor Hamiltonian,

$$H_{\text{rot}} = B\,\mathbf{R}^2, \qquad B = \frac{\hbar^2}{2I_m}, \tag{2.7}$$

where $r = |\mathbf{r}|$, $I_m = \mu r^2$ is the moment of inertia of the molecule's nuclei, and $\mathbf{R}$ is the nuclear rotational angular momentum operator. This leads to rotational energy levels (Fig. 2.1(b)) of unequal spacing given by $E_R = BR(R+1)$.

The radial motion describes molecular vibrations. The potential energy surface $E_e(r)$ typically exhibits a minimum at an equilibrium bond length r_{bond}, arising from the competition between short-range repulsion and long-range attraction. Near this minimum, the potential can be approximated as harmonic,

$$E_e(r) \approx E_e(r_{\text{bond}}) + \frac{1}{2}\mu\omega_v^2(r - r_{\text{bond}})^2, \tag{2.8}$$

leading to equally spaced vibrational energy levels (Fig. 2.1(a)) described by

$$E_v = \hbar\omega_v \left(v + \frac{1}{2}\right). \tag{2.9}$$

Anharmonic corrections to this potential can be captured using more realistic models, such as the Morse potential.

To leading order, rotational and vibrational degrees of freedom can be treated independently. However, they are weakly coupled: rotational motion modifies the effective bond length through centrifugal distortion, while the moment of inertia depends on the vibrational state. These effects can be incorporated perturbatively and are commonly described using the Dunham expansion, which provides a systematic parametrization of rovibrational energy levels. For more details on these higher order terms, see Yukai's Thesis [90].

2.1.2 Angular Momentum

The internal angular momentum of a diatomic molecule arises from several contributions: the total electronic orbital angular momentum $\mathbf{L}$, the total electronic spin $\mathbf{S}$, the total rotational angular momentum of the nuclei $\mathbf{R}$, and the total nuclear spin $\mathbf{I}$. The total

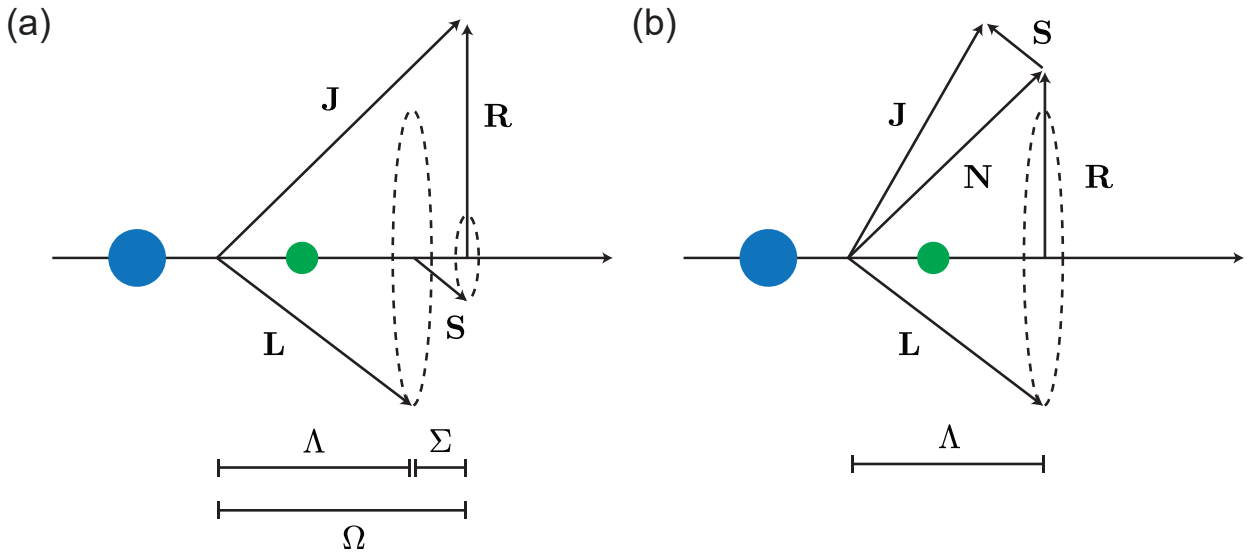


Figure 2.2: Hund's cases (a) and (b).

angular momentum excluding nuclear spin is given by

$$\mathbf{J} = \mathbf{L} + \mathbf{R} + \mathbf{S}, \tag{2.10}$$

while inclusion of nuclear spin leads to $\mathbf{F} = \mathbf{J} + \mathbf{I}$.

The appropriate set of quantum numbers depends on the relative strength of the couplings between these angular momenta. These different coupling regimes are classified by Hund's cases, with those relevant to CaF illustrated in Fig. 2.2.

In Hund's case (a), the electronic orbital angular momentum $\mathbf{L}$ is strongly coupled to the internuclear axis arising from electrostatic interactions with the molecular bond, so only its projection onto the internuclear axis, Λ, is a good quantum number. The electronic spin $\mathbf{S}$ couples to $\mathbf{L}$ via spin-orbit interaction, with projection onto the internuclear axis Σ. The total projection of the electronic angular momentum along the internuclear axis is $\Omega = \Lambda + \Sigma$. Hund's case (a) describes CaF molecules in the A and C states.

In Hund's case (b), spin-orbit coupling is weak compared to the coupling between the rotational motion and the electronic orbital angular momentum. In this case, Λ remains a good quantum number, but $\mathbf{S}$ largely decouples from the internuclear axis. The rotational

angular momentum $\mathbf{N} = \mathbf{R} + \mathbf{L}$ is first formed, and $\mathbf{S}$ subsequently couples to $\mathbf{N}$ to produce $\mathbf{J}$. Hund's case (b) describes CaF molecules in the X and B states.

The internal structure of a diatomic molecule is characterized by a hierarchy of energy scales,

$$E_{\text{electronic}} \gg E_{\text{vibrational}} \gg E_{\text{rotational}} \gg E_{\text{hyperfine}}, \tag{2.11}$$

which justifies the sequence of approximations leading from the full molecular Hamiltonian to an effective description in terms of well-defined quantum numbers.

2.1.3 Nomenclature

The electronic states of diatomic molecules are denoted by the following "heiroglyphic"

$$\eta^{2S+1}\Lambda_{\Omega,(u/g)}^{(+/-)} \tag{2.12}$$

The η denotes the electronic configuration, starting from the ground state X then working upwards alphabetically starting from A roughly in order of energy. The $2S+1$ denotes the electron spin multiplicity; in molecules with two valence electrons, the capitalization of η is often also dependent on whether the electron spin is in a singlet or triplet state. For doublet molecules like CaF, capital letters are always used. For Λ, states with $\Lambda = \{0, 1, 2, \dots\}$ are given the Greek capital letters $\{\Sigma, \Pi, \Delta, \dots\}$.[1] The Ω is included when it is defined. For Σ states, the reflection symmetry about a plane containing the internuclear axis is specified by $(+/-)$; for homonuclear molecules, the inversion symmetry is specified by (g/u).[2]

Additional quantum numbers, when they exist, are specified parentheses after the heiroglyphic. These include the vibration quantum number (v), total orbital angular momentum quantum number (N), total angular momentum excluding nuclear spin quantum number

[1] Note the unfortunate coincidence of Σ denoting either $\Lambda = 0$ or the projection of $\mathbf{S}$ onto the internuclear axis. Context nearly always clarifies this ambiguity.

[2] German abbreviations for *gerade* (even), or *ungerade* (odd).

(J), total angular momentum quantum number (F), projection of $\mathbf{F}$ onto a quantization axis (m_F), and parity ($\mathcal{P}$).

2.2 CaF Structure

We discuss the structure of CaF, which is particularly well suited for laser cooling, trapping, and coherent quantum control. CaF can be effectively treated as a single valence-electron system. Due to the high electronegativity of fluorine, one valence electron is transferred from Ca to F, leading to an ionic bond of the form Ca^+F^-. The valence electron experiences a repulsive interaction from the negatively charged fluorine ion, resulting in a spatial distribution localized predominantly on the Ca atom and away from the internuclear bond. As a consequence, electronic excitations primarily involve this valence electron while only weakly perturbing the molecular bond. This separation between electronic and nuclear degrees of freedom provides an intuitive explanation for the highly diagonal Franck-Condon factors observed between low-lying electronic states.

These features make CaF an excellent candidate for direct laser cooling. In particular, the near-diagonal Franck-Condon factors enable a nearly closed optical cycling transition, requiring only a small number of additional lasers to address vibrational leakage. Furthermore, the nuclear spins $I_{\mathrm{Ca}} = 0$ and $I_{\mathrm{F}} = 1/2$ result in a relatively simple hyperfine structure. The presence of an unpaired electron in the $X^2\Sigma^+$ ground state leads to a magnetic response on the order of a Bohr magneton (μ_B), much larger compared to the magnetic response in singlet molecular ground states, such as those of many bialkali molecules. Additionally, the ionic character of the bond gives rise to a permanent electric dipole moment, leading to dipolar interactions between molecules, which is discussed in Section 2.4.

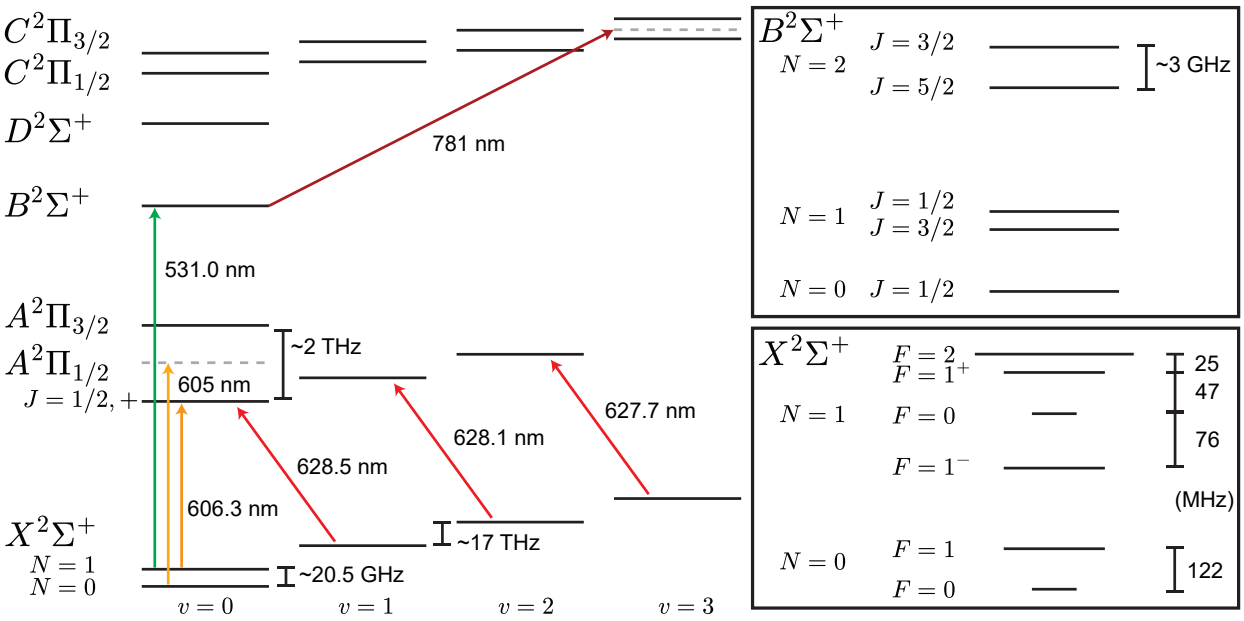


Figure 2.3: CaF Level Structure: States and optical transitions relevant to cooling, trapping, and coherent manipulation. Separation between levels are specified when relevant. Relative spacing is not to scale.

2.2.1 Low-Lying Electronic States

The electronic structure relevant to this work is dominated by several low-lying states (see Fig. 2.3). The primary states used for laser cooling and detection are the $X^2\Sigma^+$, $A^2\Pi_{1/2}$, and $B^2\Sigma^+$ manifolds. Additional excited states, including $A^2\Pi_{3/2}$, $C^2\Pi_{1/2}$, $C^2\Pi_{3/2}$, and $D^2\Sigma^+$, play roles in the experiments described in Chapters 6 and 9. The X, B, and D states are described by Hund's case (b), reflecting relatively weak spin-orbit coupling. In contrast, the A and C states follow Hund's case (a), where spin-orbit coupling is strong.

The $X^2\Sigma^+ \rightarrow A^2\Pi_{1/2}$ transition serves as the primary transition for laser cooling, fluorescence detection, and vibrational repumping, and is commonly referred to as the $X - A$ transition. The $X^2\Sigma^+ \rightarrow B^2\Sigma^+$ transition is used for laser slowing and optical pumping between rotational states, and is referred to as the $X - B$ transition.

Vibrational States

The potential energy surfaces of the X, A, and B states exhibit similar equilibrium bond lengths and vibrational level spacings of $\omega_v \approx 2\pi \times 17\,\mathrm{THz}$. The similarity of these potentials results in strong overlap between vibrational wavefunctions in different electronic states, and therefore highly diagonal Franck-Condon factors. This property is essential for maintaining closed optical cycling, as discussed in Section 2.2.2.

Rotational and Hyperfine Structure

Within the X and B electronic states, rotational levels are organized into manifolds labeled by the quantum number N, with energies scaling approximately as $N(N+1)$. The parity of these states alternates as $\mathcal{P} = (-1)^N$, leading to electric dipole selection rules $\Delta N = \pm 1$.

Each rotational manifold splits into two hyperfine manifolds labeled by $J = N \pm 1/2$, arising from the coupling of rotational motion with the electron spin. These J levels are further split by interactions with the fluorine nuclear spin $I = 1/2$, yielding total angular momentum states $F = J \pm 1/2$. As a result, each N manifold contains four hyperfine states with $F = \{N-1, N, N, N+1\}$.

In the A states, N is not a good quantum number due to strong spin-orbit coupling. Instead, the states are labeled by J, with the lowest levels given by $J = 1/2$ in $A^2\Pi_{1/2}$ and $J = 3/2$ in $A^2\Pi_{3/2}$. Each J manifold is split into two opposite-parity manifolds due to Λ-doubling, with splittings on the order of GHz for low-lying states (see Yukai's Thesis [90] for additional details). In practice, electric dipole transitions from a given N manifold in $X^2\Sigma^+$ address only one of these parity doublets.

2.2.2 Considerations for Closed Optical Cycling

Efficient photon scattering for laser cooling, trapping, and detection requires that molecules repeatedly return to the same internal state after each optical excitation. While this is

straightforward in atomic systems, molecular structure introduces additional decay channels that must be carefully controlled.

A primary challenge arises from rotational branching. For example, an excited $B^2\Sigma^+$ state can decay to ground-state rotational levels along $N \to N \pm 1$ transitions, resulting in population loss from the optical cycling transition.[3] Additionally, for a generic molecule, spontaneous emission can populate several vibrational levels, leading to additional population loss from the optical cycling transition.

Without additional considerations, achieving closed optical cycling would require addressing many rotational and vibrational transitions simultaneously, with frequency spacings ranging from tens of GHz to tens of THz. Optical cycling in CaF and other directly-cooled molecules relies on a combination of angular momentum selection rules and favorable Franck-Condon factors to reduce leakage from a closed cycling transition.

Selection Rules

Rotational closure of the cycling transition can be achieved by exploiting angular momentum and parity selection rules for electric dipole transitions [91]. In CaF, this is accomplished by initializing molecules in the $X^2\Sigma^+(N = 1, \mathcal{P} = -)$ state.

For the $X - A$ transition, excitation to the $A^2\Pi_{1/2}(J = 1/2, \mathcal{P} = +)$ state is allowed. From this state, spontaneous emission is restricted to ground states with $J = 1/2$ or $J = 3/2$ and parity $\mathcal{P} = -$. The only state satisfying these constraints is the original $X^2\Sigma^+(N = 1, \mathcal{P} = -)$ state. Similarly, for the $X - B$ transition, excitation from $X^2\Sigma^+(N = 1, \mathcal{P} = -)$ to $B^2\Sigma^+(N = 0, \mathcal{P} = +)$ results in decay exclusively back to the initial state. As a result, all laser cooling, slowing, and detection schemes only work for molecules in the ground state $N = 1$ rotational manifold.

[3] For population equally distributed across all hyperfine levels in a given N manifold, the $N+1 : N-1$ branching ratio is $(N+1)/N$.

Franck-Condon Factors

While rotational branching can be suppressed using selection rules, vibrational branching is governed by the overlap between vibrational wavefunctions in different electronic states. The electric dipole transition matrix element can be factorized into an electronic component and a vibrational overlap,

$$\mathcal{M} = \langle \eta', \dots | \mathbf{d} | \eta, \dots \rangle \, \langle v'_{\eta'} | v_\eta \rangle, \tag{2.13}$$

where η labels the electronic state and v the vibrational quantum number. The squared vibrational overlap $f_{v',v} = |\langle v'_{\eta'} | v_\eta \rangle|^2$ is called the Franck-Condon factor (FCF).

For electronic states with similar potential energy surfaces, the vibrational wavefunctions are closely matched, leading to predominantly diagonal Franck-Condon factors, $f_{v',v} \approx \delta_{v',v}$. This is the case for the $X-A$ and $X-B$ transitions in CaF, enabling efficient optical cycling. Nevertheless, small off-diagonal elements lead to population leakage into higher vibrational states. These states must be repumped using additional lasers to maintain closed optical cycling. However, slightly non-diagonal Franck-Condon factors can actually be advantageous for vibrational repumping. In particular, a non-zero overlap between neighboring vibrational states allows efficient driving of $v \to v-1$ transitions, reducing the laser power required for repumping vibrational state population.

Finally, the vibrational branching ratios are not determined solely by Franck-Condon factors. According to Fermi's golden rule, the spontaneous emission rate also depends on the density of photon states, which scales as ω^3. As a result, the vibrational branching ratios (VBRs) are proportional to $f_{v',v}\, \omega^3_{v',v}$, where $\omega_{v',v}$ is the transition frequency between vibrational levels.

2.3 Interactions with Electric & Magnetic Fields

In this section, we provide breif details on CaF's interaction with electric and magnetic fields. For more details, we refer the interested reader to Yukai's Thesis [90].

2.3.1 Magnetic Fields

An external magnetic field causes shifts in energies of molecular states, which is described by the Zeeman Hamiltonian

$$H_Z = g_S \mu_b \mathbf{S} \cdot \mathbf{B} + g_L \mu_b \mathbf{L} \cdot \mathbf{B} - g_I \mu_N \mathbf{I} \cdot \mathbf{B}, \tag{2.14}$$

where $g_S \approx 2$, $g_L \approx 1$, $g_I \approx 5.6$. Note that the nuclear spin term is highly suppressed since $\mu_B/\mu_N = m_e/m_p \approx 1/1836$. For small magnetic fields, this Hamiltonian can be approximated by

$$H_Z = g_F \mu_B F_z B_z \tag{2.15}$$

with g_F factor given by

$$g_f = g_s \frac{S(S+1) + J(J+1) - N(N+1)}{2J(J+1)} \frac{F(F+1) - I(I+1) + J(J+1)}{2F(F+1)}. \tag{2.16}$$

For a more elaborate discussion, including on an anisotropic Zeeman term, see Yukai's Thesis [90].

2.3.2 Electric Fields

An external electric field leads to the Hamiltonian

$$H_S = -\mathbf{d} \cdot \mathbf{E} \tag{2.17}$$

which couples opposite-parity molecular states. For interactions with sinusoudally oscillating electric fields of the form $\mathbf{E}(t) = \frac{1}{2} E_0 (\hat{\epsilon} e^{-i\omega_L t} + \hat{\epsilon}^* e^{i\omega_L t})$, the Hamiltonian under the rotating wave approximation is given by

$$H_{\mathrm{EM}} = -\frac{E_0}{2} \Big(\langle 1|\mathbf{d} \cdot \hat{\epsilon}|0\rangle |1\rangle\langle 0| + \langle 0|\mathbf{d} \cdot \hat{\epsilon}^*|1\rangle |0\rangle\langle 1| \Big) \tag{2.18}$$

where the two states $|0\rangle$ and $|1\rangle$ are coupled by the electric field. Explicit details on how to evaluate these matrix elements and elaborations on selection rules are given in Yukai's Thesis [90].

2.3.3 Off-Resonant Optical Fields

When optical fields are far-detuned from a molecular transition, states are affected due to a second-order perturbation effect, leading to an effective AC Stark Hamiltonian. Within a given Hilbert space of interest ($\mathcal{H}_0$), the matrix elements of this effective Hamiltonian are given by

$$\langle i|H_{\mathrm{SS}}|i'\rangle = -\frac{1}{4}E_0^2 \sum_{j\notin\mathcal{H}_0} \left(\frac{\langle i|\mathbf{d}\cdot\hat{\epsilon}^*|j\rangle\langle j|\mathbf{d}\cdot\hat{\epsilon}|i'\rangle}{\hbar(\omega_{ji}-\omega_L)} + \frac{\langle i|\mathbf{d}\cdot\hat{\epsilon}|j\rangle\langle j|\mathbf{d}\cdot\hat{\epsilon}^*|i'\rangle}{\hbar(\omega_{ji}+\omega_L)} \right) \tag{2.19}$$

with $|i\rangle$ and $|i'\rangle$ belonging to $\mathcal{H}_0$ [92].

When this matrix only has diagonal components, its effect is to shift energy levels. For laser frequencies close to but not resonant with the transitions, the first term of Eq. 2.19 dominates; for laser frequencies smaller than the optical transitions ($\omega_{ij} - \omega_L > 0$, red-detuned light), this shift is negative. Thus, the molecule will be attracted to regions of maximum light intensity. This is the basic operating principle of attractive optical dipole traps and optical tweezers.

Invariably, this matrix will also contain off-diagonal elements. In this case, in addition to shifting energy levels, this perturbation mixes "free-space" eigenstates to form "dressed" eigenstates. Control over this mixing is critical to achieve high-fidelity optical pumping and attaining matched optical trapping potentials between different levels in $\mathcal{H}_0$.

This Hamiltonian can also be decomposed into a basis of spherical tensors, with scalar, vector, and tensor components. The scalar component affects all m_F sublevels of a manifold equally, leading to equal trapping potentials. A vector component only arises for elliptically polarized light, acting like an effective magnetic field which shifts energies proportional to

m_F. The tensor components act on states with different $|m_F|$ values – applying a quadratic shift as a function of m_F for linearly polarized light.

2.3.4 Vibrational State Transitions

Transitions between vibrational states within the same electronic state can be driven by and decay via infrared radiation. For the ground $X^2\Sigma^+$ state of CaF, these transitions are at the vibrational trapping frequency of $\omega_v \approx 2\pi \times 17\,\mathrm{THz}$.

From the perspective of Frank-Condon factors, it would at first seem like these transitions are impossible. Indeed, they are not allowed under the Condon approximation, which states that the dipole moment is independent of nuclear separation. However, this approximation is not exact. From the Born-Oppenheimer approximation, the electron cloud redistributes as the nuclei move, leading to a dipole moment that can change with the internuclear separation. By breaking the Condon approximation, the full dipole moment can be Taylor expanded about the equilibrium bond length as

$$\mathbf{d}(r) = \mathbf{d}(r_{\mathrm{bond}}) + \frac{d\mathbf{d}}{dr}(r - r_{\mathrm{bond}}). \tag{2.20}$$

Although the transition matrix element of the first term is zero, the second term gives a transition dipole moment of strength

$$d^{\eta}_{v',v} = \frac{d\mathbf{d}}{dr}\langle v'|r - r_{\mathrm{bond}}|v\rangle. \tag{2.21}$$

Properties of harmonic oscillator states lead to the selection rule $\Delta v = \pm 1$ and the scaling of this dipole moment as $d^{\eta}_{v-1,v} = \sqrt{v}\, d^{\eta}_{0,1}$. Note that if the dipole moment is locally flat, or if $\mathbf{d}(r) = 0$, such as is the case for homonuclear molecules, single-photon E1 vibrational-changing transitions are not allowed. Importantly, this means that homonuclear vibrational states do *not* radiatively decay.

These transitions can be driven by IR radiation; coincidentally, the peak in room-temperature black-body radiation (BBR) is exactly overlapped with these $\Delta v = \pm 1$ transisions in CaF. This leads to a $X^2\Sigma^+(v=0)$ lifetime of $\sim 3.4\,\mathrm{s}$. Excited vibrational states also decay via spontaneous emission, leading to a $X^2\Sigma^+(v=1)$ radiative lifetime of $\sim 0.2\,\mathrm{s}$. Excitations and decays are governed by the E1 selection rule $\Delta N = \pm 1$. This means that the $X^2\Sigma^+(v=0, N=0)$ state can only be excited to $X^2\Sigma^+(v=1, N=1)$, which has important consequences for our work on erasure conversion of BBR population leakage, which is presented in Chapter 9.

2.4 Dipolar Interactions Between Polar Molecules

In this section, we develop a description of electric dipole-dipole interactions between two polar molecules and show how these interactions give rise to effective spin models. The same framework applies broadly to other dipolar systems, including Rydberg atoms and magnetic atoms [93–96]. These interactions are used to realize a molecular two-qubit gate, presented in Chapter 8, and generate a spin squeezed states in a small chain of molecules, presented in Chapter 10.

2.4.1 General Formulation

We consider two molecules, labeled 1 and 2, with electric dipole operators $\boldsymbol{d}_1$ and $\boldsymbol{d}_2$, separated by a vector $\boldsymbol{r}$ (magnitude r, direction $\hat{r}$). The dipole-dipole interaction Hamiltonian is

$$H_{dd} = \frac{1}{4\pi\varepsilon_0} \frac{\boldsymbol{d}_1 \cdot \boldsymbol{d}_2 - 3(\boldsymbol{d}_1 \cdot \hat{r})(\boldsymbol{d}_2 \cdot \hat{r})}{r^3}. \tag{2.22}$$

It is useful to write this using spherical tensors, separating the spatial dependence from the internal-state dynamics. In this representation,

$$H_{dd} = -\frac{1}{4\pi\varepsilon_0 r^3} \sqrt{6}\, T^2(\boldsymbol{d}_1, \boldsymbol{d}_2) \cdot T^2(\boldsymbol{C}), \tag{2.23}$$

where $T^2(\boldsymbol{d}_1, \boldsymbol{d}_2)$ acts on the internal molecular states and $T^2(\boldsymbol{C})$ describes the geometry of the intermolecular separation. The spatial tensor is given by

$$T^2_p(\boldsymbol{C}) = \sqrt{\frac{4\pi}{5}} Y_{2,p}(\theta, \phi), \tag{2.24}$$

where (θ, ϕ) specify the orientation of $\hat{r}$ relative to a chosen quantization axis. The internal-state coupling tensor can be expressed in terms of rank-1 dipole operators,

$$T^2_p(\boldsymbol{d}_1, \boldsymbol{d}_2) = (-1)^p \sqrt{5} \sum_{p_1, p_2} \begin{pmatrix} 1 & 1 & 2 \\ p_1 & p_2 & -p \end{pmatrix} T^1_{p_1}(\boldsymbol{d}_1) T^1_{p_2}(\boldsymbol{d}_2). \tag{2.25}$$

This form makes explicit how different components of the dipole operators couple internal states while the geometry is encoded separately in $T^2_p(\boldsymbol{C})$.

In our experiment, molecules are tightly confined in optical tweezers, such that their spatial wavefunctions are much smaller than their separation. As a result, the relative position $\boldsymbol{r}$ can be treated as a fixed classical parameter. The dipolar interaction Hamiltonian then only affects internal degrees of freedom.

We present a simplified model of a molecule without electronic or nuclear spin. The relevant internal states are rotational states $|N, m_N\rangle$, with the dipole operator coupling states according to the selection rule $\Delta N = \pm 1$. We take the rotational splitting to be much larger than the dipolar interaction strength; in this regime, the dipolar interaction cannot change the total number of rotational excitations, and only near-resonant processes are relevant.

We work in the Hilbert space spanned by $N = 0$ and $N = 1$ rotational states. The interaction gives rise to two classes of processes. The dominant contribution is a resonant exchange process,

$$|0, 0; 1, m_N\rangle \;\leftrightarrow\; |1, m'_N; 0, 0\rangle\,, \tag{2.26}$$

which conserves total rotational energy. In contrast, processes that simultaneously create or annihilate two excitations are off-resonant by an energy $\sim 2B$ and can be neglected.

Further simplification arises from the tensor structure. The operator $T^2_p(\boldsymbol{d}_1, \boldsymbol{d}_2)$ can only couple states with $\Delta(m_{N_1} + m_{N_2}) = p$. In the presence of an external field defining the quantization axis, the degeneracy of the m_N sublevels is lifted. When this splitting is large compared to the interaction strength, terms with $p \neq 0$ become off-resonant and can be neglected. We therefore retain only the $p = 0$ component.

Under these approximations, the Hamiltonian simplifies to

$$H_{dd} = \frac{1}{4\pi\varepsilon_0 r^3}(1 - 3\cos^2\theta)\frac{\sqrt{6}}{2}\, T^2_0(\boldsymbol{d}_1, \boldsymbol{d}_2), \tag{2.27}$$

which acts within the resonant subspace spanned by $\{|0,0;1,m_N\rangle\,, |1,m_N;0,0\rangle\}$. The interaction conserves m_N, so each m_N sector evolves independently.

2.4.2 Resonant Exchange Interaction

Within each m_N subspace, the interaction describes coherent exchange of a rotational excitation between the two molecules. Evaluating the matrix elements yields

$$\mathcal{M}_{m_N} = \langle 1, m_N; 0, 0|H_{dd}|0, 0; 1, m_N\rangle\,. \tag{2.28}$$

This interaction strength depends on the internal state and can be interpreted in terms of an effective dipole moment associated with the transition. For more details on evaluating these matrix elements, see Yukai's Thesis [90].

At this stage, we can identify two important features of the dipolar interaction. First, it is long-ranged, with a $1/r^3$ dependence. Second, it is anisotropic, with an angular dependence given by $1 - 3\cos^2\theta$. This angular factor allows the interaction strength to be tuned by geometry, and even to vanish at the magic angle $\theta \approx 54.7°$.

2.4.3 Mapping to a Spin Model

The exchange interaction can be mapped onto an effective spin-1/2 model by encoding a qubit in the states $|0,0\rangle$ and $|1,m_N\rangle$. Identifying $|0,0\rangle \equiv |\downarrow\rangle$ and $|1,m_N\rangle \equiv |\uparrow\rangle$, the Hamiltonian becomes

$$H = \mathcal{M}_{m_N} \left(|\uparrow\downarrow\rangle \langle\downarrow\uparrow| + |\downarrow\uparrow\rangle \langle\uparrow\downarrow| \right), \tag{2.29}$$

which describes the exchange of an excitation between two spins. This is equivalent to the XX spin Hamiltonian,

$$H_{\mathrm{XX}} = \frac{J}{2}(S_1^+ S_2^- + S_1^- S_2^+) = J(S_1^x S_2^x + S_1^y S_2^y) \tag{2.30}$$

with $J = 2\mathcal{M}_{m_N}$.

2.4.4 Role of Motional Degrees of Freedom

The above description assumes that the molecules are tightly confined, so that their relative position is fixed. When this is not the case, the dipole-dipole interaction can couple internal and motional degrees of freedom.

In particular, dipolar interactions can exchange angular momentum between internal rotation and relative motion. As a result, changes in internal quantum numbers can be accompanied by changes in orbital motion, a process known as dipolar relaxation. This mechanism allows internal energy to be converted into kinetic energy, leading to heating and loss in weakly confined systems.

In tightly confining optical tweezers, motional degrees of freedom are effectively frozen out, suppressing dipolar relaxation and allowing the interaction to be described purely in terms of internal-state dynamics.

Chapter 3

Experimental Apparatus

Connor come quick – there's water EVERYWHERE!

– A slightly panicked Lysander Christakis

In this chapter, we provide an overview of the experimental apparatus. The goal of this overview is to introduce the key components and design principles that enable the experiments described throughout this thesis, while deferring more specialized discussions to later sections where appropriate.

We begin with a brief description of the cryogenic beam source, in which molecules are produced and extracted, followed by an outline of the ultra-high vacuum (UHV) system where all subsequent experimental steps take place. We then describe the lasers used for slowing, cooling, and repumping population from molecular dark states. In addition, we discuss a far-detuned laser system designed for coherent two-photon Raman manipulation of a hyperfine qubit, as introduced in Chapter 9. These laser systems are central to both state preparation and coherent control within the experiment.

One of the distinguishing features of our setup is a high numerical aperture (NA) microscope objective, which is used both to project optical trapping potentials and to collect molecular fluorescence for imaging. We outline the design and implementation of this sys-

tem, emphasizing considerations necessary to achieve high-resolution imaging and precise control over optical potentials.

We also highlight a novel in-situ, in-vacuum alignment technique developed in our group, based on a retractable spherical bead. This alignment tool enables diffraction-limited performance for both the imaging and optical tweezer paths. The bead provides nearly 4π steradians of optical access, greatly simplifying the alignment of multiple beams that must intersect at the focal plane of the objective.

Finally, we provide a brief overview of the computer control infrastructure used to operate the experiment, along with the architecture for designing and executing microwave and Raman pulse sequences. These sequences are implemented using a script-based interface, allowing for the creation of more complex control protocols. This flexibility is particularly important for applications such as dynamical decoupling, Floquet engineering, and the fine-tuning of pulse shapes.

3.1 Cryogenic Beambox

Molecules are produced in a cell housed at the center of a cryogenic beambox. The beambox has a matroiska-doll like structure, with four roughly concentric boxes (Fig. 3.1)(a).

1. The outer-most box is a room-temperature box. This box has electrical feed-throughs used primarily to interface with thermometers and heaters. The box has two gas feed-throughs for delivering the bugger gas (He) and one half of the chemical pre-cursor to CaF (SF_6 gas). The aluminum box also has vacuum-flange connections to which we attach pressure gauges, a turbo-pump, and a connection to a house-vacuum system. The box also has room for a cryo-cooler, which delivers cooling power to the inner components of the beambox. Finally, the beambox to a gate-valve, which can provide isolation between the beambox and the UHV section of our apparatus. This box is sealed from the environment using a combination of different vacuum gaskets. For ease

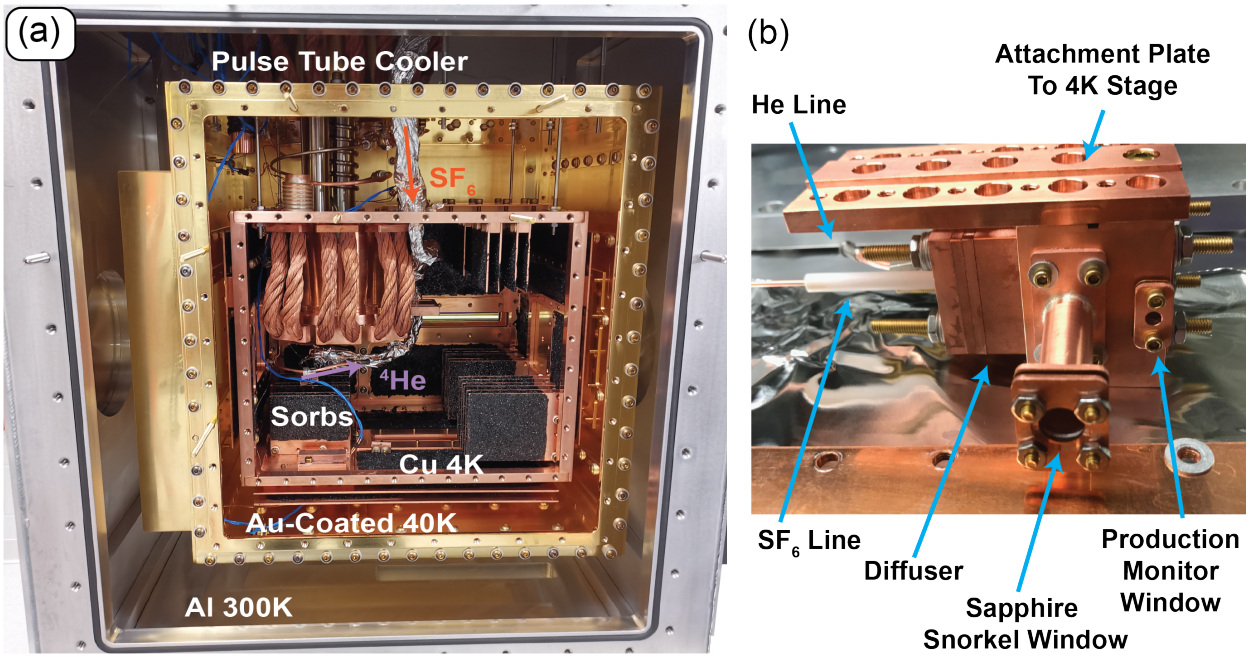


Figure 3.1: Cryogenic Beambox (a) and Cell (b).

of servicing, maintenance, and replacing the calcium target, the left and right sides of the beambox can be detached, where there is an o-ring to maintain good sealing.

2. The next box down (called the 40K shield) consists of gold-plated copper. This box is hung from the top of the 300K box by several stainless steel threaded rods, which minimizes thermal conductivity to RT. This box is coated in gold since gold has low thermal emissivity, helping to limit black-body radiation from reaching the inner boxes, which are kept at 4 K. When the pulse tube is on, this gold-plated box is kept around 35 K. A few heaters (resistors) are also attached to this box.

3. The next box (4K shield) is made of copper. This is attached to the 4K stage of the cryo-cooler. The cryo-cooler also has a He damper, which consists of a bucket that can fill with liquid helium, providing a certain amount of thermal mass to accommodate breif heat-loads from the system. Importantly, the inside of this box is filled with Cu plates, onto which activated coconut charcoal has been epoxied. These are the charcoal sorbs, which help provide cryo-pumping, which is especially important to provide a

sink for the decent amount of He gas flowed into the beambox. This 4K shield also has several heaters attached to it. We regularly use these heaters to preferentially sublimate accumulated adsorbed gas on the surfaces, sorbs, and inner cell every night. This 4K shield also has a bobbin for the He line, consisting of the He tube wrapped several times around a cylindrical Cu piece, which helps the gas thermalize to 4K.

4. The inner-most component is the cryogenic buffer gas source of CaF, also referred to as the cell (Fig. 3.1)(b). This cell has roughly three sections. In the rear of the cell, the He gas line and SF_6 gas line are combined and pass through a diffuser, which is purported to ensure good laminar flow of the gas to the central chamber. The central chamber contains a puck of Ca metal, providing the Ca side of CaF. The third component is a "snorkel" tube with a sapphire window at the end. This window allows a high-power pulsed laser to hit the puck of metallic Ca. Ca is vaporized, reacts with SF_6, and some CaF is produced. The top of the cell interfaces with an adjustable attachment to the 4K stage of the pulse tube. This allows tilting and translating the cell for best molecular beam delivery to the UHV section of the experiment.

To elaborate on the gas delivery lines, there is a He delivery line and a SF_6 delivery line, both of which are delivered by copper tubes. The He line is thermally sunk to the $\sim 4\,\mathrm{K}$ shield via a bobbin. The SF_6 line, on the other hand, must be kept above $\sim$ 200K so that the gas does not freeze. This is accomplished by wrapping the SF_6 line insuperinsulation, which consists of thin sheets of a layered material, resulting in very low thermal conductivity between sheets. The SF_6 line has a separate heater at the end to minimize freezing. The SF_6 line does not directly attach to the cell, instead it goes through a thin plastic tube molded to fit the final copper tube. This tube sticks into the cell; a Teflon and rubber ring ensures that this tube has minimal thermal contact with the cell to prevent to the SF_6 line from freezing. The flow of each gas is controlled by a flow regulator, which is fed by a high-pressure bottle of either He or SF_6 which are regulated by a gas regulator.

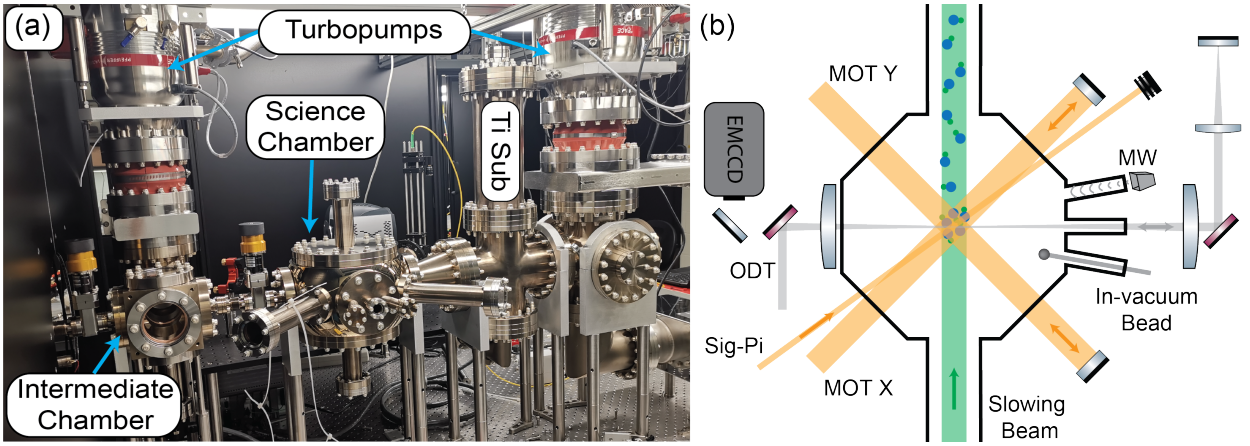


Figure 3.2: UHV System: (a) The UHV system is shown with an early iteration of various attachments to the science chamber. In the final iteration, bucket windows are attached to the top and bottom and no extension tubes are attached to the $\hat{x} - \hat{y}$ MOT arms. The MOT/ODT fluoresence detection camera was also mirrored to the other side. Shown in this photo is the custom three-port adapter which eventually delivers the ODT, microwave, and in-vacuum bead alignment system. (b) A top-down illustration of the octagonal science chamber, showing the molecular beam, slowing beam, retro-reflected $\hat{x} - \hat{y}$ MOT beams, sig-pi optical pumping beam, ODT, microwave, and in-vacuum bead systems.

3.2 Vacuum System

The UHV system consists of three main sections (Fig. 3.2(a)).

1. The first section is the "Intermediate Chamber", which interfaces with the cryogenic beambox. It serves several purposes. Primarily, this first section provides the $\sim$ 75cm needed to slow molecules from $\sim$ 200m/s to zero velocity at the center of the science chamber. There is a small cubic steel vacuum chamber that provides optical access to the molecular beam from four directions. This was intended to be used for transverse cooling, but no signatures were ever seen. Also attached to this cube is a tube that has an ion gauge and large turbopump. This provides some pumping of the He gas before it reaches the subsequent UHV chambers. Importantly, the beambox is connected to this cube via a flexible bellow and a small gate valve. This gate valve provides vacuum isolation from the beambox when it reaches high pressures during sublimation, target changes, etc. There is also a gate valve right before the science chamber, mostly added

as a safety precaution. This helps protect the low-vacuum science chamber if servicing of the first gate valve is needed (which is opened and closed at least once per day).

2. The second section is the "Science Chamber". This consists of an octagonal steel vacuum chamber (Fig. 3.2(b)), with two recessed bucket windows – one from the top and another form the bottom. The top recessed bucket window contains one MOT coil and the objective. The bottom contains the other MOT coil and a custom Delrin mount to deliver a small angled beam for 5-beam Λ-imaging. Two opposing ports of the octagon accomodate the molecular beam and counter-propogating $X - B$ slowing laser. An additional four windows deliver the $x - y$ beams of our MOT. The last two opposing sides of the octagon have one large window providing optical access to image the MOT and for the ODT. On the opposite side to that window is a custom flange with three ports. We send our MW through one of these ports which is delivered via a microwave horn, the central port is where the ODT passes; this port has served many purposes including early-implementations of a repulsive blue-detuned ring, a σ^+ optical pumping beam, and a global $N12$ rotational pumping beam. These auxiliary beams are combined with the ODT path using a backside-polished mirror designed to reflect high-power 1064 nm light; this mirror happens to transmit some visible light, but is also highly polarization-dependent. The final port is attached to a flexible bellow and vacuum-compatible translation stage. This is where the in-vacuum spherical alignment target is attached, which is detailed in Section 3.5.

3. The third section contains an ion gauge, a Titanium-sublimation pump, a turbo-pump, and an ion-pump. Toward the very end of this section is the slowing window where we deliver the slowing beam, $v = 2$ and $v = 3$ repumps, and 605 nm Raman beam.

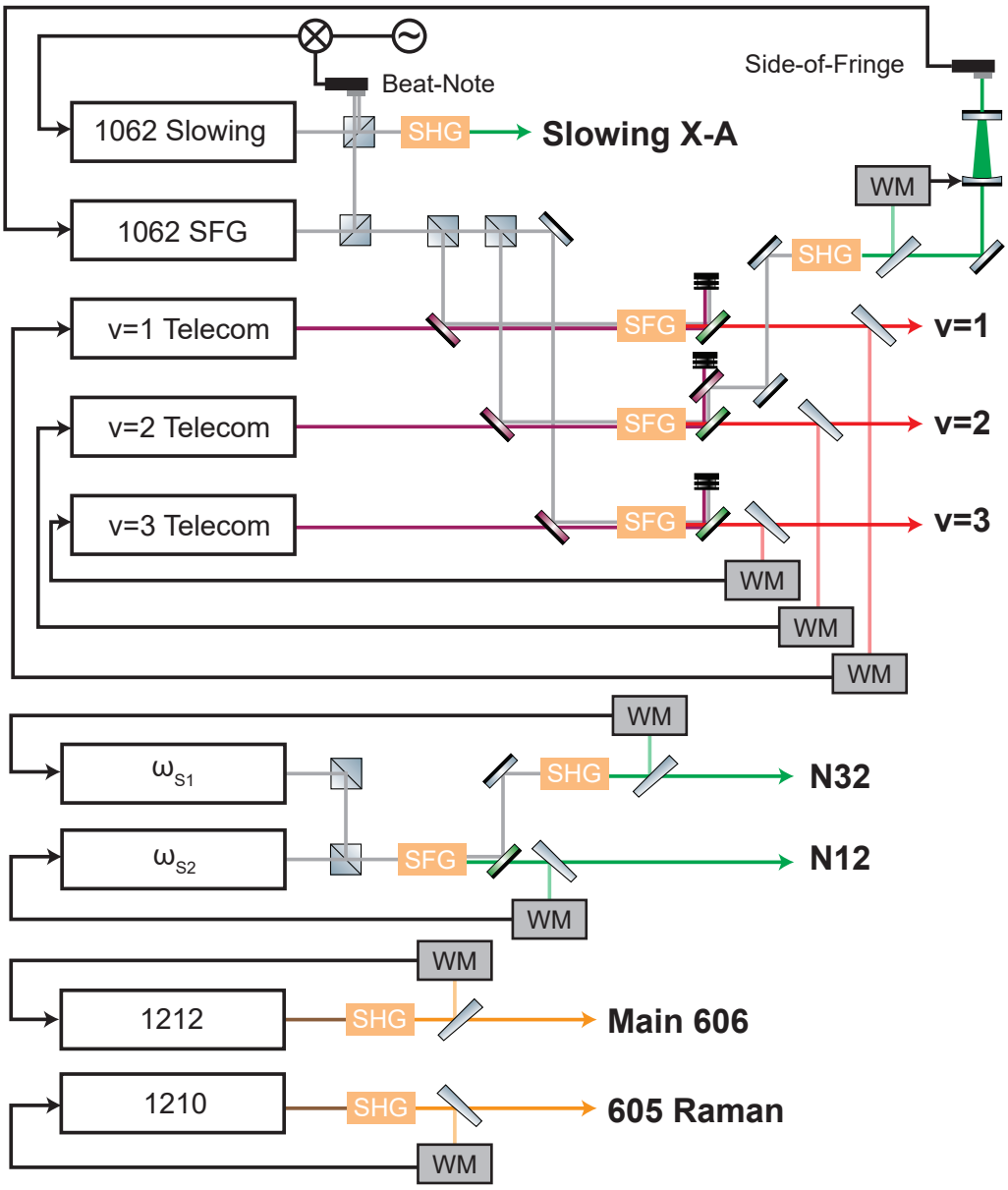


Figure 3.3: Light Generation and Laser Locking Schematic

3.3 Lasers

In this section, we provide brief details on several lasers systems. An overview of how all optical frequencies are generated and locked is illustrated in Fig. 3.3. Details on each system are provided in the subsequent subsections.

3.3.1 Laser Locking

The absolute frequency of all lasers are referenced to a wavemeter (HighFinesse: WS7-60). This wavemeter can read out eight separate visible optical frequencies to a precision of 100 kHz. To improve the wavmeter accuracy and minimize fluctuations from the environment, we place the wavemeter in a sealed vacuum canister (kept at atmospheric pressure) inside our climate-controlled laser enclosure. After a few years of operation, the absolute frequency of the 606 nm laser for producing a MOT drifts by less than ~ 1 MHz each year, indicating good long-term stability.

Up to eight optical wavelengths are delivered to the wavemeter via a voltage-controlled mirror (galvo) switchyard [97]; the wavelengths of these eight lasers are measured sequentially. Accounting for wavemeter camera exposure and mirror switching times, a bandwidth of ~ 20 Hz can be achieved using all eight channels. The frequency of each laser is sent to a Labview digital PID, and feeds back on frequency actuators to stabilize each laser's frequency. Fig. 3.3 illustrates this feedback network for the eight stabilized frequencies.

In addition to stabilizing the absolute frequency of each laser, we perform fast feedback on the 1062 nm SFG seed used to generate the vibrational repumper lasers. This feedback is implemented using a scanning Fabry-Perot cavity (Thorlabs SA200-5B) and helps narrow the seed laser's linewidth. In this case, the digitial PID adjusts the the length of the scanning Fabry-Perot, and the seed is locked to a cavity transmission feature via side-of-fringe locking.

3.3.2 Slowing $(X - B)$ Laser

Slowing light addressing the $X^2\Sigma^+(v = 0, N = 1) \rightarrow B^2\Sigma(v = 0, N = 0)$ transition is generated from a seed at 1062 nm. This seed is offset-locked via a beat-note lock to a second seed, which is used to generate the vibrational repumpers (see Section 3.3.4). The beat-note between these two lasers is stabilized to an externally supplied voltage-controlled frequency reference. This setup enables chirping the slowing seed laser's frequency over the ~ 150 MHz during the ms-scale chirped slowing protocol.

Following the offset lock, the slowing seed has sidebands added using a fiberized-EOM (see Chapter 5 for details). The light is amplified and frequency-doubled to 531 nm using a Precilaser system. The slowing light is finally delivered counter-propagating to the molecular beam through the slowing window of our vacuum chamber.

3.3.3 Main 606 nm ($X - A$) Laser

Light at 606 nm drives the $X^2\Sigma^+(v = 0, N = 1) \rightarrow A^2\Pi_{1/2}(v = 0, J = 1/2, +)$ transition. It is generated from a seed at 1212 nm, which is amplified and frequency-doubled using a Precilaser system.

This light first passes through a double-pass AOM, which enables rapid power switching and global frequency control. Next, the light passes through the 606 AOM switchyard, consisting of a series of cubes to split the light into four paths. The power splitting of these cubes roughly produce a power ratio of $5 : 3 : 1 : 3$ for the $F = 2, 1^+, 0, 1^-$ paths. The $F = 1^-$ AOM is in a double-pass configuration while the other three paths use single-pass AOMs. Each frequency component is delivered to one of the inputs of a 4×4 PM fiberized power-splitter. The splitter distributes the input power equally between the four outputs. The four outputs are delivered to 1) a MOT XY breakout, which generates MOT light in two retro-reflected MOT beams in the $\hat{x} - \hat{y}$ plane, 2) the MOT Top delivery system (detailed in Section 3.4.3), 3) the MOT Bottom path, and 4) an auxiliary breakout system, which splits light for use in 5-beam Λ-imaging and single-beam optical pumping.

3.3.4 Vibrational Repumping Lasers

Three independent vibrational repumper lasers drive the $X^2\Sigma^+(v = v, N = 1) \rightarrow A^2\Pi_{1/2}(v = v - 1, J = 1/2, +)$ transition for $v = \{1, 2, 3\}$. Each repumper is generated using a home-made SFG system, which combines light at 1062 nm and telecom light at $15xx$ nm. Each SFG system uses the same wavelength of 1062 nm light, which is amplified from the reference

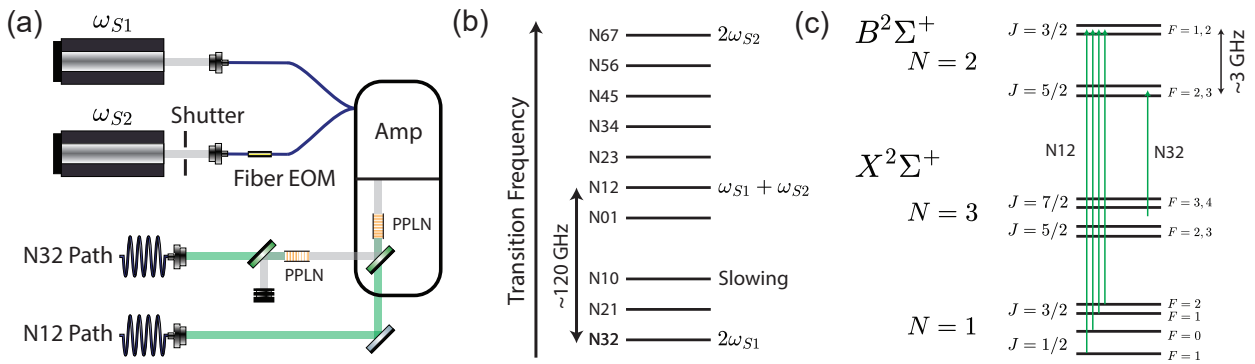


Figure 3.4: Rotational Repumper Lasers: (a) Two seeds (with frequencies ω_{S1} and ω_{S1}) are combined on a fiber splitter and amplified. The ω_{S2} seed can be shuttered off and sidebands are added using a fiberized EOM. After amplification, laser head's nonlinear crystal produces $N12$ light. The IR dump port from the laser head is directed to an external nonlinear crystal, which generates $N32$ light. (b) The allowed $N \to N \pm 1$ transitions along the $X - B$ transitions are roughly equally spaced in energy by $2B \sim 20\,\text{GHz}$. The seed configuration producing the frequencies of $N32$, $N12$, and the unused component are denoted, along with the main $X^2\Sigma^+(N=1) \to B^2\Sigma^+(N=0)$ light used for laser slowing (generated separately). (c) The $N12$ addresses the $B^2\Sigma^+(N=2, J=3/2)$ excited state while the $N32$ addresses $B^2\Sigma^+(N=2, J=5/2)$. Sidebands resonant with all hyperfine manifolds in $X^2\Sigma^+(N=1)$ are added to the $N12$ light.

seed used to offset-lock the slowing seed. After amplification, the power is split in three and each is delivered to a nonlinear PPLN crystals in a temperature-stabilized oven.

Three separate lasers amplify telecom seeds to produce light at 1540 nm, 1538 nm, and 1534 nm, which are each delivered to one of the nonlinear crystals to generate the $v = 1, 2, 3$ repumpers, respectively. The resulting light at 628 nm has optical sidebands added via free-space resonant EOMs. The sidebands are spaced by 25 MHz to address the four hyperfine F-levels in $X^2\Sigma^+(v = \{1, 2, 3\}, N = 1)$.

Unconverted light at 1062 nm from the $v = 2$ path is sent through a room-temperature nonlinear crystal to generate light at 531 nm which is used for frequency locking (details in Section 3.3.1). The $v = 1$ light is split between the MOT and slowing paths. $v = 2, 3$ light is exclusively delivered along the slowing path.

3.3.5 Rotational Repumping Lasers

Two rotational repumpers are used to pump population between the $X^2\Sigma^+(v=0, N=1)$ and $X^2\Sigma^+(v=0, N=3)$ rotational state manifolds. The first repumper addresses the $X^2\Sigma^+(v=0, N=3) \rightarrow B^2\Sigma(v=0, N=2)$ transition, which we call "$N32$". The second addresses the $X^2\Sigma^+(v=0, N=1) \rightarrow B^2\Sigma(v=0, N=2)$ transition, which we call "$N12$".

Two seeds at 1062 nm are used to generate these repumpers. The seed light is combined using a fiber splitter and amplified using a Precilaser system. We use the nonlinear crystal in the precilaser head itself to generate $N12$ light. The laser head also has an IR dump port, which we deliver to a nonlinear PPLN crystals in a temperature-stabilized oven to generate $N32$ light (Fig. 3.4(a)). Denoting the two seed frequencies ω_{S1} and ω_{S2}, we configure the frequencies so that $\omega_{N32} = 2\omega_{S1}$ and $\omega_{N12} = \omega_{S1} + \omega_{S2}$. This configuration ensures that the third undesired component at $\omega_u = 2\omega_{S2}$ is far away from transitions that would lead to additional population leakage (Fig. 3.4(b)).

For applications in which spectrally-pure $N32$ is needed, we shutter-off the ω_{S2} seed. Sidebands are added to the ω_{S2} seed using a high-bandwidth EOM, which enables the $N12$ light to address all hyperfine manifolds of the $X^2\Sigma^+(v=0, N=1)$ ground state. The $N32$ light remains unaffected, and no sidebands are produced.

One last important note regarding the two $J = \{3/2, 5/2\}$ manifolds in $B^2\Sigma^+(v=0, N=2)$. Starting from the $X^2\Sigma^+(v=0, N=1)$ state (containing $F = \{0, 1, 2\}$ manifolds), selection rules dictate that the $N12$ light should address the excited $J = 3/2$ level (containing $F = \{1, 2\}$) for all transitions to be allowed. Similarly, starting from the $X^2\Sigma^+(v=0, N=3)$ state (containing $F = \{2, 3, 4\}$ manifolds), selection rules dictate that the $N32$ light should address the $J = 5/2$ level (containing $F = \{2, 3\}$) for all transitions to be allowed (Fig. 3.4(b)). The large (negative) spin-rotation coupling in the B state separates these excited J levels by ~ 3 GHz.

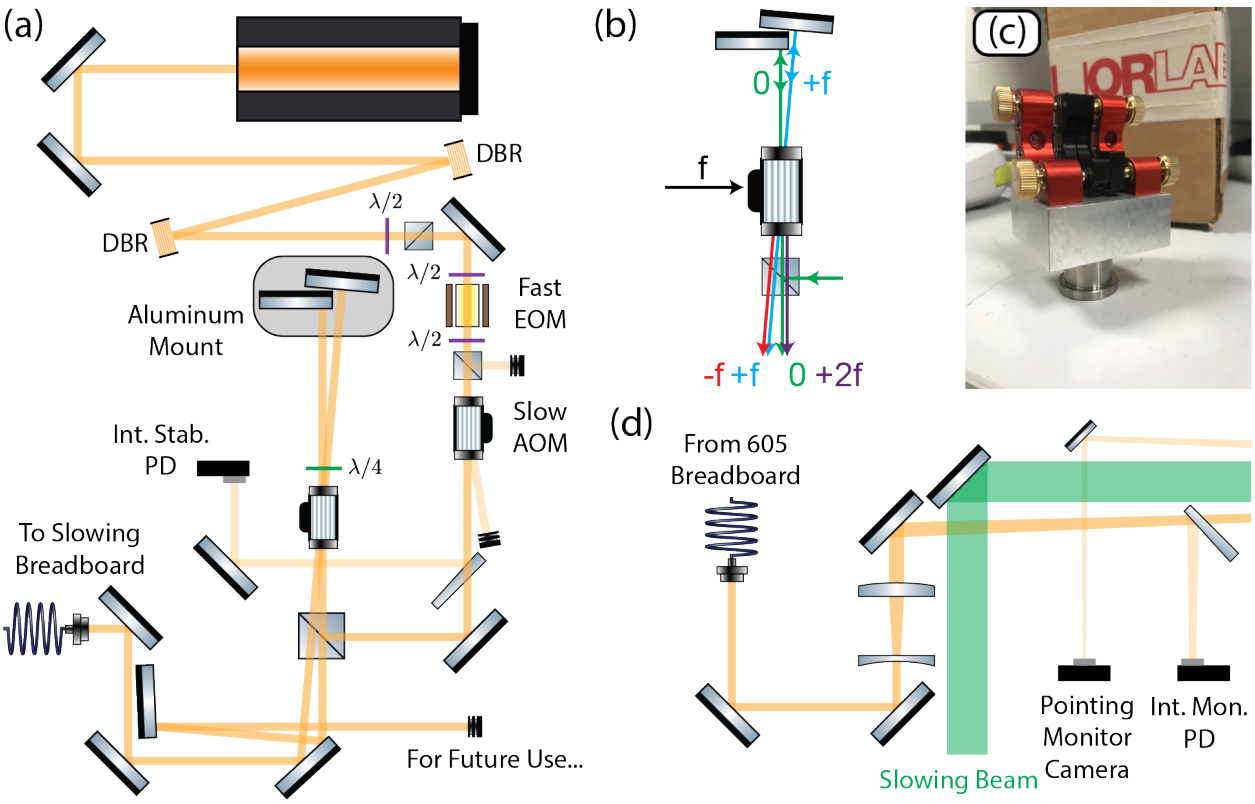


Figure 3.5: 605 Laser System and Associated Components: (a) The 605 laser spectrum is cleaned using two distributed Bragg reflectors (DBR). The power is stabilized using an EOM and AOM to compensate for fast and slow frequency fluctuations, respectively. The power is monitored using a pickoff and photodiode. Sidebands are then added using a single AOM that acts both as a switch and sideband generator. When RF is sent to the AOM, diffracted light is delivered to an optical fiber; when no RF is applied, a D-shaped mirror separates the 0th order beam for downstream use. (b) Operating principle of the switch-sideband AOM, with colors exaggerating the shifted frequencies of the sidebands when the AOM is turned on. The two optical frequencies within each beam exiting the AOM are offset for clarity. (c) Monolithic mount for the two AOM retro-reflection mirrors. We find this monolithic mount is necessary to stabilize the optical path-length fluctuations to the sub-nm level, which is crucial for low phase noise in this system. (d) Light is delivered to the molecules via the slowing window. The 605 beam makes a small angle with the window, allowing optics to not interfere with the slowing path. The power is monitored via a pickoff and photodiode; beam pointing is monitored using the reflection off the slowing window and a camera.

3.3.6 Coherent Two-Photon Raman (605 nm) Laser

As explored in Chapter 9, the detuning that maximizes the ratio of coherent two-photon Rabi coupling to off-resonant scattering for driving a hyperfine qubit encoding lies approximately 1 nm away from the main cycling transition at 606.3 nm. This detuning is too large to

be accessed using standard sideband generation techniques, and since high optical power at this wavelength is essential, we implemented an independent laser system to generate the required light. The system consists of a homemade Steck external-cavity diode laser (ECDL) operating at 1210 nm, which is subsequently amplified and frequency doubled using a Precilaser Raman fiber amplifier system. In addition to enabling the new qubit encoding, this wavelength is well-suited for other coherent manipulations, such as applying local S_z shifts and implementing an upgraded Raman sideband cooling scheme.

Given these multiple use cases, the laser system was designed to maximize optical efficiency while maintaining flexibility, without resorting to a conventional switchyard architecture that would divide optical power among multiple beam paths. Instead, our approach relies on daisy-chaining multiple optical manipulations onto a single beam, allowing different functionalities to be accessed sequentially. As long as these operations are not required simultaneously, this configuration provides an efficient and flexible solution.

The implementation of this system is shown in Fig. 3.5(a). To suppress optical pedestals near the main cycling transition that would drive population out of the qubit manifold, we use two distributed Bragg reflectors (Coherent: 633 nm Beam Splitter PN118-ER315-004), achieving at least 60 dB suppression at the cycling transitions located approximately 1 nm from the carrier frequency. Power stabilization over a broad bandwidth is achieved using a feedback loop incorporating both an EOM and AOM, with the AOM correcting low-frequency intensity noise and the EOM suppressing high-frequency fluctuations.

A key component of the system is a single-AOM configuration that simultaneously functions as an optical switch and a sideband generator, producing two frequency components separated by ~ 122 MHz. The operating principle, illustrated in Fig. 3.5(b), involves diffracting an incident beam into both the 0th and 1st orders using an AOM driven at ~ 61 MHz. Both beams are retro-reflected using a monolithic retro-reflector mount (Fig. 3.5(c)), which achieves sub-wavelength (measured even to be sub-nm) differential path-length stability. On the second pass through the AOM, a portion of the 0th order beam is diffracted into the

-1st order, while a portion of the 1st order remains undiffracted. These two resulting beams, which are not collinear with the input, are shifted by $\pm 61\,\mathrm{MHz}$, forming the desired sidebands to drive a two-photon transition between the qubits states. When no RF power is applied, the beam remains in the 0th order and is simply retro-reflected, allowing the full optical power to be redirected for downstream applications. In this case, the undiffracted beam is picked off using a D-shaped mirror for future use, such as in Raman sideband cooling or local S_z control. Generating the sidebands can be done with an overall power efficiency of $\sim 45\%$, close to the expected optimum.

Proper spatial overlap of the forward and retro-reflected beams within the AOM crystal is critical. Due to the finite speed of sound in the crystal, imperfect overlap can lead to timing mismatches between the $\pm 61\,\mathrm{MHz}$ sidebands, which becomes particularly significant for short pulses on the order of $\sim 10\,\mu\mathrm{s}$.

Finally, the 605 nm light is delivered to the main experiment table via a polarization-maintaining fiber. A telescope is used to focus the beam to the microscope objective plane. A small pick-off monitors the optical power, while a reflection from the slowing window is imaged onto a camera to track beam pointing. Precise beam alignment is especially important because the array axis is perpendicular to the propagation direction of the 605 nm beam, requiring careful positioning to ensure uniform illumination across the array.

3.4 Microscope Objective Paths

The microscope objective is used for the following:

1. Deliver tightly focused light at 781 nm, which forms the optical potentials used to trap and rearrange individual CaF molecules.

2. Collect light at 606 nm or 531 nm, which is released from the (point-source) molecules during fluoresence detection. Collecting light at 531 nm was only breifly used during

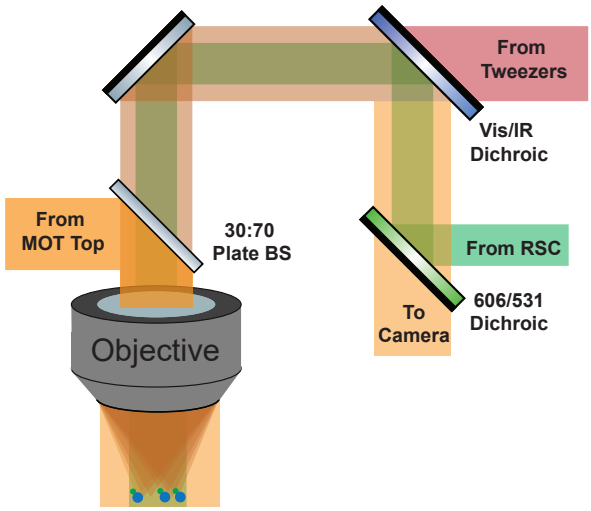


Figure 3.6: Optical Paths Through Objective: Starting from the objective, a 2" 30:70 (R:T) plate non-polarizing beamsplitter (Thorlabs BSS10) is used to combine the MOT-top path beam. Next, a 2" long-pass dichroic mirror (Thorlabs DMLP650) combines/separates the fluorescence at 606 nm and Raman control at 531 nm from the tweezer light at 781 nm. Finally, the fluoresence is separated from Raman control using a long-pass dichroic mirror (Semrock FF562-Di03-25x36).

an investigation of bichromatic imaging (Chapter 6). For all other work involving fluoresence imaging through the objective, 606 nm light was collected.

3. Deliver a large collimated beam of 606 nm light for the top MOT beam.

4. Deliver a small collimated 531 nm beam, which was used to manipulate axial motional states in a Raman sideband cooling investigation detailed in Refs. [5, 90].

These four optical paths are delivered to the objective using a combination of dichroics and beamsplitters. In brief, fluoresence at 606 nm, Raman control at 531 nm, and the tweezers at 781 nm can all be combined using a sequence of dichroics; combining with the MOT top light (also at 606 nm), requires using a non-polarizing plate beamsplitter. This configuration is illustrated in Fig. 3.6. More details on each path and their integration is given in the subsequent sections.

3.4.1 Tweezer Path

In this section, we present details on the optical tweezer path and the two 2D-AODs. Briefly, a pair of collimated beams of waist $w_0 \approx 2\,\text{mm}$ are sent through a pair of 2D-AODs. After cleaning the polarization, the diffracted orders from each AOD are combined on a polarizing beamsplitter. A subsequent waveplate and PBS allow adjusting the relative power balance between these two paths (Fig 3.8). The power into each AOD is stabilized via feedback using a reflection off the non-polarizing side of a plate polarizing beamsplitter (Thorlabs PBSW-780). This this signal is fed to a PID controller connected to a switch-AOM (not illustrated in Fig 3.8). The set point of the PID is provided by a programmable analog voltage. We also monitor the power in the tweezer path (post-AODs) via the reflection off the Vis-IR dichroic mirror.

A notable feature of this setup is that the interlaced AOD is mounted upside-down relative to the main AOD. This somewhat unusual configuration arose from a series of technical constraints encountered during the first iteration of integrating two AODs into the same optical system. In that initial implementation, both tweezer arrays were derived from a single laser source. To prevent the light from the two paths from driving unwanted two-photon Raman transitions when overlapping on the molecules, we used power-control AOMs with opposite diffraction orders ($\pm 90\,\text{MHz}$), along with AODs configured to produce opposite-signed diffraction orders along both axes (each centered at $\sim 100\,\text{MHz}$). As a result, two overlapping tweezers from the main and interlaced arrays were separated on average by $\sim 580\,\text{MHz}$, far exceeding the $\sim 150\,\text{MHz}$ span of the $N = 1$ hyperfine manifold.

After assembling this initial system (with the interlaced AOD in its standard orientation), we observed an unexpected distortion while aligning the two arrays (Fig. 3.7(a)). Specifically, there was a mismatched quadratic spacing term: the outermost tweezers could be aligned, but the central tweezers failed to overlap. Interestingly, this discrepancy appeared only along one axis. Although it was possible to compensate for this nonlinearity by adjusting the RF tones applied to one of the AODs, doing so introduced unequal frequency spacing, which in

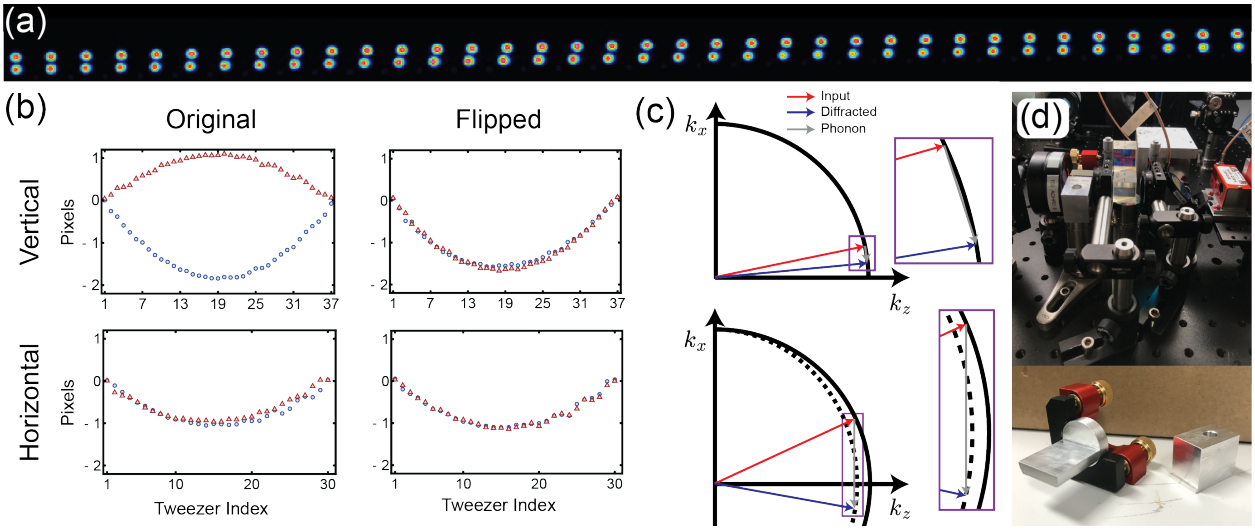


Figure 3.7: Nonlinearities in High-Bandwidth AODs: (a) With the two end tweezers of the main and interlaced AODs aligned, the center tweezers do not align, indicating a relative quadratic term in the frequency-to-spacing transfer function. (b) Left: Before flipping the relative orientation of the AODs, only one axis had matching quadratic terms. Right: after a spatial inversion and one (horizontal) reflection from a PBS, both the horizontal and vertical nonlinearity matched. The data show the spacing (camera pixels) with the dominant linear term removed for the main array (blue circles) and interlaced array (red triangles). Tweezers are generated by RF tones spaced by 1 MHz (c) We believe the non-linearity arises from the working mechanism of a high-bandwidth AOD. Top: a conventional AOM that utilzes an isotropic (not birefringent) material operates with the phonon and photon nearly orthogonal, leading to negligible frequency-to-angle nonlinearities. Right: a high-bandwidth AOD utilizes a birefringent material to maximize bandwidth, and consequently operates with a large relative angle between the photon and phonon. The diffraction from the phonon at this large angle cannot be captured by a small-angle approximation, leading to high-order terms in the frequency-to-angle conversion factor, leading to the observed nonlinearity. (d) Top: main (right) and interalced (back) AOD with beamsplitters and cleanup polarizers. Bottom: custom mounts and adapters to maximize space efficiency.

turn led to significant intermodulation-induced heating and population loss. This made it clear that the underlying distortion itself needed to be addressed.

We first hypothesized that aberrations were introduced by the cube beamsplitters, affecting only the reflected (interlaced) path. However, careful measurements of the beam flatness in both the transmitted and reflected ports ruled out this possibility. We then considered whether an intrinsic nonlinearity in one of the AOD axes could explain the effect. Detailed characterization of both AODs along both axes revealed a more subtle picture: each axis

of each AOD exhibited a quadratic spacing term, but while the horizontal-axis nonlinearities were well matched between the two arrays, the vertical-axis terms were nearly equal in magnitude and opposite in sign.

This pattern pointed to the RF frequency ordering used to generate the tweezers as the underlying culprit. Along the horizontal direction, the leftmost (rightmost) tweezers in both arrays correspond to low (high) RF frequencies. In contrast, along the vertical direction, the topmost tweezer is generated by a high-frequency tone in the main array but a low-frequency tone in the interlaced array. This reversal implies an opposite sign of the quadratic distortion between the two arrays along that axis.

To test this hypothesis, we constructed a mount that allowed the interlaced AOD to be installed upside-down. An additional reflection was introduced to preserve the handedness of the horizontal axis; this was implemented using a PBS, which also served to clean the polarization of the interlaced beam and leaves open the possibility of incorporating additional beam paths in the future. As shown in Fig. 3.7(b), this modification aligns the sign of the quadratic term across both axes of both arrays.

We attribute the origin of this nonlinearity to the intrinsic physics of high-bandwidth AODs, which are widely used in tweezer array experiments. To maximize bandwidth, birefringent crystals are cut such that the input light lies on a specific energy–momentum contour (see Fig. 3.7(c)). Upon diffraction, the photon absorbs a phonon and changes polarization, emerging on a different contour. By carefully choosing the orientation of the crystal axes and acoustic propagation direction, energy and momentum conservation can be satisfied over a broader range of phonon energies, thereby increasing the usable bandwidth.

A consequence of this geometry is that the deflection angle of the diffracted light becomes nonlinear in the phonon energy (i.e., RF frequency). Importantly, reversing the ordering of frequencies across the array (i.e., swapping which spatial position corresponds to high versus low RF tones) reverses the sign of this nonlinearity. This explains the observed behavior

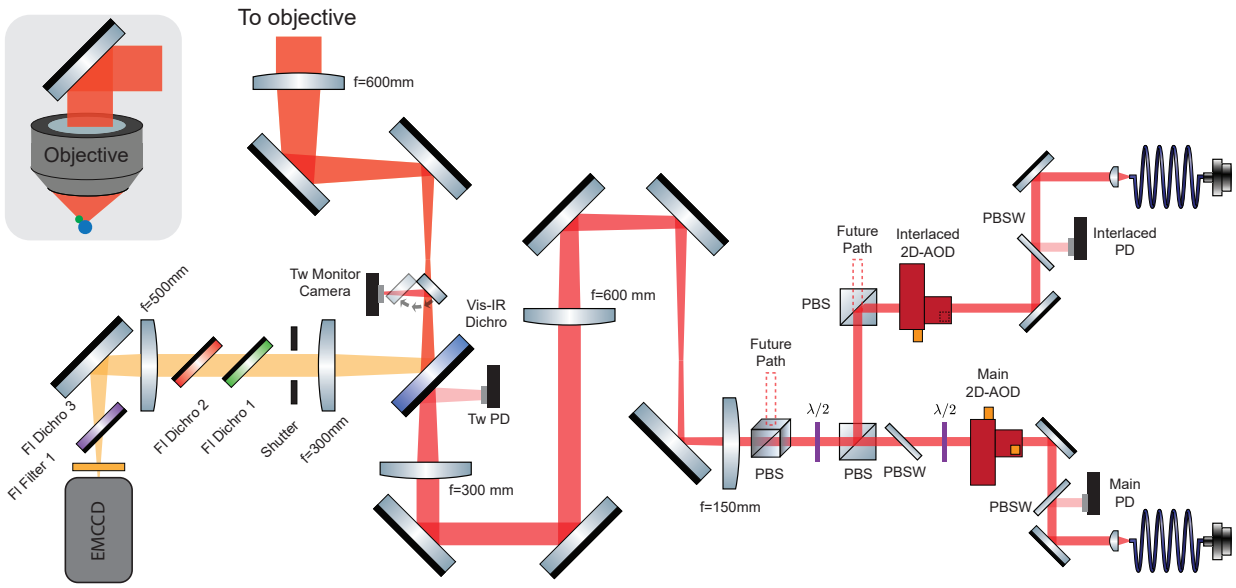


Figure 3.8: Tweezer and Fluoresence Optical Paths: The tweezer path (right) begins with two collimated beams, whose power are stabilized by monitoring the non-polarizing reflection off a plate polarizer. After each 2D-AOD the polarization is cleaned before the two paths are combined on a PBS. Note that the interlaced 2D-AOD is mounted upside-down relative to the main 2D-AOD. A final $\lambda/2$ waveplate and PBS control the relative power of the main and interlaced paths sent into the tweezer path. Unused ports of PBS cubes will eventually be interfaced with hologram-generated optical potentials. The downstream tweezer optics consist of two telescopes and the objective. A flip mirror in an intermediate imaging plane allows monitoring the position and intensity of the tweezers, helpful for power balancing and fine alignment. The tweezer light passes through a long-pass Vis-IR dichroic mirror (Thorlabs DMLP650); the reflection off the back surface is used to monitor the tweezer power. The fluorescence imaging path (left) begins at the molecules. Fluoresence is collected through the objective and reflected off the Vis-IR dichroic mirror. A shutter is placed in the fluoresence path to protect the EMCCD camera from light that propagates directly through the objective during laser cooling steps. A series of dichroics and filters allow sending light near the $X-B$ transition through the objective (Fl Dichro 1; Semrock FF562-Di03), filter stray tweezer and vibrational repump light (Fl Dicro 2; Semrock FF625-Di01), filter additional tweezer light (Fl Dichro 3; Semrock FF749-SDi01), and filter all light except a 15 nm band around the molecular fluorescence (Fl Filter 1; Semrock FF01-605).

and motivates the upside-down mounting of the interlaced AOD (Fig. 3.7(d)), which restores consistent quadratic spacing across both axes of both arrays.

3.4.2 Fluoresence Imaging Path

In this section, we present more details about the optical components involved in the fluoresence imaging path. Light emitted from the molecules are collected through the objective and imaged on an EMCCD camera (Andor iXon Ultra: DU-897U-CS0-BV). Stray light is filtered via a series of dichroic mirrors and filters. One of these dichroic also enables sending light near the $X-B$ transition to the molecules, which has been used for both our investigations into Raman sideband cooling and enables spatially separated optical pumping zones. This path also has a large shutter to protect the EMCCD camera from high-intensity light propagating directly through the objective during various free-space laser cooling stages. Additional details about the dicroics and filters, are presented in Fig. 3.8 and its caption.

3.4.3 MOT Top Path

In some experiments using a microscope objective, one axis of the MOT beams is along the microscope objective axis. In these cases, a collimated beam will traverse "backwards" through the objective and, if the Fourier plane of the objective is outside the objective, the beam will come to a focus on the other side of the objective. In these scenarios, a mostly transparent plate with a small mirror at its center can be used to retro-reflect the MOT along this axis. Unfortunately, for our objective, the Fourier plane is "inside" the objective. In this scenario, we decided it would be more straightforward to send an independent beam through the objective, which would emerge collimated. Although this strategy is less efficient with power, it is convenient to have independent degrees of freedom controlling the top and bottom MOT arms. This is especially helpful for optimizing the power balance and beam size in the top and bottom MOT arms.

We began with a Zemax simulation with a collimated beam propagating backwards through the objective. Adding a lens afterward does collimate this beam, but significant aberrations remain. To remove these aberrations, we converged on a design utilizing three singlet lenses shown in Fig. 3.9(a). This design utilizes three singlet lenses, one of which is

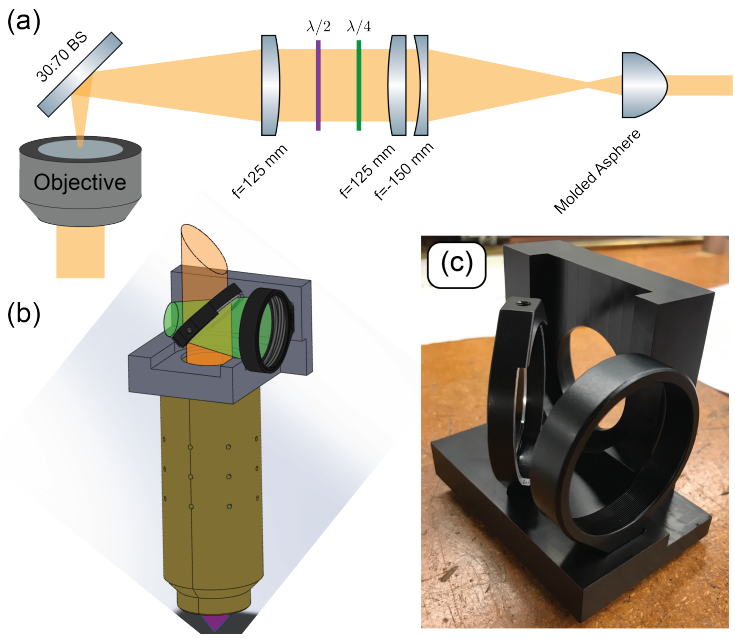


Figure 3.9: MOT Top Path: (a) The following four optics are used between the objective and fiber collimator: f=16mm Molded Aspheric Condenser (Thorlabs: ACL25416-A); f=-150mm Singlet (Thorlabs: LC1611-A); f=125mm Singlet (Thorlabs: LA1384-A); f=125mm Singlet (Thorlabs: LA1384-A). (b) Solidworks rendering of objective, Delrin mount, and exemplary tweezer/fluoresence beam (orange) and MOT top beam (green). (c) Delrin custom mount with the lens tube mount (for the final f=125mm singlet), milled fixed mirror mount (for the 30:70 plate beamsplitter), and alignment groove used for preliminary alignment targets described in Section. 3.5.3.

operated in the conventionally "wrong" orientation;[1] in particular, the convex side of the negative focal length lens faces towards the focused beam. This configuration adds a controllable amount of spherical aberation that compensates for the aberrations introduced by running the objective in the "wrong" orientation. A final molded asphere then collimates the beam to a size compatible with standard fiber collimators.

From an optomechanics perspective, this configuration is quite spatially constrained due to how rapidly the beam diverges from the objective. To maximize spatial efficiency, a custom-machined Delrin mount was made, which slips into the outer diameter of the micro-

[1]Lenses are almost always designed to be oriented to minimize the largest incidence/transmission angle of light. In particular, plano-convex lenses (+ focal length) should have the flat side face the focused beam. Plano-concave lenses (− focal length) should have the flat side face the diverging beam. Thus, in a telescope (both Galilean and Keplerian), *both* flat surfaces face inward. Non-singlet lenses have a "most flat" and "most curved" side, which follow the same rule.

scope objective. It has grooves and mounting holes for a lens tube mount and mirror mount, whose sides were milled out to maximize the clear aperture (Fig 3.9(b,c)). Importantly, the wedge angle, wedge orientation, and thickness of the beamsplitter plate must be accounted for when designing the angle and position of the beamsplitter grove and mounting hole.

3.5 In-Situ Interferometric Alignment of a High-NA Microscope Objective

In this section, we detail a novel protocol for achieving in-situ diffraction limited performance of an imaging system utilizing an in-vacuum spherical bead. This bead is placed on a vacuum-compatible translation stage, enabling the bead to be extended for alignment and then retracted for subsequent operation of the experiment. This allows achieving diffraction-limited performance of both the fluoresence imaging and tweezer generation paths. Beyond alignment of the objective, this in-vacuum spherical reflector can greatly assist in aligning auxiliary beams and imaging paths.

Diffraction limited performance of a microscope objective is important in an optical tweezer array experiment. When imaging scattered photons collected by an objective, diffraction-limited performance ensures that all of the fluorescence can be concentrated onto a small region of a camera, increasing the signal-to-noise during readout. High signal-to-noise increases the fidelity of identifying the occupation of each tweezer during state detection. For creating optical potentials, diffraction limited performance allows optical power to be used more efficiently, creating the same trap depth for less total optical power sent through the objective. This practically means that more tweezers can be generated for fixed total laser power. Additionally, the smaller waist at the focal plane increases trapping frequencies, which plays an important role in detection and cooling protocols such as Λ-enhanced imaging and Raman sideband cooling.

3.5.1 Principle of Operation

The essential components of this alignment apparatus are shown in Fig. 3.10. A low-aberration and collimated beam is sent through a large non-polarizing beamsplitter (NPBS) cube and wedged window. The prompt reflection from the wedged window serves as a phase reference beam, which is reflected from the NPBS. To account for the possibility of a small angle in the reflection from the wedge window, we model this reference beam as $E_1 = E_0(x, y)e^{-i(k_x x + k_y y)}$. The beam that is transmitted through the wedged window passes through optical components and the objective, resulting in a focused beam. The center of a spherical bead is placed at the beam's focus. Assuming a perfect imaging system, the equal phase wavefronts of the focused beam will be spherical waves concentric with the bead for a bead radius much larger than beam's Raleigh-range $r_B \gg z_{\mathrm{R}} = \frac{\pi w_0^2}{\lambda}$. Thus, the bead forms a perfect retroreflector, causing the bead's reflection to retrace the input beam's path through the imaging system. This reflected beam is reflected by the NPBS with electric field E_2.

Slight departures from the idealized case of an aberration-free imaging system can be modeled by a spatially dependent phase pattern $e^{i\phi(x,y)}$ and a perfect lens; we also assume a spatially uniform transmission t. This results in an effective aberration element $\tilde{A} = te^{i\phi(x,y)}$, giving $E_2 = E_0(x, y)t^2 e^{2i\phi(x,y)}$. Assuming a plane-wave $E_0(x, y) = E_0$, the reflected port of the NPBS is $E_{\mathrm{NPBS}} = E_1 + E_2 = E_0(e^{-i(k_x x + k_y y)} + t^2 e^{2i\phi(x,y)})$, leading to an interference pattern

$$\begin{aligned} I_{\mathrm{NPBS}}(x, y) &= |E_0(e^{-i(k_x x + k_y y)} + t^2 e^{2i\phi(x,y)})|^2 \\ &\propto 1 + t^2 \cos\left[2\phi(x, y) + (k_x x + k_y y)\right]. \end{aligned} \tag{3.1}$$

In principle, $\phi(x, y)$ contains all information about all aberrations deviating from a diffraction-limited system. In Section 3.5.4, we present more details on how we generate this interference signal, and how it is incorporated into a real-time feedback protocol to

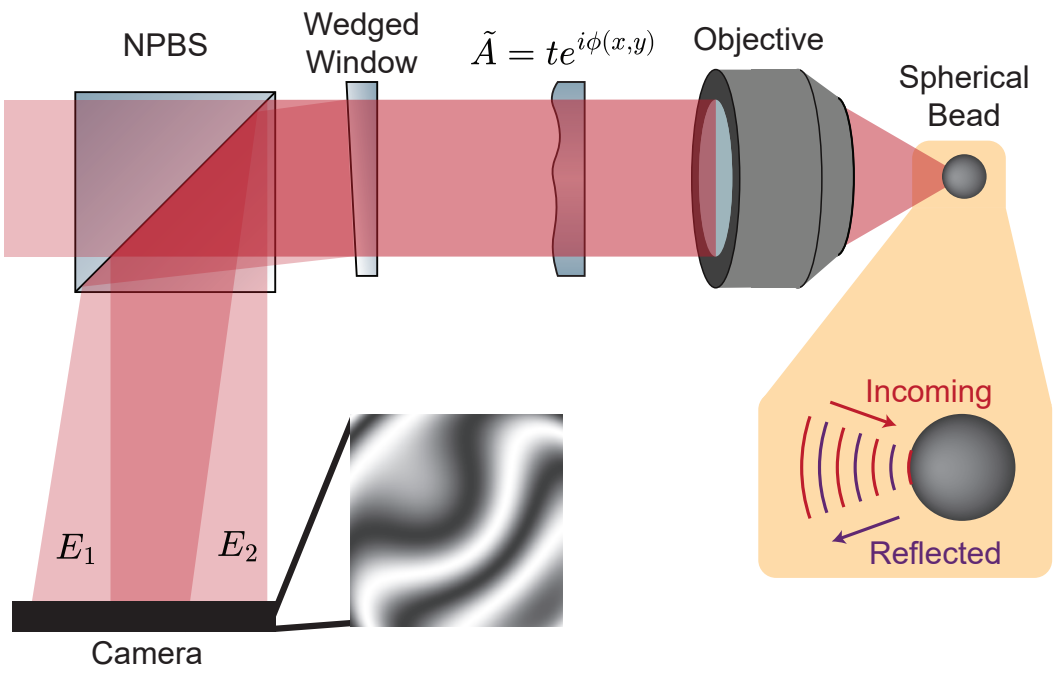


Figure 3.10: Operating Principle of Bead Measurement: The promptly reflected beam (E_1) is interfered with a beam traversing the entire optical system (E_2), which has been subjected to imperfections and aberrations captured by $\tilde{A}$. For a perfect beam, the incoming wavefronts after the objective are spherical, concentric with the bead, which forms a perfect retro-reflector. An exemplary simulated interference pattern is shown, which can be monitored in real-time using a camera.

minimize astigmatism and spherical aberration in our fluorescence detection and tweezer projection paths. A test-setup of this interferometer is shown in Fig. 3.11(d).

3.5.2 Mounting and Installation

The vacuum-compatible bead apparatus can be separated into three components: 1) the bead itself, 2) a custom-made stainless-steel rod to which the bead is glued, and 3) a vacuum-compatible translation stage attached to a flexible bellow and a 3-axis control setup.

The bead itself is a high-sphericity 1/4" diameter SiN sphere, commonly used in ball-bearings (Boca Bearing Company: 1/4 IN-C SI3N4 BALL GRADE 3). The Grade 3 sphericity means that there is a maximum deviation of $\approx 75\,\text{nm}$ from a perfect sphere across the entire bead. Since the NA of our objective implies that at most only 12% of this bead's

surface will be utilized, the bead can be well-approximated as a perfect sphere at the sub-wavelength level.

The bead is glued using a UHV compatible epoxy (Accu-Glass: UHV Epoxy PN111785) on a custom-made stainless steel mount (Fig. 3.11(a)). On the bead-side, a 1/4" diameter spherical drill head was used to mill an indentation into a nub on the stainless steel mount. The indentation depth, nub height, and nub placement was designed so that minimal optical access to the bead is restricted. A small square path was milled using the 1/4" spherical drill head so that the bead only makes contact with the bottom of the indentation. This ensures minimal glue is needed and no air bubbles are trapped between the bead and indentation. Finally, two thru-holes at the non-bead end allow attaching to the vacuum-compatible translation stage.

The vacuum-side of the translation stage (Huntington Manufacturing Labs: L-2172) has two threaded holes, which are used to attach the stainless steel mount. The room-side of the translation stage is attached to a flexible bellow, enabling full 3-axis movement of the bead. Fine control over the tip-tilt degrees of freedom is enabled by a custom-made collar attached to the translation stage, which sits inside a 2" mirror mount. The extension and retraction of the bead is controlled coarsely by a threaded rod. In practice, the translation stage can be moved by hand, so we simply add a 1"-diameter stainless steel pedestal as a spacer when the bead is not in use. In total, the translation stage has a range of 100 mm. When the bead is extended, fine control over extension and retraction is accomplished using a micrometer. The aluminum plates interfacing the micrometer and coarse threaded rod with the translation stage are custom-made. See Fig. 3.11(c) for the room-side translation stage 3-axis control components.

3.5.3 Preliminary Alignment

The microscope objective is concentric with the MOT coils, all of which are concentric with and sit inside the top recessed bucket window. To maintain the designed distance between

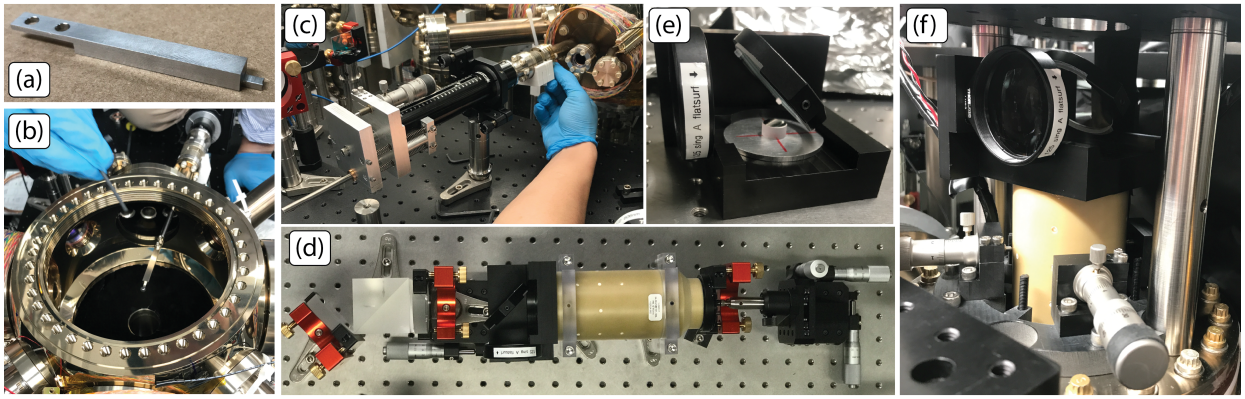


Figure 3.11: Bead and Associated Components Pictures: (a) Custom stainless steel bead mount with two thru holes for mounting onto a vacuum-compatible translation stage, and a nub with a spherical indentation where the bead is eventually glued. (b) Installation of the bead attached to the stainless steel component from (a), and attached to the vacuum-compatible translation stage. (c) The translation stage is attached to flexible bellows, which are attached to one of the three ports of a custom flange opposite to the ODT window. (far right). Extension and retraction of the stage is controlled by a coarse and fine micrometer stage (aluminum at far left). Tip-tilt is controlled by a mirror mount (black center). Advisor's hand for scale. (d) Test setup of the bead interferometry protocol. From left to right: NPBS (frosted glass), wedged window in red mirror mount, Delrin mount with the 30:70 (R:T) beamsplitter for combining optical paths with the top-MOT beam (black Delrin); microscope objective (tan cylinder); placeholder window in mirror mount; bead attached to 3-axis translation stage. Not shown is the telescope and camera to record the interference pattern. (e) Delrin MOT-top piece, showing one of the aluminium disks for coarse alignment of the incoming optical axis. The entire mount snuggly fits over the top of the objective. From top to bottom: anodized aluminum breadboard with hole to main tweezer breadboard; Delrin adapter, with one of the top-MOT lenses and beamsplitter visible; objective (tan); tip-tilt control micrometers making contact with objective (back spring-loaded plungers not visible); Delrin mount attached to top edge of the bucket window.

the microscope objective and the glass window, a Delrin sleeve is added to the bottom of the objective, making contact with the bottom of the bucket. A custom-designed Delrin mount is also attached to the outside edge of the recessed bucket (on top of the outer bucket lip sealing the recessed bucket to the science chamber). Attached to this Delrin mount are two micrometer-plunger pairs; each pair makes two points of contact with the outside of the microscope objective, allowing fine-adjustment of the angle between the microscope objective and the window (Fig. 3.12(f)). The spring-loaded plunger ensures that the circumference of

the objective is firmly held using four points of contact. The objective is initially positioned so that its optical axis is roughly perpendicular to the bucket window.

Alignment of the optics leading up to the objective for the tweezer, imaging, and MOT paths are described in Section 3.4. To summarize, the center of the tweezer and imaging paths (defined by a series of irises) are co-aligned; each component in the path is centered and made perpendicular to the optical axis.

The final two mirrors before the objective are reserved to align the optical path to the center of and perpendicular to the objective. To do so, we use aluminum disks that slide into a slot in the top-MOT Delrin mount with a rounded edge concentric with the objective (see Section 3.4.3). Two aluminum 2"-diameter alignment plates are used: one with a small hole in the center, another with a 1/2" mirror glued to its surface (Fig. 3.12(e)). The center of the incoming beam is referenced to the small hole. The angle of the optical path is defined by retro-reflecting an irised beam before the final two mirrors; the beam position is recorded using the camera illustrated in Fig. 3.10. The retro-mirror is then removed and the aluminum plate with the mirror is inserted; importantly, to mitigate small angles during the mirror mounting process, the aluminum plate is rotated, causing the reflected beam to trace out a circle. The center of this circle defines the axis normal to the objective. The objective axis is aligned to the center of the optical axis. These two steps (aligning the center and aligning the angle) are repeated until convergence.

3.5.4 Interferometric Alignment

To generate a clean collimated beam for the input of the bead alignment system, we collimate the output of a single-mode fiber using a long focal length ($f = 500\,\mathrm{mm}$) achromatic lens; we mount the lens on a mirror mount for fine-control over its angle. Using a shear-plate interferometer (Thorlabs SI254), we take extra care to iterate on lens centering and angle to ensure flat fringes measured by the shear plate.

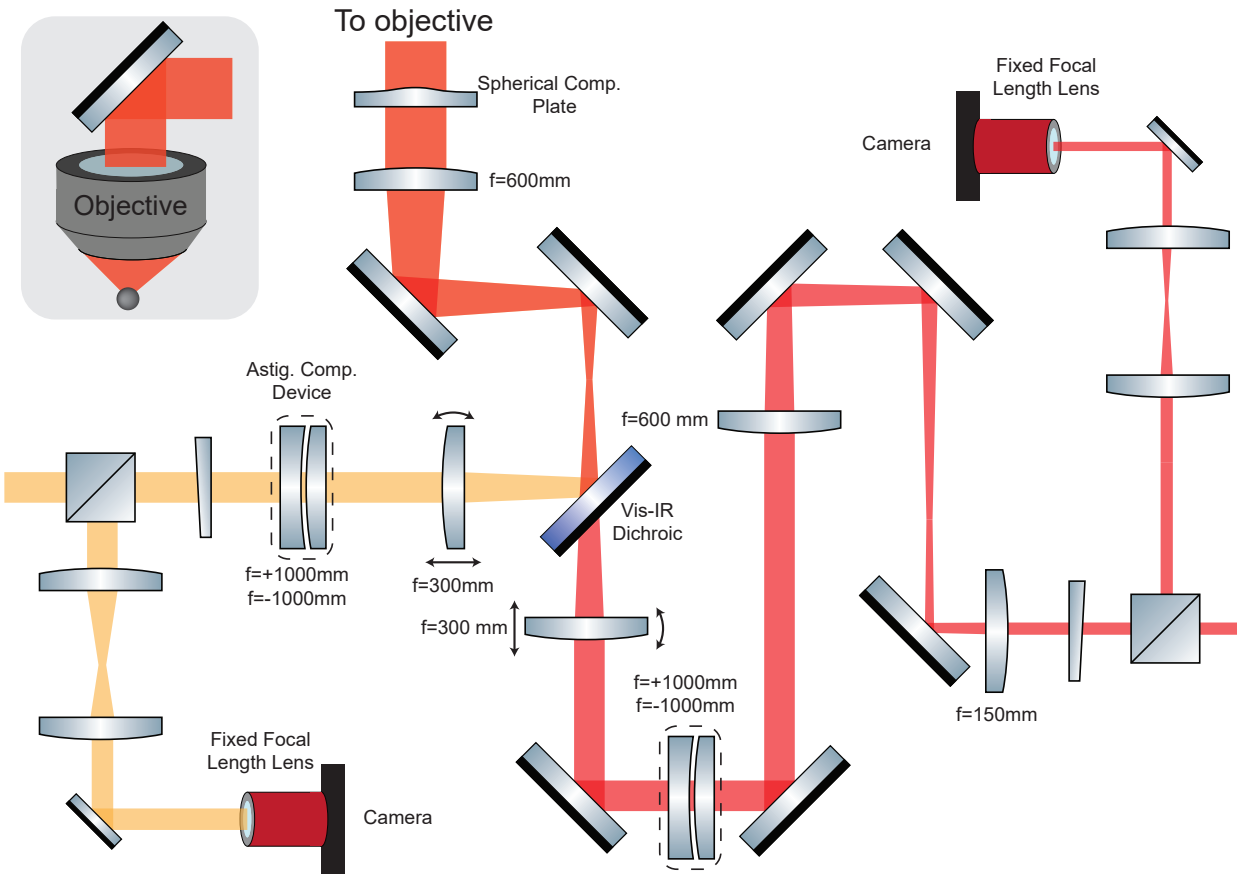


Figure 3.12: Optics for Spherical Bead Interferometry: Towards the left, light at 606 nm is collimated and sent through the imaging path optics; fine control knobs include the relative angle between the spherical lenses in the Astigmatism Compensating Device, the position and tip-tilt of the $f = 300$ mm lens. The promp and bead reflections are combined on the reflection port of the NPBS and imaged onto a camera. Towards the right is a nearly identical setup to align the 781 nm tweezer light path. A Spherical Compensation Plate is common to both paths.

Regarding the camera, to assist in the preliminary alignment discussed in the above section, we place a lens ($f \sim 200$ mm) directly after the NPBS and adjust the camera into its focus; this configuration is used to monitor reflected spots during the preliminary alignment described in Section 3.5.3. For monitoring the interference fringes, we insert a telescope after the NPBS and attach a fixed focal length lens (Thorlabs MVL12WA, f=12 mm) to a camera, enabling fine-focusing of the interference pattern. In particular, we reference the focus of this system to an iris placed in the Fourier plane (where the beam is collimated) of the alignment system, resulting in a sharp interference fringe.

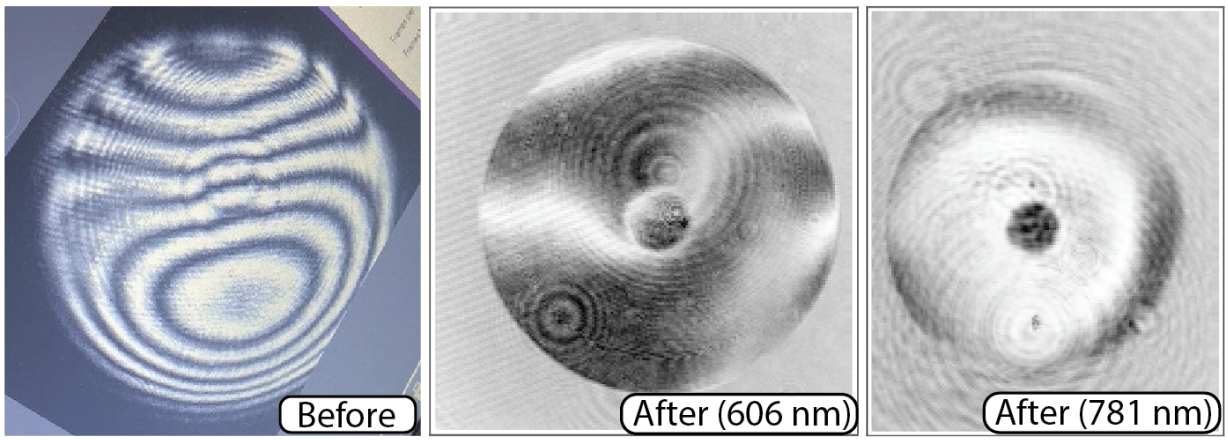


Figure 3.13: Interference Fringe Pictures: (a) Initial observed fringe before any optimization, showing substantial phase-front errors. (b,c) Final optimized interference fringe for imaging path (606 nm) and tweezer path (781 nm). An (intentional) linear phase gradient is added to (b) using the wedged window angle. Adding these linear gradients is often helpful to visually evaluate the wavefront flatness. The circular phase-jump defect seen in all images is also seen in the test data provide by Special Optics; diffraction-limited performance is expected even with this defect.

The components for the tweezer and imaging path alignment are illustrated in Fig. 3.12. In each path, the final lens before the Vis-IR dichroic mirror is mounted on a translation stage that can be translated along the optical axis. This lens is also mounted on a mirror mount, enabling fine angle control. In each path, a custom-made astigmatism compensation device is used. This device consists of two closely-separated plano-convex(-concave) cylindrical lenses with f=(-)1000 mm mounted in two concentric rotation mounts. With no relative angle between the cylindrical axis of the lenses, no astigmatism is introduced. By rotating one cylindrical lens, a variable-focus cylindrical lens is formed; rotating both lenses rotates the astigmatism axis.

The alignment proceeds as follows:

1. The spherical bead is inserted and adjusted using the degrees of freedom on its mounting stage described in Section 3.5.2 until a roughly collimated reflection exits the objective. The bead location is then adjusted until fringes are visible on the camera.

2. The dominant interference feature we observed corresponded to a defocus term (many concentric rings); this arises from an offset of the bead along the optical axis, which can be adjusted until the defocus is minimized. The next dominant term is astigmatism (leading to defocus only along one axis).

3. A significant portion of this astigmatism can be removed by adjusting the tip-tilt of the objective. From separate measurements of the bucket window glass itself, we observed a sizable wedge between the two glass surfaces. Modeling in Zemax confirmed that this should lead to astigmatism, and can be compensated by tilting the objective.

4. Residual defocus is removed by translating the lens closest to the dichroic (f=300 mm in each path).

5. Residual astigmatism is removed using the astigmatism compensation device.

6. These last two steps leave residual spherical aberration. This spherical aberration can be adjusted via the tip-tilt of lens closest to the dichroic, but the fine-adjustment steps must be repeated for each lens tip-tilt adjustment.

7. The spherical aberration cannot be completely minimized. To compensate for the residual spherical aberration term, we use the interference fringe itself to measure the magnitude of spherical aberration. The appropriate number of spherical compensation plates are then inserted directly before the objective to cancel the average spherical aberration measured in each path.

Illustrative interference fringes before and after this procedure are shown in Fig. 3.13, showing good cancellation of the optical aberrations.

Finally, the NPBS in each path is removed. For final integration into the imaging path, we send collimated light "backward" through the system along the optical axis of the system (defined by irises). The final lens and the camera are installed, and lens is adjusted until the spot size on the camera is minimized. For the final integration into the tweezer path,

collimated light is delivered so that it follows the optical axis of the tweezer system. The 2D-AOD is then installed a focal length behind the first lens in the tweezer optics system. We note that the 2D-AOD crystals are cut so that the doubly diffracted light is roughly parallel to the input beam, requiring no adjustment to the angle of this input beam.

3.5.5 Alignment of Other Beams

In addition to interferometric alignment of the microscope objective paths, the in-vacuum spherical bead is used to align auxiliary imaging paths and to rapidly position small beams at the focal plane of the objective.

To align auxiliary imaging paths, we first establish a "guide beam" centered on the bead and focused at its center. Rather than performing a full interferometric alignment, the back-reflected beam is used as a probe of both centering and focus. A collimated beam is sent through a lens with focal length approximately equal to the distance to the bead. The beam is centered when the back-reflection retraces the incident path. The axial position of the lens is then adjusted until the reflected beam is also collimated, indicating that the focus lies at the bead center. With the bead retracted, the guide beam is imaged onto a camera; minimizing the spot size ensures that the imaging plane coincides with the bead center.

Small (collimated) beams can be aligned by steering them onto the bead and maximizing the reflected signal. The spherical surface provides a geometric lever arm that enhances sensitivity to transverse offsets. For a bead of radius r and an alignment mirror located a distance $d \gg r$ away, a displacement δ at the bead produces a return displacement of $\frac{2d}{r}\,\delta$ at the mirror. For typical parameters ($r = 3.2\,\mathrm{mm}$, $d = 50\,\mathrm{mm}$), this corresponds to an amplification factor of ~ 30. This procedure reliably places the beam within the vicinity of the tweezers, after which the molecular signal is used for final optimization.

3.6 Computer-Experiment Interface

We use the software Cicero [98] for high-level programming of experimental sequences. Cicero is particularly well-suited for constructing time-ordered sequences spanning durations from $\sim$ 100 ms down to a few μs. Its interface enables rapid modification and debugging of straightforward, sequential protocols, as both analog and digital control words can be easily inserted and adjusted within a linear time-flow representation. However, Cicero has several limitations: its support for looped operations is restricted to a single level of nesting, and while control words can be grouped for convenience, the platform offers little to no capability for conditional logic within a sequence.

Cicero compiles experimental instructions and passes them to a server Atticus, which in turn distributes the corresponding instructions for digital and analog signals to a set of National Instruments (NI) cards responsible for hardware control. This architecture provides an interface between high-level sequence design and low-level experimental execution. A more detailed description of the Cicero–Atticus–NI control system can be found in Yukai's thesis [90].

Within the NI card interface, several channels are reserved for specialized functions. In particular, a dedicated trigger channel allows the system to pause execution until a digital trigger is received, after which the next Cicero loop begins. The system also supports mid-sequence triggering, enabling precise synchronization of specific experimental steps with external signals. For example, such triggering can be used to align sensitive operations with the phase of ambient 60 Hz electrical noise.

Although mid-sequence re-triggering is not employed in our sequences, we do synchronize the start of each sequence to a well-defined phase of the 60 Hz mains line. This ensures consistent timing relative to environmental noise sources.

3.7 Microwave and Raman Pulse Control

Both the microwave and 605 nm Raman systems are not directly controlled through Cicero. Instead, they are operated using a separate arbitrary waveform generator (AWG) in combination with a digital pulse generator (DPG). In this architecture, Cicero serves primarily as a high-level sequence manager, issuing trigger signals that initiate pre-programmed subroutines within the AWG+DPG system. This separation allows time-critical and structurally complex pulse sequences to be handled by dedicated hardware, while maintaining compatibility with the broader experimental timing framework.

More specifically, the DPG generates digital TTL signals used to gate microwave and Raman power switches, and also provides a variable sample clock to the AWG. This clock advances the AWG through a sequence of pre-loaded waveforms in a controlled manner, enabling precise timing and shaping of analog signals. A central control module interfaces with the DPG, allowing it to be triggered multiple times within a single experimental sequence. Each trigger executes a predefined pattern of TTL outputs and clock pulses, offering substantial flexibility in constructing intricate and well-timed pulse sequences. Because both the microwave and Raman systems are integrated within this shared control architecture, combined sequences be implemented seamlessly. Interaction with this system is handled through a Python-based scripting interface, which enables a higher degree of sophistication in pulse design and facilitates rapid iteration of complex control protocols. For more details on this system, see Yukai's Thesis [90].

Chapter 4

Preparing Tweezer-Trapped CaF

Time flies like an arrow, fruit flies like a banana.

– Cicero (the software)

In this chapter, we present an overview of the full experimental sequence used to produce and prepare ultracold CaF molecules, beginning from their initial creation and culminating in individually trapped molecules occupying a single internal hyperfine state. In addition to describing the preparation protocol, we also present measurements characterizing the trapping potential, including the trapping frequencies of the optical tweezers and the temperature of the trapped molecular ensemble.

More specifically, CaF molecules are first produced in a cryogenic buffer gas beam and subsequently slowed to the center of the MOT chamber. There, both red-detuned and blue-detuned magneto-optical traps (MOTs) are implemented to cool and confine the molecules. The molecules are then transferred into an optical dipole trap (ODT), which is translated to the focal plane of a high-resolution microscope objective. From this intermediate trap, molecules are loaded into tightly focused optical tweezers. Once loaded into the tweezers, we perform non-destructive imaging using a five-beam Λ-configuration, allowing us to determine tweezer occupation with high fidelity while minimizing loss. The occupied tweezers are subsequently rearranged to form defect-free configurations. Finally, the molecules are initialized

into a single internal hyperfine state via optical pumping, providing a low-entropy controlled quantum system for all subsequent coherent manipulation and evolution experiments.

4.1 Producing a CBGB

CaF molecules are produced in a cryogenic buffer gas beam (CBGB) apparatus consisting of a buffer gas cell and beambox described in detail in Section 3.1. In brief, a pulsed laser ablates a calcium target in the presence of SF_6 and helium buffer gas maintained at 4 K. The ablation process produces excited calcium atoms, which react with SF_6 to generate a variety of chemical products, including CaF. Collisions with the cold helium buffer gas rapidly thermalize the internal degrees of freedom of the CaF molecules to approximately 4 K. To probe the internal-state equilibrium temperature, we measure the population in a few rotational levels of $X^2\Sigma^+$ via spectroscopy along the $X - A$ transition. As shown in Fig. 4.1, the molecules primarily populate only the lowest few rotational states. Of particular importance is the population in the $N = 1$ rotational state, which supports closed optical cycling transitions as discussed in Section 2.2.2.

After the ablation pulse, a short burst of molecules exits the buffer gas cell, forming a beam with a mean forward velocity of approximately 200 m/s. A detailed characterization of the velocity distribution and temporal profile of this molecular beam can be found in Yukai's Thesis [90].

4.2 Chirped Slowing

The CaF molecules emerging from the buffer gas cell are next slowed to near zero velocity at the center of the science chamber using chirped slowing. This process relies on momentum transfer from photons that counter-propagate with the molecular beam, imparting repeated momentum kicks that reduce the molecular velocity. For a two-level system interacting with near-resonant laser light, the photon scattering rate depends sensitively on both the laser

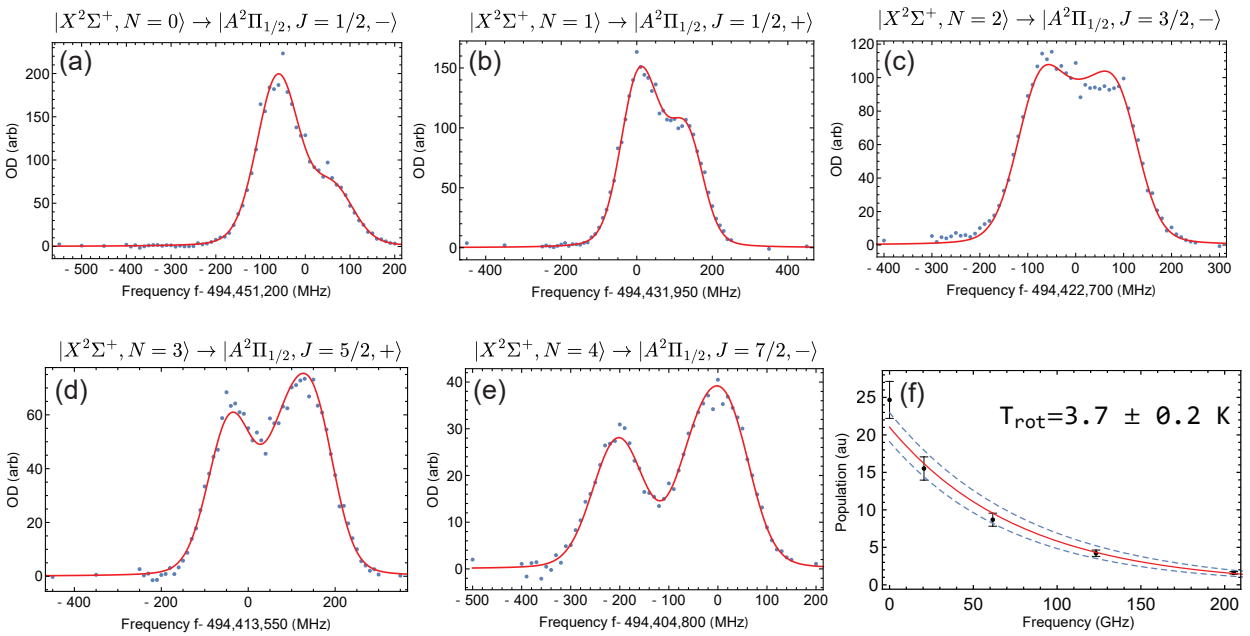


Figure 4.1: Beambox Rotational Temperature: (a-e) Absorbtion spectroscopy along the $X - A$ transition. Integrated optical density as a function of $X - A$ probe detuning is fit to the predicted absorbtion lineshape convolved with a Voight profile. (f) Molecular population as a function of rotational state energy enables inferring the rotational temperature of the produced molecules.

detuning and the Doppler shift associated with the molecular velocity, and scattering is maximized when the effective detuning is close to zero.

As the molecules slow, their Doppler shift changes, causing them to move out of resonance with a fixed-frequency laser and thereby reducing the scattering rate. To compensate for this effect and maintain efficient slowing, the laser frequency is dynamically adjusted in time—a process known as chirping—so that it remains resonant with the progressively slowed molecules. In our implementation, chirped slowing is performed using light at 531 nm addressing the $X - B$ transition. To maintain vibrational closure, repumping light addressing the $v = 1$ and $v = 2$ vibrational states is also chirped synchronously. This is achieved by temporarily disengaging the software locks on the lasers and modulating the seed frequencies via current control. Details on the optical setup used to deliver the chirped slowing light are provided in Yukai's Thesis [90], while a novel technique for adding arbitrary spectral content onto the slowing beam is discussed in Chapter 5.

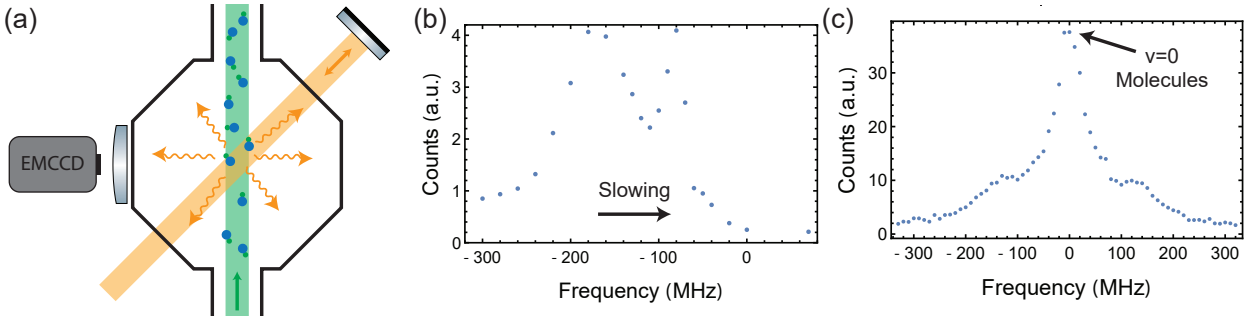


Figure 4.2: Molecular Beam Doppler Spectroscopy: (a) Spectroscopy setup using $X - A$ light (orange), with the probe beam making a 45° angle to the molecular beam. Molecules are slowed via a counter-propagating $X - B$ beam (green). Molecular fluoresence is imaged onto a side camera. (b) Integrated fluoresence counts as a function of probe detuning in an un-retroed configuration. (c) With the probe beam retro-reflected, symmetric features about the zero-velocity detuning appear.

To characterize the slowed molecular population, we perform velocity-selective spectroscopy using the $X-A$ transition at 606 nm, addressing all hyperfine levels of the $X^2\Sigma^+(v = 0, N = 1)$ state. The spectroscopy beam is delivered at an angle of 45° relative to the molecular beam and can be retro-reflected. Without retro-reflection, only the velocity difference between slowed and unslowed molecules can be probed (Fig. 4.2(b)); with retro-reflection, mirrored features about the $v = 0$ resonance are produced (Fig. 4.2(c)), enabling accurate determination of the absolute beam velocity. The chirp profiles for both the slowing and repumping lasers are optimized in a piecewise manner by maximizing the population of slow molecules, with the goal of delivering molecules at near-zero velocity to the center of the science chamber at the conclusion of the sequence.

4.3 MOT

After chirped slowing brings the molecules to near-zero velocity, they must be further cooled and spatially confined. This is achieved using a magneto-optical trap (MOT), which combines spatially varying magnetic fields with laser cooling to provide both confinement and damping. MOTs were first developed for atomic systems, and have since been extended to molecular

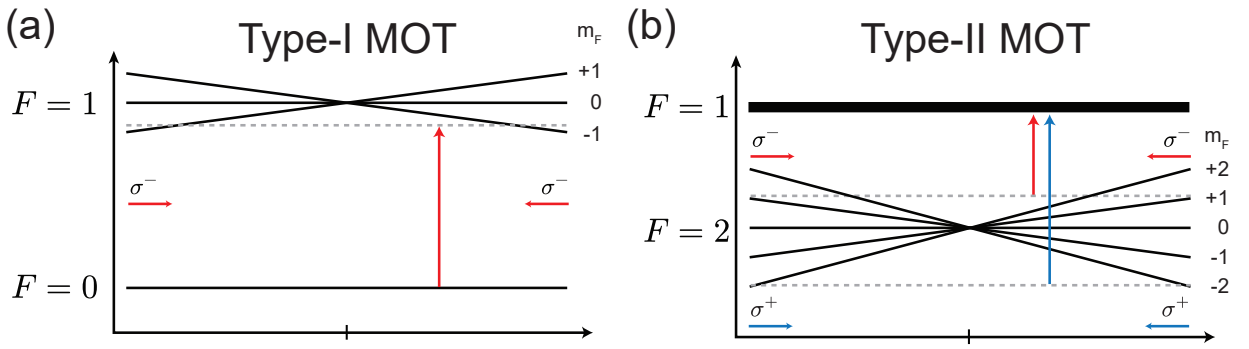


Figure 4.3: Type I and II MOTs: (a) Type I MOTs are formed using red-detuned light. Due to selection rules, atoms starting in $F = 0$ can only scatter off beams with σ^+ projection, providing spatial confinement. (b) Type II MOTs utilize both red- and blue-detuned light, which destabilizes dark states while still providing spatial confinement.

species, beginning with SrF [39] and later including CaF, YO, CaOH, BaF, SrOH, AlF, and CaH [40–42, 51–53, 57, 58].

To illustrate the basic principle, we first consider a type-I atomic MOT, where the number of ground states is smaller than the number of excited states ($F < F'$). In such a MOT, a quadrupole magnetic field is generated using a pair of anti-Helmholtz coils, producing a magnetic field that increases linearly away from a central zero. Along a given axis, two counter-propagating laser beams with opposite circular polarizations are applied, both red-detuned from the zero-field atomic resonance. For a simple $F = 0 \rightarrow F' = 1$ transition, the magnetic field induces position-dependent Zeeman shifts of the excited-state sublevels, as illustrated in Fig. 4.3(a). An atom displaced from the trap center experiences an imbalance in scattering rates from the two beams due to the combined effects of Zeeman shifts and polarization selection rules, resulting in a net restoring force toward the trap center. At the same time, the red-detuned light provides velocity damping, as atoms preferentially scatter photons from the beam opposing their motion. The combination of a restoring force and velocity damping enables simultaneous cooling and confinement.

For molecules such as CaF, which are cooled on type-II transitions ($F > F'$), this standard mechanism breaks down because population can be optically pumped into dark states that do not interact with the cooling light. One approach to destabilizing these dark states is

the RF MOT, in which the magnetic field and laser polarizations are rapidly modulated in time [41, 99]. In our experiment, we instead employ a dual-frequency DC-MOT that uses light that is both red- and blue-detuned to certain hyperfine transitions [40, 100, 101], allowing all fields to remain static while maintaining large confining forces.

To understand the operation of a dual-frequency MOT, consider a $F = 2 \rightarrow F' = 1$ transition with an excited-state g-factor near zero, as is approximately the case for CaF (Fig. 4.3(b)). By applying both red- and blue-detuned light with opposite polarizations, polarization dark states are destabilized. With an appropriate choice of detunings and polarizations, the molecule preferentially scatters photons that produce a restoring force toward the trap center. Doppler cooling is maintained by ensuring that the red-detuned component is closer to resonance than the blue-detuned component. Further details on MOT operation are provided in Yukai's Thesis [90], while our implementation of a blue-detuned MOT (BDM), which can mitigate sub-Doppler heating mechanisms and enable lower temperatures, is discussed in Chapter 7.

4.4 Lambda-Cooling

Following MOT cooling and compression, we implement Λ-enhanced cooling techniques to reach sub-Doppler temperatures and improve loading into conservative optical traps. In earlier versions of the experiment, prior to implementing the BDM, a free-space Λ-cooling stage was applied before transfer into the ODT.

One approach to achieving sub-Doppler temperatures is gray molasses cooling (CMG), in which the cooling light is blue-detuned. In this regime, polarization gradients create spatially varying bright and dark states, as illustrated in (Fig. 4.4(a)). Fast molecules moving through this dark and bright state landscape undergo non-adiabatic transitions from dark to bright states, followed by Sisyphus cooling as they climb up the hills in the bright states manifold.

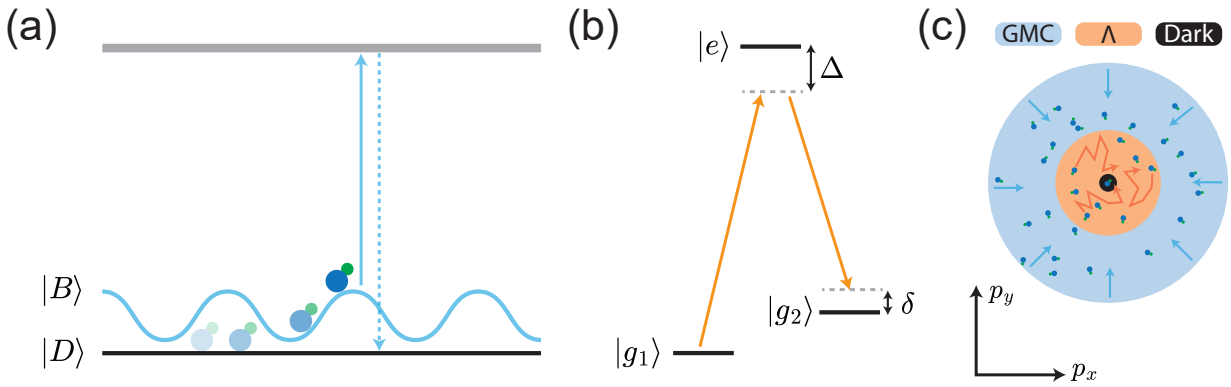


Figure 4.4: GMC and Λ-Cooling Mechanism: (a) Hot molecules undergo non-adiabatic transitions from dark ($|D\rangle$) to bright ($|B\rangle$) states. A Sisyphus mechanism causes molecules to lose kinetic energy, after which they are pumped back to $|D\rangle$. (b) Λ-cooling involves forming a coherent superposition between ground states into which molecules accumulate. (c) While GMC always leads to cooling, the Λ mechanism alone is diffusive in momentum space. The combination of both mechanisms is necessary for efficient cooling.

The molecules are then pumped back into the dark states near the top, resulting in a net loss of kinetic energy.

This cooling can be further enhanced using velocity-selective coherent population trapping (VSCPT), which operates in a three-level Λ system (Fig. 4.4(b)). Two ground states $|g_1\rangle$ and $|g_2\rangle$ are coupled to a common excited state $|e\rangle$ by counter-propagating laser beams. At exact two-photon resonance, the system supports a dark state $\psi_D = \frac{1}{\sqrt{2}}(|g_1\rangle - |g_2\rangle)$ that does not scatter light. Molecules with non-zero velocity experience a Doppler-induced shift that moves them out of the two-photon resonance condition, causing them to scatter photons. Population accumulates into the dark state via random diffusion in momentum-space due to the photon recoil events. Molecules that diffuse away from zero-velocity are re-cooled via the gray molasses mechanism (Fig. 4.4).

In our implementation, Λ-cooling uses a two-photon resonance between the $F = 2$ and $F = 1^-$ hyperfine manifolds. A single-photon detuning of $\Delta \sim 25\,\mathrm{MHz}$ is chosen, which also helps deplete population from the $F = 1^+$ manifold. This cooling mechanism is highly sensitive to magnetic fields and requires careful cancellation of stray fields to maintain the zero-velocity two-photon resonance between the two ground state Λ-manifolds. The optimal

parameters are determined experimentally: in free space by minimizing the temperature via time-of-flight expansion, and in optical traps by maximizing imaging lifetimes and loading efficiencies. Further details on these optimizations are provided in Yukai's Thesis [90].

4.5 ODT & Tweezer Loading

Following Λ-cooling, molecules are loaded into a retro-reflected optical dipole trap (ODT) formed by 1064 nm light. The trap position and intensity are controlled using a 2D acousto-optic deflector (AOD), and a cat-eye configuration is used to maintain retro-reflection (see Yukai's thesis for details [90]). At full power, 22 W is delivered to the chamber and focused to a waist of $w_0 = 60\,\mu$m, corresponding to a single-pass trap depth of $U_0 = k_B \times 160\,\mu$K. Molecules are loaded into the ODT by spatially overlapping it with the sub-Doppler-cooled cloud, with loading parameters optimized to maximize transfer efficiency into the ODT.

Once loaded, the ODT is translated by approximately 1 mm to the focal plane of the microscope objective using the ODT 2D-AOD. The position is optimized by minimizing the apparent size of the molecules trapped in the ODT, which is imaged through the objective, and aligning it with the projected tweezer array. The final axial alignment is achieved via magnetic field shimming during the BDM stage of the MOT.

Molecules are then transferred into optical tweezers, consisting of 37 tightly focused beams generated using a 2D-AOD (see Section 3.4.1). Each tweezer delivers approximately 20 mW of light at 781 nm, corresponding to a trap depth of $U_0 = k_B \times 1.3$ mK during loading and imaging. Loading is assisted by Λ-cooling light applied along all six axes with a detuning of $\Delta \sim 60$ MHz. The ODT position is fine-tuned to maximize transfer into the tweezers.

We observe that the fraction of occupied tweezers saturates at approximately 35%, indicating loss processes during loading. This behavior is consistent with light-assisted collisions, where both two-body and three-body processes contribute to loss. Compared to atomic tweezer experiments, which typically saturate near 50%, the lower saturation frac-

tion observed here suggests an increased role of three-body loss, consistent with the higher densities achieved in tightly focused molecular tweezers. This loss mechanism is corroborated by observations of saturated loading to 50% when less tightly-focused traps are utilized.

4.6 5-Beam Λ-Imaging

Due to optical access constraints, two of the MOT beams propagate through the microscope objective (see Section 3.4.3), producing significant background on the fluorescence detection camera. As a result, imaging cannot be performed with all six MOT beams active. Using only the four horizontal beams avoids this issue but fails to provide cooling along the axial direction of the tweezers, leading to rapid heating and reduced imaging fidelity.

To address this limitation, we introduce an additional beam at a $\sim 45^\circ$ angle through the bottom recessed bucket window using a custom Delrin mount. This beam couples axial and radial motion while largely avoiding the objective. Residual light entering the objective is filtered in a Fourier plane using a hex key, which blocks a thin streak of light produced by the angled beam. Further details on this five-beam Λ-imaging configuration can be found in Yukai's Thesis [90] and Chapter 8.

4.7 Optical Pumping

After Λ-imaging, molecules are distributed among the 12 hyperfine states of the $X^2\Sigma^+(v = 0, N = 1)$ manifold. For applications in quantum simulation and information processing, it is necessary to initialize all molecules into a single internal hyperfine level. Earlier approaches used "F-pumping", in which three frequencies drive population out of the $F = \{1^-, 1^+, 2\}$ manifolds, leading to population accumulation in the $F = 0$ state. However, this method is limited to optical pumping efficiencies of only 70% due to off-resonant scattering, which also introduces heating.

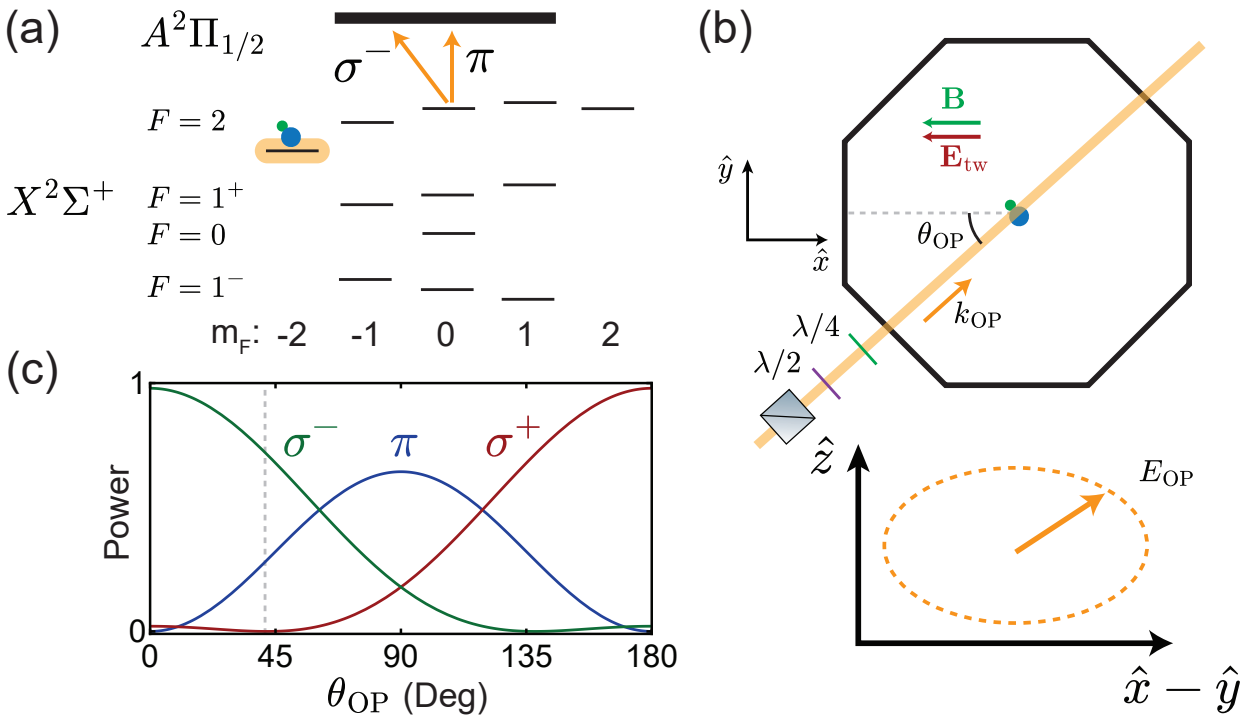


Figure 4.5: Single-Beam m_F Pumping: (a) Tensor shifts (quadratic) from the optical tweezer and the Zeeman shift (linear) leads to $|2,-2\rangle$ having the largest gap to neighboring hyperfine states; consequently, it has minimal admixtures with other free-space eigenstates. Both σ^- and π projections are needed for optical pumping using this $F \rightarrow F-1$ transition. (b) Optical pumping is provided by a single beam oriented at $\theta_{OP} = 42°$ to the quantization axis. Careful control via two waveplates enables making an ellipically polarized beam with major axis in the $\hat{x} - \hat{y}$ plane. (c) In this configuration, the "sig-pi" beam provides no σ^+ power but roughly equal σ^- and π power.

To improve performance, we instead implement an m_F pumping scheme based on polarization selection rules. In free space, the $(F = 2, m_F = \pm 2)$ are the only states in $N = 1$ which are dark to π and $\sigma^\pm$ light, making them ideal target states for m_F pumping. However, in the presence of the tweezer trapping light, mixing between m_F states can degrade how dark the $(F = 2, m_F = \pm 2)$ can be made. By aligning the magnetic field parallel to the tweezer polarization, the $(F = 2, m_F = -2)$ state maintains good overlap with its corresponding free-space eigenstate. This can be intuitively understood by noting that the energy gap to neighboring $F = 2$ levels is much larger for $m_F = -2$ due to the linear Zeeman shift from the applied field and the negative quadratic tensor shift from the optical tweezer light (Fig. 4.5(a)). A full simulation of state purity is provided in Yukai's thesis [90].

Optical pumping in th3is configuration requires generating light with σ^- and π components, while containing no σ^+ component. We generate this light using a single-beam containing light resonant with all four ground state hyperfine levels in $X^2\Sigma^+(N=1)$. The geometry of this beam is illustrated in Fig. 4.5(b). For a given polarization ellipticity (with major axis in the $\hat{x}-\hat{y}$ plane) and angle between the B-field and optical pumping axis k_{OP} (θ_{OP}), the electric field projection onto σ^+ can be nullifed. One of the science chamber windows provides a $\theta_{\mathrm{OP}} = 42°$ angle to the B-field direction; at this angle, an optical pumping beam can have roughly equal powers in σ^- and π while nullifying the σ^+ component. A simulation of the power in each projection is given in Fig. 4.5(c) as a function of θ_{OP} at this optimum ellipiticity.

In practice, this optical pumping beam is first aligned to the center of the tweezers using the in-vacuum spherical bead (See Section 3.5.5). The polarization is cleaned via the transmission port of a PBS. Next, a $\lambda/2$ and $\lambda/4$ waveplate are inserted into the path. First, the $\lambda/2$ is inserted and aligned to produce horizontally polarized light ($\hat{x}-\hat{y}$); next, the $\lambda/4$ is inserted and oriented with one of its principle axes aligned along $\hat{z}$. Note, the ordering of $\lambda/2$ and then $\lambda/4$ is critical. Each waveplate orientation is verified via an analysis PBS. The angle of the $\lambda/2$ waveplate is recorded and the analysis PBS is removed. Finally, the $\lambda/2$ waveplate is rotated by precisely the desired angle to achieve the correct ellipticity to minimize the σ^+ projection. This angle is calculated using Jones matrices. Importantly, only the $\lambda/2$ should be adjusted; this ensures that the principle axis of the elliptical polarization remains in the $\hat{x}-\hat{y}$ plane (Fig. 4.5(b)). Finally, fine-adjustment of the magnetic field angle by one or two degrees is performed while monitoring population survival after extended application of the optical pumping beam. The configuration with the longest lifetime has the least σ^+ power.

This single-beam "sig-pi" pumping method has proven to be highly robust in practice, requiring little to no adjustment over several years of operation. Details on subsequent coherent microwave manipulation between hyperfine levels are provided in Yukai's Thesis [90].

4.8 Tweezer Parameters and Molecular Temperature

4.8.1 Tweezer Parameters

The optical trap depth and optical beam waist can be determined via trap frequency measurements combined with measured tweezer beam intensities. First, we perform trap frequency measurements via parametric modulation of the trap depth. In detail, the molecules are first loaded at maximum tweezer trap depth. Subsequently the tweezer depths are modulated, and the depths are lowered to allow parametrically heated molecules to exit the traps. Finally, the trap depths are ramped back to their initial value, and the occupations are detected.

The fraction of molecules detected following trap modulation displays two loss features, which we attribute to twice the radial frequency ω_r and twice the axial frequency ω_z. The measurements yield $\omega_r = 2\pi\times187.7(6)\,\mathrm{kHz}$ and $\omega_z = 2\pi\times42.2(3)\,\mathrm{kHz}$, where the error bars are from the fits and do not take into account systematic effects. Assuming a Gaussian beam in the paraxial approximation, the trap frequency ratio provides an estimate of the beam waist w_0:

$$w_0 = \frac{\lambda}{\pi\sqrt{2}}\frac{\omega_r}{\omega_z}. \tag{4.1}$$

This provides an estimate of $w_0 = 781(3)\,\mathrm{nm}$. However, optical aberrations lead to deviations from a perfect Gaussian beam, which affect the trap frequency ratios, and hence the beam waist estimate. While the radial profile of a beam is typically well described by a Gaussian, aberrations can significantly distort how the trap depth varies along the optical axis. Typically, these aberrations lower ω_z/ω_r as rays at different incoming angles focus to different axial positions.

To provide a better estimate of the radial beam waist w_0, which is important for determining the overall ac Stark shifts and molecular temperatures, we use a second method that relies on power measurements and a calculation of the ground state polarizability of CaF. We assume that the molecules, which are distributed among the various $N = 1$ hyperfine

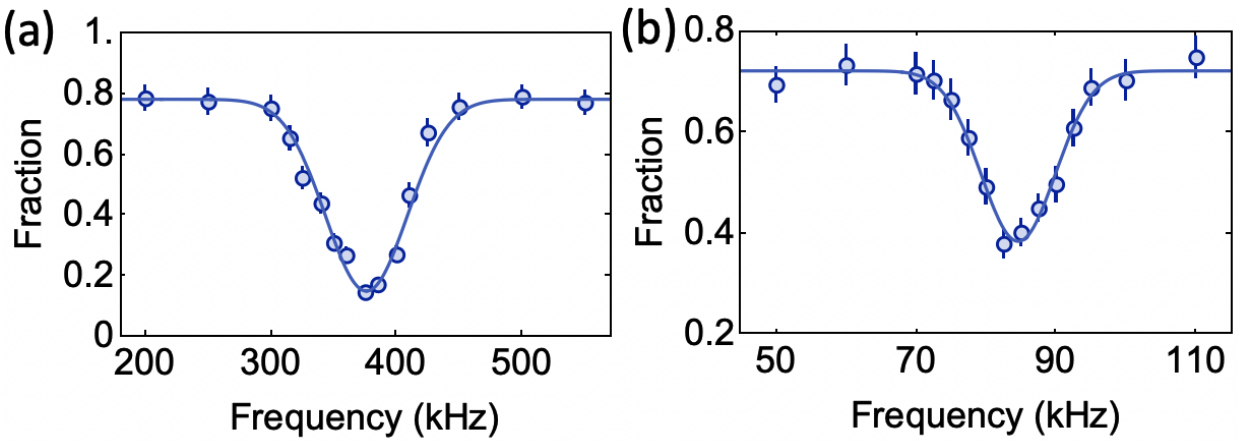


Figure 4.6: Remaining fraction versus modulation frequency. Shown in blue are the remaining fractions following trap intensity modulation. The solid lines indicate Gaussian fits. Radial (a) and axial (b) trapping frequencies are inferred from half the modulation frequency leading to the most population loss. Measurements are averaged across 20 optical tweezers.

states during the trap depth modulation, on average experience the scalar polarizability. Using this method, we find a Gaussian waist of $w_0 = 720(14)\,\mathrm{nm}$ and a trap depth of $V = k_B \times 1.28(11)\,\mathrm{mK}$. Since we have high confidence in the measured power and the calculated polarizability, we model the trap as an ideal Gaussian beam with beam waist $w_0 = 720(14)\,\mathrm{nm}$ and tweezer trap depth $V = k_B \times 1.28(11)\,\mathrm{mK}$ throughout the investigations presented in this thesis.

4.8.2 Molecular Temperatures

To estimate the molecular temperature in the optical tweezers, we employ two complementary approaches. The first method, known as release-and-recapture, involves briefly turning off the tweezer light, allowing the trapped molecules to expand ballistically for a variable duration, and then rapidly restoring the trapping potential. During this free expansion, a fraction of the molecules escape the trapping region and are therefore not recaptured when the tweezer is turned back on. By measuring the survival probability as a function of the release time, one obtains a release-and-recapture curve that is sensitive to the molecular temperature. Exemplary release-and-recapture measurements are presented in Section 6.4.

Despite its conceptual simplicity, several important caveats must be considered when performing release-and-recapture thermometry. Quantitative extraction of the temperature requires accurate modeling of both the trapping potential (which may not be precisely known) and the recapture dynamics (including the detection process). For sufficiently long release times, we have found that the inferred temperature becomes unreliable since the molecular kinetic energy becomes comparable to the trap depth following recapture, and the Λ-imaging used for detection ceases to function reliably. One practical workaround is to perform release-and-recapture measurements at reduced tweezer depths. Additionally, this technique primarily probes the most tightly confined (radial) direction of the tweezer, which expands most rapidly out of the recapture region during the ballistic expansion step.

A more reliable and comprehensive thermometry method is provided by sideband spectroscopy. In this approach, two-photon Raman transitions are used to transfer population between internal states of the molecule while simultaneously changing the motional quantum number. The resulting sideband spectrum can be used to infer the distribution of motional state occupations and allows independent determination of both radial and axial temperatures. Despite these benefits, sideband thermometry is experimentally more demanding, requiring high-fidelity state preparation, coherent control, and state-selective detection. Our implementation of sideband spectroscopy is described in detail in Ref. [5] and in Yukai's Thesis [90]. Using this technique, we measure typical temperatures of $T_r \sim 20\,\mu$K in the radial direction and $T_a \sim 40\,\mu$K along the axial direction at full tweezer depth.

Chapter 5

Generating Arbitrary Optical Spectra using High-Bandwith EOMs

Alles Gescheite ist schon gedacht worden.

Man muss nur versuchen, es noch einmal zu denken.

– Johann Wolfgang von Goethe

An unexpectedly fruitful investigation arose when placing orders for AOMs – motivated in part by my shock at the pricetag of the AOMs and associated RF components. The first draft of this ideas was to use a high-bandwidth AOM in a double-pass configuration to replace the "606 switchyard" described in Section 3.3.3. Like many of my initial ideas, this was a terrible idea.[1] Nevertheless, the nugget of a good idea remained hidden within the terribleness, which was revealed by replacing the AOM with an EOM.

In this chapter, we explore a powerful connection uncovered that unifies spectral engineering and computer generated holography. We outline a simple protocol for measuring and compensating for non-ideal behavior in high-bandwidth EOMs. We highlight a proof-of-principle demonstration of synthesizing an optical spectrum relevant to slowing CaF on

[1] To any grad-students reading this thesis: try to come up with one "crazy idea" per week throughout your PhD. The creativity to generate these ideas (even if bad), and the diligence to separate the wheat from the chaff (identify the bad ideas before they get out of hand), is *really* what you're trying to master during your PhD. After a while, it also becomes fun!

the $X - B$ transition. OBE simulations indicate that the generated spectra saturate the maximum possible optical cycling rates on the $X - B$ transition. Concluding remarks are made about the broader adoption and future extensions of this technique.

The work presented in this chapter resulted in the following publication [1]:

Connor M. Holland, Yukai Lu, Lawrence W. Cheuk. "Synthesizing optical spectra using computer-generated holography techniques" New J. Phys. ***23****, 033028 (2021).*

5.1 A Need for Sidebands

Optical transitions are an indispensable part of the AMO experimental toolbox; they are used to cool, trap, prepare, and detect atoms and molecules. Substructure, such as hyperfine structure or spin-rotation structure, often leads to multiple optical transitions spaced by MHz to GHz. For many tasks, such as fluorescence detection and laser cooling [102, 103], these closely-spaced transitions must be simultaneously addressed to achieve sustained optical scattering. However, generating the closely spaced optical content on a laser becomes challenging (and expensive) when the number of desired frequencies is large. In some cases, a clever use of selection rules permits closed optical cycling by adding little to no additional spectral content on a laser.[2] That being said, these selection-rule strategies are often difficult or impossible to find when working with complex molecules [55, 56], atoms in large magnetic fields [104–107], and even the D1 line of Alkali atoms.

To elaborate, even at zero magnetic field, optical cycling in molecules often requires multiple frequencies. Even in the case of a $^2\Sigma$ diatomic molecule with a single nuclear spin $I = 1/2$, four frequencies are needed when the spin-rotation and hyperfine splittings are resolved in the ground electronic manifold [35, 37, 38]. In more complicated molecules such as those with multiple nuclear spins or larger nuclear spins, the number of frequencies needed

[2]The canonical example is optical cycling on the so-called stretched transition $(F, m_F) = (F, F) \rightarrow (F + 1, F + 1)$ on the D2 line of Alkali atoms. In practice, even this idealized situation is not achieved due to off-resonant scattering, requiring a repump laser offset by $\sim 0.1 - 10\,\mathrm{GHz}$ depending on the atom and isotope.

grows even more. In atoms, a similar situation occurs at finite magnetic fields. Even for the case of an alkali atom, the ground and excited electronic manifolds split into a total of $4(2I+1)$ levels, where I is the nuclear spin. One would generically need $2(2I+1)$ distinct frequencies in order to optically cycle photons.

A straightforward but expensive solution to generate spectral content uses an acousto-optic modulator (AOM) to shift monochromatic laser light to a desired target frequency. In this approach, a single AOM is used to generate a single sideband, and thus the number of AOMs and associated optical and electronic components scales linearly with sideband number. Hence, this approach quickly becomes impractical. Additionally, AOMs have limited bandwidths and changes in their modulation frequencies are accompanied by changes in beam pointing, which is undesirable in many cases. Another common method to generate multiple frequencies is sinusoidal phase modulation, which can be accomplished by passing light through an electro-optic modulator (EOM). When the phase of monochromatic light is sinusoidally modulated, sidebands spaced by the modulation frequency are created about the carrier. Although there exist fortuitous cases where the resulting spectrum produces a near match to the target sideband pattern, invariably, undesired spectral components remain.

5.2 Spectral Engineering is Holography

In light of this pressing motivation for cheap, simple solutions to generate arbitrary optical spectral content, we consider arbitary phase modulation profiles applied to EOMs. Although arbitrary phase modulation is, in principle, capable of generating arbitrary optical spectra, it is not trivial to find the appropriate phase modulation profiles to produce a target spectrum. In this Section, we show that this inversion problem is equivalent to a computer-generated holography (CGH) problem, where well-known algorithms such as the Gerchberg-Saxton algorithm (GSA) exist [108, 109].

Spectral engineering via phase modulation is equivalent to a well-known problem in optics – how to generate a light intensity pattern $I(\tilde{x}, \tilde{y})$ in the image plane ($\tilde{x}$-$\tilde{y}$ plane) by modulating only the light's phase in the Fourier plane (x-y plane). For concreteness, consider an imaging system consisting of a single lens with focal length f. Suppose an electric field of the form $E(x, y) = E_0 e^{i\phi(x,y)}$ is in the Fourier plane. In the image plane (under the paraxial approximation), the electric field is given by

$$E(\tilde{x}, \tilde{y}) = \frac{e^{i4\pi f}}{i} \int dxdy\, E_0 e^{i\phi(x,y)} e^{-ik_0(x\tilde{x}+y\tilde{y})/f}, \tag{5.1}$$

where $k_0 = 2\pi/\lambda$, and λ is the wavelength of the light. Thus, the electric field $E(\tilde{x}, \tilde{y})$ in the image plane is the Fourier transform of the electric field $E(x, y)$ in the Fourier plane, a well-known result in Fourier optics.

In CGH, given a desired target intensity pattern $I(\tilde{x}, \tilde{y})$ in the image plane, one seeks the optimal 2D phase profile $\phi(x, y)$. Explicitly, one tries to invert

$$I(\tilde{x}, \tilde{y}) = \left| \int dxdy\, E_0 e^{i\phi(x,y)} e^{-i(x\tilde{x}+y\tilde{y})} \right|^2, \tag{5.2}$$

where we have picked units such that k_0 and f are 1. In 1D, the corresponding equation to invert is

$$I(\tilde{x}) = \left| \int dx\ E_0 e^{i\phi(x)} e^{-i\tilde{x}x} \right|^2, \tag{5.3}$$

where one seeks an optimal $\phi(x)$ when given $I(\tilde{x})$.

The 1D hologram problem is in fact equivalent to the problem encountered in engineering spectra. When creating spectra via phase modulation, one attempts to produce a target power spectral density $S(\omega)$ by applying a temporally varying phase $\phi(t)$ to a monochromatic light field $E_0 e^{i\omega_0 t}$. The problem is thus to invert

$$S(\omega) = \left| \int dt\ E_0 e^{i(\omega_0 t+\phi(t))} e^{-i\omega t} \right|^2. \tag{5.4}$$

Identifying time (frequency) with the spatial coordinate in the Fourier (image) plane ($\{x, \tilde{x}\} \rightarrow \{t, \omega\}$), we see that Eq. (5.3) and Eq. (5.4) are identical up to a frequency offset of ω_0 in ω. Therefore, finding a temporal phase modulation profile $\phi(t)$ that produces a desired spectrum $S(\omega)$ is equivalent to finding a spatial phase profile $\phi(x)$ that produces a target image $I(\tilde{x})$ in 1D hologram generation. Hence, algorithms developed for CGH can directly be used to engineer spectra via phase modulation.

5.2.1 Spectral Engineering with Computer Holography Solutions

In order to find a phase modulation profile $\phi(t)$ that produces a target spectrum $S(\omega)$, one has to invert Eq. (5.4). While many algorithms have been developed for this purpose [110–112], in this work, we will use GSA [108], a well-known iterative Fourier transform algorithm (IFTA) that produces approximate solutions.

We describe GSA in brief (Fig. 5.1a). Given a target amplitude $\tilde{G}_0(\omega)$ in the frequency domain and an input amplitude $G_0(t)$ in the time domain, the algorithm returns a phase modulation profile $\phi(t)$ that closely reproduces $\tilde{G}_0(\omega)$. For the particular case of inverting Eq. (5.4), one sets $\tilde{G}_0(\omega) = \sqrt{S(\omega)}$ and $G_0(t) = E_0$. Starting with a seed phase $\phi_0(t)$, one follows the following steps:

1. The time domain signal $G_0(t)e^{i\phi_j(t)}$ is propagated to the frequency domain via a Fourier transform, producing $\mathcal{F}[G_0(t)e^{i\phi_j(t)}] = \tilde{G}_{j+1}(\omega)e^{i\tilde{\phi}_{j+1}(\omega)}$, expressed in terms of a propagated amplitude $\tilde{G}_{j+1}(\omega)$ and phase $\tilde{\phi}_{j+1}(\omega)$.

2. The propagated amplitude is discarded and replaced with the target amplitude $\tilde{G}_0(\omega)$ to generate the frequency domain signal $\tilde{G}_0(\omega)e^{i\tilde{\phi}_{j+1}(\omega)}$. This step enforces a constraint on the amplitude in the frequency domain.

3. The frequency domain signal is propagated back to the time domain via an inverse Fourier transform, producing $\mathcal{F}^{-1}[\tilde{G}_0(\omega)e^{i\tilde{\phi}_{j+1}(\omega)}] = G_{j+1}(t)e^{i\phi_{j+1}(t)}$.

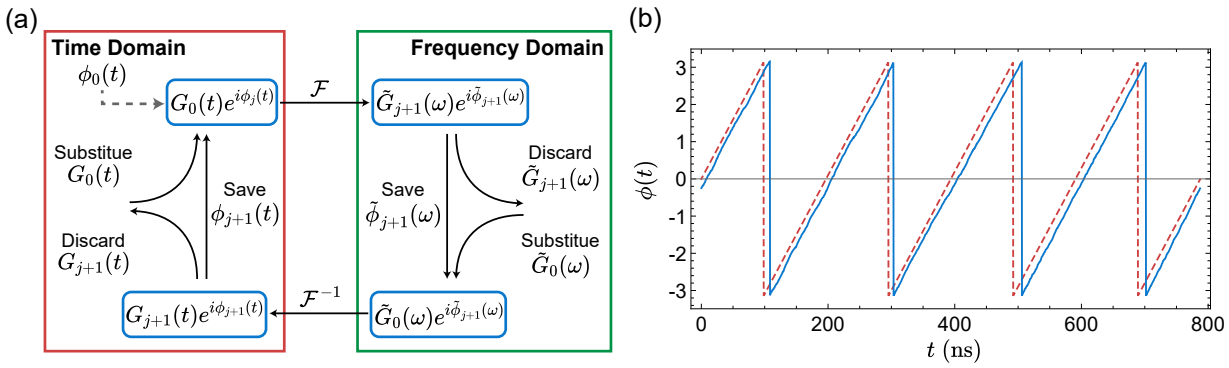


Figure 5.1: The Gerchberg-Saxton Algorithm (GSA). (a) GSA is an iterative algorithm that enforces amplitude constraints on a signal and its Fourier transform. In spectral engineering, the amplitudes in the time and frequency domains are constrained via $G_0(t)$ and $\tilde{G}_0(\omega)$, respectively. (b) A GSA solution (blue solid) for a Lorentzian target (+5 MHz from carrier, 100 kHz FWHM) closely resembles a serrodyne solution (+5 MHz, red dashed).

4. The propagated amplitude $G_{j+1}(t)$ is discarded and replaced with the input amplitude $G_0(t)$ acting as a constraint, producing the subsequent time domain signal $G_0(t)e^{i\phi_{j+1}(t)}$.

The algorithm terminates either after a predetermined number of steps or when $|\tilde{G}_j(\omega) - \tilde{G}_0(\omega)| < \varepsilon$ for a specified convergence tolerance ε.

5.2.2 Creating a Single Frequency

Although CGH algorithms such as IFTAs often appear as "black boxes" whose solutions elude physical intuition, GSA solutions for simple target spectra can often be interpreted. A simple case concerns shifting the angular frequency of an input light field $E_0e^{i\omega t}$ by δ, $E_0e^{i\omega_0 t} \rightarrow E_0e^{i(\omega_0+\delta)t}$. It is clear that $\phi(t) = \delta t + \Phi_0$ is a solution, where Φ_0 is a constant that does not affect the spectrum. As shown in Fig. 5.1b, GSA reproduces this solution up to the constant offset Φ_0 and modulo 2π. This sawtooth-like solution, the so-called "serrodyne" solution, has been used to shift frequencies both in the microwave [113] and optical domains [114, 115]. Note that since the constant Φ_0 does not affect the spectrum, this constant is not unique and depends on the initial seed $\phi_0(t)$. Hence, as in hologram generation, there always exist multiple $\phi(t)$ yielding identical spectra.

5.2.3 Creating Multiple Frequencies

Simple solutions to generate multiple frequencies are not always available. One approach involves stitching together multiple serrodyne waveforms to create multiple frequencies [116]. The power in each sideband is primarily determined by the duration of each serrodyne chunk. However, concatenation introduces imperfections, since the transitions between different serrodynes contribute additional frequency content. This content becomes particularly problematic when the duration of each serrodyne is short. One explicit benefit of using GSA seeded with a serrodyne solution is that these transients can be smoothed out, resulting in a solution closer to the target spectrum.

Although GSA is a powerful catch-all technique to find approximate phase modulation waveforms solutions, certain simple solutions are obscured by the range-constraint of GSA solutions to $\phi(t) \in [-\pi, \pi)$. For example, it is well-known that modulation with a sinusoidal drive $\phi(t) = \beta \cos(\Omega t)$ generates multiple sidebands spaced by $n\Omega$ from the carrier, with strengths $|J_n(\beta)|^2$, where β is the modulation depth and $J_n(x)$ is the n^{th} order Bessel function of the first kind:

$$\left| \int dt \; e^{i\beta \cos(\Omega t)} e^{-i\omega t} \right|^2 \propto \sum_{n=-\infty}^{\infty} |J_n(\beta)|^2 \delta(\omega - n\Omega). \tag{5.5}$$

For target spectra which can be generated by sinusoidal modulation with a modulation depth $\beta > \pi$, GSA would not find this simple sinusoidal solution. We comment on a protocol that could circumvent this limitation in Section 5.6.2, which was not explored during this initial investigation.

5.3 Technical Considerations

In this section, we discuss technical considerations which are relevant to any experimental implementation of spectral engineering. We generate a phase modulation signal $\phi(t)$ by applying a voltage $V(t)$ to an EOM. The advent of high-bandwidth fiberized EOMs, available

with bandwidths up to 10's of GHz, makes this a feasible approach for generating optical spectra spanning 100s of MHz. Nevertheless, various effects make the system non-ideal, leading to behavior deviating from Eq. (5.4). These effects can arise at the level of $V(t)$ (electronic) or after the phase $\phi(t)$ has been imprinted by the EOM on the light field (optical). The electronic effects can be separated into linear ones and nonlinear ones. Effects that are linear in the voltage signal $V(t)$ can be described by a transfer function. Once the transfer function is known, it can be compensated. Electronic effects that are non-linear are trickier to deal with; we choose to operate such that non-linear effects are negligible. Beyond electronic effects, a major possible source of non-ideal behavior is chromatic dispersion, which can be large in long optical fibers. Encouragingly, as long as chromatic dispersion is linear over the target spectral width, CGH spectra are unaffected.

5.3.1 Compatibility with Non-Linear Frequency Generation

The CGH approach can be applied even in the presence of non-linear optical processes such as SFG and multiple harmonic generation. In SFG, two monochromatic light fields $E_1 e^{i\omega_1 t}$ and $E_2 e^{i\omega_2 t}$ combine to produce a new field proportional to $E_1 E_2 e^{i(\omega_1+\omega_2)t}$. Since the second light field only acts to scale the amplitude and frequency-shift the first light field by ω_2, a spectrum centered about $\omega_1 + \omega_2$ can be generated by creating the same spectrum on the first light field but centered about ω_1.

For n^{th} harmonic generation, an input of $E_0 e^{i\omega_0 t}$ produces an output proportional to $E_0^n e^{in\omega_0 t}$. Phase-modulating the input light by $\phi(t)$ produces a phase modulation of $n\phi(t)$ on the output light. Thus, a desired spectrum $S(\omega)$ in the n^{th} harmonic can be generated by applying $\phi(t) = \phi_{\text{soln}}(t)/n$ to the input light, where $\phi_{\text{soln}}(t)$ is the CGH solution.

The compatibility with non-linear processes provides practical advantages. High power visible light is commonly generated via SFG or SHG applied to near-infrared light, where high power fiber amplifiers and high-bandwidth fiberized EOMs are available. In Section 5.4,

we provide a proof-of-principle demonstration of such an implementation, where a target spectrum centered about 531 nm is produced by phase-modulating light at 1062 nm.

5.3.2 Chromatic Dispersion in Long Fibers

We first consider the influence of chromatic dispersion, commonly encountered when light travels through long optical fiber. We find that the only effect of linear chromatic dispersion is a global time-delay of the phase modulation signal. This global delay leads to no change in the synthesized spectrum.

Suppose a material has linear chromatic dispersion, i.e. its index of refraction is approximately described by $n(\lambda) \approx n_0 + \alpha(\lambda - \lambda_0)$, where λ is the wavelength, n_0 is the index of refraction at λ_0, and $\alpha = \frac{dn}{d\lambda}$. After light propagates a length L through the material, an input light field with Fourier spectrum $\tilde{E}(\omega) = \int dt\, E(t) e^{-i\omega t}$ becomes

$$\begin{aligned} E_{\text{out}}(t) &= \int \frac{d\omega}{2\pi}\, \tilde{E}(\omega) e^{-in(\lambda)\frac{2\pi}{\lambda}L} e^{i\omega t} \\ &= e^{-i2\pi\alpha L} \int \frac{d\omega}{2\pi}\, \tilde{E}(\omega) e^{-i(n_0 - \alpha\lambda_0)\frac{\omega}{c}L} e^{i\omega t} \end{aligned} \tag{5.6}$$

Now, suppose the input light is monochromatic with frequency ω_0 and is phase-modulated by $\phi(t)$, i.e. $E(t) = E_0 e^{i(\omega_0 t + \phi(t))}$. After propagation, the output light field is given by

$$\begin{aligned} E_{\text{out}}(t) &= E_0 e^{-i2\pi\alpha L} \int \frac{d\omega}{2\pi} \int dt'\, e^{i(\omega_0 t' + \phi(t'))} e^{-i(t' - t + (n_0 - \alpha\lambda_0)L/c)\omega} \\ &= E_0 e^{-i\omega_0 n_0 L/c} e^{i(\omega_0 t + \phi(t - \Delta t))}, \end{aligned} \tag{5.7}$$

where $\Delta t = (n_0 - \alpha\lambda_0)L/c$. Therefore, linear dispersion leads to a trivial phase factor $e^{-i\omega_0 n_0 L/c}$ and a time delay Δt in the phase modulation $\phi(t)$, which does not affect the spectrum. In the case of optical fibers, linear chromatic dispersion is a good approximation over $\sim$ GHz bandwidths.

5.3.3 Linear Electronic Effects

Certain electronic effects encountered when generating $V(t)$, such as finite bandwidth and frequency-dependent amplitude responses in various components, modify the resulting phase modulation waveform from $\phi(t)$ to $\phi_{\text{eff}}(t)$. As long as these effects are linear, they can be captured by a transfer function acting in the frequency domain. Specifically, the resulting phase modulation in the frequency domain, $\tilde{\phi}_{\text{eff}}(\omega) = \int dt\, \phi_{\text{eff}}(t) e^{-i\omega t}$, is given by $\tilde{\phi}_{\text{eff}}(\omega) = T(\omega)\tilde{\phi}(\omega)$, where $T(\omega)$ is the transfer function and $\tilde{\phi}(\omega)$ is the Fourier transform of the initial signal. The transfer function $T(\omega)$ can be expressed as $T(\omega) = A(\omega)e^{i\Phi(\omega)}$, where $A(\omega)$ is the amplitude response and $\Phi(\omega)$ is the phase response. In Section 5.4, we outline simple procedures to measure $A(\omega)$ and $\Phi(\omega)$.

5.3.4 Minimizing RF Non-linearities

Non-linear electronic effects can occur when generating a time-dependent voltage $V(t)$. For example, suppose $V(t)$ consists of a single tone at Ω. Amplifier non-linearities will produce higher harmonics at $n\Omega$. This situation worsens when $V(t)$ contains multiple frequencies, since electronic spectral content can be generated at the sums and differences of the input frequencies. Since non-linear effects are difficult to simulate and compensate, we simply minimize these non-linearities through an appropriate choice of rf components. Specifically, in our implementation, we apply a high frequency cutoff of 500 MHz to the compensated phase modulation signal, and verify that harmonics in the electronic signal $V(t)$ after the rf amplifier are suppressed by at least 40 dB.

5.4 Experimental Realization and Characterization

In this section, we present methods to measure the amplitude and phase response, $A(\omega)$ and $\Phi(\omega)$, of the transfer function. Compensation can then be applied by dividing the calculated phase modulation signal by the transfer function in the frequency domain. When this com-

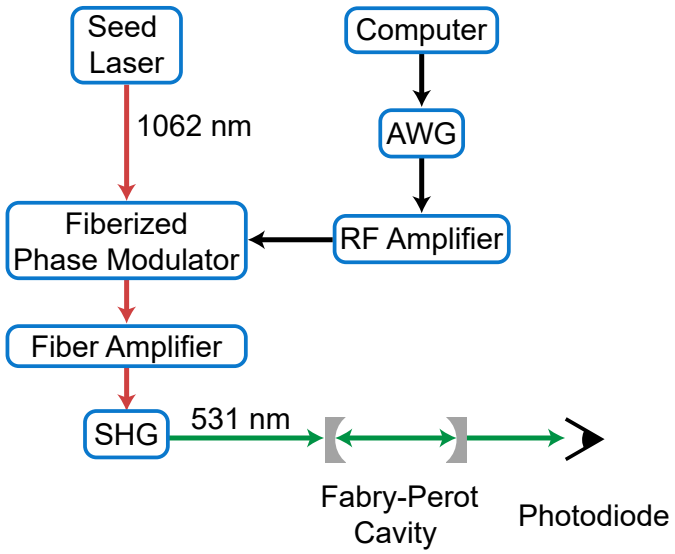


Figure 5.2: Experimental Setup. 1062 nm light from a seed laser is sent through a fiberized phase modulator, amplified, and then frequency doubled (SHG) to 531 nm. The phase applied by the modulator is controlled by the amplified output of an AWG. To measure the spectrum of the 531 nm light, we observe the tranmission through a scanning Fabry-Perot cavity.

pensation protocol is applied to serrodyne waveforms, we see a substantial improvement in spectral quality and a reduction in spurious peaks.

Our system (Fig. 5.2) consists of a seed laser at 1062 nm whose light passes through a 2 GHz bandwidth fiberized phase modulator (iXblue: NIR-MPX-LN-02) that is controlled by the amplified output of an arbitrary waveform generator (Tektronix AWG610). After phase modulation, the light enters a high-power fiber amplifier, whose output is frequency doubled to 531 nm. To characterize the spectrum of the doubled light, we measure the transmission $\mathcal{T}$ through a scanning Fabry-Perot cavity (Thorlabs SA200-5B), 1.5 GHz free spectral range, 5.8(1) MHz full-width-half-max linewidth) as a function of the cavity length, which is scanned using a piezo-electric actuator. By converting the piezo drive voltage to an angular frequency difference δ and aligning $\delta = 0$ with the carrier, one produces a transmission curve $\mathcal{T}(\delta)$, which is directly proportional to the power spectrum of the light $S(\omega)$, with $\delta = \omega$. To calibrate the piezo response, we apply sinusoidal phase modulation to the light at frequency Ω, which produces sidebands spaced by $n\Omega$ about the carrier. We approximate the piezo

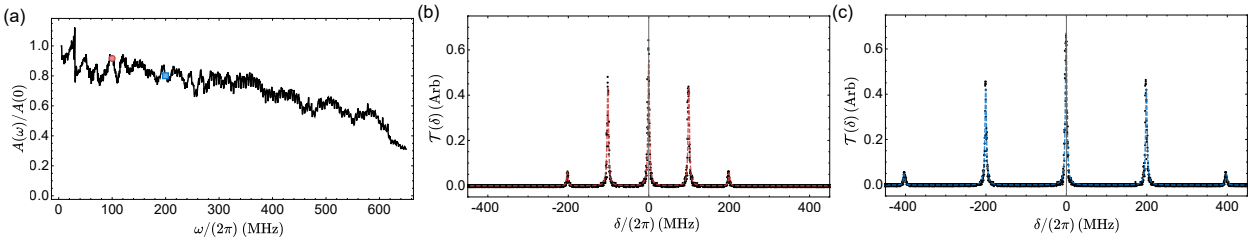


Figure 5.3: Amplitude Response. (a) Measured amplitude transfer function $A(\omega)/A(0)$ obtained by fitting cavity transmission spectra of sinusoidally modulated light. Example transmission spectra $\mathcal{T}(\delta)$ (black points) and their fits are shown in (b) 100 MHz (red dashed) and (c) 200 MHz (blue dashed). These frequencies are marked in (a) by the red circle and blue square, respectively.

response to be linear in the drive voltage. Piezo non-linearities lead to small deviations, which are unimportant for our present work.

5.4.1 Calibrating the Amplitude Response

To measure the amplitude response $A(\omega)$, we apply a voltage to our EOM of the form $V(t) = V_0 \cos(\Omega t)$ with frequencies $\Omega/(2\pi)$ ranging from 5 to 650 MHz. This creates a phase modulation profile of the form $\phi(t) = \beta \cos(\Omega t)$, which produces sidebands at $n\Omega$ on the undoubled light. The effect of frequency-doubling can be absorbed into the modulation depth via $\beta \to 2\beta$. We measure the resulting optical spectra of the doubled light using a scanning Fabry-Perot cavity, fit the results to the known sinusoidal modulation solution (Eq. (5.5)), and extract the effective modulation depth β_{eff}. This provides the amplitude transfer function $A(\omega)$ (Fig. 5.3). In detail, we perform two iterations of estimating the amplitude response. First, we perform a rough estimate of $A(\omega)$, often just by-eye and over a sparse set of frequencies. In the second iteration, we change the applied voltage amplitude as a function of modulation frequency to keep the effective modulation depth near $\beta_{\text{eff}} \approx 1.2$. This ensures that only a few sidebands are generated whose amplitudes remain most sensitive to variations in β_{eff}.

5.4.2 Calibrating the Phase Response

To measure the phase response $\Phi(\omega)$, we developed an interferometric method that is sensitive to the relative phase shift between frequency harmonics in a phase modulation signal. This protocol was inspired by noting that non-symmetric moduation spectra are produced when the modulation signal $\phi(t)$ breaks time-reversal symmetry.[3] With this insight, we apply modulation of the form

$$\phi(t) = \beta_1 \cos(\Omega t) + \beta_2 \cos(2\Omega t + \varphi). \tag{5.8}$$

As long as $\varphi \neq 0$, $\phi(t)$ breaks time-reversal. Incorporating the amplitude and phase response of the system, the effective modulation signal is then

$$\phi_{\text{eff}}(t) = A(\Omega)\beta_1 \cos(\Omega t + \Phi(\Omega)) + A(2\Omega)\beta_2 \cos(2\Omega t + \Phi(2\Omega) + \varphi).$$

Shifting the time coordinate by $t \to t - \Phi(\Omega)/\Omega$, we obtain

$$\phi_{\text{eff}}(t) = A(\Omega)\beta_1 \cos(\Omega t) + A(2\Omega)\beta_2 \cos(2\Omega t + \Delta\Phi(\Omega) + \varphi),$$

where $\Delta\Phi(\Omega) = \Phi(2\Omega) - 2\Phi(\Omega)$. The sidebands generated by the 2Ω modulation will interfere with the sidebands generated by the Ω modulation, and the resulting spectrum encodes information about the relative phase $\Delta\Phi(\omega)$. Applying Eq. (5.5), one finds that the cavity spectrum $S(\omega)$ is given by

$$\left| \sum_m J_{n-2m}(\beta_{1,\text{eff}}) J_m(\beta_{2,\text{eff}}) e^{in\pi/2} e^{-im(\Delta\Phi+\varphi+\pi/2)} \right|^2 \times \delta(\omega_0 - n\Omega), \tag{5.9}$$

where $\beta_{1,\text{eff}} = A(\Omega)\beta_1$ and $\beta_{2,\text{eff}} = A(2\Omega)\beta_2$.

The experimental protocol to obtain $\Phi(\omega)$ proceeds as follows. First, we calibrate the amplitude response as described in Section 5.4.1. We then set the modulation depths to

[3] Consider serrodyne modulation, which generates a maximally asymmetric spectrum.

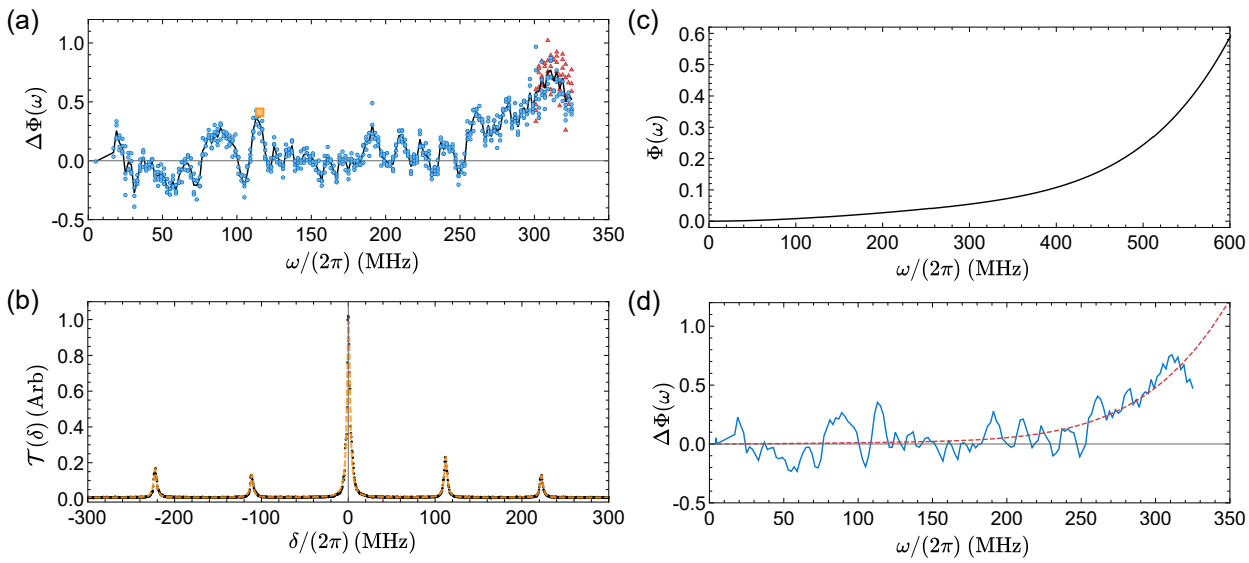


Figure 5.4: Phase Response. (a) The measured relative phase response $\Delta\Phi(\omega) = \Phi(2\omega) - 2\Phi(\omega)$ extracted from modulation with $\varphi = 0$ (blue circles) and $\varphi = \pi/2$ (red triangles). Shown in black is the rolling average. The two sets of φ data are plotted in the frequency ranges where they are sensitive to $\Delta\Phi(\omega)$. (b) Cavity scan (black dots) and the fitted curve (orange dashed) of a representative interferometric spectrum at the frequency indicated by the orange square in (a). (c) Phase response $\Phi(\omega)$ (black solid) reconstructed from the measured $\Delta\Phi(\omega)$. (d) Comparison between the measured relative phase $\Delta\Phi(\omega)$ (blue solid) and the relative phase obtained from the reconstructed phase response $\Phi(\omega)$ (red dashed).

$\beta_{1,\text{eff}} = \beta_{2,\text{eff}} = 0.7$ and measure the resulting spectra for $\varphi = 0$ and $\varphi = \pi/2$. The amplitudes are chosen to maximize contrast while keeping the spectra relatively simple. The two values of φ help resolve a quadrant ambiguity in Eq. (5.9). Fig. 5.4a shows the extracted relative phase $\Delta\Phi(\omega)$ and Fig. 5.4b shows a representative fitted spectrum.

To reconstruct $\Phi(\omega)$ from $\Delta\Phi(\omega)$, we make the following assumptions. We assume that $\Delta\Phi(\omega) \approx 0$ at the lowest measured frequency. We also assume that the leading order term in $\Phi(\omega)$ is quadratic. We rule out a linear leading order term since this would only produce a common time delay; this delay cannot be measured using this interferometric protocol nor does it affect any generated spectrum.[4] We further assume that $\Phi(\omega)$ is smooth and slowly varying over the measured frequency range. Therefore, we fix $\Phi(0) = 0$ and fit the $\Delta\Phi(\omega)$

[4]The justification closely follows the discussion of chromatic dispersion in Section 5.3.2, just applied to frequency instead of wavelength.

data to a low-order polynomial with zero offset and vanishing linear term. The fitted and smoothed version of $\Delta\Phi(\omega)$ is then used to reconstruct $\Phi(\omega)$.

To obtain the total phase response $\Phi(\omega)$, we start near $\omega = 0$ and proceed in a ladder-like manner. For example, $\Phi(2\Omega)$ is obtained from lower frequency measurements using $\Phi(2\Omega) = \Delta\Phi(\Omega) + 2\Phi(\Omega)$. As a sanity check, we run the process in reverse and extract the relative phase $\Delta\Phi(\omega)$ from the reconstructed total phase $\Phi(\omega)$ (Fig. 5.4c) and compare it against the measured relative phase $\Delta\Phi(\omega)$. We find good agreement, indicating proper reconstruction of $\Phi(\omega)$ from the measurements (Fig. 5.4d).

5.4.3 Compensated Signal Comparison

This transfer function estimation protocol is only worthwhile if it generates cleaner spectra. Thus, as a final check, we compare measured and simulated spectra with and without transfer function compensation. All measured spectra are obtained from Fabry-Perot cavity scans. The simulated spectra come from applying the measured modulation transfer function to the phase modulation profiles and convolving the spectra with the measured Fabry-Perot lineshape (Fig. 5.5).

To generate the compensated waveforms, we apply the inverse of the measured transfer function to the uncompensated modulation profiles. The frequency range of our serrodynes is between 12.5 and 190 MHz, with the highest frequency chosen so that all serrodynes contain at least two compensated Fourier components. Apart from small horizontal deviations in the peak locations, attributred to the nonlinear piezo response, we find good agreement between measured and simulated spectra. This validates our transfer function calibration protocol.

We find that compensating for the transfer function leads to improved spectra. For example, the -1 order sideband and the carrier are suppressed on average to 24(8)% and 16(10)% of their respective values in uncompensated spectra. Furthermore, the 1st order sideband increases on average by 6(5)%, suggesting improved efficiency. Nevertheless, even with compensation, the overall modulation efficiency, as measured by the power in the desired

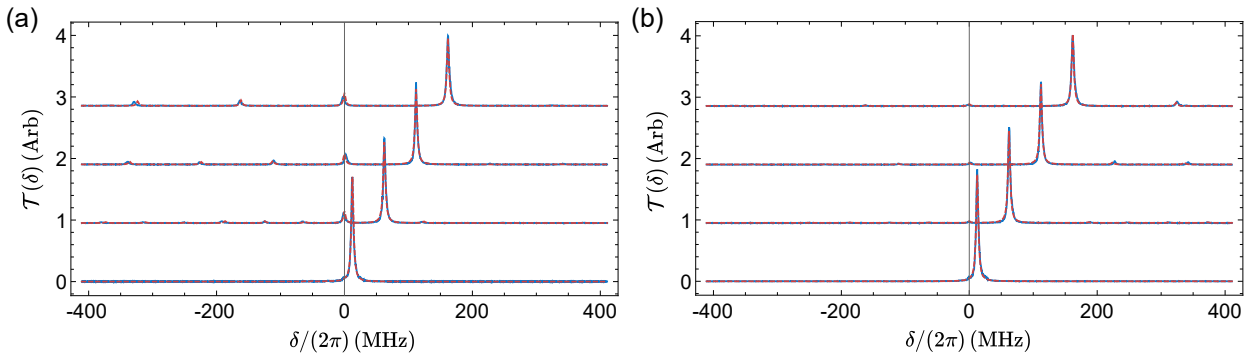


Figure 5.5: Compensated and Uncompensated Serrodyne Spectra. (a) Measured (blue solid) and simulated spectra (red dashed) of uncompensated serrodynes, for serrodyne frequencies of 12.5 MHz, 63.5 MHz, 145 MHz, and 165 MHz. (b) Measured (blue solid) and simulated (red dashed) spectra of compensated serrodynes for the same serrodyne frequencies. For the simulated spectra, we apply a single vertical scaling factor, which is obtained by comparing the maxima of the simulated and measured spectrum for the uncompensated 12.5 MHz serodyne. The cavity traces are shifted horizontally to align the main peaks with the simulation, and a single horizontal scaling factor is used for all traces.

sideband, decreases with increasing serrodyne frequency. For (un)compensated modulation profiles, the efficiency decreases from (88)90% at 12.5 MHz to (48)50% at 190 MHz. While the improvements in efficiency are modest, compensation greatly suppresses spurious peaks within the modulation bandwidth, as shown in Fig. 5.5.

5.4.4 Proof-of-Principle Demonstration

As a proof-of-principle demonstration, apply these newly developed techniques to generate a spectrum relevant to laser-cooling CaF [40, 41, 46]. In CaF, closed optical cycling can be achieved by addressing the $X(v = 0, N = 1) \rightarrow B(v = 0, N = 0)$ optical transition at 531 nm. The ground state $X(N = 1)$ is composed of four hyperfine states while the excited state hyperfine structure is unresolved (Fig. 5.6a). As a result, four optical frequencies are needed to prevent molecules from falling into unaddressed hyperfine manifolds. However, even when each transition is addressed, magnetic dark states (m_F states) can still persist. However, these dark states can be destabilized either by applying a small magnetic field or using a beam with a time-varying optical polarization. Here, we use GSA to generate a

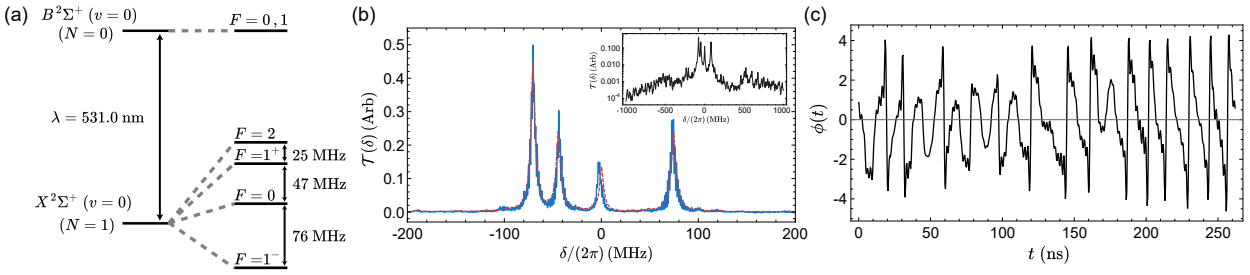


Figure 5.6: Proof-of-Principle Spectrum Generation for $X(N = 1) \rightarrow B(N = 0)$ Transition in CaF. (a) Hyperfine structure of CaF for states in the $X(N = 1) \rightarrow B(N = 0)$ optical cycling transition. The excited hyperfine structure is unresolved. (b) A spectrum that can address all the ground hyperfine states in (a) is generated using GSA, and compensated by the measured transfer function. The hyperfine components are addressed with relative powers $5 : 3 : 1 : 3$, and a target linewidth of 2 MHz is used. Shown in blue solid (red dashed) is the measured (simulated) cavity transmission $\mathcal{T}(\delta)$. Inset shows the simulated spectral weight on a logarithmic scale. The horizontal scaling is identical to that in Fig. 5.5. A horizontal shift is applied to overlap the measured and simulated maxima ($F = 2$ feature). (c) Compensated $\phi(t)$ used to generate the spectrum in (b).

spectrum addressing all hyperfine manifolds spaced in frequency by the zero-field hyperfine energy levels. The intensities in each sideband in chosen proportional to the number of targeted m_F levels $(2F + 1)$ in each hyperfine manifold. In addition, to demonstrate GSA's ability to generate arbitrary spectral distributions, the target hyperfine components are intentionally broadened to have Lorentzian profiles with FWHM linewidths of 2 MHz. As shown in Fig. 5.6(b), the measured spectrum generated using GSA and the simulated target spectrum agree well, demonstrating that our method can be used to generate and shape multi-frequency spectra for practically relevant hyperfine level spacings. The good agreement also shows that our method works in SHG systems and that chromatic dispersion in long fibers is not a concern.

We next characterize the efficiency of producing spectral weight about the targeted frequencies. We find that 74% of the power is contained in the four hyperfine lines. The power in each line is obtained by integrating over a frequency width of 14 MHz, roughly twice the observed FWHM in the cavity transmission. As shown in the inset in Fig. 5.6(b), the residual power is distributed over a broad background at the $\leq 10^{-2}$ level relative to the peak features. This background is better suppressed in the spectral window of width

2×500 MHz surrounding the carrier, with the half-width determined by the electronic bandwidth (500 MHz) of our system. In heavy molecules with small rotational constants, this could be problematic since non-rotationally closed transitions can be excited. Nevertheless, GSA is just one of many CGH algorithms, and more advanced algorithms can potentially produce solutions with lower backgrounds within this window. We briefly highlight some variants of GSA and other CGH protocols in Section 5.6.2.

5.4.5 GSA vs Concantenated Serrodynes

To gain insight into the differences between concatenated serrodynes and GSA solutions, we examine serrodyne and GSA solutions all targeting the same CaF spectrum but differing by the total phase modulation waveform duration. The spectra of concatenated serrodynes contain unintended spectral content due to transients between the different serrodyne sections. For long waveform durations, these transients are sparse and hence the spectral deviations are small. Therefore, the GSA solutions, when seeded with concatenated serrodyne solutions, closely resemble the initial serrodyne seeds (Fig. 5.7a). However, for short waveform durations, switching transients occur often, and the GSA solution significantly deviates from the initial concatenated serrodyne seed. At waveform durations much shorter than $1/\Delta\omega$, where $\Delta\omega$ is the typical difference between two adjacent target frequencies, the GSA solution no longer resembles the serrodyne seed.

5.5 Simulation of Optical Scattering

While we have shown that multi-frequency spectra can be generated successfully (e.g. to address the $X(N=1) \rightarrow B(N=0)$ transition in CaF), producing the desired spectrum is not the only consideration when addressing optical transitions in atoms and molecules. While the energies of the internal states determine the required spectrum, the excited state lifetimes of atoms and molecules also affect the internal state dynamics and therefore provide

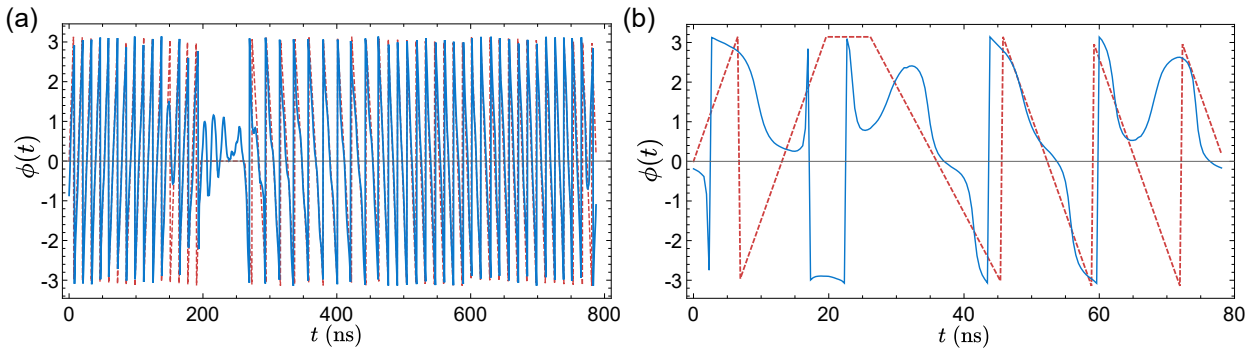


Figure 5.7: Comparison of Concatenated Serrodynes and GSA Solutions: The target spectrum is the same as in Fig. 5.6. (a) Shown are the seeded GSA solution $\phi(t)$ (bue solid) and the initial seed $\phi_0(t)$ (red dashed) for a waveform duration of $\tau = 787\,\text{ns}$. This waveform duration yields a Fourier limit $1/(2\pi\tau) = 200\,\text{kHz}$, and the smallest hyperfine spacing of 25 MHz is therefore fully resolvable. (b) For a shorter waveform duration of 78.7 ns, the corresponding Fourier limit is $1/(2\pi\tau) = 2\,\text{MHz}$. The seeded GSA solution $\phi(t)$ (blue solid) deviates significantly from the concatenated serrodyne seed $\phi_0(t)$ (red dashed).

additional timescales to consider when generating phase modulation profiles. For example, if one tries to address resolved hyperfine manifolds by concatenating a series of serrodynes, but at a rate much slower than the excited state decay rate, optical pumping into unaddressed manifolds will occur and molecules will fall into these dark states. This is very different from the case where all hyperfine frequency components are simultaneously present. This concern of falling into dark states is especially relevant in the context of photon cycling.

The question then becomes, given an excited state decay rate of Γ, what is the optimal waveform duration for the application at hand. In this section, we specifically consider the problem of maximizing the photon scattering rate, which is relevant to fluoresence detection and laser-cooling. Specifically, we will show that for the case of the $X(N = 1) \rightarrow B(N = 0)$ transition in CaF, GSA solutions and concatenated serrodynes comparable to and even better than the AOM-only solution of combining four frequency components. We refer to this AOM-only protocol as "simultaneous frequencies".

5.5.1 Optical Bloch Equation Simulations

We perform OBE simulations of the $X(N = 1) - B(N = 0)$ system in CaF to compare photon cycling rates obtained using different schemes of frequency generation. The goal in photon cycling is to maximize the photon scattering rate Γ_{sc}, which is related to the excited state population P_e via $\Gamma_{sc} = \Gamma P_e$. For the B-state in CaF, $\Gamma = 2\pi \times 6.3\,\mathrm{MHz}$. In our OBE simulations, we calculate the time-averaged steady-state excited state population P_e for concatenated serrodynes and GSA solutions with different waveform periods τ and light intensities I/I_{sat}, where $I_{\mathrm{sat}} = \frac{\pi hc\Gamma}{3\lambda^3}$ is the saturation intensity. The results are compared to the case of simultaneous frequencies.

To allow a fair comparison between the different schemes, the external fields and the light polarizations in the simulations are fixed. To avoid the formation of dark states, the following parameters are used. A small magnetic field of 5 G is applied, and two beams of orthogonal linear polarizations are used. The polarizations are oriented 45 degrees with respect to the magnetic field, and the spectrum of the two beams are identical except for a 12 MHz frequency shift. These parameters were found by optimizing for the case of simultaneous frequencies in the intensity range of $I/I_{\mathrm{sat}} \approx 100 - 500$, where an excited state population of $P_e \approx 0.19$ is reached. We note that under steady-state conditions, the theoretical maximum excited state population is given by $N_e/(N_g + N_e)$ where N_e and N_g are the number of states in the excited and ground manifolds, respectively. For the $X(N = 1) \rightarrow B(N = 0)$ transition, this ratio is 0.25.

Fig. 5.8 shows the excited population P_e for simultaneous frequencies, concatenated serrodynes, and GSA solutions as a function of the intensity I/I_{sat} and the dimensionless waveform duration $\Gamma\tau$. For short waveform durations, the excited state populations P_e produced by concatenated serrodynes and GSA solutions are comparable to those produced by sending in simultaneous frequencies. At high intensities, the GSA solution and concatenated serrodynes both produce high excited state populations out to waveform durations of $\tau \approx 10\Gamma^{-1}$, much longer than the simple expectation of $\tau \approx \Gamma^{-1}$. In addition, we find that at high intensities

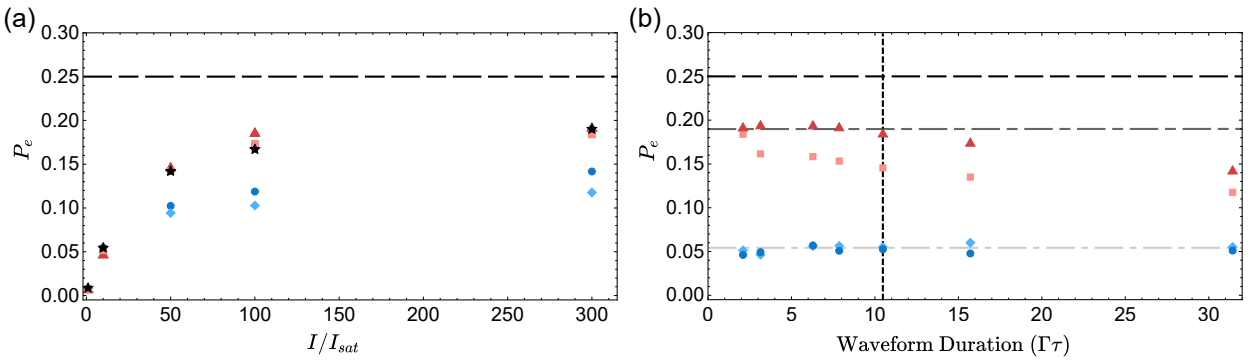


Figure 5.8: Optical Bloch Equation Simulations for the $X(N=1) - B(N=0)$ System in CaF: (a) The average steady-state excited state population P_e as a function of intensity I/I_{sat}. Shown in red triangles and light-red squares are the results of the GSA solution and the concatenated serrodynes, respectively, for a waveform duration of $\Gamma\tau = 2.1$. For a longer waveform duration ($\Gamma\tau = 31.4$), both the GSA solution (blue circles) and the concatenated serrodynes (light-blue diamonds) produce lower excited state populations. For comparison, black stars indicate the results for simultaneous frequencies and the black dashed line marks the theoretical maximum. (b) Excited state population P_e as a function of waveform duration $\Gamma\tau$. At high intensity ($I/I_{\text{sat}} = 300$), the GSA solutions (red triangles) shows higher P_e than the concatenated serrodynes (light-red squares). At a lower intensity ($I/I_{\text{sat}} = 10$), the GSA solutions (blue circles) and concatenated serrodynes (light-blue diamonds) yield similar P_e. For comparison, P_e obtained using simultaneous frequencies at the corresponding high (dark-gray dashed line) and low intensities (light-gray dashed line) are shown. Also shown is the theoretical maximum (black dashed line). The vertical black dashed line denotes the waveform duration used in Fig. 5.6.

($I/I_{\text{sat}} = 300$), GSA solutions produce higher excited state populations than concatenated serrodynes. At lower intensities, the two methods produce similar results.

We believe that the long waveform duration threshold ($\tau \gg \Gamma^{-1}$) before the scattering rate decreases likely comes from the following three effects. First, the rate of going into an unaddressed hyperfine level is lower than Γ. When a single hyperfine manifold is addressed, the total population in the dark manifolds will grow at a rate of $\frac{N_g - N_A}{N_g}\Gamma$, where N_A is the number of addressed states. The critical waveform duration (τ_c) at which the dark state population becomes significant can be estimated by summing the inverses of these rates. For the present transition, this gives $\Gamma\tau_c = 5.5$. Second, at $I/I_{\text{sat}} = 300$, power broadening means that closely-spaced hyperfine manifolds, such as $F = 2$ and $F = 1^+$, can be simultaneously addressed, which further extends τ_c. Third, the finite excited state lifetime implies that

molecules experience a spectrum that is obtained from a time window of $\sim 1/\Gamma$ rather than the entire waveform. This means that the molecules see additional spectral content that can address multiple hyperfine manifolds simultaneously, further increasing τ_c. In the case of photon scattering, the third effect likely leads to higher scattering rates in general, and could explain why the GSA solutions outperform the concatenated serrodynes at high intensities.

To summarize, for the case of CaF at the aforementioned external fields and laser configurations, our simulations show that both concatenated serrodynes and GSA solutions produce excited state populations P_e comparable to that obtained using simultaneous frequencies. We also find that these solutions continue to perform well at longer waveform durations ($\tau \gg \Gamma^{-1}$). In our setup, we have sufficient bandwidth to generate waveform durations as short as $\tau = 2\Gamma^{-1}$ ($\tau = 52\,\mathrm{ns}$), implying that favorable scattering rates can be achieved. From the above considerations, we expect that for the purpose of cycling photons in molecules, our method is robust and will perform favorably for molecules with similar excited state lifetimes and ground state energy splittings.

5.6 Outlook

We conclude with a few comments and projections on novel capabilities enabled by CGH spectral engineering. We also comment on the growing relevance of generating arbitrary spectra for direct slowing of molecules relevant to both the precision measurement and quantum science communities.

Although our CGH-based method offers only modest improvements in scattering rates compared to concatenated serrodynes, our CGH-based method is far more general and can create extended spectral distributions that are difficult to create otherwise. Our method also allows extended spectra to be controlled dynamically on timescales as fast as typical excited state lifetimes, which can open up new possibilities. For example, in Doppler

cooling, one can first use broadened and far-detuned spectra to capture fast particles, and subsequently narrow and ramp the spectra closer to resonance to achieve Doppler-limited temperatures. Finally, our method simplifies the problem of generating N arbitrary frequencies. Compared to existing solutions that require physical resources that scale with N, our method requires only a single device. This is especially important in light of the push towards controlling molecules of ever-increasing complexity, which generically require light of ever-increasing spectral complexity. Based on the features and limitations of our CGH-based spectral engineering method, we have identified the following scenarios where our method can be advantageous: 1) situations where a large number of arbitrary frequencies are needed, 2) situations where extra spectral content at the 10^{-2} level can be tolerated, 3) situations where a weak broadband background is much more desirable than spurious peaks. The third situation is encountered when non-linearities are present. This occurs, for example, in laser slowing and atomic/molecular beam experiments, where the finite interaction time implies that spectral content below a certain intensity threshold is negligible.

The situations we identified above already occur in ongoing searches for nuclear magnetic quadrupole moments (MQM) in molecules and in a theoretically-proposed molecular slowing scheme. In a molecular MQM search, molecules with sufficient nuclear spin ($I \geq 1$) are required, leading to an increase in the number of relevant optical transition frequencies [117–119]. In a proposed molecular Zeeman slower [120], multiple optical frequencies are also needed since large Zeeman splittings are encountered at the proposed magnetic fields. Beyond these two examples, this method could open up molecular experiments whose laser systems would be otherwise prohibitively complicated or expensive.

5.6.1 Adoption in Molecular Laser-Cooling Platforms

We provide a breif summary of other experiments that have adopted the high-bandwidth EOM techniques developed in this work.

BaF

In addition to its utility in laser-slowing CaF, we hoped this protocol could be broadly used across many molecular AMO experiments. To our delight, it has been adopted by the Langin BaF experiment, now at TU Wein [121].

The BaF experiment is a precision-measurement experiment utilizing the heavy mass of Ba and its many isotopes to search for party violation. The high abundance of ^{138}Ba makes producing ^{138}BaF relatively easy. Additionally, the $I_{\mathrm{Ba}} = 0$ nuclear spin in ^{138}BaF results in hyperfine structure resembling that of ^{40}CaF. However, the absence of a nuclear spin in ^{138}Ba results in low sensitivity to parity-violation. In contrast, the $I_{\mathrm{Ba}} = 3/2$ in ^{137}BaF makes it both sensitive to parity-violating effects and more difficult to laser-cool. In this isotopologue, there are 11 hyperfine manifolds in $N = 1$ (up from 4 without the nuclear spin), increasing the number of resolvable transitions by a factor of $\sim 3 - 5$ [122, 123].

This molecule is well-poised to benefit from spectral engineering. In fact, even in the simpler isotopologue of ^{138}BaF, the Langin group reports improved cooling efficiency using serrodyne waveforms compared to a sinusoidally modulated free-space EOM [124]. Insights this group gained about the relative importance of addressing each resolved transitions led to a hybrid approach employing both synthesized spectra via serrodynes and sinusoidal modulation to slow, cool, and detect the more complicated ^{137}BaF isotopologue [125].

Beyond BaF, the relative increase in complexity to achieve optical cycling in Fermionic isotopologues is encountered for all metal-fluoride molecules. Increased interest in these Fermionic isotopologues, particularly for their application to quantum simulation of extended Fermi-Hubbard models using directly-slowed ultracold molecules, suggests that synthesized spectra could also play an increasingly important role as experiments using laser-cooled fermionic MgF and SrF come online.

YbOH

The Hutzler group at Caltech has identified synthesized spectra as an exciting and potentially enabling technology, especially as increasingly complicated polyatomic molecules are targeted for slowing, cooling, and optical detection. In particular, for YbOH and other molecules with similar structure exhibiting "congested" molecular transitions, spectra without unwanted sidebands could be more easily generated using CHG methods [126].

Beyond Molecules

Beyond applications to photon cycling, fine-control over optical spectra could prove useful as high-bandwidth optical technology is interfaced with state-of-the-art quantum computation platforms. For example, a recently-demonstrated high-bandwidth SLM, essentially acting as a high-resolution spectrometer, requires fine-control over optical spectra to achieve fast and parallelizable control [127]. The techniques and insights from CHG spectral engineering may prove critical to increasing the efficiency of this and other technologies relying on precise spectral control.

5.6.2 CGH Variants and Waveform Modifications

The exploration of variants of GSA and other CGH protocols was beyond the scope of our initial spectral engineering exploration. However, several improvements to the spectral quality and effective bandwidth of this system could be easily realized.

On the CGH algorithm front, variants to GSA involving dynamic feedback on the target spectrum help improve solution convergence. Relatedly, high-quality holograms can be generated in a specific region-of-interest (ROI) of the hologram at the expense of additional uncontrolled content outside the ROI [110, 111]. This "don't-care" region effectively reduces constraints across the entire hologram, and helps increase solution quality in the ROI.

Beyond GSA, several advances have been made on the front of CGH, including insights about how the hologram problem relates to the problem of "optimal transport" [128]. Along

another front, AI-assisted techniques have enabled dynamic hologram generation in the context of tweezer-trapped atom rearrangement [129]. This technique should also have immediate application to the spectral engineering problem. It would be interesting to see whether AI-assisted algorithms provide an advantage to engineering and dynamically changing spectrally-extended target patterns.

We finally comment on a limitation and work-around for GSA-generated solutions in 1D. The nature of the Fourier transforms in the IFTA restricts the range of solutions to span 2π. In contrast to 2D holograms, it is relatively straightforward to "unwrap" a 1D hologram (removing the 2π phase jumps) to produce a continuous $\phi(t)$. Since commercially available high-bandwidth EOMs often support modulation depths beyond a 2π range, unwrapped waveforms are practically relevant to experimental implementations. Even an extension of the modulation width to 4π would generically decrease the spectral content in $\phi(t)$ by a factor of 2, decreasing bandwidth requirements on the rf and EOM components. This trade-off between range and bandwidth could be interesting to explore in the future.

Chapter 6

Background-Free Detection via Bichromatic Imaging

Cuiusvis hominis est errare, nullius nisi insipientis in errore perseverare.

– Cicero (the Roman)

Our investigation of birchomatic imaging in CaF is a great example of being stumped by and then resolving unknown-unknowns; I would characterize this as another fundamental job of a PhD student. This investigation was arguably a bit of a "sidetrack" once we realized the imaging performance was sub-par. However, these investigations provided important insights that enabled subsequent progress. In particular, the investigations into rotational repumping helped start the ball rolling towards our eventual implementation of rotational shelving and unshleving, which are now critical steps during tweezer loading and imaging.

In this chapter, we highlight successful implementations of bichromatic imaging in other atomic and molecular platforms. We next elaborate on the need for this imaging protocol in the first place, and details on the "final-draft" of the protocol. We also detail the analysis techniques developed during this investigation which allow estimating imaging identification errors. Finally, we present a detailed investigation into an unexpected coincidence arising

from the tweezer wavelength being near-resonant with a $B - C$ transition. These investigations suggest a substantial revision to the $B - C$ transition dipole moment in CaF.

The work presented in this chapter resulted in the following publication [1]:
Connor M. Holland, Yukai Lu, Lawrence W. Cheuk. "Bichromatic Imaging of Single Molecules in an Optical Tweezer Array" Phys. Rev. Lett. ***131****, 053202 (2023).*

6.1 Dual-Frequency Background-Free Detection

In many fluorescence detection protocols, an atom or molecule absorbs a photon on an electronic transition and subsequently emits a photon at nearly the same wavelength. Despite this apparent simplicity, it is often challenging to distinguish photons scattered by the atom or molecule from those scattered or reflected by surrounding optics (e.g., dust on mirrors, imperfect anti-reflection coatings, or the vacuum chamber itself). When these stray photons reach the detection camera, they contribute to a background count that limits the fidelity of fluorescence detection. That being said, for many atomic species, closed cycling transitions are readily available, and a good choice of beam geometry can significantly suppress stray light.

However, in situations where imaging infidelity must be minimized, where geometric constraints (both fundamental and technical) prevent clean separation of excitation and detection paths, or where the fluorescence signal is intrinsically weak due to inefficient optical cycling or low particle number, reducing photon backgrounds becomes paramount.

The requirements for fluorescence detection are also largely orthogonal to those for laser cooling. Efficient detection favors high photon scattering rates, enabling rapid readout and minimizing the time over which background photons accumulate. In contrast, laser cooling relies on the presence of dark states, where population accumulates and entropy is reduced [130]. Generally, lower temperatures are associated with darker dark states and

thus lower scattering rates. This fundamental tension motivates approaches that decouple detection from cooling.

Two general strategies have emerged to achieve this separation. The first employs distinct electronic transitions for cooling and fluorescence detection. Heating induced during detection can be mitigated by simultaneous cooling, allowing for rapid, low-loss imaging. When the wavelengths used for detecting and cooling are well-separated, dichroic optics and spectral filtering enable efficient suppression of cooling light from reaching the camera. This approach is used in alkaline-earth-like atoms such as Sr [81, 131] and Yb [76], which offer both broad transitions for rapid scattering and narrow lines suitable for cooling.

The second strategy avoids direct excitation on the fluorescence transition altogether. Instead, population is transferred via intermediate states to an excited state that subsequently decays, producing detectable photons. This can be realized through either two-photon excitation or multi-level pump–depump schemes. The latter is particularly well suited to molecules with near-diagonal Franck–Condon factors. During laser cooling, population accumulates in excited vibrational states, which are then repumped back to states participating in laser cooling through an intermediate excited state. In many cases, this spontaneous emission is spectrally separated from the excitation lasers, enabling photons emitted during the decay to be spectrally separated from all driving fields, leading to background-free detection. The two-photon excitation scheme has been employed in early CaF laser-slowing investigations [38], while pump–depump schemes have been demonstrated in both diatomic [132] and polyatomic molecules [57]

6.2 Bichromatic Imaging in CaF

6.2.1 Imaging Scheme

Our investigation of bichromatic imaging begins with laser-cooled CaF molecules loaded in the presence of Λ-cooling light into a linear array of 20 identical optical tweezer traps.

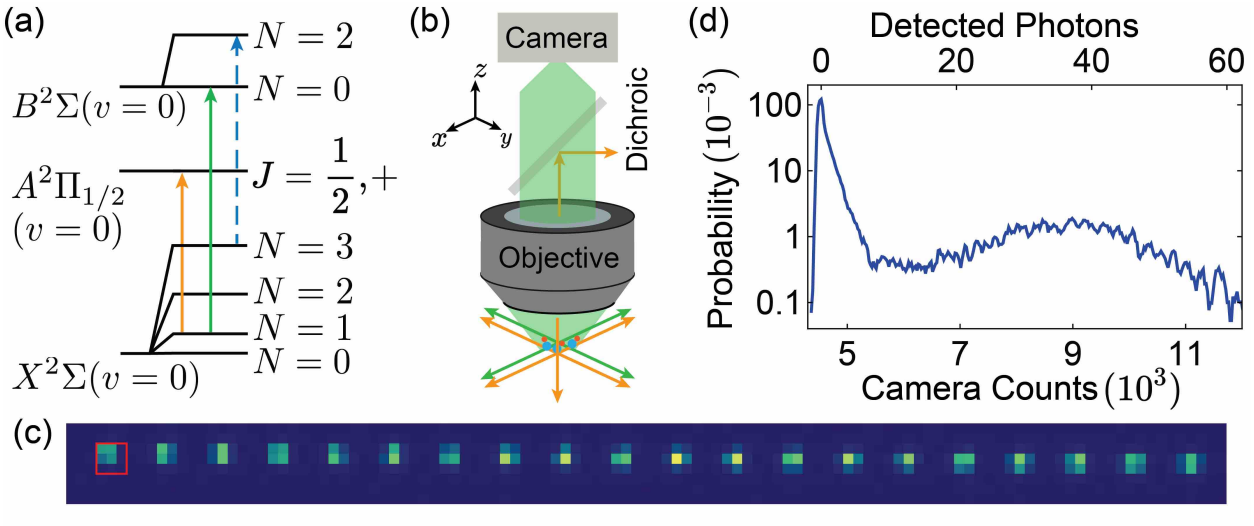


Figure 6.1: (a) CaF Levels and Transitions in Bichromatic Imaging. Shown in orange (green) is the $X - A$ Λ-cooling light ($X - B$ imaging light) at 606 nm (531 nm) used to provide cooling (to elicit $X - B$ imaging photons). Also indicated in blue is light addressing the $X(v = 0, N = 3) - B(v = 0, N = 2)$ transition, which is used to address a rotational leakage channel. (b) Λ-cooling light (orange) illuminates molecules along three directions $(\pm\hat{x}, \pm\hat{y}, \pm\hat{z})$ while $X-B$ imaging light is sent approximately along the $\pm\hat{x}$ and $\pm\hat{y}$ directions. $X-B$ fluorescence (green) enters the objective, passes through dichroic filters, and is detected by an EMCCD camera. (c) Average image of molecules in a 20-site optical tweezer array. The red square indicates an exemplary region for obtaining imaging histograms. (d) Example histogram at an average tweezer occupation of $p = 0.21$.

The tweezer traps are created using focused beams of 781 nm light propagating through the objective along $-\hat{z}$ (Fig. 6.1(b)). Each tweezer trap has a Gaussian beam waist of $w_0 = 720(14)$ nm, and has a trap depth of $V = k_B \times 1.28(11)$ mK for molecules in the electronic ground state $X^2\Sigma(v = 0)$.

The imaging scheme implemented is of the first variety outlined in the introduction, where molecules are cooled along one transition and imaged along another. We apply Λ cooling on the $X^2\Sigma(v = 0, N = 1) \rightarrow A^2\Pi_{1/2}(v = 0, J = 1/2, +)$ transition at 606 nm, while excite and detect along on the $X^2\Sigma(v = 0, N = 1, F = 0) \rightarrow B^2\Sigma(v = 0, N = 0)$ transition at 531 nm. Vibrational repumpers addressing the $X^2\Sigma(v = 1, 2, 3, N = 1) \rightarrow A^2\Pi_{1/2}(v = 0, 1, 2, J = 1/2, +)$ transitions are present. Additionally, light addressing the $X^2\Sigma(v = 0, N = 3) \rightarrow B^2\Sigma(v = 0, N = 2)$ transition is applied to repump molecules that decay into $X^2\Sigma(v = 0, N = 3)$ (Fig. 6.1(a)). The resulting $X - B$ fluorescence is collected

through the microscope objective and imaged onto an EMCCD camera. Dichroic filters in the imaging path remove the Λ-cooling light, $X - A$ fluorescence, and stray optical tweezer light. In detail, the Λ-cooling light is applied along all three directions ($\pm\hat{x}$, $\pm\hat{y}$ and $\pm\hat{z}$), while the $X - B$ excitation light avoids the objective axis ($\hat{z}$) and only propagates roughly in the $\hat{x} - \hat{y}$ plane. As shown in Fig. 6.1(c), the average images obtained using bichromatic imaging reveal the presence of molecules in the tweezer traps. Optimizing for maximal survival at a fixed $X - B$ light intensity of $I = 12(1)\mathrm{mW/cm}^2$, we find Λ-cooling parameters similar to those for Λ-imaging [86]. We obtain an imaging lifetime of $\tau = 148(14)\,\mathrm{ms}$, and a $X - B$ photon scattering rate of $\Gamma_{\mathrm{sc}} = 1.95(4) \times 10^4\,\mathrm{s}^{-1}$.

6.3 Evaluating Imaging Performance

6.3.1 Performance Summary

To evaluate the imaging performance, we construct histograms of the total camera counts in cropped image regions surrounding each tweezer (Fig. 6.1(c)). The histograms reveal a bimodal distribution (Fig. 6.1(d)), with the two peaks corresponding to empty and occupied tweezers. When the collected fluorescence is below (above) a threshold θ, we classify the corresponding tweezer as empty (occupied). We parameterize the classification errors, ϵ_{10} and ϵ_{01}, the probabilities of incorrectly classifying an occupied tweezer as empty and vice versa, respectively. The total misclassification probability depends on the average occupation p and is given by $\epsilon(p) = p\,\epsilon_{10} + (1-p)\epsilon_{01}$. We define the imaging fidelity f as the probability of correctly classifying a tweezer when $p = 0.5$, i.e. $f = 1 - \epsilon_{\mathrm{opt}}(0.5)$, at the optimal threshold θ_{opt}. By applying a rescaling procedure to histograms (see the subsequent Section 6.3.2), we obtain the errors ϵ_{10} and ϵ_{01} for 30 ms-long images, from which we extract an imaging fidelity of $f = 0.977(2)$ (Fig. 6.2(a)). During the images, ≈ 35 photons are collected per molecule, well above the background value of ≈ 0.3 photons per tweezer.

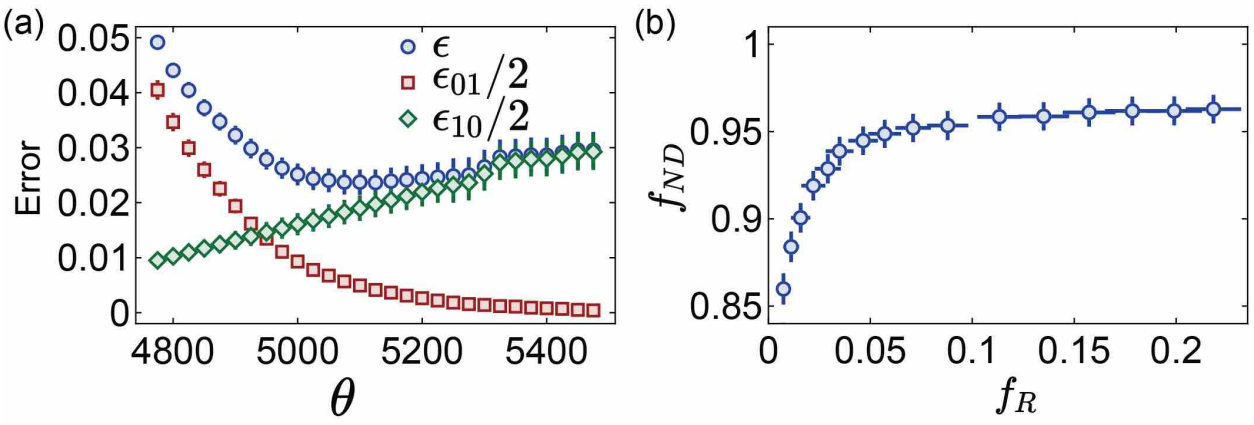


Figure 6.2: (a) Error Probabilities Versus Classification Threshold θ. Shown in green diamonds and red squares are the measured error probabilities $\epsilon_{10}/2$ and $\epsilon_{01}/2$, respectively. The total error ϵ for an average occupation of $p = 0.50$ is shown in blue circles. ϵ is minimal at an optimal threshold of $\theta_{\text{opt}} \approx 5100$ and corresponds to an imaging fidelity of $f = 0.977(2)$. (b) The non-destructive fidelity f_{ND} (blue circles) versus the data rejection rate f_{R}. Both f_{ND} and f_{R} are controlled by θ. By increasing θ, f_{ND} is improved at the expense of higher f_{R}.

A second imaging metric is the non-destructive detection fidelity f_{ND}, which we define as the probability that a tweezer initially classified as occupied remains occupied following imaging. f_{ND} is given by

$$f_{\text{ND}} = \frac{p(1-\epsilon_{10})}{p(1-\epsilon_{10}) + (1-p)\epsilon_{01}} f_{\text{surv}}, \tag{6.1}$$

where f_{surv} is the survival probability following non-destructive detection. This metric is relevant to rearranging molecules into defect-free arrays, since the success probability of creating an array of size N is limited by $(f_{\text{ND}})^N$. At high survival probabilities and low error rates, $f_{\text{ND}} \approx f_{\text{surv}} - \epsilon_{01}(1-p)/p$. This implies that unlike f, f_{ND} primarily depends on ϵ_{01}, which is approximately the false-positive rate. The detection threshold θ can therefore be increased to reduce ϵ_{01} at the expense of increasing ϵ_{10}, the probability of rejecting occupied tweezers. Because f_{ND} is affected by f_{surv}, the imaging duration should be chosen to balance between minimizing imaging loss and maximizing fluorescence; we find that a 10 ms-long imaging duration strikes this balance.

Experimentally, we measure f_{ND} by taking two consecutive images with durations of 10 ms followed by 30 ms. The fraction of molecules classified as occupied in the second image is corrected using ϵ_{10} and ϵ_{01} to yield f_{ND}. Note that f_{ND} is a property of the first non-destructive image. It is dependent on the classification threshold θ in the first image, but is independent of the fidelity of the second image. As expected, we find that f_{ND} increases at the expense of rejecting occupied tweezer instances (Fig. 6.2(b)). At a moderate data rejection rate of $f_{\mathrm{R}} = 15\%$, we achieve a non-destructive detection fidelity of $f_{\mathrm{ND}} = 95.5(6)\%$. Both f and f_{ND} are comparable to or better than previously reported [86, 133], and are sufficient for experiments with small-scale rearrangeable tweezer arrays.

We next compare the bichromatic imaging performance to that of single-color Λ-imaging. We first examine the dependence of the bichromatic loss rate $\gamma = 1/\tau$ on the $X - B$ imaging power I and find that it increases with I. In particular, the excess loss rate beyond Λ-imaging loss, given by $\gamma_{\mathrm{excess}} = \gamma(I) - \gamma(0)$, is observed to increase linearly with I (Fig. 6.5(a)). To allow further comparison with single-color Λ-imaging, we define a figure-of-merit $\eta = \Gamma_{\mathrm{sc}}\tau$, where Γ_{sc} is the fluorescence rate of imaging photons and τ is the imaging lifetime, which encodes how many photons can be scattered before a molecule is lost. At high $X - B$ powers, η saturates to $\approx 3\times10^3$, roughly 10 times lower than that of Λ-imaging ($\eta \approx 40\times10^3$) (Fig. 6.5(b)). Hence, Λ-imaging is superior if the background from scattered light is identical for both methods. However, in practice, bichromatic imaging performs similarly well because of the significantly reduced background light.

6.3.2 Model-Free Estimation of Imaging Identification Errors

In this section, we present the full details on how we extract classification errors, the imaging fidelity, and the non-destructive detection fidelity. Of particular note, our method makes no assumptions about the probability distribution of fluorescence counts from occupied tweezers.

Classification Errors

Two errors may occur during imaging classification: occupied tweezer sites identified as empty, and empty sites identified as occupied. We denote these errors as follows: ϵ_{10} is the probability of classifying an occupied tweezer site (at the beginning of the imaging pulse) to be empty; ϵ_{01} is the probability of classifying an empty tweezer site (at the beginning of the imaging pulse) to be occupied. The total imaging error ϵ is given by $\epsilon = p\epsilon_{10} + (1-p)\epsilon_{01}$, which depends both on the the threshold θ and the true tweezer occupation probability p.

Definition of Imaging Fidelity

We first define the occupation-dependent detection fidelity $f_{\mathrm{det}}(p) = \mathrm{Max}_{\theta}(1-\epsilon)$ as the maximum fidelity (minimum total error) achieved for a given a tweezer occupation probability p, optimized over all thresholds θ. We note that both the detection fidelity $f_{\mathrm{det}}(p)$ and the optimal threshold is also a function of p. For example, for $p = 1$, $f_{\mathrm{det}}(1) = 1$ can be achieved with $\theta = 0$. To provide an occupation-independent metric for detection fidelity, we define the imaging fidelity f as the detection fidelity obtained for $p = 0.5$, i.e. $f = f_{\mathrm{det}}(p = 0.5)$. We note that $f_{\mathrm{det}}(0.5)$ is typically lower than $f_{\mathrm{det}}(p \approx 1)$ or $f_{\mathrm{det}}(p \approx 0)$.

Definition of Non-Destructive Detection Fidelity

A second metric of imaging performance relevant to rearrangeable tweezer arrays is the non-destructive detection fidelity f_{ND}, which we define as the probability that a trap classified to be occupied remains occupied following imaging. The error $\epsilon_{ND} = 1 - f_{\mathrm{ND}}$ is also known as the retention error [134]. This error can be written as

$$\epsilon_{ND} = 1 - \frac{p(1-\epsilon_{10})f_{\mathrm{surv}}}{p(1-\epsilon_{10}) + (1-p)\epsilon_{01}} \tag{6.2}$$

where f_{surv} is the survival probability following non-destructive detection. For high detection fidelities and survival probabilities,

$$\epsilon_{ND} \approx (1 - f_{\text{surv}}) + \left(\frac{1}{p} - 1\right) \epsilon_{01}. \tag{6.3}$$

This means that the retention error can be minimized by reducing ϵ_{01}, which can be achieved by using a higher threshold θ. A higher threshold, however, comes at the expense that an occupied tweezer has a higher probability of being misclassified as unoccupied, which reduces the data rate for single tweezers and effectively lowers the tweezer loading rate for tweezer arrays. This effect can be captured by the data rejection rate f_R, defined as the probability that an occupied tweezer will be classified as unoccupied. f_R increases as the threshold increases, and is given by

$$f_R = \epsilon_{10}. \tag{6.4}$$

Error Model and Imaging Fidelity Extraction

To estimate the imaging fidelity, we first determine the errors $\epsilon_{10}(\theta)$ and $\epsilon_{01}(\theta)$, which can be extracted from the histogram for an empty tweezer and the histogram for an occupied tweezer. While creating empty tweezers is straightforward, creating occupied tweezers with 100% probability directly is not possible since tweezer loading is stochastic.

To infer the histogram for an occupied tweezer, we load molecules into the 20 tweezers stochastically, and then take two consecutive images of durations 10 ms and 30 ms, respectively. We next generate a series of post-selected histograms of the second image conditioned upon camera counts exceeding a series of classification threshold θ_1 in the first image. In this analysis, all 20 tweezers are assumed to have identical imaging performance.

As shown in Fig. 6.3(a), the post-selected histograms are bimodal and their shapes depend on θ_1. For sufficiently large θ_1, the post-selected histograms still contains some weight in the lower peak, corresponding to unoccupied tweezers. This empty tweezer peak persists since

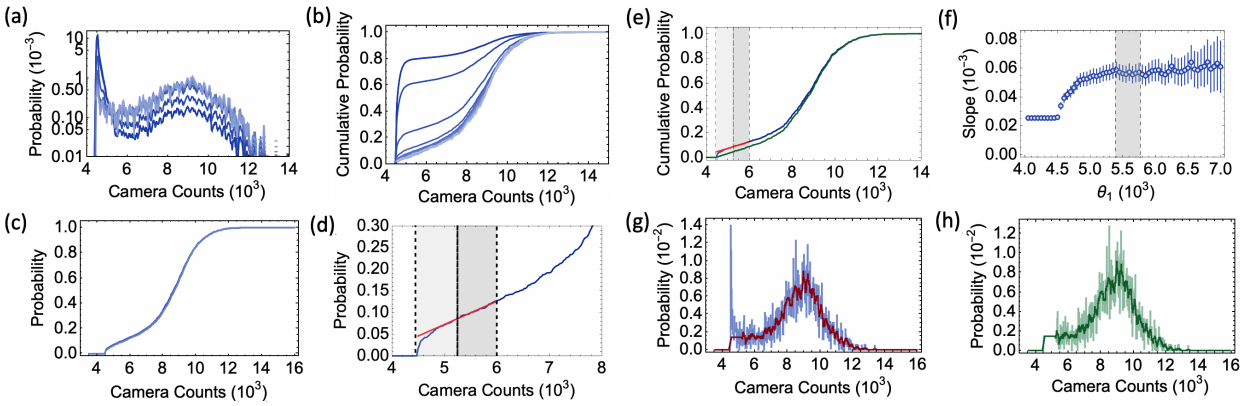


Figure 6.3: Inferring Loaded-Tweezer Fluoresence Histogram (a) Normalized histograms from the second images versus camera counts θ_2. The curves correspond to different post-selection threshold θ_1 used in the first image, which controls the effective loading rate in the post-selected datasets. (b) Cumulative probability functions $g(\theta_2)$ as a function of camera counts θ_2 in the second image, corresponding to the curves in (a). As θ_1 increases, the histograms have less contribution from unoccupied tweezers, but the noise grows as the post-selected dataset becomes smaller. In (a,b), from dark to light, θ_1 ranges from 4050 to 6800 in steps of 250. (c) Cumulative probability curves $g(\theta_2)$ for the range of post-selection parameter θ_1 that is used to extract the histograms for occupied tweezers. (d,e) Subtraction procedure. In (d), data in the right shaded region is fit to a linear curve, shown in red. Data in the left shaded region is discarded and replaced by the linear fit, producing $g'(\theta_2)$. The subtracted distribution is shifted down and renormalized, producing $g''(\theta_2)$, shown in green in (e). (f) Sensitivity of linear fitting. The fitted slope in (e) is shown as a function of post-selection threshold θ_1. To obtain the true distribution for occupied sites, $g''(\theta_2)$ are averaged for θ_1 in the shaded gray region. (g) The post-selected histogram averaged over the range of θ_1 indicated in (e) is shown in blue. The subtracted histogram, before normalization, is shown in red. A moving average of 5 bins is applied for clarity. (h) The subtracted and renormalized histogram, given by the derivative of $g''(\theta_2)$, is shown in light green. The green line shows the curve with a moving average of 5 bins.

the first image leads to a small amount of loss. To infer the fluorescence histogram from only occupied tweezers, we subtract the lower-peak contribution using the following procedure.

Over a range of θ_1 where the lower peak is suppressed but sufficient data remains to provide acceptable signal-to-noise ratios, we create normalized cumulative distribution functions (CDFs) $g(\theta_2)$ from the histograms. As shown in Fig. 6.3(b), the CDF rises abruptly at a threshold θ_{thres}, and then increases approximately linearly above the threshold. This linear portion corresponds to a flat histogram distribution near zero photon counts, which arises because of the finite imaging lifetime [131]. The sharp rise near θ_{thres} in the CDF cor-

responds to the small unoccupied peak. We remove the contribution from the unoccupied tweezers by fitting the linear portion of the CDF, and replacing the non-linear portion near θ_{thres} with a fitted linear curve truncated at θ_{thres} (Fig. 6.3(d)). As shown in Fig. 6.3(e), this distribution, $g'(\theta_2)$, contains a jump at θ_{thres}, which corresponds to the area under the lower peak in the imaging histogram. In the final step, we subtract this jump and normalize the CDF to obtain the true CDF $g''(\theta_2)$ for occupied tweezers. Specifically, we subtract $g'(\theta_{\text{thres}})$ from $g'(\theta_2)$ and rescale the resulting curve such that $g''(\infty) = 1$ (Fig. 6.3(e)). We note that $g''(\theta_2)$ in fact coincides with $\epsilon_{10}(\theta_2)$, the probability of classifying an occupied site as empty for a classification threshold θ_2. The normalized histogram for an occupied tweezer, $h(\theta_2)$ can be obtained by taking the derivative of $g''(\theta_2)$ with respect to θ_2 (Fig. 6.3(h)).

To obtain ϵ_{01}, we use the histogram for an unoccupied tweezer. This can be accomplished simply by shifting the region about each tweezer to be be sufficiently far away from the tweezer position (10 binned camera pixels (2x2 binning), 7.2 μm away). The resulting histograms simulate unoccupied tweezers with similar background light as the imaging regions for the tweezers. The function $\epsilon_{01}(\theta_2)$ can then be obtained by summing the number of counts above θ_2, and normalizing by the total number of counts.

Estimating Uncertainties in Fidelity Estimation

Uncertainty bands for the above procedures are extracted using a boot-strapping procedure. We use a dataset of 500 pairs of images, each with 20 tweezers, giving a total dataset corresponding to 10,000 tweezers. Each of the 10,000 realizations gives a pair of numbers corresponding to the ROI counts in the two consecutive images. We then generate 100 boot-strap datasets each with 10,000 realizations, by sampling the 10,000 realizations with replacement. The above analysis procedures are then carried out for each of these 100 boot-strap datasets. The uncertainties in the extracted error functions $\epsilon_{10}(\theta_2)$ and $\epsilon_{01}(\theta_2)$ are obtained from the standard deviation over the 100 boot-strap datasets.

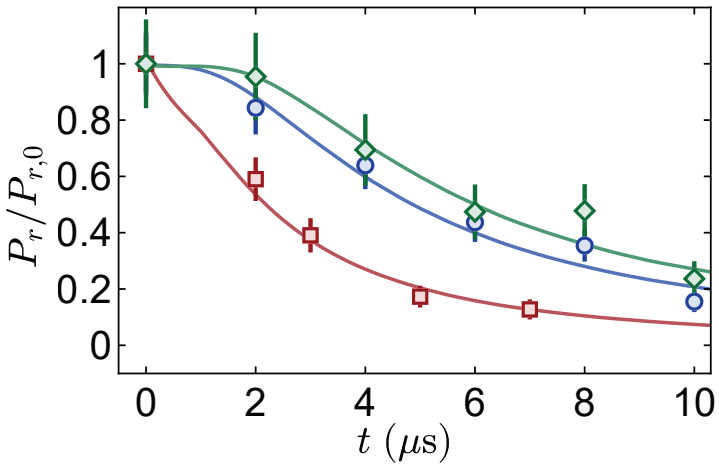


Figure 6.4: Imaging Configuration Thermometry: Normalized release-and-recapture fraction versus expansion time. Shown in green diamonds, blue circles, and red squares are release-and-recapture curves after 100 ms of bichromatic imaging, no imaging, and 10 ms of $X - B$ excitation alone, respectively. Solid curves show fits to classical Monte-Carlo simulations.

6.4 Imaging Loss Mechanisms

6.4.1 Loss Due to Heating

We first examine whether higher molecular temperatures explain the observed excess losses. We perform release-and-recapture thermometry after 100 ms of Λ-cooling and bichromatic imaging, and obtain temperatures of 123(20) μK and 90(20) μK, respectively. For comparison, $X - B$ light heats the molecules to 310(30) μK in 10 ms in the absence of Λ-cooling (Fig. 6.4).

6.4.2 Loss Due to Rotational Branching

We next investigate loss into undetected rotational states, which can be separated into parity-conserving and parity-changing ones. One mechanism of parity-conserving loss arises even under Λ-cooling alone. Molecules off-resonantly excited to $A^2\Pi_{1/2}\,(v = 0, J = 3/2, 5/2, +)$ can decay into $X^2\Sigma\,(v = 0, N = 3)$ (Fig. 6.6(a)). We find that adding a rotational repumping laser addressing the $X^2\Sigma\,(v = 0, N = 3) \rightarrow B^2\Sigma\,(v = 0, N = 2)$ transition greatly reduces this to negligible levels. Nevertheless, removing the rotational repumping laser does not

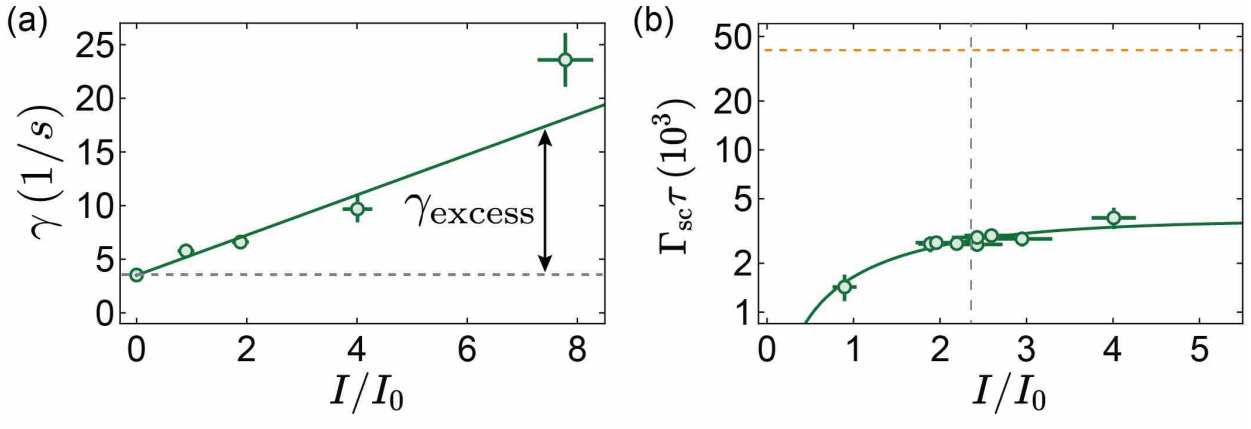


Figure 6.5: Loss and Scattering During Bichromatic Imaging: (a) Green circles show the bichromatic imaging loss rate γ versus the $X-B$ imaging intensity I/I_0 ($I_0 = 5.2(5)\,\mathrm{mW/cm^2}$). The solid line shows a linear fit. (b) The figure-of-merit $\eta = \Gamma_{\mathrm{sc}}\tau$ for bichromatic imaging (green circles) saturates to $\eta \approx 3\times10^3$, far lower than that for single-color Λ-imaging (orange dashed line, $\eta \approx 40\times10^3$). The green curve shows the fit to an exponential saturated curve. The vertical dashed line indicates the $X-B$ intensity used for bichromatic imaging in all measurements. At this intensity, $\eta = 2.7(2)\times10^3$.

significantly increase γ_{excess}. We note that vibrational-changing loss into $X^2\Sigma\,(v=1, N=3)$ should be negligible because of the highly diagonal Franck-Condon factors of the $A^2\Pi_{1/2}\,(v=0) \rightarrow X^2\Sigma(v=0)$ and $B^2\Sigma\,(v=0) \rightarrow X^2\Sigma(v=0)$ transitions.

We next quantify parity-changing rotational loss, which could arise from stray electric fields mixing in excited states of opposite parity or molecules decaying via the two-photon pathway $B \rightarrow A \rightarrow X$ (Fig. 6.6(b)). The population admixture of an opposite-parity state due to a small electric field scales inversely with the square of the energy difference. Therefore, the $B^2\Sigma(v=0, N=0)$ state, with a frequency splitting of 20 GHz to the nearest opposite parity rotational state, is expected to have a much smaller $\mathcal{O}(10^{-3})$ opposite parity admixture than the $A^2\Pi_{1/2}(v=0, J=1/2, +)$ state, which has a Λ-doublet splitting of $\sim 1\,\mathrm{GHz}$. Because the $X-A$ photon scattering rate is higher than that of $X-B$ light during imaging, while γ_{excess} is comparable to $\gamma(0)$, we can rule out stray electric fields as a cause for loss.

To measure the loss due to two-photon decay, which shelves molecules in the opposite parity rotational states $X^2\Sigma(v=0, N=0, 2)$, we directly measure the population in

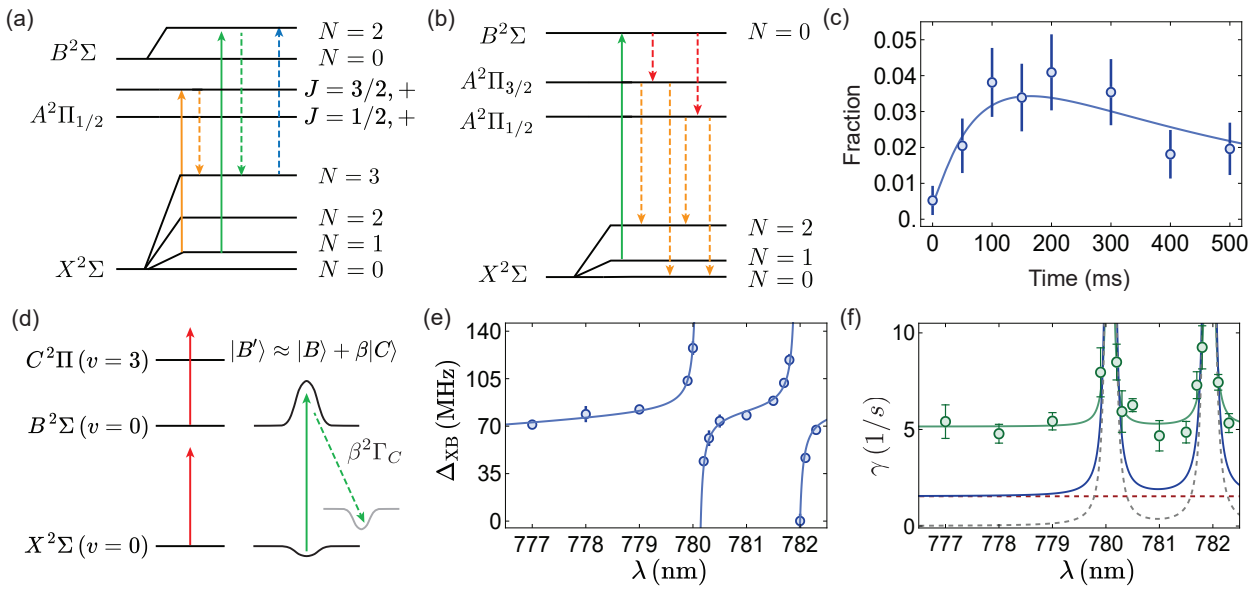


Figure 6.6: Loss and Dispersive Shifts vs Tweezer Wavelength: (a) Parity-conserving rotational loss. Solid arrows show off-resonantly excited transitions. Dashed green and orange arrows show decay channels. The blue arrow indicates the $N = 3$ repumper. (b) Parity-changing rotational loss due to two-photon decay ($B \to A \to X$). (c) Detected $X^2\Sigma(v = 0, N = 0, F = 1)$ fraction versus imaging duration at $I = 4.8(4)I_0$. Solid curve shows the fit to a rate equation model. (d) Decay induced by $C^2\Pi$-state admixture into the $B^2\Sigma(v = 0)$-state. Tweezer light (red) gives rise to repulsive trapping for the $B^2\Sigma(v = 0)$ state by admixing in the near-resonant $C^2\Pi$ states. The dressed state $|B'\rangle$ decays into dark rovibrational states (gray) due to C-state admixture. (e) Δ_{XB} versus tweezer wavelength λ. (f)Excess loss rate γ_{excess} (green circles) versus trapping wavelength λ, at $I = 2.4(2)I_0$. The red (gray) dashed curve shows the estimated parity-changing loss (C-state admixture loss); the solid blue curve is the total estimated excess loss due to both contributions.

$X^2\Sigma\,(v = 0, N = 0, F = 1)$ versus the imaging duration t. The population initially rises before decaying slowly (Fig. 6.6(c)). Using a rate-equation model with independently measured parameters (see SM of Ref. [3] for details), we extract a $B \to A$ branching ratio of $7.9(16) \times 10^{-5}$, slightly lower than the theoretically predicted value of 1.3×10^{-4} [135], but much higher than previously measured in free-space in a molecular beam $(9(2) \times 10^{-6})$ [136]. The branching ratio indicates an $A - B$ transition dipole moment of $|d_{AB}| = 0.30(3)ea_0$, $0.07\,ea_0$ smaller than theoretically predicted [135].

6.4.3 Loss Due to Admixtures of Excited States

Lastly, we investigate loss arising from admixtures of higher-lying C states into the excited B states due to the optical tweezer light. Although the trapping light is far off-resonant from transitions involving the ground $X^2\Sigma(v = 0)$ state, it is close-detuned to the $B - C$ transitions. Sufficient coupling between the B and C states can lead to observable losses via two mechanisms.

First, strong anti-trapping of molecules in the B state can lead to heating and subsequent loss. This anti-trapping occurs since the tweezer light is blue-detuned from the strongest $B^2\Sigma(v = 0) - C^2\Pi(v = 0, 1, 2)$ transitions. We have, however, already ruled out heating from our thermometry measurements. Second, admixture of the C state into the B state can lead to decay into unaddressed rotational and vibrational states during imaging, since the C state admixture can decay via multi-photon pathways and the $X - C$ Franck-Condon factors are non-diagonal (Fig. 6.6(d)). To estimate the loss rate due to this pathway, we first use the theoretically predicted value of the $B - C$ transition dipole moment $|d^{th}_{BC}| = 7.33\, ea_0$ [137], which predicts a loss rate 6 times higher than what we observe. This motivates a careful measurement of $|d_{BC}|$.

A consequence of the large value of the predicted dipole moment $|d^{th}_{BC}|$ is that the polarizabilities of the X and B state differ by a factor of ~ 20, in addition to differing in sign. Specifically, at the tweezer depth used for imaging, the predicted peak differential ac Stark shift between the X and B states is $\Delta^{th}_{XB} \approx h \times 600\,\mathrm{MHz}$. This shift is large enough to be probed optically by measuring the optical frequency of $X - B$ light that produces maximal loss. To achieve optical cycling during this measurement, sidebands addressing the four $X^2\Sigma(v = 0, N = 1)$ hyperfine levels are added to the $X - B$ light [1]. Taking into account trap-averaging, we infer a peak differential ac Stark shift of $\Delta_{XB} = h \times 78(2)\,\mathrm{MHz}$, which is much smaller than Δ^{th}_{XB}, indicating that $|d_{BC}|$ is smaller than predicted.

Next, we keep the tweezer intensity fixed and scan the wavelength of the tweezer light. As shown in Fig. 6.6(e), Δ_{XB} displays two dispersive features originating from the $B^2\Sigma(v =$

$0) - C^2\Pi_{1/2}(v = 3)$ and $B^2\Sigma(v = 0) - C^2\Pi_{3/2}(v = 3)$ transitions. The amplitudes of the features directly measure $f_{\mathrm{BC,03}}\, d_{BC}^2$, where $f_{\mathrm{BC,03}}$ is the Franck-Condon factor between the $B^2\Sigma(v = 0)$ and $C^2\Pi(v = 3)$ states. Fitting the lineshapes and using $f_{\mathrm{BC,03}}$ calculated from spectroscopic data [138, 139], we find a $B-C$ transition dipole moment of $|d_{BC}| = 2.0(1)\, ea_0$, much smaller than the predicted value of $|d_{BC}^{th}| = 7.33\, ea_0$ [137].

Assuming that C-state decays always lead to loss, the C-state admixture into the B state contributes a rate of $\beta^2\Gamma_C P_B$ to γ_{excess}, where β is the amplitude of the C-state admixture, P_B is the excited fraction in the B state, and Γ_C is the C state decay rate. We determine β from the observed Stark shifts, and determine $P_B = \Gamma_{sc}/\Gamma_B$ using Γ_{sc}, the measured $X - B$ scattering rate, and Γ_B, the B-state linewidth. We estimate Γ_C by assuming that $C^2\Pi$ molecules decay only via E1 transitions, i.e. $\Gamma_C = \Gamma_{C,\mathrm{rad}}$. Using the measured value of $|d_{BC}|$, along with theoretical values of $|d_{XC}|$ and $|d_{AC}|$, we find a radiative decay rate $\Gamma_{C,\mathrm{rad}}$ of $2\pi \times 5.3(2)\,\mathrm{MHz}$. The resulting estimated loss rate is much smaller than γ_{excess} (Fig. 6.6(f)).

Away from the two $B^2\Sigma(v = 0) - C^2\Pi(v = 3)$ resonances, we only account for $\sim 30\%$ of the observed excess loss rate γ_{excess}. This suggests that either $f_{BC,03}$ is different than calculated or that additional loss mechanisms exist. The former is unlikely since extensive spectroscopy has been performed on the $X - A$, $X - B$ and $X - C - D$ systems [138, 139]. In addition, away from the two dispersive features, the value of Δ_{XB} is weakly sensitive to the $B - C$ Franck-Condon factors, and is consistent with our measurement of d_{BC}. This leaves two possible explanations, significant predissociation of certain C states, which would lead to $\Gamma_C > \Gamma_{\mathrm{C,rad}}$, and photoionization of B-state molecules, which could arise for example from absorption of an $X - A$ photon and a tweezer photon [140]. The possible involvement of tweezer light could be probed in the future with rapidly modulated traps, where the temporal overlap of the imaging light and trapping light can be varied [141].

6.5 The $B - C$ Transition Dipole Moment

In this section, we describe in detail how the $B - C$ transition dipole matrix element is extracted from differential ac Stark-shift measurements between the X and B states.

6.5.1 Measurement Procedure

We measure the variation of the differential ac Stark shift between the $X^2\Sigma(v = 0, N = 1)$ and $B^2\Sigma(v = 0, N = 0)$ states as a function optical tweezer wavelength (λ). On the $X - B$ light at 531 nm, four sidebands each addressing the four hyperfine levels in $X^2\Sigma(v = 0, N = 1)$ are created using a phase modulator [1] (See Chapter 5). The tweezer depth is held constant while 531 nm light is applied for 5 ms. We then detect the number of surviving molecules 30 ms following the illumination pulse. The $X - B$ detuning that produces maximum loss probes the average differential Stark shift between the $X^2\Sigma(v = 0, N = 1)$ and $B^2\Sigma(v = 0, N = 0)$ states. We assume that the measured shift is $1/2$ of the peak differential ac Stark shift, arising from the trap-averaged differential shift as molecules exit the trap.

To verify the linear dependence of the Stark shift with power, we measure the differential Stark shift versus tweezer power at $\lambda = 781.1$ nm and the magic wavelength of 782 nm. We find that both curves scale linearly with power (Fig. 6.7(a)). Extrapolation to zero tweezer power gives the bare $X - B$ transition frequency.

6.5.2 Extracting Transition Dipole Moment from Lineshape

The measured differential ac Stark shifts versus trapping wavelength reveals two dispersive features that originate from the $B^2\Sigma(v = 0, N = 0) - C^2\Pi_{1/2}(v = 3, J = 1/2, 3/2)$ and $B^2\Sigma(v = 0, N = 0) - C^2\Pi_{3/2}(v = 3, J = 3/2)$ transitions. We fit the data to a model of the expected ac Stark shifts with three free parameters: the overall offset, the centers of the two dispersive features, and the overall strength of the two features. Shifts from states other than the $C^2\Pi(v = 3)$ states are expected to contribute an approximately constant

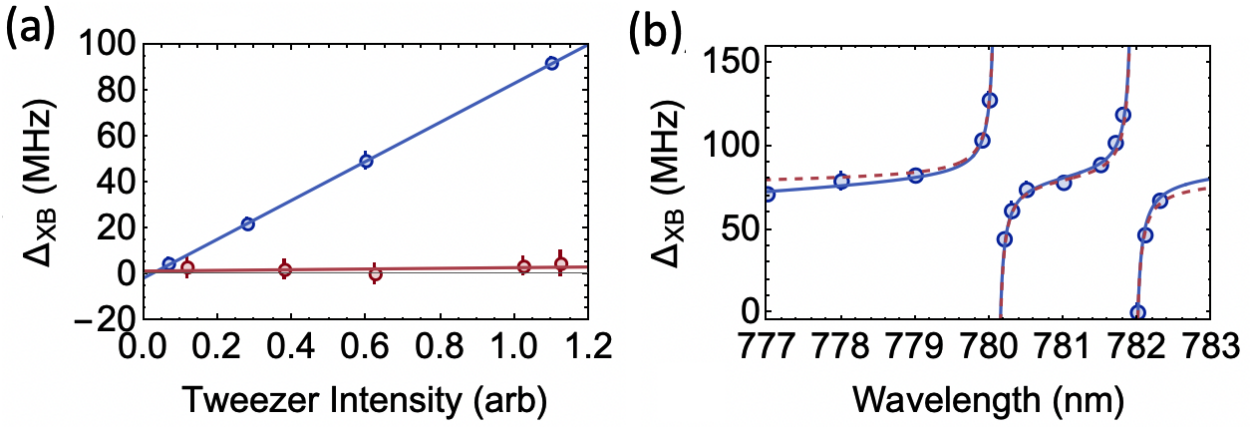


Figure 6.7: Measured differential ac Stark shifts Δ_{XB} between $X^2\Sigma(v = 0, N = 1)$ and $B^2\Sigma(v = 0, N = 0)$. (a) Δ_{XB} versus tweezer intensity. Shown in blue (red) circles are data for 781.1 nm (782.0 nm). Solid lines are linear fits to the data. The difference in the extrapolated ac Stark shift at zero intensity is consistent with the absolute frequency accuracy of ± 1 MHz our X-B optical frequency stabilization system. (b) Δ_{XB} versus tweezer wavelength at fixed tweezer intensity. The tweezer intensity corresponds to a trap depth of 1.28 mK for molecules in the $X^2\Sigma(v = 0, N = 1)$ state. Shown in the dashed red line is a fit to the Stark shift model, where the amplitude of the $B - C$ dipole matrix element is allowed to vary and an overall offset is allowed. The fit yields a dipole moment reduction factor of 0.259(7) relative to the value in [137], and an overall offset of 4.4(14) MHz. The solid blue line is a fit to the ac Stark shift model plus a term linear in the wavelength. The fit yields a dipole moment reduction factor of 0.259(5) relative to the value in [137], and an overall offset of 5.0(10) MHz.

background. This can account for excited state transitions we do not explicitly consider and/or inaccurate theoretical dipole matrix elements and Franck-Condon factors for the excited electronic states.

The measured Stark shift and fitted curve are shown in Fig. 6.7. In our fit, we take into account the calibrated tweezer depth and the known expected ac Stark shifts. In brief, for the $X^2\Sigma$ state, we include ac Stark shifts from the excited A, B, C, D, E and F states. For the $B^2\Sigma$ state, we include Stark shifts due to the X, A, B, D states. To allow for slight variation in transmission and AOD diffraction efficiency as the wavelength is varied, we allow for a background term that is linear in wavelength. As shown in Fig. 6.7, this extended model fits the data well. We have verified that the addition of a background term that is linear in wavelength does not change the fitted constants beyond the fit errors.

From the fit, we find that the spin-orbital splitting between the $C^2\Pi_{1/2}(v = 3)$ and $C^2\Pi(v = 3)$ states is 280(1) GHz, agreeing well with previous spectroscopy. The extracted product of the Franck-Condon factor $f_{BC,03}$ and the dipole matrix element between $B^2\Sigma(v = 0)$ and $C^2\Pi(v = 3)$, d_{BC}, is $5.2(3) \times 10^{-3} ea_0$. Using $f_{BC,03} = 2.71 \times 10^{-3}$ ($B^2\Sigma(v = 0) - C^2\Pi(v = 3)$) computed from spectroscopy data [135, 138, 139], we obtain a $B - C$ dipole moment of $2.0(1)\, ea_0$, differing significantly from the much larger theoretical value of $7.33\, ea_0$ computed in Ref. [137].

From the fit, the overall residual shift is 5.0(1.5) MHz, which is 10% of the overall background offset away from the two resonances. Since most of the total Stark shift is accounted for, this provides further support that the extracted $B - C$ dipole moment is indeed much smaller than computed in Ref. [137]. If one assumes that the residual shift is entirely due to the nearby $D^2\Sigma(v = 0, 1, 2, 3, 4)$ states, and uses Franck-Condon factors computed from spectroscopic data, the residual shift suggests a $B - D$ dipole moment of $1.6(3)\, ea_0$. Except for the overall offset, the uncertainties for the above are dominated by the uncertainty in the overall trap depth.

6.5.3 Comparison of Measured and Predicted Differential ac Stark Shifts

Table 6.1 lists the estimated contributions to the differential ac Stark shift to the $X^2\Sigma(v = 0) - B^2\Sigma(v = 0)$ transition computed with the $B - C$ dipole moment of $2.0(1)\, ea_0$ and, for comparison, the differential Stark shift using the theoretical $B - C$ transition dipole moment of $7.33\, ea_0$ from Ref. [137].

6.6 Outlook

This chapter has highlighted our efforts to realize a background-free bichromatic imaging scheme for single CaF molecules in an array of μm-sized optical tweezer traps. We achieve an

Transition(s)	Inferred Shift (MHz)	Predicted Shift (MHz)
$X(v=0)$ due to A,B,C,D,E,F states	26.6	26.6
$B(v=0)$ due to $C(v=0)$	27.3	365
$B(v=0)$ due to $C(v=1)$	13.3	178
$B(v=0)$ due to $C(v=2)$	4.1	54
$B(v=0)$ due to $C(v=3)$	-0.02	-2.2
$B(v=0)$ due to $C(v=4)$	-0.008	-0.1
Total	71.3	621.3
Observed	78(2)	78(2)

Table 6.1: Breakdown of contributions to the $X - B$ differential ac Stark shift, using our measured value of the $B - C$ transition dipole moment $d_{BC} = 2.0ea_0$, and using the theoretical prediction from Ref. [137] of $d_{BC} = 7.33ea_0$.

imaging fidelity and non-destructive detection fidelity sufficient for small-scale rearrangeable molecular tweezer array experiments. Crucially, because of our method's background-free nature, only a moderate photon budget of $\eta \sim 10^3$ is required, opening the door for high-fidelity single-molecule detection of complex laser-coolable polyatomic species for which a high degree of optical cycling is much harder to achieve. We note that our technique relies on the presence of two largely closed optical cycling transitions, which has been observed in certain polyatomic molecules [142, 143].

While investigating bichromatic imaging loss, we identified many loss mechanisms generically relevant to fluorescence detection of trapped molecules and have established a framework to systematically quantify their rates. We also developed a method to measure transition dipole moments between short-lived excited states, and performed the first measurement of the $B - C$ transition dipole moment of CaF. This technique could be used to measure arbitrarily small Franck-Condon factors, which could aid in efforts to achieve optical cycling in complex polyatomic molecules [144, 145].

Chapter 7

Λ-Enhanced Blue-Detuned MOT

I'm blue da-ba-dee, da-ba-di

Da-ba-dee, da-ba-di, da-ba-dee, da-ba-di.

– Eifel 65

In this chapter, we present an implementation of a blue-detuned MOT (BDM) for CaF molecules. The BDM achieves temperatures well below the Doppler limit, and provides the highest densities and phase-space densities reported in CaF MOTs at the time of this investigation. Our results suggest that the variant of BDMs explored in this work are likely achievable in many relatively light molecules including polyatomic ones. However, our measurements suggest that this variant of BDM will be challenging to realize in substantially heavier molecules due to sub-mK trap depths. In addition to record temperatures and densities, we find that the BDM substantially simplifies and enhances the loading of molecules into optical tweezer arrays, which are a promising platform for quantum simulation and quantum information processing. Notably, the BDM reduces molecular number requirements nine-fold compared to a conventional red-detuned MOT, while not requiring additional hardware. In practice, this technique makes preparing large-scale molecular tweezer arrays more immune to fluctuations of the number of molecules produced in the beambox.

The work presented in this chapter resulted in the following publication [1]:

Samuel J. Li, Connor M. Holland*, Yukai Lu, Lawrence W. Cheuk. "Blue-Detuned Magneto-optical Trap of CaF Molecules" Phys. Rev. Lett.* ***132****, 233402 (2024).*

7.1 Operating Principle of a (Λ-Enhanced) BDM

In molecular MOTs, optical cycling is achieved by addressing a rotational-lowering transition [146] (e.g., the $N = 1 \rightarrow N' = 0$ transition, where N denotes the rotational quantum number). In these so-called type-II systems, the number of excited states is less than or equal to the number of ground states. As discussed in [147], red-detuned light leads to Doppler cooling at high velocities but sub-Doppler heating at low velocities. In contrast, blue-detuned light produces Doppler heating and sub-Doppler cooling [43, 100, 147–149].

It was subsequently realized that blue-detuned MOTs (BDMs), which provide both spatial confinement and sub-Doppler cooling, can be realized in type-II systems [150–152]. The first BDM was demonstrated with Rb atoms [150], and then extended to molecules, including YO [153] and SrF [154]. In these molecular implementations, further improvements in density and temperature were achieved by tuning two frequency components of the MOT light near two-photon resonance.

This enhancement can be understood as a Λ-assisted cooling mechanism, in which two optical frequencies couple a pair of ground states to a common excited state, forming a coherent Λ system. Near two-photon resonance, velocity-selective dark states emerge, leading to enhanced cooling and reduced photon scattering, analogous to free-space Λ-cooling. Importantly, in the context of a BDM, this mechanism operates most effectively near the magnetic field zero, where Zeeman shifts are small and long-lived dark states can form. Away from the field zero, the spatially varying Zeeman shifts detune the Raman condition, which both limits the lifetime of the dark states and restores scattering necessary for trapping forces.

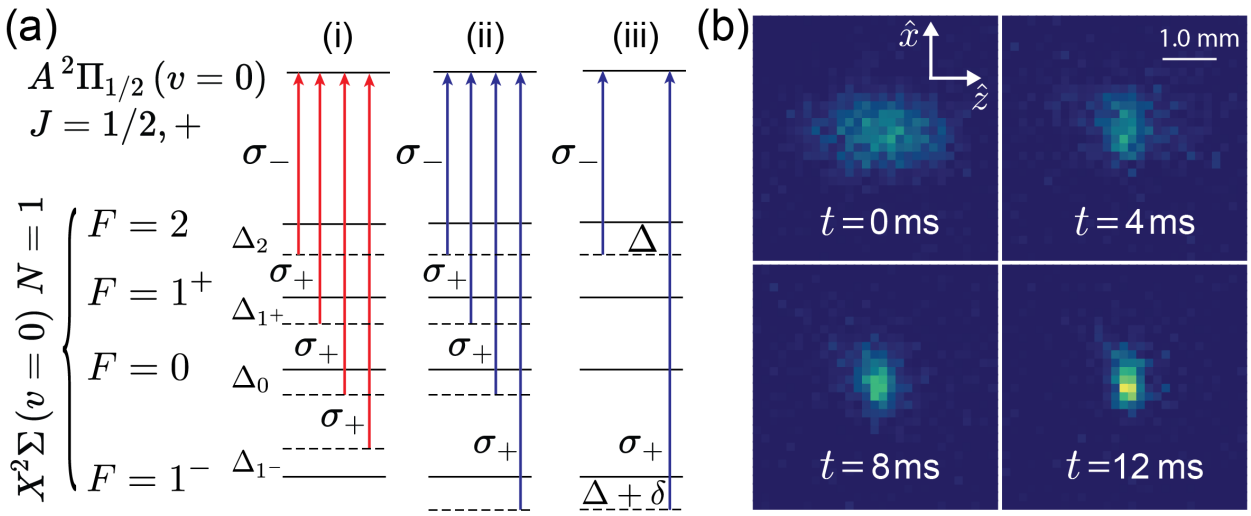


Figure 7.1: MOT Laser Configurations and Λ-BDM Loading Dynamics. (a) Laser configurations for (i) a red-detuned DC MOT, (ii) the four-frequency BDM, and (iii) the two-frequency Λ-BDM. The single-photon (two-photon) frequency detuning is denoted Δ (δ). The hyperfine splittings from top to bottom are 25 MHz, 47 MHz and 76 MHz. (b) In-situ images of a Λ-BDM at time t following direct loading from a Λ-cooled cloud ($B'_z = 27\,\mathrm{G/cm}$).

The interplay between these effects enables hybrid MOT operation: Λ-enhanced sub-Doppler cooling near the trap center and conventional BDM restoring forces at larger displacements. This extension of Λ-cooling to a spatially inhomogeneous MOT environment provides a natural explanation for the observed improvements in phase-space density.

7.2 Integration into the Existing Sequence

To create a blue-detuned CaF MOT, we start with a red-detuned MOT formed using a DC quadrupolar magnetic field (symmetry axis along $\hat{z}$) and light red-detuned from the $X\,^2\Sigma(N=1) \rightarrow A\,^2\Pi_{1/2}(J=1/2,+)$ transition. The cooling light is sent along three orthogonal directions and consists of four frequency components nominally addressing the four ground hyperfine manifolds (Fig. 7.1(a,i)). After initial capture of molecules from a cryogenic buffer gas beam, the red-detuned MOT is magnetically compressed [2, 155], reaching a mean Gaussian width of $\sigma = 680(30)\,\mu$m and a temperature of $T = 3.9(4)\,$mK.

Since BDMs have low capture velocities [147, 150–152], we further pre-cool the molecules in free space with Λ-enhanced gray molasses cooling to $\sim 10\,\mu$K before loading into a BDM [43, 153, 154]. The sample expands negligibly during this stage and 49(1)% of molecules remain.

We next transfer molecules into a BDM with four frequency components, operating at a detuning of $\approx +20\,$MHz and a gradient of $B'_z = 14.6\,$G/cm. At optimal parameters, $\approx 70\%$ of molecules are transferred. Notably, the BDM rapidly approaches equilibrium over a $1/e$ time of 7.9(4) ms. The equilibrium axial (radial) Gaussian width is $\sigma_z = 294(2)\,\mu$m ($\sigma_r = 215(2)\,\mu$m), and the axial (radial) temperature is $T_z = 195(5)\,\mu$K ($T_r = 186(12)\,\mu$K). The corresponding mean size is $\sigma = \sigma_r^{2/3}\sigma_z^{1/3} = 239(2)\,\mu$m and mean temperature is $T = T_r^{2/3}T_z^{1/3} = 189(8)\,\mu$K, around the Doppler limit of $T_D = 200\,\mu$K. The equilibration time is similar to that reported for SrF and is significantly faster than observed in YO ($\sim 50\,$ms). We attribute the rapid equilibration to the high photon scattering rate of $\Gamma_{\rm sc} = 2.0(2) \times 10^6\ \mathrm{s}^{-1}$. Although the high photon scattering rate provides large trapping and damping forces, it limits the achievable temperature in the BDM.

To cool further, we use a two-frequency configuration (Fig. 7.1(a,iii)) with light addressing the highest ($J = 3/2, F = 2$) and lowest ($J = 1/2, F = 1^-$) hyperfine manifolds. This configuration, which we call the Λ-BDM, is similar to that used in Λ-cooling, where velocity-dependent coherent dark states enable cooling to sub-Doppler temperatures. Similar to the four-frequency BDM, the equilibrium size is reached rapidly over several milliseconds (Fig. 7.1(b)).

During early optimizations of this protocol, we observed significant shearing and movement of the BDM as the magnetic gradient increased during the BDM compression stage. This limits the lifetime of the BDM and lengthens the equilibration timescale. We believe that this is due to power imbalances between opposing MOT beams, which leads to a slight offset of the BDM center position from the location of zero magnetic field. To counteract

this effect, we ramp an external bias magnetic field in rough proportion to B'_z to ensure that the equilibrium BDM position remains largely fixed.

7.3 Optimizing the BDM

To optimize the Λ-BDM, we investigate its temperature (T) and lifetime (τ) dependences on the single-photon frequency detuning (Δ), two-photon frequency detuning (δ), and intensity (I). First, we fix the gradient at $B'_z = 10.4\,\mathrm{G/cm}$ and probe the dependences of T and τ on δ. We observe a temperature minimum and lifetime maximum near two-photon resonance ($\delta = 0$), with a striking rise in temperature and decrease in lifetime for $\delta > 0$ (Fig. 7.2(a,b)). These features are similar to those observed in free-space Λ-cooling [43] and in a BDM of YO [153], indicating the presence of velocity-dependent coherent dark states. Notably, at $B'_z = 10.4\,\mathrm{G/cm}$ and $\delta = -0.7\,\mathrm{MHz}$, we obtain a temperature of $T = 36.7(2)\,\mu\mathrm{K}$, 5 times below the Doppler limit of $T_D = 200\,\mu\mathrm{K}$ (Fig. 7.2(a)).

We next explore the dependences of T and τ on the light intensity I. Similar to free-space Λ-cooling [43], the robustness of the dark states increases with intensity due to increased two-photon coupling. Because the two-photon resonance varies across the BDM due to the magnetic gradient, one expects that a minimum intensity is needed to counteract magnetic broadening. However, at high intensities, photon scattering is increased and leads to higher temperatures. These two competing factors means that we would expect an optimal intensity for reaching the lowest temperatures, which we indeed observe (Fig. 7.2(c,d)). Notably, we find that the lifetime improves with intensity at the expense of higher temperatures. As a compromise, we operate at $I = I_0 = 5.8(2)\,\mathrm{mW/cm^2}$.

Similar to the dependence on I, we expect an optimum in the single-photon detuning Δ. The optimum occurs as a balance between increased off-resonant scattering at small Δ and decreased two-photon coupling at large Δ, which reduces the robustness of coherent dark states [43]. Fixing $I = 5.8(2)\,\mathrm{mW/cm^2}$ and $\delta = -0.7\,\mathrm{MHz}$, we find an optimum of

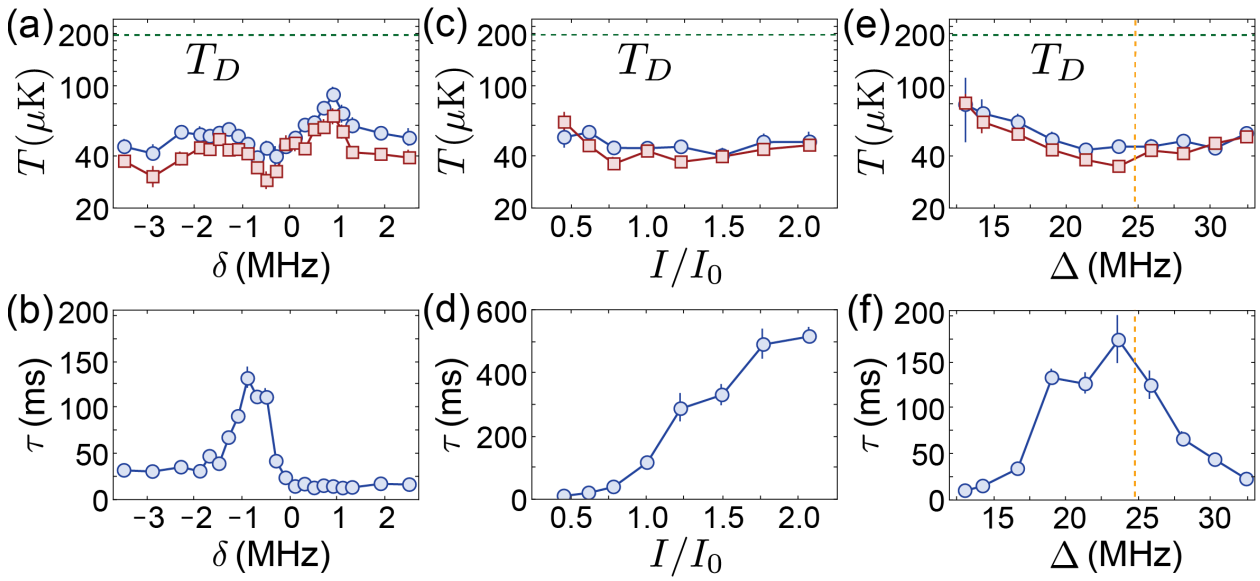


Figure 7.2: Parameter Dependences of the Λ-BDM Temperature T and Lifetime τ. (a),(b) T and τ versus two-photon detuning δ, with $\Delta = 23.8\,\mathrm{MHz}$ and $I = 5.8(2)\,\mathrm{mW/cm^2}$. (c),(d) T and τ versus the intensity I/I_0 per beam ($I_0 = 5.8(2)\,\mathrm{mW/cm^2}$, $\Delta = 23.8\,\mathrm{MHz}$, $\delta = -0.7\,\mathrm{MHz}$). (e),(f) T and τ versus single-photon detuning Δ ($\delta = -0.7\,\mathrm{MHz}$, $I = 5.8(2)\,\mathrm{mW/cm^2}$). The vertical dashed line shows the value of Δ where the $F = 2$ frequency component is resonant with the $F = 1^+$ manifold. In (a),(c),(e), axial (radial) temperatures T_z (T_r) are shown in blue circles (red squares) and the horizontal dashed line shows the Doppler temperature T_D. For all plots, $B_z' = 10.4\,\mathrm{G/cm}$.

$\Delta \approx 24\,\mathrm{MHz}$ (Fig. 7.2(e,f)). With optimized parameters ($\Delta = 23.8\,\mathrm{MHz}$, $\delta = -0.7\,\mathrm{MHz}$, $I = 5.8(2)\,\mathrm{mW/cm^2}$), we measure a scattering rate of $\Gamma_{\mathrm{sc}} = 0.65(19) \times 10^6\,\mathrm{s^{-1}}$, substantially lower than the four-frequency BDM, but much higher than free-space Λ-cooling [43].

Motivated by the practical objective of increasing molecular densities, we next explore the dependence of the Λ-BDM on magnetic gradient B_z'. In red-detuned MOTs, a strategy to increase density is magnetic compression through increasing B_z' [40, 156]. At a fixed temperature T, the MOT size decreases as $1/\sqrt{B_z'}$. Consequently, the density rises as ${B_z'}^{3/2}$ [156]. In detail, the MOT can be modeled with an equation-of-motion containing a restoring force and velocity damping: $\ddot{x} = -\alpha(x)\dot{x} + F(x)/m$ [39, 41, 153, 156]. Near the MOT center and at low velocities, the damping coefficient α is approximately constant, and the restoring force is approximated by Hooke's law $F(x) = -kx$, where k is the spring constant. The restoring force arises from magnetic-field dependent light scattering. Therefore, F is

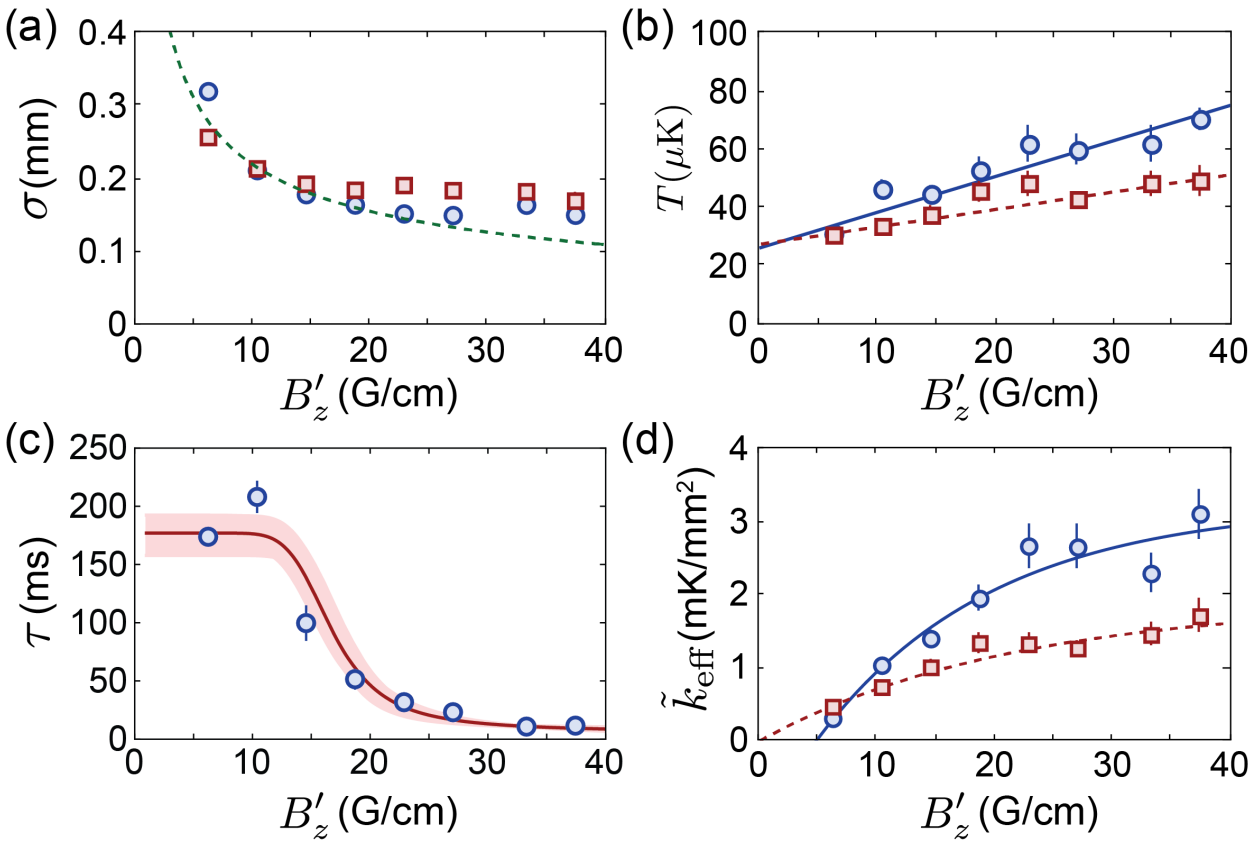


Figure 7.3: Λ-BDM Properties versus Axial Magnetic Gradient B'_z. (a) Gaussian axial (radial) width σ_z (σ_r) shown in blue circles (red squares). Green dashed line shows a fit of the mean size $\sigma = \sigma_r^{2/3}\sigma_z^{1/3}$ to $1/B_z'^{1/2}$ for data up to 20 G/cm. (b) Axial (radial) temperature T_z (T_r) shown in blue circles (red squares). The blue solid (red dashed) line is a linear fit of the axial (radial) temperature. (c) Lifetime τ (blue circles) versus B'_z. Solid line shows a fit to the loss model described in the main text that uses the measured MOT damping forces, restoring forces, temperatures, and sizes. The shaded regions are uncertainty bands from 1σ uncertainties of fitted parameters. (d) Effective spring constant $\tilde{k}_{\rm eff} = T/\sigma^2$ for the axial (radial) direction shown in blue circles (red squares). The blue solid (red dashed) line is a fit of the axial (radial) data to an exponential saturation curve. The axial fit includes a horizontal offset to phenomenologically capture the effect of gravity, which is along $\hat{z}$.

a function of the local magnetic field B. At the center of a quadrupole field in a MOT, $F(x) = F(B(x)) \approx B'x$ (dF/dB). Hence, near the MOT center, $k \propto B'_z$. Using a generalized Virial theorem that equates potential and kinetic energies, one finds that $\sigma \propto 1/\sqrt{B'_z}$ and the density grows as $(B'_z)^{3/2}$ at a fixed T.

Fig. 7.3 shows the observed dependence of the size (σ), temperature (T), and lifetime (τ) versus B'_z. We find that σ scales as $1/\sqrt{B'_z}$ up to ≈ 20 G/cm (Fig. 7.3(a)). T increases

slightly with gradient, but remains well below T_D even up to 40 G/cm (Fig. 7.3(b)). The rising temperature is likely because the mean magnetic field experienced by the molecules rises as $\sqrt{B'_z}$, which in turn perturbs the coherent dark states responsible for sub-Doppler cooling. Notably, τ decreases significantly starting at $B'_z \approx 15$ G/cm (Fig. 7.3(c)). At 30 G/cm, τ becomes comparable to the equilibration timescale. Density enhancement via further magnetic compression is therefore not a viable method for our BDM, and the optimal gradient is a compromise between minimizing σ and T and maximizing τ.

7.3.1 Measuring Cloud Size

All images of the BDM are obtained using two-image background subtraction. When extracting the molecular size is important, a four-image protocol is used. We elaborate on both of these protocols in this section.

For each sequence, two images are taken under identical light conditions – one containing molecules and one not containing molecules. This procedure allows us to isolate the molecular fluorescence by subtracting stray background light. Typically, 30-100 background-subtracted images are averaged.

For data sets in which the center-of-mass or widths are measured, we integrate the averaged image along the two camera axes (aligned with $\hat{x}$ and $\hat{z}$) in an appropriate region of interest (ROI). We fit a Gaussian to the resulting signal. Using the known magnification of the imaging system, the cloud size and center-of-mass position along the x and z axes are then determined.

To obtain the in-situ images appearing Fig. 7.1(b), we employ a four-image procedure. This procedure enables robust subtraction of a smearing effect caused by the non-zero shifting and cleaning speed of our EMCCD camera. In detail, we first take a pair of images of the molecular cloud (as described above) to generate the in-situ image. Next, we take a second pair of images during an identical experimental sequence, but with no imaging light applied during the two camera exposures. This generates the "smear" image. We next normalize

the "smear" image to a corresponding region in the in-situ image, and then subtract the two images.

7.3.2 Measuring (Phase Space) Density

The phase-space density of a molecular cloud depends on three quantities: molecule number, cloud size, and cloud temperature. We can measure the MOT sizes and temperatures along the axial and one radial directions. We assume the system is radially isotropic.

The number of molecules is measured by a 20 ms-long Λ-imaging pulse. After summing camera counts within an ROI, we convert the camera counts into the number of collected photons using known camera conversion factors. To convert the photon number into a molecule number, the scattering rate during imaging and the collection efficiency of our imaging system are needed. We calibrate the scattering rate by comparing the imaging lifetime with and without the $X^2\Sigma(v=3, N=1) \rightarrow A^2\Pi(v=2, J=1/2, +)$ repumper. Using the known vibrational branching ratios for the $A^2\Pi \rightarrow X^2\Sigma$ decay pathway, we estimate a scattering rate of $6.7(16) \times 10^4\,\mathrm{s}^{-1}$. Combining this with the light collection efficiency of our imaging system, we obtain an estimate of the molecule number.

We measure the in-situ size of the BDM using a 2 ms exposure. The size of the free-space Λ-cooled cloud is measured using a 5 ms exposure. We extract cloud parameters using the fitting procedure described in Sec. 7.3.1. The temperature is measured via time-of-flight expansion, where the expanded cloud is imaged resonantly for 1 ms.

To obtain peak phase-space densities, we use the measured sizes, temperatures, and molecule number. The phase-space density is given by $\mathrm{PSD} = n_0\lambda_{\mathrm{dB}}^3$, where n_0 is the peak spatial density and λ_{dB} is the thermal de Broglie wavelength given by $\lambda_{\mathrm{dB}} = \sqrt{2\pi\hbar^2/(mk_BT)}$. The dependences of n_0 and PSD of the Λ-BDM on the axial magnetic gradient B_z' are shown in Fig. 7.4.

Empirically, the smallest sizes occur at $B_z' = 27\,\mathrm{G/cm}$ ($\sigma = 172(4)\,\mu\mathrm{m}$, $T = 60(4)\,\mu\mathrm{K}$), the lowest temperatures at $B_z' = 6.2\,\mathrm{G/cm}$ ($\sigma = 277(5)\,\mu\mathrm{m}$, $T = 31(1)\,\mu\mathrm{K}$), and the highest

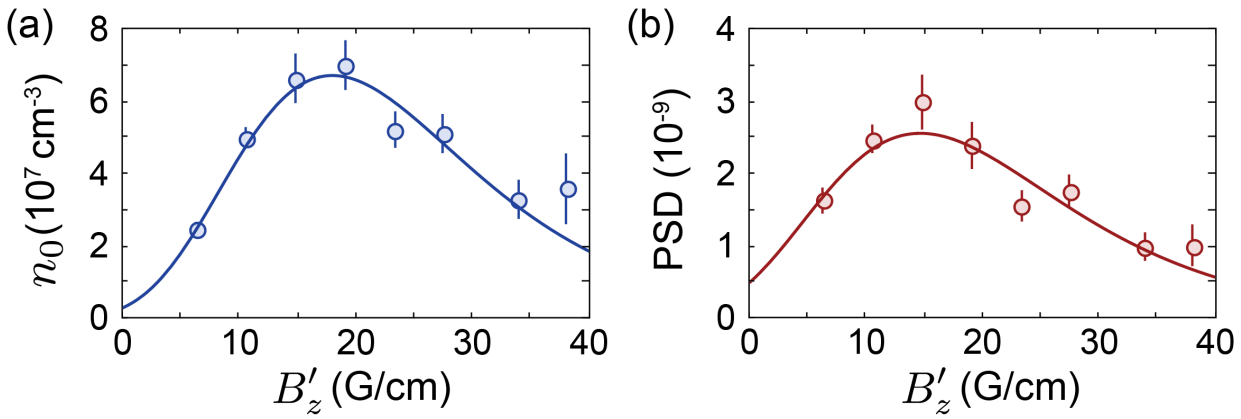


Figure 7.4: Λ-BDM Density and PSD Dependences on Axial Magnetic Gradient B'_z. (a) Peak density n_0 versus B'_z. (b) Peak phase-space density PSD versus B'_z. Solid lines are guides to the eye.

peak phase space density (PSD) at $B'_z = 14.6\,\mathrm{G/cm}$ ($\sigma = 188(3)\,\mu\mathrm{m}$, $T = 39(2)\,\mu\mathrm{K}$). At optimal parameters and with $N = 6.2(15) \times 10^3$ molecules in the Λ-BDM, we obtain a peak density of $n_0 = 7(2) \times 10^7\,\mathrm{cm}^{-3}$ and a peak PSD of $3.0(8) \times 10^{-9}$. Compared to the compressed red-detuned MOT, these values correspond to a density improvement of 19(3) and a PSD enhancement of $1.6(3) \times 10^4$.

Lastly, by applying free-space Λ-cooling to a cloud released from a Λ-BDM ($B'_z = 18.7\,\mathrm{G/cm}$), we obtain a peak PSD of $2.3(6) \times 10^{-8}$ ($\sigma = 182(2)\,\mu\mathrm{m}$, $T = 10.6(6)\,\mu\mathrm{K}$), the highest reported at the time of this exploration for CaF in free space.

7.4 Characterizing Loss in the BDM

7.4.1 Loss and Temperature

To investigate the origin of the short lifetimes at high gradients, we examine the dependence of the restoring force on B'_z, since an insufficient restoring force could lead to loss. Assuming Hooke's law and constant velocity damping, the spring constant k can be obtained from T and σ via $k_{\mathrm{eff}} = k_B T/\sigma^2$. In Fig. 7.3(d), we show $\tilde{k}_{\mathrm{eff}} = k_{\mathrm{eff}}/k_B$ versus B'_z for both the radial and axial directions. At gradients below $B'_z \approx 10\,\mathrm{G/cm}$, $\tilde{k}_{\mathrm{eff}}$ is linear in B'_z, as expected,

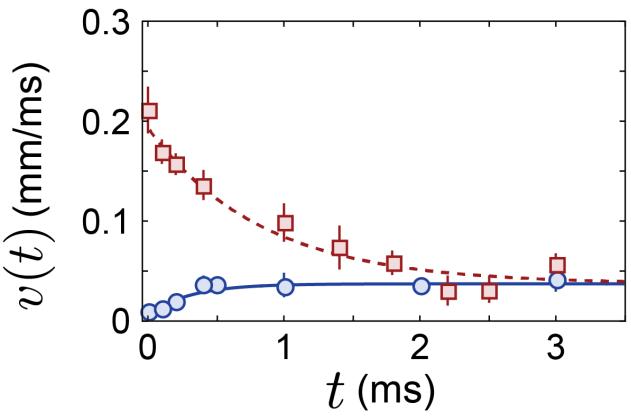


Figure 7.5: Exemplary Velocity Damping Curves. The figure shows the center-of-mass velocity $v(t)$ versus the time t that the Λ-BDM light is on. Blue circles (red squares) show data without (with) the push beam applied initially. The data without the push beam (blue circles) is used to determine v_∞ (exponential fit shown by the blue solid line). The data with the push beam (red squares) is then fit with an exponential curve to determine α (v_∞ fixed for the fit). The fitted values for α and v_∞ are used to obtain $a(B)$ via $a(B) = \alpha v_\infty$. The data shown was acquired at a magnetic field of $B = -1.14\,\mathrm{G}$. For data shown in the main text, v_∞ is determined from a measurement at a time t well into the saturated regime ($t \gg 1/\alpha$).

with values similar to those reported for YO [153]. At higher gradients, $\tilde{k}_{\mathrm{eff}}$ appears to saturate, indicating that the restoring force decreases. Because molecules experience an average magnetic field that grows as $\sqrt{B'_z}$, the saturation of $\tilde{k}_{\mathrm{eff}}$ suggests that $F(B)$ is substantially sub-linear at higher magnetic fields.

7.4.2 Force, Damping, Effective Depth

To test this hypothesis, we directly measure $F(B)$. We create dense and cold samples by loading a Λ-BDM and subsequently applying free-space Λ-cooling. We then impart an initial radial velocity of $v_0 \approx 200\,\mathrm{mm/s}$ by pulsing on a beam resonant with the $X^2\Sigma(N=1) \rightarrow B^2\Sigma(N=0)$ transition. We next apply a uniform magnetic field $\vec{B}$ along the push direction ($\vec{B} \parallel \vec{v}_0$) and switch on Λ-BDM light for a variable duration t. At each t, we measure the velocity v via time-of-flight expansion. By fitting to $v(t) = Ae^{-\alpha t} + v_\infty$, we extract the damping coefficient α and the terminal velocity v_∞. The restoring force $F(B)$ is then obtained via $F = m\,\alpha\,v_\infty$. To determine v_∞ more accurately, we perform a second set of

measurements where the push beam is not applied and the molecules start with $v_0 = 0$. Exemplary data for these two protocols are given in Fig. 7.5.

Fig. 7.6(a,b) show the extracted damping curve $\alpha(B)$ and acceleration curve $a(B) = F(B)/m$. For $a(B)$, we observe the expected sign change upon reversing B. We also find that $\alpha(B)$ and $a(B)$ are significant only when $|B| < 1\,\mathrm{G}$. Furthermore, the restoring force is approximately linear only for $|B| < 0.5\,\mathrm{G}$. At $B'_z = 20\,\mathrm{G/cm}$, this corresponds to a radial size of 0.5 mm.

The acceleration curve $a(B)$ explains why short lifetimes are observed at high gradients. In short, we find that the effective BDM trap depth becomes comparable to the molecular temperatures, leading to loss. Using $a(B)$, we define an effective conservative trapping potential $U(x) = -m \int a(B(x))dx$ along the radial and axial directions.[1] It follows that both the spatial scale and the magnitude of $U(x)$ scale inversely with B'_z (Fig. 7.6(c)). That is, both the trap size and depth decrease with B'_z. Assuming $U(x)$ is Gaussian, given by $U(x) = -U_0 \exp\{[-x^2/(2d^2)]\}$, we obtain a trap depth of $U_0(B'_z) = k_B \times 4.6(10)\,\mathrm{mK} \cdot (\mathrm{G/cm})/B'_z$, and a trap size of $d(B'_z) = 0.62(4)\,\mathrm{G}/B'_z$. Notably, at a typical gradient of $20\,\mathrm{G/cm}$, $U_0 = k_B \times 230(50)\,\mu\mathrm{K}$, which is only four times higher than the observed temperature. These trap depths are much smaller than the $\sim 50\,\mathrm{mK}$ depths reported for red-detuned molecular MOTs [151, 156, 157] and $\sim 0.5\,\mathrm{K}$ depths reported for red-detuned atomic MOTs [158].

To further support our hypothesis that short lifetimes arise from low trap depths, we quantitatively examine both the trap-averaged damping constant $\langle\alpha\rangle$ and the temperature-to-trap-depth ratio $\langle\eta\rangle = \langle(k_B T)/U(x)\rangle$. Monte-Carlo simulations using measured curves of $\alpha(B)$ and $a(B)$ show that $\langle\alpha\rangle$, which determines the average cooling rate, varies by no more than 20% over experimentally relevant gradients. On the other hand, $\langle\eta\rangle$ varies significantly and even exceeds unity. Because the molecular fraction above the local trap depth is given by $\exp(-1/\eta)$, this confirms that a shallow trap depth, rather than a lack of velocity damping, is the primary loss mechanism at high gradients. Simulations using a

[1] The restoring force is in general non-conservative, but it is conservative when restricted to the x-y plane ($z = 0$) or along the symmetry axis z.

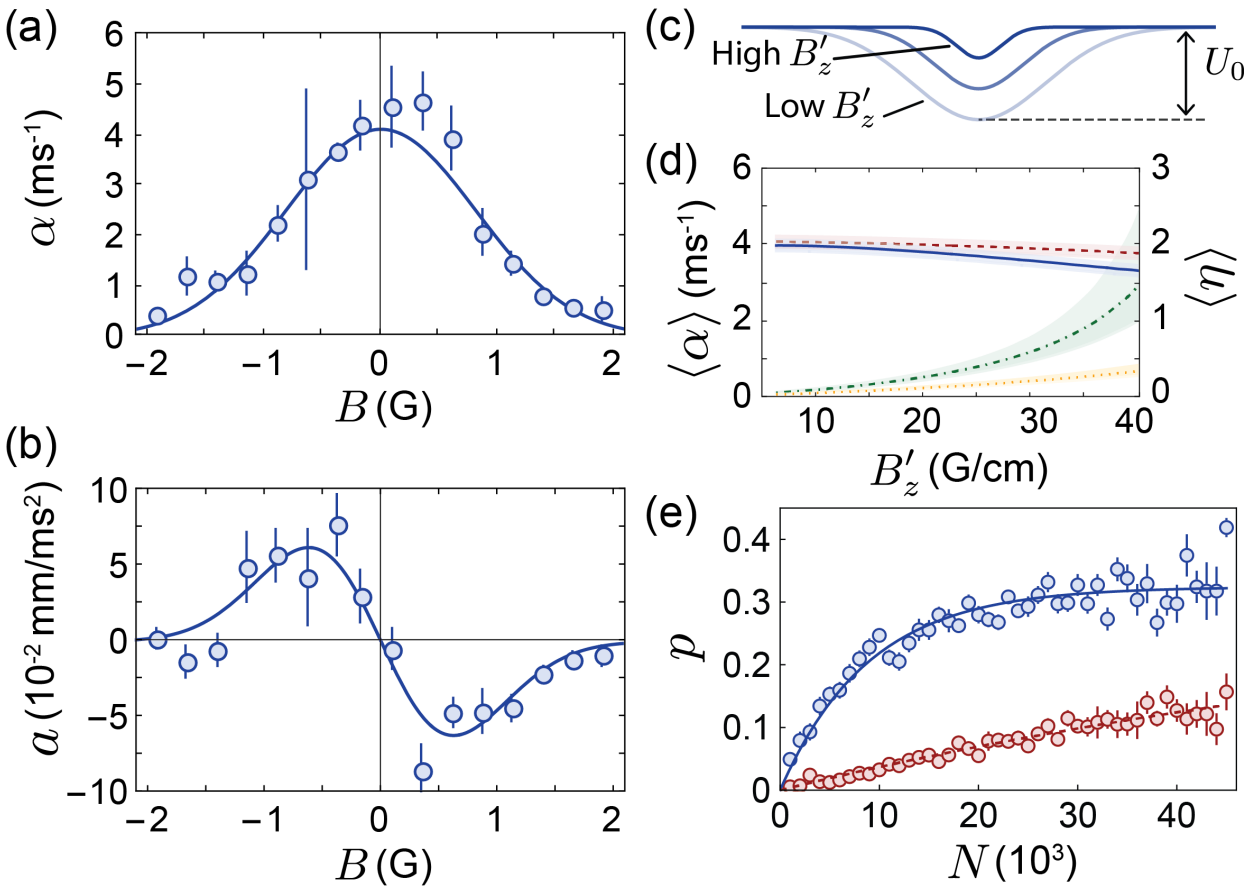


Figure 7.6: Velocity Damping, Restoring Force, and Enhanced Tweezer Loading. (a) Damping constant α versus magnetic field B. Solid blue line shows a Gaussian fit. (b) Acceleration $a(B)$ versus B. Solid line is a fit to the derivative of a Gaussian. (c) Illustration showing decreasing trap depths U_0 and trap sizes d with increasing magnetic gradient B'_z. Both U_0 and d scale as $1/B'_z$. (d) Simulated average damping $\langle\alpha\rangle$ and temperature to trap depth ratio $\langle\eta\rangle$, versus magnetic gradient B'_z. $\langle\alpha\rangle$ for the axial (radial) directions are shown by the blue solid (red dashed) line; $\langle\eta\rangle$ for the axial (radial) directions are shown by the green solid (orange dashed) line. (e) Tweezer loading probability p versus initial MOT number N. Solid blue (dashed red) line is an exponential fit to data with (without) using a BDM.

loss model incorporating α and η also agrees with the data within experimental uncertainty (Fig. 7.3(c)), confirming our hypothesis. Our identification of shallow trap depths at high magnetic gradients has implications for extending BDMs to other molecular species. In particular, because a minimum gradient is needed to counteract gravity, BDMs could be challenging to implement for much heavier molecules. Specifically, BDMs of molecular species with mass > 1000 amu and similar optical properties are likely not possible.

7.5 Robust Tweezer Loading

Lastly, to demonstrate a key practical benefit of our work, we compare the loading of an optical tweezer array using a Λ-BDM versus using only a red-detuned MOT. In both cases, the molecules are transferred into an intermediate optical dipole trap (ODT), and then into tweezers with the aid of Λ-cooling, where the final tweezer occupations are determined by fluorescence imaging. By examining the tweezer loading probability p versus initial MOT number (Fig. 7.6(e)), we find that the Λ-BDM reduces the required molecule number by a factor of 9.3(8). Notably, the BDM allows saturated loading ($p \approx 0.35$ [87]) robustly over a wide range of experimentally accessible initial MOT numbers. It also significantly outperforms optical compression [2] robustly and without requiring additional hardware. Notably, dynamical optical compression used in [2] increased ODT numbers by ≈ 2 compared to using a red-detuned MOT alone. For tweezer loading, this directly reduces initial MOT number requirements by the same factor of 2, much lower than the factor of ≈ 9 achieved here with the Λ-BDM. Notably, our current work allows saturated tweezer loading, which opens the door to creating large molecular arrays needed to study quantum spin models in the many-body regime and quantum circuits with large arrays of molecular qubits.

7.6 Upgraded BDM & Outlook

Contextualizing our BDM results with those reported recently for YO [153] and SrF [154], we find that despite different spin-rotation and hyperfine structure, a CaF BDM is also possible. This lends further support that BDMs could be widely applicable to other laser-coolable molecules, including polyatomic ones such as CaOH and SrOH [54–57]. Nevertheless, our work has revealed that extension of BDMs to much heavier molecules could be challenging because of limited trap depths.

Soon after the investigations presented in this chapter were completed, a significant advancement in blue-detuned MOTs was demonstrated. This improved scheme enables substantial increases in MOT density through a compression mechanism that is effective even for higher-mass molecules. The technique was first implemented for CaOH [159] and subsequently extended to CaF [160]. Although the precise mechanism underlying the observed density enhancement is still under investigation, this variant of BDM consistently produces substantial improvements to molecular density with little to no added experimental complexity. We likewise observe a significant increase in density when implementing the scheme described in Ref. [160].

Beyond molecular systems, BDMs have also been proposed as a means to enhance atomic densities in a recently proposed ultracold tin experiment [161]. This points to a broader applicability of techniques developed in molecular systems to atomic species exhibiting type-II transitions. More generally, the transfer of ideas from molecules back to atoms provides an unexpected but compelling motivation to continue exploring novel or previously overlooked cooling and trapping protocols within the AMO community.

Chapter 8

Coherent Interactions and Entanglement Between CaF Molecules

Do you think the molecules are happy?

– Samuel J. Li

Entanglement is *the* defining feature of quantum mechanics.[1] Entanglement also lies at the heart of many applications in quantum science including quantum information processing, quantum simulation, and quantum-enhanced sensing. While the improvements in state preparation, control, and readout in CaF tweezer arrays, which were detailed in previous chapters, are all crucial ingredients to a molecule-based quantum science platform, coherent two-particle control is still lacking. In particular, coherent control over the interactions between molecules is the fundamental building block to realizing molecular two-qubit gates, simulating interacting many-body Hamiltonians, and generating the entanglement powering quantum-enhanced sensors.

[1]More accurately, entanglement and projective measurements are the defining features, since entanglement is a basis-dependent quantity. For instance, a Bell state is "not entangled" in the Bell state basis while the product state $|\uparrow\uparrow\rangle$ is entangled. However, in many quantum platforms, a natural basis is inherited from the constituent qubits in the platform (i.e., individual atoms, ions, transmons, etc). Thus, generating entanglement between these qubits is the goal.

In this chapter, we demonstrate the long-standing goal in molecular quantum science of coherent control over the interactions between pairs of individually trapped molecules in an dynamically reconfigurable optical tweezer array. We first highlight how pairs of CaF molecules are prepared in single internal states, and how long single-particle coherence times can be achieved. Next, we demonstrate a simple protocol to probe for coherent interactions between molecules requiring no local single-particle control. By placing a pair of molecules at different separation distances r, which we achieve via dynamic rearrangement in our tweezer array, we observe coherent two-particle dynamics in agreement with the expected $1/r^3$ interaction strength decay of interacting dipoles. We take advantage of these interactions to realize the first molecular two-qubit gate, which, along with single-particle control, is sufficient for universal quantum computation. This two-qubit gate is used to generate a Bell state of molecules; we probe this state's lifetime and realize a first demonstration of site-resolved coherent control over molecules.

The work presented in this chapter resulted in the following publication [4]:
Connor M. Holland, Yukai Lu*, Lawrence W. Cheuk. "On-Demand Entanglement of Molecules in a Reconfigurable Optical Tweezer Array" Science.* ***382****, 1143 (2023).*

8.1 Preparing Defect-Free Arrays

Our work starts with single laser-cooled CaF molecules trapped in a dynamically reconfigurable array of optical tweezer traps [3, 86].

To remove the randomness in tweezer occupation, we use a rearrangement approach pioneered in neutral atom experiments [70, 71]. We non-destructively detect the tweezer occupations using a variant of Λ-imaging [43]. The empty tweezers are identified, switched off, and the remaining occupied tweezers are then rearranged into the desired 1D pattern. We characterize the rearrangement procedure by measuring the probability of successfully creating uniform arrays, and find a single particle rearrangement fidelity of 97.4(1)%. As

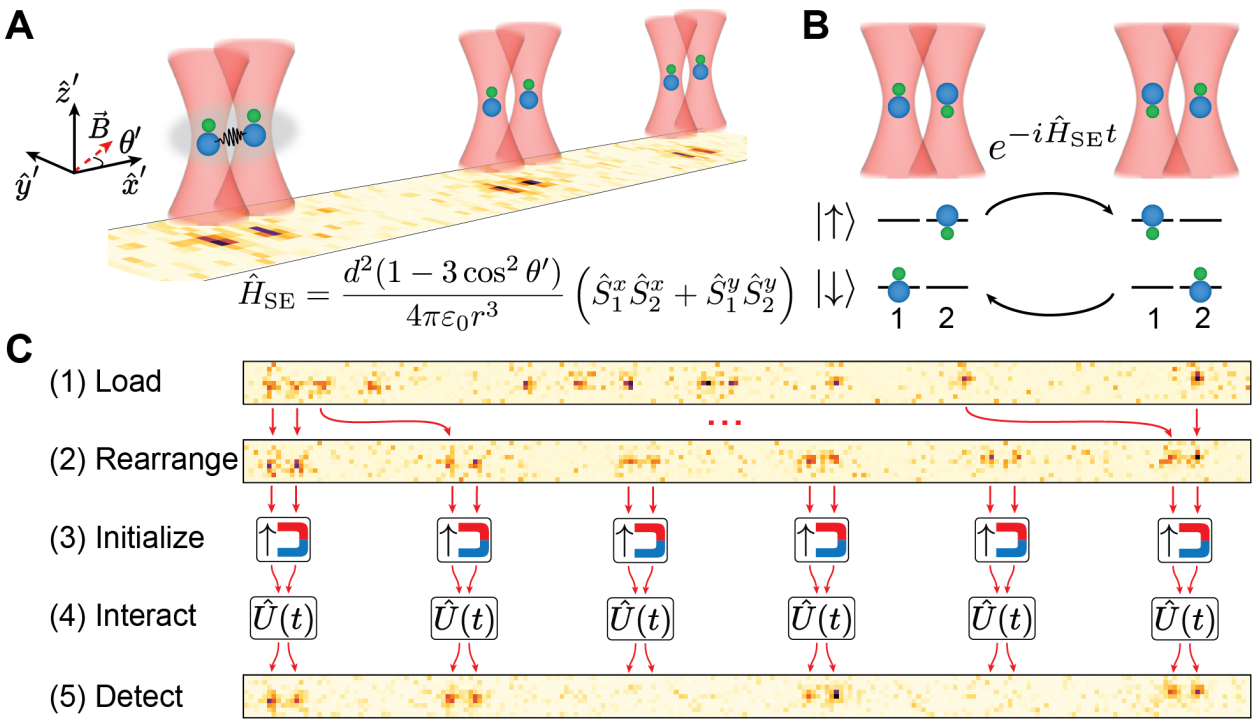


Figure 8.1: Laser-cooled Molecules in a Reconfigurable Optical Tweezer Array. (a) Single CaF molecules trapped in an optical tweezer array are prepared into closely separated tweezer pairs. Molecules in each pair held by separate tweezer traps interact via the long-range electric dipolar interaction $\hat{H}_{\rm SE}$. (b) The electric dipolar interaction leads to dipolar spin-exchange of rotational excitations. (c) Molecules are loaded stochastically, detected non-destructively, and rearranged into the desired 1D configuration. The molecules are then initialized into a single internal state and the pair separations are reduced in order to switch on interactions. After specific interaction times, the pairs are separated and detected state-selectively.

shown in Fig. 8.2(a,b), we are able to create uniform arrays up to a size of 16 with a probability > 0.6. The rearrangement fidelity is limited by the non-destructive detection fidelity, with minimal loss $(0.2(10)\%)$ caused by movement of the tweezer traps.

After rearrangement, we initialize the internal state of the molecules, which are distributed among the 12 hyperfine states in the $X^2\Sigma(v=0, N=1)$ rovibrational manifold. To prepare molecules into a single hyperfine state, we optically pump molecules into $|D\rangle = X^2\Sigma(v=0, N=1, J=3/2, F=2, m_F=2)$, where J denotes the total angular momentum excluding nuclear spin, F denotes the total angular momentum, and m_F denotes its projection onto the quantization axis. Subsequent microwave sweeps along with an opti-

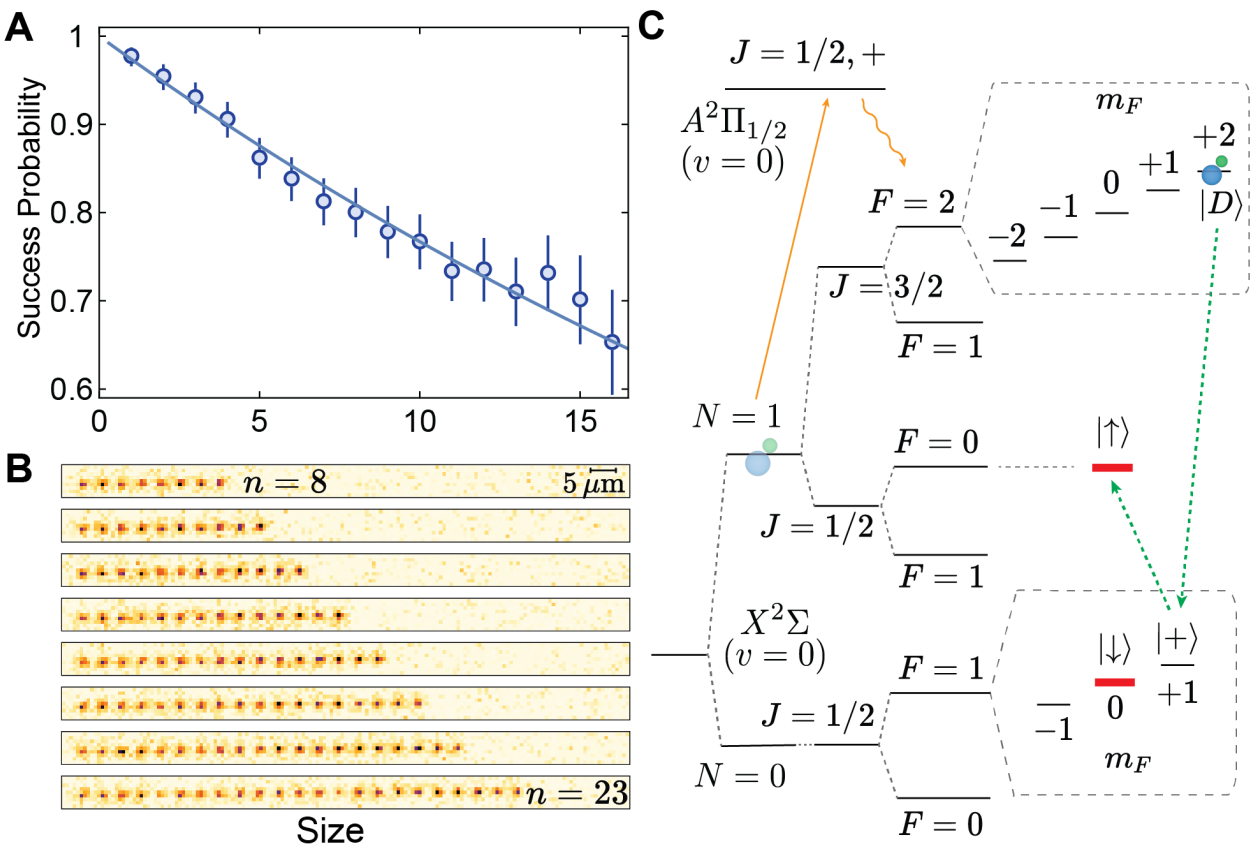


Figure 8.2: Tweezer Rearrangement and Internal State Initialization: (a) Probability of creating defect-free molecular arrays via rearrangement. A fit to p^n, where n is the array size, gives a single particle rearrangement fidelity of $p = 0.974(1)$. (b) Exemplary images of defect-free arrays. (c) Optical pumping (orange arrow) prepares molecules in $|D\rangle$. Microwave sweeps (dashed green arrows) transfer $|D\rangle$ molecules to $|\uparrow\rangle$.

cal clean-out pulse transfer the molecules into the target final state $|\uparrow\rangle = X^2\Sigma(v = 0, N = 1, J = 1/2, F = 0, m_F = 0)$ (Fig. 8.2(c)). The overall fidelity of preparing molecules in $|\uparrow\rangle$ is 82.4(11)%. Our preparation sequence ensures that the dominant preparation error is in the form of unoccupied tweezers, with a small contribution coming from molecules prepared in the incorrect internal state $|+\rangle = X^2\Sigma(v = 0, N = 0, J = 1/2, F = 1, m_F = 1)$. The state initialization errors come from imperfect microwave transfer, polarization impurity of the optical pumping light, and loss caused by heating in the tweezer traps. Following state preparation, we measure a molecular temperature of $T = 151(10)\,\mu$K.

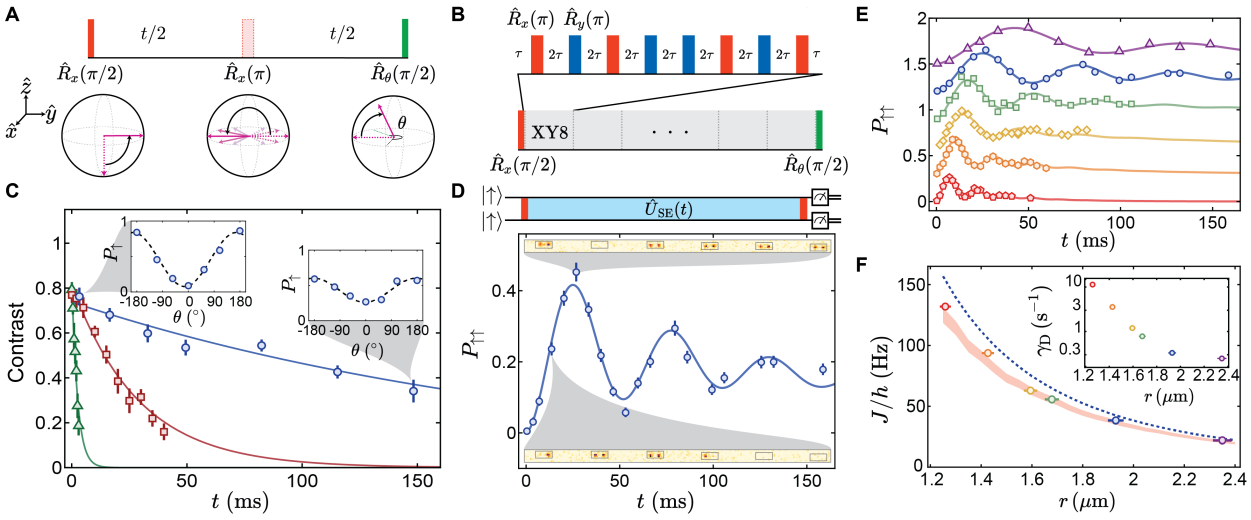


Figure 8.3: Single Particle Coherence and Spin-Exchange Oscillations: (a) Ramsey pulse sequence used to measure rotational coherence. The bottom Bloch sphere diagrams show the action of the various pulses for a molecule initialized in $|\downarrow\rangle$. (b) The XY8 dynamical decoupling sequence. (c) Ramsey contrast of non-interacting molecules versus free evolution time t. Green triangles, red squares, and blue circles show the cases when no spin-echo, one spin-echo, and the XY8 sequence is applied, respectively. Exponential fits give coherence times $(1/e)$ of 2.5(3) ms, 29(2) ms, and 215(30) ms, respectively. Insets show exemplary Ramsey fringes with corresponding sinusoidal fits shown by the dashed lines. (d) Spin-exchange oscillations at a tweezer separation of 1.93(3) μm. Shown are the $|\uparrow\uparrow\rangle$ populations measured after the Ramsey pulse sequence, $P_{\uparrow\uparrow}$, as a function of interaction time t, for molecular pairs initialized in $|\uparrow\uparrow\rangle$. The solid curve is a fit to a phenomenological model. Insets show exemplary fluorescence images at the indicated times. (e) Spin-exchange oscillations at separations of 1.26(2) μm (red pentagons), 1.43(2) μm (orange hexagons), 1.60(2) μm (yellow diamonds), 1.68(2) μm (green squares), 1.93(3) μm (blue circles), and 2.35(3) μm (purple triangles). Curves are offset vertically by 0.3 for clarity. (f) The extracted spin-exchange strength J versus pair separation r. The light red band indicates the theoretical prediction taking into account the finite temperature of the molecules and the uncertainty in the electric dipole moment of CaF. The dashed blue curve shows the prediction without taking into account finite temperature. Inset shows the single particle loss rate $\gamma_{\rm D}$ versus pair separation r.

8.2 Long Coherence Times in a Rotational Qubit

In order to produce entanglement via the dipolar interactions between molecules, we require long coherence times compared to the typical interaction timescales of ~ 10 ms at our tweezer separations. Achieving long coherence times for optically trapped molecules has been an ongoing experimental challenge with steady advances being made. For molecules, differ-

ent internal states can experience different trapping potentials, which, in combination with motion caused by finite temperature, can lead to decoherence. For $^1\Sigma$ bialkali molecules, long coherence times of different nuclear spin states have been reported [62]. Work using "magic" trapping conditions has also demonstrated extended coherence times between rotational states in both $^1\Sigma$ and $^2\Sigma$ molecules [31, 61, 63–65].

Because the effective spin-exchange interactions couple different rotational states, we desire long rotational coherence times between the two interacting states $|\uparrow\rangle$ and $|\downarrow\rangle = X^2\Sigma(v=0, N=0, J=1/2, F=1, m_F=0)$. Building upon previous work in CaF [65], we identify a pseudo-magic trapping condition where both spin states experience approximately identical trapping potentials. Our pseudo-magic condition takes into account vector and tensor shifts and is achieved by applying a magnetic field orthogonal to the tweezer light polarization at a reduced tweezer depth compared to that used for initial loading and imaging.

To measure the resulting coherence time, we prepare pairs of tweezer traps where one trap is empty and the other is occupied by a molecule initialized in $|\uparrow\rangle$. We next apply a Ramsey pulse sequence consisting of two $\pi/2$ microwave pulses (first pulse along $\hat{x}$, second pulse along $\hat{n} = \cos\theta\,\hat{x} + \sin\theta\,\hat{y}$) separated by a variable free evolution time (Fig. 8.3a). The remaining fraction of $|\uparrow\rangle$ molecules, $P_\uparrow$, oscillates as a function of θ, with the oscillation amplitude directly measuring the coherence. Fitting to an exponential decay curve yields a bare coherence time T_2^* of 2.5(3) ms. Adding a spin-echo improves the coherence time to $T_2 = 29(2)$ ms. Following previous work exploring dipolar interactions of KRb molecules in an optical lattice [68, 69], we implement the XY8 dynamical decoupling sequence depicted in Fig. 8.3(b), and find that the $1/e$ coherence time is further extended to 215(30) ms (Fig. 8.3(c)). This is consistent with our understanding that the bare coherence times are primarily limited by slow (ms-timescale) fluctuations of ambient magnetic fields.

8.3 Observing $1/r^3$ Dipolar Interactions

Having achieved sufficiently long rotational coherence times, we next set out to observe coherent spin-exchange interactions. The long-range electric dipolar interaction between the molecules gives rise to resonant exchange of rotational excitations between $|\uparrow\rangle$ and $|\downarrow\rangle$. The resulting spin-exchange interaction is described by the Hamiltonian

$$\hat{H}_{\mathrm{SE}} = \frac{J}{2}\left(\hat{S}_1^+\hat{S}_2^- + \hat{S}_1^-\hat{S}_2^+\right) = J\left(\hat{S}_1^x\hat{S}_2^x + \hat{S}_1^y\hat{S}_2^y\right),$$

where $\hat{S}_i^+$, $\hat{S}_i^-$, $\hat{S}_i^x$, $\hat{S}_i^y$ are spin-1/2 operators for molecule i and

$$J = \frac{d^2}{4\pi\varepsilon_0}\frac{1}{r^3}(1 - 3\cos^2\theta'),$$

with $d = \langle\uparrow|\hat{\mathbf{d}}|\downarrow\rangle$ being the transition dipole moment, $r = |\vec{r}|$ being the intermolecular separation, θ' being the angle between $\vec{r}$ and the quantization axis, and ε_0 being the free space permittivity. Starting with two molecules in a product state, time evolution under $\hat{H}_{\mathrm{SE}}$ can lead to entanglement. For example, two molecules initially prepared in the product state $|\uparrow\rangle \otimes |\downarrow\rangle$ become maximally entangled after interacting for a time $t = \pi\hbar/(2J)$. In our system, the quantization axis is orthogonal to the intermolecular separation, i.e. $\theta' = 90°$.

To observe the effect of spin-exchange interactions, we first create pairs of $|\uparrow\rangle$ molecules at an initial separation of $4.20(6)\,\mu$m, over which interactions are negligible. We next reduce the pair separation to $1.93(3)\,\mu$m over 3 ms, where the interaction strength J ($J = h \times 43$ Hz) becomes appreciable on the coherence timescale. Subsequently, we apply the Ramsey pulse sequence used above with $\theta = 0$. To retain long coherence times, the XY8 decoupling pulses are kept on during the free evolution time. Because the π-pulses in the XY8 sequence leave $\hat{H}_{\mathrm{SE}}$ unchanged, spin-exchange interactions are preserved [162].

For a molecular pair initialized in $|\uparrow\uparrow\rangle$, the resulting state following the Ramsey sequence is given by

$$|\psi\rangle = ie^{-i\frac{Jt}{4\hbar}}\left(\sin\left(\frac{Jt}{4\hbar}\right)|\uparrow\uparrow\rangle + i\cos\left(\frac{Jt}{4\hbar}\right)|\downarrow\downarrow\rangle\right), \tag{8.1}$$

and $P_{\uparrow\uparrow}$ oscillates at an angular frequency of $J/(2\hbar)$. As shown in Fig. 8.3(d), we indeed observe oscillations of $P_{\uparrow\uparrow}$, directly revealing the presence of coherent spin-exchange interactions. By varying the pair separation between 1.26(2) μm and 2.35(3) μm, we verify that the interaction strength J, as extracted from the oscillation frequency, approximately scales as $1/r^3$, as expected for dipolar interactions (Fig. 8.3(f)). We note that experiments with bulk samples of bialkali molecules in optical lattices have observed coherent spin-exchange both through macroscopic measurements [68, 69] and with single molecule resolution [31], whereas we here observe coherent interactions between individually prepared, laser-cooled molecules.

Examining the $P_{\uparrow\uparrow}$ oscillations in detail, we find that they damp more quickly when the molecules are closer. This could arise from increased molecular loss and reduced single particle coherence times at close separations. Additionally, the thermal motion of molecules gives rise to disorder in the spin-exchange coupling constant J through variations in the intermolecular separations, leading to damping. At a fixed molecular temperature, this effect increases at closer separations. To determine which damping mechanism is dominant, we first measure single particle loss rates and find that they increase at close separations (Fig 3F inset). We believe the loss is caused by parametric heating specific to our scheme of generating tweezer traps using an acousto-optical deflector (AOD), and can be circumvented with other tweezer generation techniques. Molecular loss, however, does not account for all of the observed damping, especially at close separations. Independently measured single particle decoherence rates are also insufficient to explain the damping. This leaves finite molecular temperature as the dominant cause of damping at close distances. Simulations using experimentally measured temperatures reveal damping rates comparable to the observations (Fig. 8.3(f), red shading).

We note in passing that this Ramsey-like protocol is well-suited for preliminary demonstrations of coherent two-particle control in molecular tweezer arrays as there are no requirements for local control. Furthermore, following the final global microwave pulse, the resulting state does not evolve under the spin-exchange Hamiltonian, relaxing the timing requirements for separating the molecules for readout. For these reasons, the protocol demonstrated in this work has been widely used in subsequent demonstrations of coherent two-particle control in other molecular tweezer array platforms, including in CaF [87], RbCs [163], and NaCs [164] tweezer arrays.

8.4 Entangled States of Molecules

8.4.1 Entangling Protocol

Having established the presence of coherent spin-exchange interactions, we next use them to entangle molecules. Specifically, as proposed in Ref. [20], time-evolution by $\hat{H}_{\mathrm{SE}}$ for a specific time of $T = \pi\hbar/J$ implements an iSWAP gate, which is maximally entangling. By applying two additional $\pi/2$ pulses along the x-axis before and after the iSWAP gate, one can convert a molecular pair prepared in $|\uparrow\uparrow\rangle$ into the Bell state $|\psi_B\rangle = \frac{1}{\sqrt{2}}(|\uparrow\uparrow\rangle + i|\downarrow\downarrow\rangle)$, which is maximally entangled. As a compromise between maximizing J and minimizing heating loss, we choose a pair separation of $1.93(3)\,\mu$m for creating $|\psi_B\rangle$.

8.4.2 Entanglement Witness

To demonstrate entanglement of molecules, we measure the Bell state creation fidelity $\mathcal{F} = \langle\psi_B|\rho|\psi_B\rangle$, where ρ is the experimentally obtained density matrix. As pointed out in Ref. [165], $\mathcal{F}$ acts as an entanglement witness, with $\mathcal{F} > 1/2$ indicating two-particle entanglement. To extract $\mathcal{F}$ experimentally, we make use of the relation [166]

$$\mathcal{F} = \frac{1}{2}(P_{\uparrow\uparrow} + P_{\downarrow\downarrow} + \mathcal{C}), \tag{8.2}$$

where $P_{\uparrow\uparrow}$ ($P_{\downarrow\downarrow}$) are the probabilities of measuring $|\uparrow\uparrow\rangle$ ($|\downarrow\downarrow\rangle$), and $\mathcal{C}$ is the amplitude of the coherence between $|\uparrow\uparrow\rangle$ and $|\downarrow\downarrow\rangle$.

To measure $P_{\uparrow\uparrow}$, we separate the two molecules after preparing $|\psi_B\rangle$ and subsequently measure the probability that both tweezers in a pair appear bright. Because our imaging scheme detects only $|\uparrow\rangle$ molecules, in order to measure $P_{\downarrow\downarrow}$, we apply an additional π-pulse prior to detection (Fig. 8.4(a)) to convert molecules from $|\downarrow\rangle$ to $|\uparrow\rangle$. To obtain the coherence envelope $\mathcal{C}$, we measure parity oscillations as follows. We apply a $\pi/2$ pulse about a variable axis $\hat{n} = \cos\theta\,\hat{x} + \sin\theta\,\hat{y}$ after preparing $|\psi_B\rangle$. From the two-tweezer probabilities P_{ij}, we construct the parity signal $\Pi = P_{11} + P_{00} - P_{10} - P_{01}$, where 1(0) denotes a bright (dark) tweezer site.

For a general density matrix that includes the possibility of empty tweezers ($|e\rangle$) caused by imperfect state preparation, Π can display modulation periodic in 2θ and θ. The 2θ modulation is directly related to the coherence between $|\uparrow\uparrow\rangle$ and $|\downarrow\downarrow\rangle$, whereas the θ modulation is related to single molecule coherences, such as that between $|e\uparrow\rangle$ and $|e\downarrow\rangle$. The amplitude of the 2θ modulation directly gives $\mathcal{C}$. As shown in Fig. 8.4b, we find that Π displays modulation periodic in 2θ. The lack of oscillations periodic in θ is consistent with the pulse sequence used. Single molecules prepared in $|e\uparrow\rangle$ or $|\uparrow e\rangle$ effectively experience a π-pulse and no single particle coherence is created.

8.4.3 Bell State & iSWAP Gate Fidelity

From the population and parity oscillation measurements, we obtain a raw Bell state fidelity of $\mathcal{F}_{\mathrm{RAW}} = 0.524(6)$. Correcting for detection errors, we obtain a Bell state fidelity $\mathcal{F} = 0.540(7)$. The raw and measurement-corrected fidelities are above $1/2$, showing that entanglement is indeed present and created on-demand.

Correcting additionally for state preparation errors, we obtain a state-preparation and measurement (SPAM) corrected fidelity of $\mathcal{F}_{\mathrm{SPAM}} = 0.80(2)$. In the context of quantum information processing, the SPAM-corrected Bell state fidelity provides an indication of the

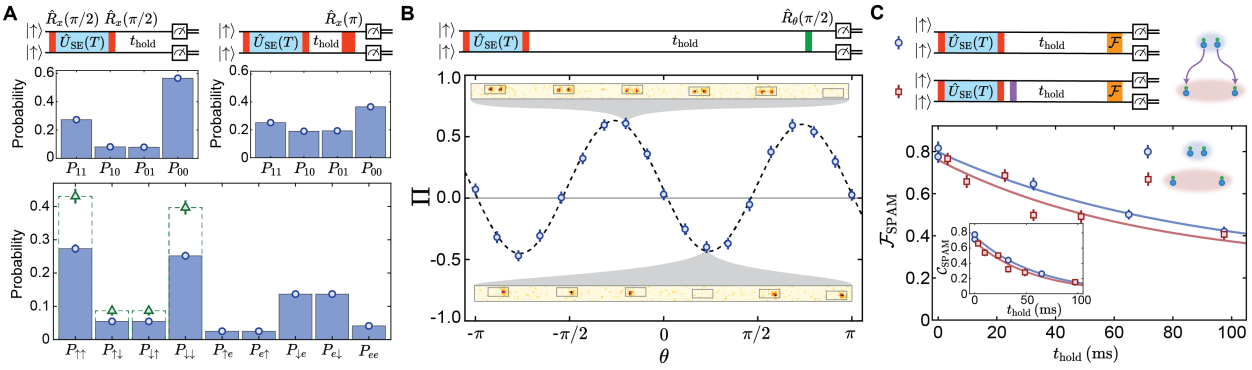


Figure 8.4: Creating and Probing Bell Pairs: (a) Top left panel shows the two-tweezer detection probabilities P_{ij} for the Bell pairs. Right panel shows corresponding probabilities when an additional π pulse is applied before measurement. Bottom panel shows the full probabilities extracted from the top panels. The SPAM-corrected populations for the $|\uparrow\rangle - |\downarrow\rangle$ subsystem are shown by the green triangles. (b) Probing Bell state coherence through parity oscillations. The coherence $\mathcal{C}$ between $|\uparrow\uparrow\rangle$ and $|\downarrow\downarrow\rangle$ is obtained from the amplitude of the oscillations in Π as a function of θ. Insets show exemplary images at the maxima and minima of Π. (c) SPAM-corrected Bell state fidelity $\mathcal{F}_{\rm SPAM}$ versus hold time t at the initial pair creation distance of 1.93(3) μm are shown in blue circles. Red squares show the corresponding data for pairs separated to a larger distance of 4.20(6) μm following creation. Inset shows the contrast $\mathcal{C}_{\rm SPAM}$ versus hold time t for the two separations. The extracted $1/e$ lifetimes are $(\mathcal{F}_{\rm SPAM}, \mathcal{C}_{\rm SPAM}) = (85(5)\,\text{ms}, 61(3)\,\text{ms})$ at the Bell creation distance, and $(70(16)\,\text{ms}, 57(8)\,\text{ms})$ at the larger separation.

quality of the iSWAP gate implemented via spin-exchange. Nevertheless, full characterization of our iSWAP gate and a measurement of its fidelity will require full quantum process tomography. With relevance to quantum simulation, our measurements of spin-exchange interactions demonstrate the fundamental building block for simulating XY spin models. In particular, the phase of the 2θ oscillation in parity measures the relative phase between $|\uparrow\uparrow\rangle$ and $|\downarrow\downarrow\rangle$ in the Bell state, which is sensitive to the sign of J. The observed phase of the oscillation shows that $J > 0$, indicating anti-ferromagnetic spin-exchange interactions. In addition to quantum information processing and quantum simulation, the ability to create entanglement in our system also paves the way towards quantum-enhanced metrology with trapped molecules [167].

8.4.4 State Preparation & Measurement Correction

Measurement Correction

In all data used in this work, two different Λ-imaging durations are used. To determine trap occupation before rearrangement and to verify successful generation of the desired loaded molecule configuration, we use a 7 ms long imaging pulse that is intended to be non-destructive. For final detection, we use a longer 30 ms imaging pulse that is optimal for detection fidelity.

The images are then analyzed to determine the occupation of each tweezer trap. We first sum camera counts over each image region corresponding to a tweezer trap. If the total counts exceed the classification threshold, the tweezer is classified as filled (1); otherwise, it is classified as empty (0). Using the procedure outlined in Section 6.3.2, the error probabilities of misidentifying an occupied tweezer trap as empty (ϵ_{10}) and vice versa (ϵ_{01}) are determined.

The error probabilities are then used to correct the measured data. Since the detected probabilities $P_{\mathrm{det},i}$ are linear combinations of the true probabilities P_i [168], one can write this in matrix form as $\mathbf{P_{det}} = \mathbf{M} \cdot \mathbf{P}$, where the entries of $\mathbf{M}$ are appropriate combinations of ϵ_{01} and ϵ_{10}. Inverting the equation gives $\mathbf{P} = \mathbf{M}^{-1} \cdot \mathbf{P_{det}}$.

For single particle probabilities $\mathbf{P} = \{P_1, P_0\}$, $\mathbf{M}_1$ is given by

$$\mathbf{M}_1 = \begin{pmatrix} \bar{\epsilon}_{10} & \epsilon_{01} \\ \epsilon_{10} & \bar{\epsilon}_{01} \end{pmatrix}, \tag{8.3}$$

where $\bar{\epsilon} = 1 - \epsilon$.

For two-particle probabilities $\mathbf{P} = \{P_{11}, P_{10}, P_{01}, P_{00}\}$, $\mathbf{M}_2 = \mathbf{M}_1 \otimes \mathbf{M}_1$ is given by

$$\mathbf{M}_2 = \begin{pmatrix} \bar{\epsilon}_{10}^2 & \bar{\epsilon}_{10}\epsilon_{01} & \epsilon_{01}\bar{\epsilon}_{10} & \epsilon_{01}^2 \\ \bar{\epsilon}_{10}\epsilon_{10} & \bar{\epsilon}_{10}\bar{\epsilon}_{01} & \epsilon_{01}\epsilon_{10} & \epsilon_{01}\bar{\epsilon}_{01} \\ \epsilon_{10}\bar{\epsilon}_{10} & \epsilon_{10}\epsilon_{01} & \bar{\epsilon}_{01}\bar{\epsilon}_{10} & \bar{\epsilon}_{01}\epsilon_{10} \\ \epsilon_{10}^2 & \epsilon_{10}\bar{\epsilon}_{01} & \bar{\epsilon}_{01}\epsilon_{10} & \bar{\epsilon}_{01}^2 \end{pmatrix} \tag{8.4}$$

State Preparation Correction

Imperfect state preparation includes the primary error of producing empty tweezers, and the small error of producing molecules in the state $|+\rangle$ (or in the improved state preparation sequence, $|-\rangle$). Importantly both empty tweezers and tweezers with molecules in $|-\rangle$ or $|+\rangle$ are dark during imaging.

The SPAM-corrected fidelity $\mathcal{F}_{\text{SPAM}}$ can be obtained from the measurement-corrected raw fidelity $\mathcal{F}$ via

$$\mathcal{F}_{\text{SPAM}} = \mathcal{F}/p_2, \tag{8.5}$$

where p_2 is the probability of initializing the two-tweezer system in the subspace spanned by $\{|\uparrow\rangle, |\downarrow\rangle\} \otimes \{|\uparrow\rangle, |\downarrow\rangle\}$. To obtain p_2, we first prepare molecules in $|\uparrow\rangle$, and then detect the fraction of molecules p_1 that are indeed in $|\uparrow\rangle$. p_2 is obtained via $p_2 = p_1^2$. For an extended discussion of the validity of this measurement correction protocol, we refer the interested reader to the SM of Ref. [4].

Extracting Self-Consistent Full Population Distributions

Since we only detect population in $X^2\Sigma(v = 0, N = 1)$, occupied tweezers with molecules in $|\uparrow\rangle$ appear bright (1), whereas occupied tweezers in $|\downarrow\rangle$ or empty tweezers $|e\rangle$ appear dark (0). To obtain the Bell state fidelity, $P_{\uparrow\uparrow}$ and $P_{\downarrow\downarrow}$ are both needed. The former directly coincides with P_{00} while the latter is obtained by applying an additional π pulse prior to

detection. The values of $P_{\uparrow\uparrow}$ and $P_{\downarrow\downarrow}$ obtained using this method, in combination with the contrast of the parity oscillations, enables estimating Bell state fidelities.

Under certain assumptions, which we describe in detail here, full information about the state of the tweezer pairs can be obtained. We denote $\{P_{11}, P_{10}, P_{01}, P_{00}\}$ and $\{\bar{P}_{11}, \bar{P}_{10}, \bar{P}_{01}, \bar{P}_{00}\}$ with and without the π-pulse, respectively. Note that this full population extraction procedure is not used to obtain Bell state fidelities. It provides a separate check on the values of $P_{\uparrow\uparrow}$ and $P_{\downarrow\downarrow}$ obtained directly using the π-pulse method.

To obtain the full population distribution, we assume the two tweezers in each tweezer pair are identical. It follows that $P_{10} = P_{01}$ and $\bar{P}_{10} = \bar{P}_{01}$. These two conditions are directly verified by our measurements. Thus, instead of 8 measured quantities, the symmetrization assumption reduces the measured quantities to 6:

$$\begin{aligned} p_{ii} &= P_{ii} \\ \bar{p}_{ii} &= \bar{P}_{ii} \\ p_{ij} &= P_{ij} + P_{ji}, j > i \\ \bar{p}_{ij} &= \bar{P}_{ij} + \bar{P}_{ji}, j > i. \end{aligned}$$

Making use of the normalization conditions $p_{11} + p_{10} + p_{00} = 1$, $\bar{p}_{11} + \bar{p}_{10} + \bar{p}_{00} = 1$, there are only 4 remaining degrees of freedom. We can encode these in a single vector $\mathbf{p}_M$ as

$$\mathbf{p}_M = \begin{pmatrix} p_{11} & p_{10} & \bar{p}_{11} & \bar{p}_{10} \end{pmatrix}. \tag{8.6}$$

Next we consider the full population distribution $\{P_{\uparrow\uparrow}, P_{\uparrow\downarrow}, P_{\downarrow\uparrow}, P_{\downarrow\downarrow}, P_{\uparrow e}, P_{e\uparrow}, P_{\downarrow e}, P_{e\downarrow}, P_{ee}\}$, where $|e\rangle$ denotes the tweezer state where the tweezer is either empty or occupied by a molecule not in $|\uparrow\rangle$ or $|\downarrow\rangle$. The symmetry of the two tweezers leaves 6 independent probabilities $\{p_{\uparrow\uparrow}, p_{\uparrow\downarrow}, p_{\downarrow\downarrow}, p_{\uparrow e}, p_{\downarrow e}, p_{ee}\}$, where $2p_{\sigma e} = P_{\sigma e} = P_{e\sigma}$, $\sigma = \uparrow, \downarrow$, $p_{\sigma\sigma'} = P_{\sigma\sigma'}$ and $p_{ee} = P_{ee}$. Using the normalization condition $p_{\uparrow\uparrow} + p_{\uparrow\downarrow} + p_{\downarrow\downarrow} + p_{\uparrow e} + p_{\downarrow e} + p_{ee} = 1$, 5 independent

probabilities are left. These are captured by a single vector $\mathbf{p}_T$:

$$\mathbf{p}_T = \begin{pmatrix} p_{\uparrow\uparrow} & p_{\uparrow\downarrow} & p_{\downarrow\downarrow} & p_{\uparrow e} & p_{\downarrow e} \end{pmatrix}. \tag{8.7}$$

The measurement procedure is a linear transformation between the probabilities $\mathbf{p}_T$ and the measured probabilities $\mathbf{p}_M$. This can be expressed as $\mathbf{p}_M = \mathbf{T}.\mathbf{p}_T$, where

$$\mathbf{T} = \begin{pmatrix} 1 & 0 & 0 & 0 & 0 \\ 0 & 1 & 0 & 1 & 0 \\ 0 & 0 & 1 & 0 & 0 \\ 0 & 1 & 0 & 0 & 1 \end{pmatrix} \tag{8.8}$$

The null space of $\mathbf{T}$ has dimension one, and is spanned by

$$\mathbf{p}_N = \begin{pmatrix} 0 & 1 & 0 & -1 & -1 \end{pmatrix}. \tag{8.9}$$

This indicates that if $p_{\uparrow\downarrow}$ is increased by the same amount as $p_{\uparrow e}$ and $p_{\downarrow e}$ are decreased, there will be no observable difference in the measured probabilities $\mathbf{p}_M$. The system is under-constrained by one degree of freedom.

By introducing an additional constraint from state preparation, the system can in fact be fully constrained. To fully constrain the system, we impose that the probabilities of doubly-occupied, singly-occupied, and empty tweezer pairs agree with an effective single-particle state preparation fidelity f (after generating the Bell state). Explicitly, this constraint is

$$\begin{aligned} f^2 &= p_{\uparrow\uparrow} + p_{\uparrow\downarrow} + p_{\downarrow\downarrow} \\ 2f(1-f) &= p_{\uparrow e} + p_{\downarrow e} \\ (1-f)^2 &= p_{ee}. \end{aligned} \tag{8.10}$$

Note that the last equation follows from the first two equations under the normalization condition for $\mathbf{p}_T$. This nonlinear constraint allows $\mathbf{p}_T$ to be fully determined.

One can verify that

$$\begin{aligned} p_{\uparrow\uparrow} &= p_{11} \\ p_{\downarrow\downarrow} &= \bar{p}_{11} \\ p_{\uparrow\downarrow} &= \frac{1}{2}(p_{10} + \bar{p}_{10} - p_{\text{sum}}) \\ p_{\uparrow e} &= \frac{1}{2}(p_{\text{sum}} - p_{\text{diff}}) \\ p_{\downarrow e} &= \frac{1}{2}(p_{\text{sum}} + p_{\text{diff}}), \end{aligned}$$

where

$$\begin{aligned} p_{\text{sum}} &= \left(1 - \frac{p_{10} + \bar{p}_{10}}{2} - (p_{11} + \bar{p}_{11})\right)^2 \\ p_{\text{diff}} &= \bar{p}_{10} - p_{10} \end{aligned} \tag{8.11}$$

Alternative expressions for p_{sum} and p_{diff} are

$$\begin{aligned} p_{\text{sum}} &= \left(\frac{a+b}{2}\right)^2 \\ p_{\text{diff}} &= a - b \\ a &= p_{00} - \bar{p}_{11} \\ b &= \bar{p}_{00} - p_{11}, \end{aligned}$$

which are equivalent to the first expressions because of normalization conditions.

In Fig. 8.5, we show the contributions to the reconstructed fluorescence histograms due to the true distributions extracted using the above procedure (same data as in Fig. **??**). Explicitly, we find

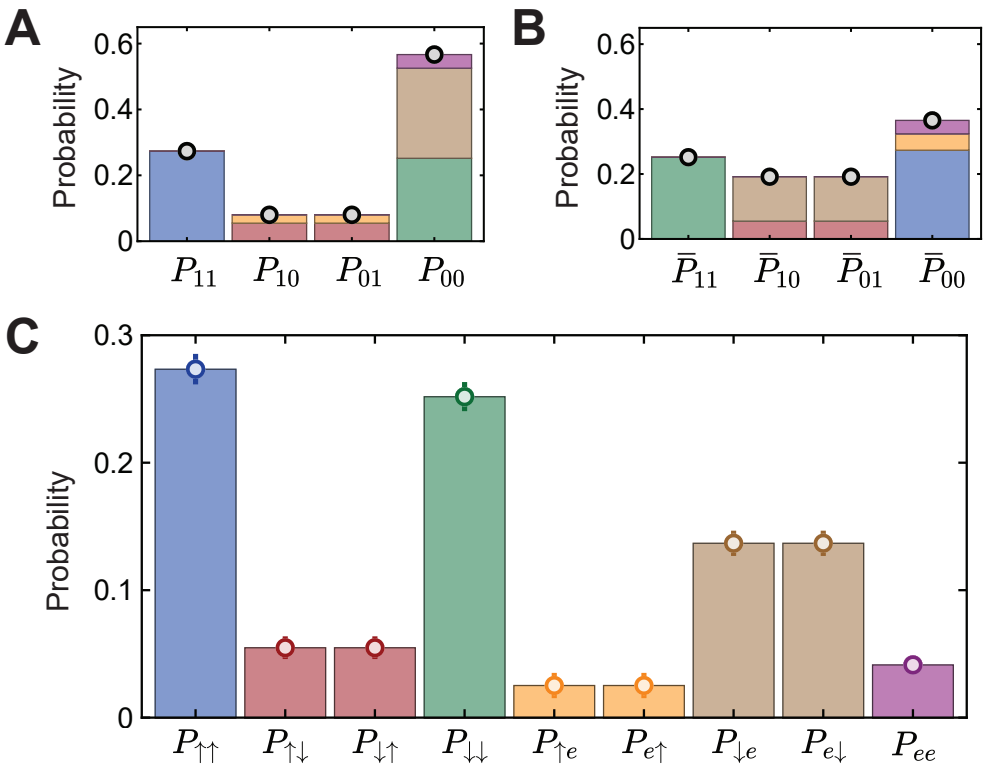


Figure 8.5: Reconstructed Two-Tweezer Occupation Probabilities: (a,b) The reconstructed measurement outcomes without (a) and with (b) a π pulse prior to detection. The various colors show contributions from the full probabilities shown in (c), the full reconstructed probabilities.

$$\begin{pmatrix} p_{\uparrow\uparrow} \\ p_{\uparrow\downarrow} \\ p_{\downarrow\downarrow} \\ p_{\uparrow e} \\ p_{\downarrow e} \\ p_{ee} \end{pmatrix} = \begin{pmatrix} 0.273(10) \\ 0.110(14) \\ 0.252(10) \\ 0.050(16) \\ 0.274(16) \\ 0.041(4) \end{pmatrix}$$

and

$$f = 0.797(11)$$

The obtained value of single-particle preparation fidelity f differs slightly from the directly measured value of $p_1 = 82.4(11)\%$. In general, p_1 is an upper bound for f, since

additional molecular loss and loss out of the $|\uparrow\rangle$-$|\downarrow\rangle$ manifold can occur during the Bell state generation procedure. This is due to heating loss and off-resonant excitation to adjacent m_F levels from the dynamical decoupling pulses. We estimate from separate population leakage measurements that these processes contribute $\approx 0.5\%$ of loss. The remaining small difference between f and p_1 is likely due to instability in the polarization of the optical pumping beams over the course of the experiment, which can lead to degraded optical pumping efficiency.

8.4.5 Coherent Transport

Having demonstrated deterministic creation of Bell pairs, we next probe their lifetime. We measure the Bell state fidelity $\mathcal{F}_{\mathrm{SPAM}}$ as a function of hold time and find a lifetime of 85(5) ms, largely consistent with but somewhat shorter than that expected from uncorrelated single particle decoherence. We also examine whether the Bell pairs survive when separated to larger distances following their creation. Specifically, we separate the Bell pairs to a distance of 4.20(6) μm over 3 ms following their creation, and measure $\mathcal{F}_{\mathrm{SPAM}}$ as a function of hold time. Within experimental uncertainty, we find a lifetime identical to the case without separation (Fig. 8.4(c)). This ability to preserve entanglement while separating molecules could allow one to bypass the limited range of dipolar interactions through movement of molecules, and obtain arbitrary connectivity useful for quantum simulation and information processing.

8.5 Contributions to Bell State Infidelity

In this section, we provide a brief discussion on the errors that limit the SPAM-corrected fidelity $\mathcal{F}_{\mathrm{SPAM}}$ and techniques to reduce these errors. We have identified two major contributing errors: finite coherence time between $|\uparrow\rangle$ and $|\downarrow\rangle$, and effective disorder in J arising from thermally excited molecules.

For thermal molecules trapped in the tweezer array, the distribution of molecule positions lead to variations in J arising from the $1/r^3$ decay of interacting dipoles. As J varies from shot-to-shot, the accumulated phase due to the interaction energy acquires a stochastic error, leading to Bell state infidelity. Importantly, however, since the tweezer trapping frequencies are much larger than the interaction energy ($\omega_x, \omega_y, \omega_z \gg J$), the dominant variation in J which depends linearly on the inter-tweezer axis ($\hat{x}'$) averages to zero. This effect, which is analogous to motional averaging, greatly reduces the variance in the shot-to-shot variation in J experienced between each run of the experiment. More quantitative details about motional averaging and our modeling of J disorder can be found in the SM of Ref. [4]. We note in passing that Rydberg arrays are in nearly the opposite regime, where interaction energies exceed trapping frequencies. Most Rydberg platforms also turn off the tweezer traps during gate operation.

In the regime accessed by the experiment, the two contributions of coherence time and thermal variation of J are both significant. Reducing the molecular temperature should decrease the contribution from each source of disorder. First, at a fixed intermolecular spacing, lowering the molecular temperature reduces the variation in J and consequently the associated error. Second, the coherence time is expected to improve at lower temperatures, since decoherence due to inhomogeneous light shifts arising from the optical tweezer traps are reduced as molecules experience a more uniform distribution of tweezer light intensity, as observed in Ref. [65]. In addition, even for a fixed coherence time, a lower molecular temperature allows one to reduce the intermolecular spacing while keeping the thermal variation of J small. Closer tweezers substantially reduce the entangling time, decreasing the relative importance of single-particle coherence times during a two-qubit gate. Lower temperatures, especially along the z-direction, are also important to reduce thermal hopping between local tweezer minima. In follow-up work where intermodulation heating was minimized at close spacing, we found that thermal hopping and the resulting pair-wise loss becomes significant at tweezer spacings less than $2\,\mu$m. Although molecular loss induced by thermal hopping is

qualitatively different than J-disorder (for instance, loss can be removed via post-selection using full-spin readout protocols), low z-temperatures will become increasingly critical as molecular tweezer arrays scale to larger sizes and explore longer coherent evolution times.

In addition to improvements in molecular temperature, gate infidelities could be improved using entangling schemes with built-in robustness to J-disorder. These gate-based approaches require site-resolved coherent control inserted between a series of interaction durations [169]. Additionally, a particularly neat protocol to reduce J-disorder has been explored in Ref. [170]. In this work, the quadratic contribution of J-disorder due to axial-motion cancels the quadratic contribution to J-disorder due to radial-motion; this is achieved by selecting a quantization axis at the correct relative angle to the inter-tweezer separation and radial/axial tweezer directions. This suppression of the quadratic terms, along with suppression of odd-order terms due to motional averaging, leaves only a 4th-order dependence of J with molecular position. From a broader perspective, both the gate-based approach and this "interaction-disorder magic-angle" suppress the effective J-disorder at the expense of increased gate times; an alternative approach that achieves the same result is simply spacing the tweezers further apart. The optimal solution among these three approaches now depends sensitively on experimental details such as the radial and axial temperatures, single-particle coherence times, and other geometric or platform-specific constraints.

We note that, after a substantial upgrade to our microwave system (for details see Yukai's thesis [90]), coherence times under XY8 dynamical decoupling were improved. This improvement largely arose from reduced MW phase noise in the improved MW generation system. Coherence times may also improve from reduced molecular temperatures. An estimation detailed in the SM of Ref. [4] indicated that fidelities in the absence of MW pulse errors could reach ≈ 0.99 at an intermolecular distance of $d = 1.0\,\mu$m. In retrospect, this estimate may be a bit too optimistic, as later investigations showed that the temperature along the z axis of the tweezer was higher than along the radial direction. These z excitations contribute the majority of J-disorder. Thus, substantial improvement to the z-confinement

and/or temperature may be required to reach 0.99-level fidelities. A few pathways exist to achieve this, including the addition of a vertical lattice and Raman sideband cooling [92]. Details on our implementation of a protocol for RSC can be found in Yukai's thesis [90] and Ref. [5]. Recent theoretical work using quantum optimal control has proposed a robust 2-qubit entangling gate for CaF molecules in tweezer traps that provides entanglement fidelities exceeding 0.999, under the assumption that they are cooled near their motional ground state [171].

8.6 Singlet-Triplet Rotations

In this section, we present our preliminary investigations of coherent single-particle site-resolved control. We use this protocol to apply site-dependent S_z shifts on the Bell state $|\Psi^+\rangle = \frac{1}{\sqrt{2}}(|\uparrow\downarrow\rangle + |\downarrow\uparrow\rangle)$, which we generate from the Bell state $|\psi_B\rangle$ via a global microwave $\pi/2$ pulse. In fact, $|\Psi^+\rangle$ is exactly the state that minimizes the parity signal in Fig. 8.4(b).

We use this state to probe local S_z control since it is insensitive to global S_z fields. The insensitivity to global S_z is quite helpful since magnetic field noise, miscalibrations in microwave detuning, and other errors leading to globally correlated effective S_z shifts could otherwise dominate the local control signature if we had instead used a simpler protocol employing singe molecules.

Beyond the technical convenience of isolating differential S_z shifts, this operation rotates the state from $|\Psi^+\rangle$ to $|\Psi^-\rangle = \frac{1}{\sqrt{2}}(|\uparrow\downarrow\rangle - |\downarrow\uparrow\rangle)$. These two orthogonal states can form the basis for a new qubit encoding which is immune to global S_z fields. In fact, the state $|\Psi^-\rangle$ is insensitive to global rotations about any axis on the Bloch sphere. This characteristic feature of the singlet ($S = 0$) state is crucial to our technique for probing the strength of the local S_z rotation.

8.6.1 Implementing Site-Dependent S_z Shifts

To implement coherent local S_z control in the tweezer array, we rely on the pseudo-magic trapping configuration developed in this work. While pseudo-magic trapping guarantees first-order insensitivity of S_z to trap depth, a second-order dependence on trap depth persists. Therefore, by dynamically imbalancing the tweezer depths, inhomogeneous S_z shifts can be applied. We note that this protocol is far from ideal, since the departure from psuedo-magic trapping could lead to decreased single-particle coherence times in the shifted tweezer. This limitation can be easily overcome by using an independent local-addressing beam with uniform intensity profile over the tweezer trap. In this configuration, the Stark shift should be independent of the molecule's motional state, and hence should enable higher-fidelity single-site local control.

Despite the concern of deviating from magic trapping, we observable no increase in the transition linewidth, probed via a weak microwave excitation along the $|\uparrow\rangle - |\downarrow\rangle$ transition, as the tweezer depth is decreased. Therefore, for this investigation, local control is applied by decreasing tweezer depths by a factor of two. From the measured shift of the $|\uparrow\rangle - |\downarrow\rangle$ transition frequency, we predict this 2x-imbalanced configuration should lead to $\sim 2\pi \times$ 650 Hz of differential shift.

To probe the differential shift, we first generate $|\Psi^+\rangle$ using the protocol illustrated in Fig. 8.4(b). Next, we decrease the tweezer depth to half-magic and increase every-other tweezer's depth by a factor of two. This configuration is held for a variable duration t before the tweezers are returned to the balanced configuration (still at half magic depth). This results in the state

$$\begin{aligned}\psi(t) &= \frac{1}{\sqrt{2}}\Big(|\uparrow\downarrow\rangle + e^{-i\Delta S_z t}|\downarrow\uparrow\rangle\Big) \\ &= \frac{1}{\sqrt{2}}\Big(\cos(\Delta S_z t)|\Psi^+\rangle + e^{-i\Delta S_z t}\sin(\Delta S_z t)|\Psi^-\rangle\Big),\end{aligned} \tag{8.12}$$

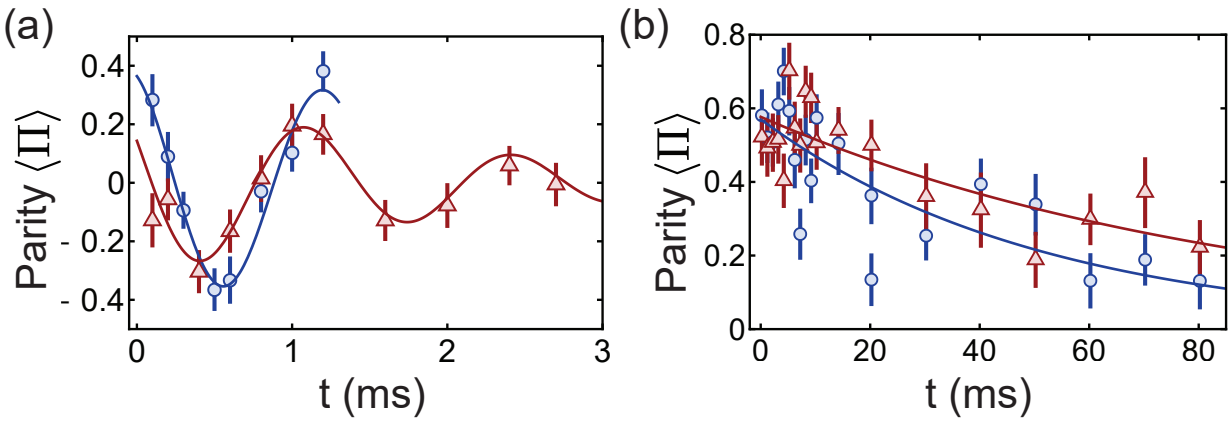


Figure 8.6: A Decoherence Free Subspace Qubit: (a) Coherent local control over S_z enables rotating $|\Psi^+\rangle$ to $|\Psi^-\rangle$ and back; the difference in population is probed via $\langle\Pi\rangle$, which oscillates at ΔS_z. The local S_z shift is inserted in a single (red) or two (blue) spin echo sequences. (b) The T_1 time of this qubit is probed by the decay in $\langle\Pi\rangle$ at the magic (blue) and half-magic (red) tweezer depths.

where ΔS_z is the differential shift between even and odd tweezer sites. Following a total duration t_0, we apply a global MW π-pulse and hold the molecules at half depth for another t_0 and ramp all tweezers back to magic depth. A final global MW $\pi/2$ pulse is applied which rotates $|\Psi^+\rangle$ back to $|\psi_B\rangle$ and leaves $|\Psi^-\rangle$ unperturbed. Importantly, since $\langle\psi_B|\Pi|\psi_B\rangle = 1$ and $\langle\Psi^-|\Pi|\Psi^-\rangle = -1$, the parity signal is expected to oscillate at ΔS_z vs imbalanced tweezer hold duration t. In Fig. 8.6(a) we show that the parity signal indeed oscillates, with a measured frequency of $2\pi \times 780(60)$ Hz, in good agreement with the predicted shift from MW spectroscopy. We also implement a double-shift protocol by concatenating two of these spin echo protocols; from this protocol, we infer a differential shift of $2\pi \times 750(30)$ Hz, in good agreement with the single spin echo result. A simple extension of this protocol potentially enabling faster differential S_z control involves shifting the even-tweezers during the first half of the echo, and the odd-tweezers during the second half; however, we never explicitly explored this protocol.

8.6.2 Decoherence-Free Subspace

In addition to our demonstration of local control, we also probe whether the T_1 time of the new qubit is longer than the single-particle T_2 time, and hence whether this new encoding has signatures of being a decoherence-free subspace (DFS). We probe the T_1 time of the DFS qubit via the parity signal decay in a balanced tweezer configuration at the pesudo-magic and half-magic depth as a function of hold time. Compared to the single particle $T_2 = 37(2)\,\mathrm{ms}$, the parity decays slower by a factor of 1.4(4) at magic depth ($T_1^{\mathrm{DFS}} = 52(14)\,\mathrm{ms}$) and a factor of 2.4(6) ($T_1^{\mathrm{DFS}} = 90(20)\,\mathrm{ms}$) at half-magic depth (Fig. 8.6(b)). These results lead us to conclude that roughly half of the contribution to single-particle T_2 is globally correlated in time (possibly arising from magnetic field noise or global tweezer power fluctuations), while the other half is uncorrelated between sites (possibly arising from imperfect pseudo-magic trapping and differential tweezer depth fluctuations).

8.7 Outlook

In summary, we have demonstrated on-demand entanglement of molecules in a reconfigurable optical tweezer array. Our work is enabled by several advances we have made in controlling laser-cooled molecules, including initialization of defect-free molecular arrays, achievement of long rotational coherence times in tightly-focused tweezer traps, and observation of coherent dipolar interactions between individual laser-cooled molecules. The ability to entangle molecules on-demand is a key building block towards simulating quantum spin models, processing quantum information, and performing quantum-enhanced measurements in the emerging platform of molecular tweezer arrays. Specifically for quantum simulation and information processing, the interactions between long-lived molecular states could offer long evolution times and deep circuit depths. With further advances in lowering molecular temperatures, molecular tweezer arrays could potentially provide performance similar to established platforms such as Rydberg atom arrays, trapped ions, and superconducting qubits.

Our work on entangling molecules on-demand, combined with the recent rapid progress in extending laser-cooling to molecular species of increasing complexity [56, 57], opens research avenues such as quantum-enhanced precision measurement using trapped molecules [59] and explorations of molecular collisions [133] and chemical reactions with entangled matter.

Chapter 9

Enhancing State Preparation and Erasing Errors

You can observe a lot just by watching.

– Yogi Berra

State preparation fidelity is a central requirement to explore the physics of large interacting systems using molecular tweezer arrays. In the upgrades following the work presented in Chapter 8, fidelities in the low 90% range were achieved through a combination of more robust optical pumping protocols and improved microwave control. While this level of performance is sufficient for initializing small ensembles of interacting molecules – such as the pairs used for generating Bell states – state preparation fidelity quickly becomes a limiting factor as the target defect-free array size increases. In particular, for arrays approaching ~ 10 molecules, the probability of preparing an error-free configuration decreases exponentially with system size, making it exceedingly unlikely to realize the pristine product state required to probe many-body phenomena such as coherent spin transport or to generate metrologically useful states.

Pushing beyond this limitation requires strategies that complement incremental improvements in control fidelity. One powerful approach is to incorporate measurement and feedback

into the state preparation process. Rather than eliminating the sources of infidelity altogether, such as imperfect optical pumping, microwave transfer infidelities, or population leakage during dwell-times, error are instead detected when they occur, and their effects are mitigated either by discarding runs of the experiment where errors occurred (postselection) or by actively correcting the system through feedback. This shift in perspective to a measurement-and-feedback-based strategy provides a pathway to substantially higher effective state preparation fidelities and provides a level of robustness to fluctuations in the experiment and its environment.

This measurement-and-feedback approach is particularly well suited to reconfigurable optical tweezer arrays. In these systems, state preparation errors are typically localized to individual trapping sites, rather than arising from correlated global failures.[1] Combined with the intrinsic site-resolved imaging and control capabilities of tweezer platforms, these localized errors can be identified with single-site resolution and, in principle, corrected on a site-by-site basis. In fact, these measurement and feedback protocols have been used for over a decade to assemble defect-free (but not internally pure) arrays of atoms from stochastically loaded arrays via tweezer rearrangement [70, 71]; in Chapter 8, we extended this protocol to molecules. In the first part of this chapter, we extend this strategy to generate not only defect-free but also internally-pure arrays (i.e., all molecules in the same internal state).

Molecules are well suited to implement these measurement-enhanced state preparation protocols due to their rich internal structure. In particular, the presence of many rotational states, well separated from each other compared to the linewidths of optical transitions, provides a large manifold of "dark" states that can be used to store correctly prepared molecules during the error detection process. Crucially, these states can be chosen such that they do not interact with the detection light, ensuring that correctly prepared molecules remain undisturbed while errors are identified. Furthermore, these low-lying rotational states

[1] That being said, when a correlated global failure does occur, such as when the author programs a sequence error, the signature of *all* sites experiencing an error is extremely useful to debug these grad-student-induced errors.

are typically long-lived, providing a robust storage manifold during intermediate steps of the protocol. This combination of spectral isolation and long lifetimes times makes molecules especially attractive for implementing measurement-enhanced state preparation protocols.

Beyond state preparation, measurement and feedback techniques can also help catch and correct population leakage errors during the coherent evolution of a quantum simulation or the application of quantum gates during a computation. Such leakage errors can arise from off-resonant scattering, spontaneous emission into unwanted states, or even loss of the atom/molecule from the trap itself. For these applications, the requirements on site-resolved detection are more stringent: both the population and the phase coherence of the encoded quantum information must survive the error detection step.

If the population leaks to, or can be transferred to, a manifold that is well-separated from the qubit states, there is a possibility to detect that population with minimal disturbance to the encoded quantum information. Errors of this form are known as *erasure errors*, and the process of transferring population leakage to a "detection manifold" and then detecting the population is referred to as *erasure conversion and detection*. To close the feedback loop, once the location of the erasure error is known, the qubit could be re-initialized and incorporated back into the quantum operation.

It is important to emphasize, however, that leakage errors represent only one class of errors affecting qubit systems. Other errors, such as dephasing or coherent rotation errors within the qubit manifold, do not result in population leakage and therefore are not amenable to erasure conversion and detection. These errors result in no population transferred to auxiliary manifolds; hence, these errors must instead be corrected through more general quantum error correction techniques, typically involving logical encoding across multiple physical qubits. As such, erasure conversion and detection is a complementary tool within a broader error mitigation and correction framework.

In this chapter, we begin by surveying existing protocols to enhance state preparation fidelities via feedback, and perform erasure conversion and detection. Next, we describe,

in detail, how the rich internal structure of CaF enables our error conversion and detection strategy. We detail a rapid detection protocol and characterize the improvement in state preparation fidelity. Notably, we demonstrate both error detection and error correction, allowing not only defect-free but also internally-pure arrays to be generated. Along the erasure error front, we probe the presence of a small but significant leakage error out of a newly developed hyperfine qubit encoding. This leakage is amenable to erasure conversion. We show that both the population and phase of the encoded hyperfine qubit is preserved during detection, allowing coherence times to be improved via post-selection. We conclude with two brief explorations to extend measurement-enhanced state preparation techniques to the motional states of the tweezer-trapped molecules.

The work presented in this chapter resulted in the following publication [7]:
Connor M. Holland, Yukai Lu, Samuel J. Li, Callum L. Welsh, Lawrence W. Cheuk. "Demonstration of Erasure Conversion in a Molecular Tweezer Array" PRX. ***15****, 031018 (2025).*

9.1 Related Protocols

In this section, we highlight quantum science platforms that implemented measurement-enhanced state preparation and erasure conversion protocols during the explorations detailed in this chapter. Following the initial theoretical proposal of Ref. [172], these ideas have been rapidly adopted across multiple architectures. While the specific physical implementations differ, all approaches share a common principle: errors are mapped onto auxiliary degrees of freedom or subspaces where they can be detected with minimal disturbance to the encoded quantum information.

An early experimental demonstration of measurement-enhanced state preparation and erasure conversion was presented in Ref. [173] using tweezer-trapped strontium atoms. The alkaline-earth level structure of Sr provides access to both ground and long-lived metastable

manifolds, with only the ground (bright) manifold fluorescing during imaging. By selectively shelving correctly prepared atoms into a metastable (dark) manifold, state preparation errors can be identified via fluorescence imaging. Furthermore, during coherent operations, leakage processes transfer a majority of population back to the ground manifold, providing a natural mechanism for erasure conversion that can be detected at the end of a circuit or simulation.

Building on this approach, Ref. [76] demonstrated a similar protocol in ytterbium atoms, while introducing a key advance: the preservation of coherence during the detection process. In this work, a nuclear-spin qubit encoded within a metastable manifold was shown to maintain coherence under erasure detection, opening the door to mid-circuit detection and error correction protocols. This represents an important step beyond post-selection-based protocols, enabling time-tagging errors and the possibility of real-time error correction.

Further progress in this direction was demonstrated in Ref. [174], where mid-circuit erasure conversion and detection was achieved in strontium by encoding quantum information in the motional states of the optical tweezer. In contrast to the original encoding utilized, where one of the qubit states was short-lived, the new motional-state qubits were long lived and remained undisturbed following erasure detection. This work highlights how alternative encoding strategies can be leveraged to meet the more stringent requirements of mid-circuit error detection.

In contrast to alkaline-earth systems, atoms with simpler level structures, such as alkali atoms, do not easily provide long-lived states far-detuned from imaging light where qubits can be stored. Thus, in these systems, erasure protocols more challenging to implement. Nevertheless, an innovative approach was demonstrated in Ref. [175] using a rubidium tweezer array. In this work, a so-called leakage-detection unit (LDU) employs Rydberg-mediated interactions between a data qubit and an ancilla qubit to flag whether the data atom has been lost from the trap. The LDU protocol effectively applies the identity operation when the data atom is present, and a bit-flip on the ancilla when the data atom is absent, thereby flagging loss events while preserving the encoded quantum information.

Moving beyond neutral atom platforms, superconducting circuit architectures have also implemented erasure-detecting schemes using dual-rail encodings, as demonstrated in both two-dimensional [176] and three-dimensional [177] cavity-transmon systems. In these approaches, a logical qubit is encoded in the subspace spanned by $|01\rangle$ and $|10\rangle$, where $|n_1 n_2\rangle$ denotes the photon occupation of two distinct cavities/transmons. Erasure detection is then performed by measuring the total photon number: any outcome with $n_1 + n_2 \neq 1$ lies outside the encoded subspace and is flagged as an erasure.

Taken together, these early demonstrations show that erasure conversion and detection can be realized through a variety of physical mechanisms, including state-selective fluorescence, ancilla-assisted detection, and encoding into protected subspaces. This diversity of approaches underscores the generality of erasure protocols; these techniques are powerful tools for enhancing state preparation and implementing quantum error correction across a variety of experimental platforms.

9.2 Leveraging Molecular Structure for Error Detection

The first step in our work is to devise a scheme that allows molecules with errors to be detected in a site-resolved manner *without affecting error-free ones*. To this end, we make use of the rich set of available internal molecular states. We encode errors into a set of "bright" states ($\mathcal{F}$) that can be optically detected, while keeping error-free molecules in "dark" states ($\mathcal{T}$) that are minimally affected during detection. Specifically, we make use of bright and dark states whose optical transitions are well-separated compared to their linewidths. This strategy is generally possible in a quantum system with sufficiently rich internal structure. For example, work in alkaline-earth atomic arrays [76, 172–174] has used ground and metastable electronic manifolds with widely separated optical transitions.

Instead of two different electronic manifolds, our strategy makes use of two different rotational manifolds. The rotational manifold $\mathcal{F} = X^2\Sigma(v = 0, N = 1)$, which permits optical

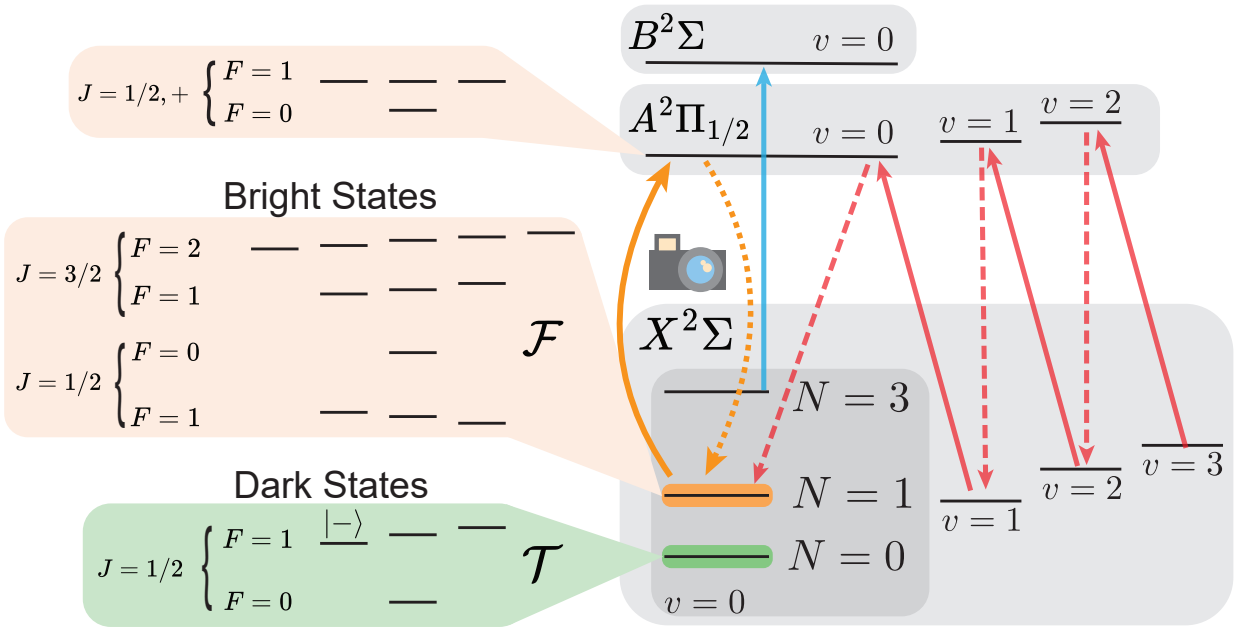


Figure 9.1: Rapid Resonant Imaging Scheme: Molecules in bright states $\mathcal{F} = X^2\Sigma(v = 0, N = 1)$ scatter light resonant with the $X^2\Sigma(v = 0, N = 1) \rightarrow A^2\Pi_{1/2}(v = 0, J = 1/2, +)$ transition (orange arrows). Vibrational (red solid arrows) and rotational repumping light (blue solid arrow) is applied. The imaging light is off-resonant for all other states including the ones in the ground rotational manifold $\mathcal{T} = X^2\Sigma(v = 0, N = 0)$.

cycling, is used to flag errors, while error-free molecules reside in the ground rovibrational manifold $\mathcal{T} = X^2\Sigma(v = 0, N = 0)$ (Fig. 9.1). The optical transitions of the bright states in $\mathcal{F}$ are separated from those in the dark states $\mathcal{T}$ by $\Delta \approx 2\pi \times 20\,\mathrm{GHz}$, which is much larger than the excited state linewidth of $\Gamma \approx 2\pi \times 10\,\mathrm{MHz}$. Optical detection of errors encoded as population in $\mathcal{F}$ should therefore minimally affect population and coherence in $\mathcal{T}$.

9.3 Rapid Resonant Imaging

Experimentally, we first show that molecules in the bright states $\mathcal{F}$ can indeed be detected while minimally affecting the population of error-free molecules residing in the dark states $\mathcal{T}$ (Fig. 9.1). To this end, we devise a new fluorescence detection scheme that is optimized for minimally affecting the dark states. This stands in contrast to previous imaging schemes that prioritize detection fidelity [3, 43, 86].

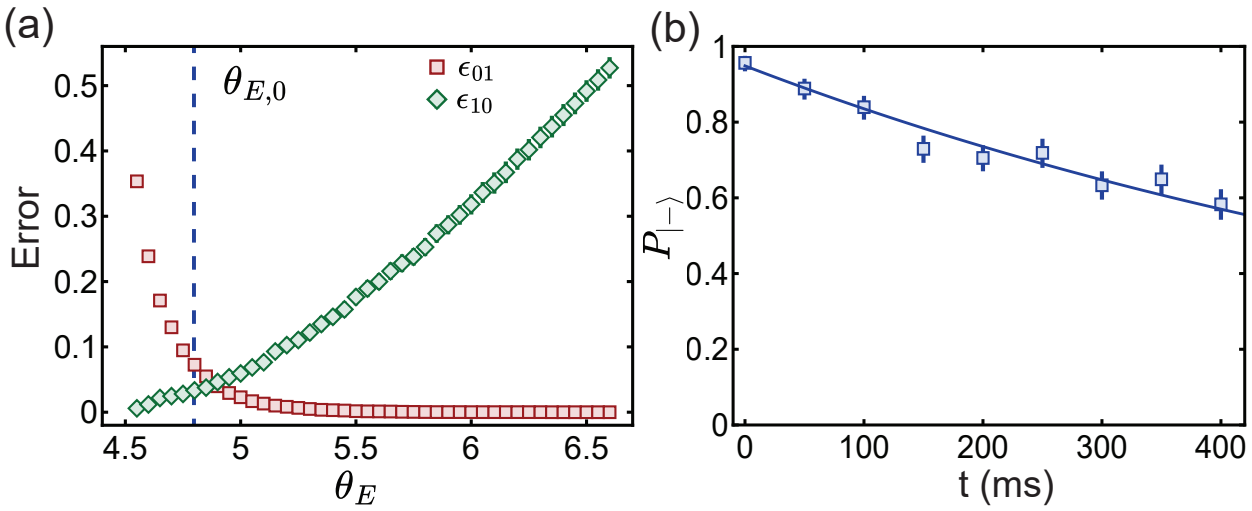


Figure 9.2: Characterizing Errors during Rapid Resonant Imaging: (a) Error Identification Performance. The false positive probability ϵ_{01} (red squares) and false negative probability ϵ_{10} (green diamonds) are shown versus the classification threshold θ_{E}. Vertical dashed line marks $\theta_{\mathrm{E}} = \theta_{\mathrm{E},0} = 4.8$, the value used in this work. (b) Population $P_{|-\rangle}$ in $|-\rangle = |X^2\Sigma(v=0, N=0), F=1, m_F=-1\rangle$ versus imaging duration t. An exponential fit gives a $1/e$ lifetime of $\tau = 790(60)$ ms, much longer than the imaging duration of 3 ms.

In our scheme, we seek to minimize exposure to imaging light in order to minimize off-resonant scattering by error-free molecules in dark states. At the same time, high photon scattering rates of the bright states improve the signal-to-noise of fluorescence detection. We therefore use light resonant with the $X^2\Sigma(v=0, N=1) \rightarrow A^2\Pi_{1/2}(v=0, J=1/2, +)$ transition. This provides the best ratio of fluorescence emission to off-resonant scattering and also enables rapid detection compared to previous imaging schemes using detuned laser-cooling light [3, 43, 86].

9.3.1 Imaging Performance Characterization

We quantify the performance of our detection scheme using two metrics: (1) the classification fidelity and (2) the effect on error-free dark states. To classify a tweezer site as having occupation in $\mathcal{F}$, i.e. having an error, we binarize the fluorescence counts with a threshold $\theta_{\mathrm{E},0}$. Sites with counts above $\theta_{\mathrm{E},0}$ are classified as errors; those below $\theta_{\mathrm{E},0}$ are classified as error-free. The classification fidelity is determined by the false negative probability ϵ_{10}, where

a site with an error is classified as error-free, and the false positive probability ϵ_{01}, where an error-free site is classified as having an error. Both misclassification probabilities depend on $\theta_{\mathrm{E},0}$. Here, we prioritize minimizing ϵ_{10} rather than the overall fidelity. This is because, for error mitigation via post-selection, ϵ_{01} only affects the data rate, while ϵ_{10} directly affects the ability to reject errors. After optimization, we find that at an imaging intensity of $I = 4.5\,\mathrm{mW/cm^2}$, imaging duration of 3 ms, and tweezer depth of $k_B \times 930(20)\,\mu\mathrm{K}$, we achieve a false negative probability $\epsilon_{10}(\theta_{\mathrm{E},0}) = 0.033(4)$ at a threshold of $\theta_{\mathrm{E}} = \theta_{\mathrm{E},0} = 4.8$ (Fig. 9.2(a)). This imaging performance allows up to a 30-fold reduction of intrinsic error rates.

Next, we quantify the effect of our imaging procedure on the dark state population. We prepare molecules in one of the dark states $|-\rangle = |X^2\Sigma(v = 0, N = 0), J = 1/2, F = 1, m_F = -1\rangle$ and measure the population loss versus imaging duration (Fig. 9.2(b)). At the imaging duration used (3 ms), we measure a population loss of $3.8(3) \times 10^{-3}$ per image, confirming that the error-free states are minimally affected. The population loss rate is in agreement with theoretical estimates. For our scheme, the ratio of the off-resonant scattering rate to the fluorescence rate is approximately $9\Gamma^2/\Delta^2 \sim 10^{-6}$. Because the dark states do not optically cycle, they leak to other internal states after $\mathcal{O}(1)$ scattering events. Since we typically scatter ~ 1000 photons to achieve sufficient signal-to-noise, the population leakage errors are expected to be at the $\sim 10^{-3}$ level. These leakage errors could in principle be corrected with more elaborate optical pumping and detection schemes.

9.3.2 Off-Resonant Scattering Rate Estimation

We measure the lifetime of the target internal state $|-\rangle$ in the rapid imaging configuration ($U = k_B \times 930(20)\,\mu\mathrm{K}$, $B = 4.4\,\mathrm{G}$, and $\theta = 53°$) with and without the resonant imaging light applied. For all lifetime measurements, a 5 ms rapid resonant imaging pulse is applied at the end of the variable hold time to remove any population shelved in $X^2\Sigma(v = 1, N = 1)$

states via blackbody pathways. From these measurements, we measure a contribution of $\gamma = 0.76(11)\,\mathrm{s}^{-1}$ due to rapid resonant imaging.

We note that the population loss is due to off-resonant scattering, and primarily results in population leakage to $X^2\Sigma(v = 0, N = 2)$ hyperfine states (20 states in total) and the other three hyperfine states in the $X^2\Sigma(v = 0, N = 0)$ manifold. We note that these leakage errors could in principle be detected in a more sophisticated leakage conversion scheme utilizing more repumpers and microwave pulses, and are therefore not a fundamental limitation.

To a good approximation, the observed loss rate is given by the off-resonant photon scattering rate. We therefore compare the observed population loss rate with the predicted off-resonant photon scattering rate by $|-\rangle$ due to the rapid imaging light. Because the off-resonant photon scattering rate is predicted to be low and causes leakage, the photon scattering rate can simply be calculated using Fermi's golden rule. The off-resonant photon scattering rate is primarily due to excitation to $A^2\Pi_{1/2}(v = 0, J = 1/2, -)$ and $A^2\Pi_{1/2}(v = 0, J = 3/2, -)$ and is given by

$$\Gamma_{\mathrm{sc}} = \frac{\pi c^2}{2\hbar\omega^3}\Gamma^2 I \left(\frac{2}{3}\frac{1}{\Delta_{1/2}^2} + \frac{1}{3}\frac{1}{\Delta_{3/2}^2}\right), \tag{9.1}$$

where I is the intensity of the imaging light, $\Delta_{1/2} \approx 2\pi \times 20\,\mathrm{GHz}$ is the detuning from the $X^2\Sigma(v = 0, N = 0) \rightarrow A^2\Pi_{1/2}(v = 0, J = 1/2, -)$ transition, and $\Delta_{3/2} \approx 2\pi \times 50\,\mathrm{GHz}$ is the detuning from the $X^2\Sigma(v = 0, N = 0) \rightarrow A^2\Pi_{1/2}(v = 0, J = 3/2, -)$ transition. The predicted off-resonant scattering rate is $\Gamma_{\mathrm{sc}} = 0.24\mathrm{s}^{-1}$, a factor of 3 lower than the observed population loss. This suggests the possible presence of small amounts of spectral impurities in the imaging light that could be filtered out using an optical cavity.

9.4 Improving State Preparation via Error Detection

Having established that bright molecules in $\mathcal{F}$ can be detected without affecting dark ones in $\mathcal{T}$, we next demonstrate how this can be used to detect and correct for internal state

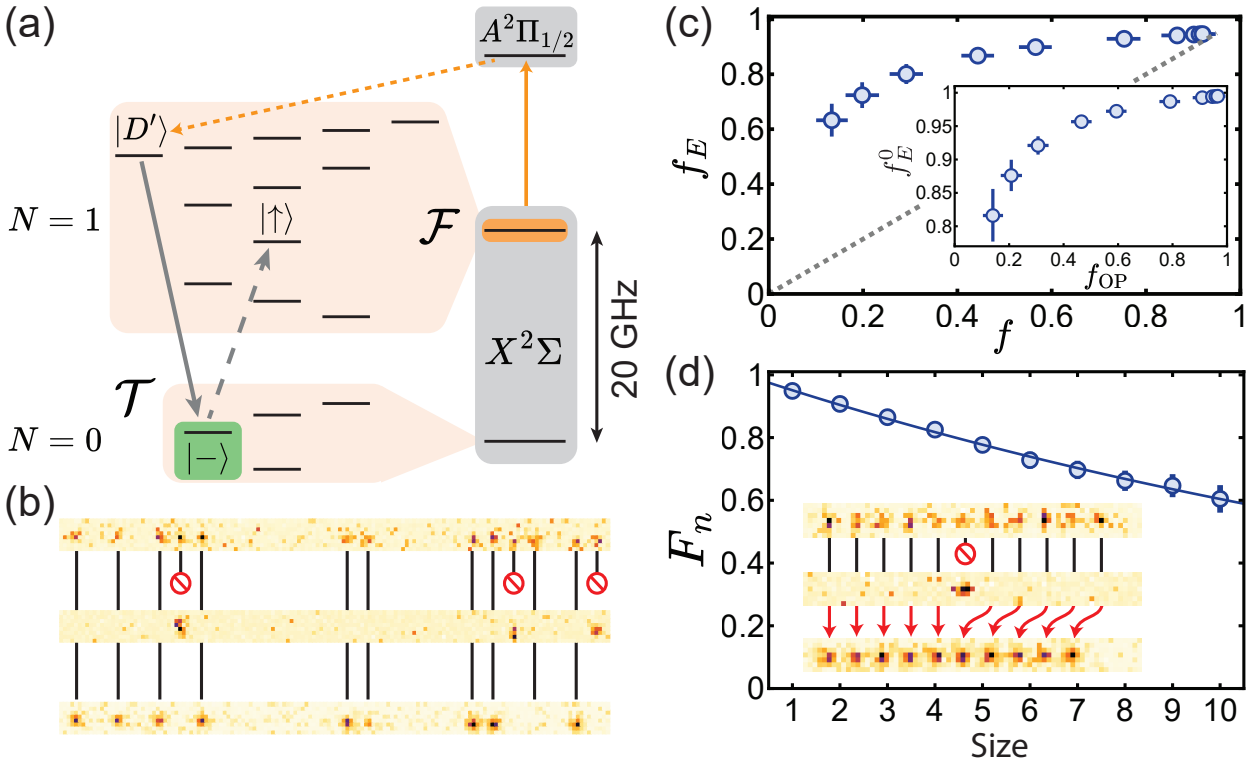


Figure 9.3: Robust and Enhanced State Preparation Using Error Detection: (a) The procedure consists of: (i) optical pumping to $|D'\rangle$ (orange arrow), (ii) population transfer to $|-\rangle$ via a state-resolved microwave pulse (gray solid arrow), and (iii) error detection of left-over molecules in $\mathcal{F}$. To detect the error-free population, a state-selective microwave pulse (gray dashed arrow) transfers $|-\rangle$ to a bright state $|\uparrow\rangle$. (b) Verifying Tweezer Preparation. A non-destructive image (top) identifies initially loaded sites. Measurement-enhanced state preparation is applied, producing an error image (middle) that flags state preparation errors. To verify error detection, we state-selectively transfer molecules from $|-\rangle$ to $|\uparrow\rangle$ for detection (bottom). (c) Error-excised overall preparation fidelity f_E (probability of being occupied and in the correct internal state) versus bare overall preparation fidelity f. Inset shows the error-excised internal state preparation fidelity f_E^0 versus the bare internal state preparation fidelity f_{OP}. (d) Removing State Preparation Errors Mid-Sequence. The probability F_n for preparing a defect-free and internally-pure array is shown versus array size n. The solid line shows a fit to $(f_R)^n$ with $f_R = 0.951(1)$. Inset: exemplary images for $n = 10$.

preparation errors. In previous work with laser-cooled molecular arrays, the best reported fidelity of having a tweezer loaded with a molecule in a single internal state was $\approx 80\%$, limited by imperfect optical pumping and microwave transfers [4, 87]. Here, we present a scheme that detects internal state preparation errors, allowing them to be subsequently removed either mid-sequence or through post-selection.

Our scheme, shown in Fig. 9.3(a), works as follows. After initial tweezer loading, molecules are optically pumped into a single hyperfine state $|D'\rangle = |X^2\Sigma(v = 0, N = 1), J = 3/2, F = 2, m_F = -2\rangle$ within $\mathcal{F}$. Subsequently, molecules are state-selectively shelved into one of the dark states $|-\rangle$ with a microwave pulse at $\approx 20.5\,\text{GHz}$. All errors due to imperfect optical pumping and microwave transfer leave a molecule in the bright states $\mathcal{F}$, which is then optically detected with our resonant imaging scheme *without substantially affecting* the correctly prepared molecules that reside in the dark state $|-\rangle$.

We quantify the performance of our measurement-enhanced state preparation scheme as follows. We first perform internal state preparation followed by error detection, which provides a list of sites that are flagged as having an error. Subsequently, we transfer correctly prepared molecules from $|-\rangle$ to $|\uparrow\rangle = |X^2\Sigma(v = 0, N = 1), J = 1/2, F = 0, m_F = 0\rangle$ (the bright state) for a final detection image. The measurement-enhanced fidelity f_E can be obtained by measuring the fraction of molecules that appear in the final image out of the occupied sites that were not flagged during error detection. To test our scheme's ability to reject errors, we intentionally lower the bare optical pumping fidelity f_{OP} by decreasing the optical pumping duration. This also lowers the overall tweezer preparation fidelity f, which is additionally affected by errors in the form of empty tweezers. In Fig. 9.3(c), we show the error-excised overall preparation fidelity f_E versus f. Additionally, the inset of Fig. 9.3(c) shows the error-excised internal state preparation fidelity f_E^0 versus f_{OP}. Both plots show that excising detected errors substantially improves preparation fidelities. We achieve an error-excised internal state preparation fidelity of $f_E^0 = 0.995(1)$ and an error-excised overall preparation fidelity of $f_E = 0.952(3)$, at a data rate reduction of 7.2(2)%. The overall fidelity f_E improves significantly upon previous reported values ($f \approx 80\%$) [5, 7, 87, 178]. In addition to improved fidelities, our method importantly provides *robustness* to fluctuations in f_{OP}. For example, at an optical pumping fidelity of $f_{\text{OP}} = 0.46$, the error-excised internal state fidelity remains at $f_E^0 \approx 0.96$. We note that the overall preparation fidelity is now limited by occupation errors arising from population loss during the initial non-destructive

image ($\sim 2\%$) used for initial rearrangement and during optical pumping ($\sim 2\%$). Thus, future work that reduce these losses could allow substantial improvement.

Lastly, our scheme enables mid-sequence removal of preparation errors via tweezer rearrangement. We first create regularly spaced defect-free arrays of molecules in $\mathcal{F}$ and non-destructively detect their occupation [4]. Subsequently, we apply our measurement-enhanced state preparation protocol. Tweezers identified to have an error are then switched off and the error-free ones are rearranged into a defect-free configuration. Fig. 9.3(d) shows the measured success probability F_n versus array size n. Fitting the probability to $F_n = (f_R)^n$, where f_R is the single-site overall preparation fidelity, we find $f_R = 0.951(1)$, in agreement with the value of $f_E = 0.952(3)$ without tweezer rearrangement. This demonstrates that no detectable additional errors occur during tweezer rearrangement.

While previous experiments with atomic arrays incorporated similar techniques to post-select for no errors [173], to our knowledge, our work was the first demonstration of mid-sequence removal of internal state preparation errors. This capability will be crucial for quantum simulation and computation applications that require large-scale arrays at low defect rates. Already, our measurement-enhanced preparation scheme opens the door to quantum simulation of interacting many-body Hamiltonians in defect-free mesoscopic molecular arrays. We achieve an overall fidelity of $60(4)\%$ for arrays of size $n = 10$, which makes possible practical post-selection for perfect arrays with only a modest data rate reduction of $\sim 40\%$.

9.5 Coherent Control of a New Hyperfine Qubit

In previous work using CaF molecules, coherent interactions and 2-qubit gates were demonstrated using a rotational qubit encoding [4, 87]. Specifically, two *interacting* states from two neighboring rotational manifolds, $|\uparrow\rangle = |X^2\Sigma(v = 0, N = 1), J = 1/2, F = 0, m_F = 0\rangle$ and $|\downarrow\rangle = |X^2\Sigma(v = 0, N = 0), J = 1/2, F = 1, m_F = 0\rangle$ were used.

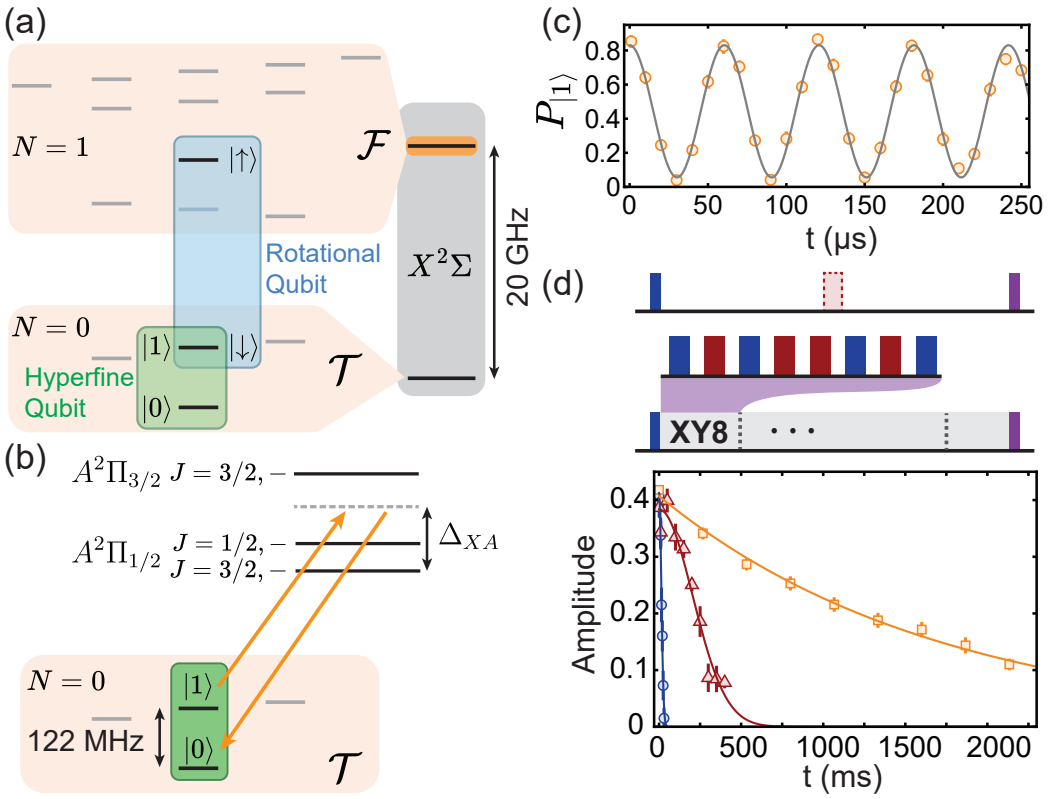


Figure 9.4: A New Hyperfine Qubit: (a) The hyperfine qubit encoding uses two non-interacting states $|1\rangle$ and $|0\rangle$ from the ground rotational manifold $X^2\Sigma(v = 0, N = 0)$. These states are dark to error detection (not in $\mathcal{F}$). (b) Coherent control is achieved using a two-photon Raman process with light detuned halfway between the X-$A^2\Pi_{1/2}$ and X-$A^2\Pi_{3/2}$ transitions. (c) Rabi oscillations between $|1\rangle$ and $|0\rangle$ (orange) are fit to a sinusoid (gray). (d) Top: Ramsey sequences are used to measure qubit coherence times. Bottom: Ramsey fringe amplitude versus hold time t. Data without (with) a spin-echo pulse are shown by blue circles (red triangles). XY8 dynamical decoupling substantially extends coherence times (orange squares). The fitted $1/e$ lifetimes are 19.5(7) ms (Gaussian fit), 288(15) ms (Gaussian fit), and 1710(60) ms (exponential fit), respectively.

Here, we utilize a new *non-interacting* qubit encoding suitable for storing quantum information. Specifically, our encoding uses the two hyperfine states $|1\rangle = |X^2\Sigma(v = 0, N = 0), J = 1/2, F = 1, m_F = 0\rangle$ and $|0\rangle = |X^2\Sigma(v = 0, N = 0), J = 1/2, F = 0, m_F = 0\rangle$, both from the ground rovibrational manifold $X^2\Sigma(v = 0, N = 0)$ (Fig. 9.4(a)). These states are predicted to have long coherence times because of the absence of tensor ac Stark shifts and their low magnetic moments. In addition, they are naturally compatible with our error mitigation scheme, as they belong to the dark state manifold $\mathcal{T}$. We note that hyperfine

qubit encodings in molecules have been previously proposed for use in quantum information processing [20] and hyperfine coherence times have been measured previously in the bialkali molecules NaK [62], RbCs [179], and NaRb [180]. Work concurrent with that demonstrated in this chapter also demonstrated a hyperfine qubit encoding in bialkali NaCs molecules trapped in an optical tweezer array [164].

We first demonstrate coherent control over this new hyperfine qubit and show that it has long coherence times. We coherently control the qubit by driving an M1 transition (at $\approx 122\,\mathrm{MHz}$) through a two-photon Raman process. Specifically, we use light detuned half-way between the $X - A^2\Pi_{1/2}$ and $X - A^2\Pi_{3/2}$ transitions (single-photon detuning of $\Delta_{XA} \approx 2\pi \times 1.1\,\mathrm{THz}$) (Fig. 9.4(b)). The two frequencies in the Raman light co-propagate and have σ^+ projections. To demonstrate coherent control, we prepare molecules in $|1\rangle$, and apply Raman light for a variable duration. As shown in Fig. 9.4(c), we observe Rabi oscillations at $\Omega_R \approx 2\pi \times 15\,\mathrm{kHz}$.

We next measure the qubit coherence time using a Ramsey sequence consisting of two Raman $\pi/2$ pulses separated by a variable duration. To minimize inhomogeneous light shifts between sites due to tweezer trapping light, we operate at a tweezer depth of $U_{\mathrm{hf}} = k_B \times 39(1)\,\mu\mathrm{K}$. By measuring the decay rate of the amplitude of the Ramsey fringe, we find a bare coherence time of $T_2^* = 19.5(7)\,\mathrm{ms}$, which can be increased to $T_2 = 288(15)\,\mathrm{ms}$ with a single spin-echo. We further extend the coherence time to $1710(60)\,\mathrm{ms}$ by applying dynamical decoupling with an XY8 pulse sequence (pulse separation of $33.3\,\mathrm{ms}$) (Fig. 9.4(d)).

In addition to having long coherence times, this hyperfine qubit can be interfaced with the rotational qubit used in previous work [4, 65, 87]. Specifically, we have verified that a quantum state can be coherently transferred from the rotational encoding ($|\uparrow\rangle, |\downarrow\rangle$) to the hyperfine encoding ($|1\rangle, |0\rangle$). Details on this procedure and the characterization of transduction fidelity is given in Section 9.8.

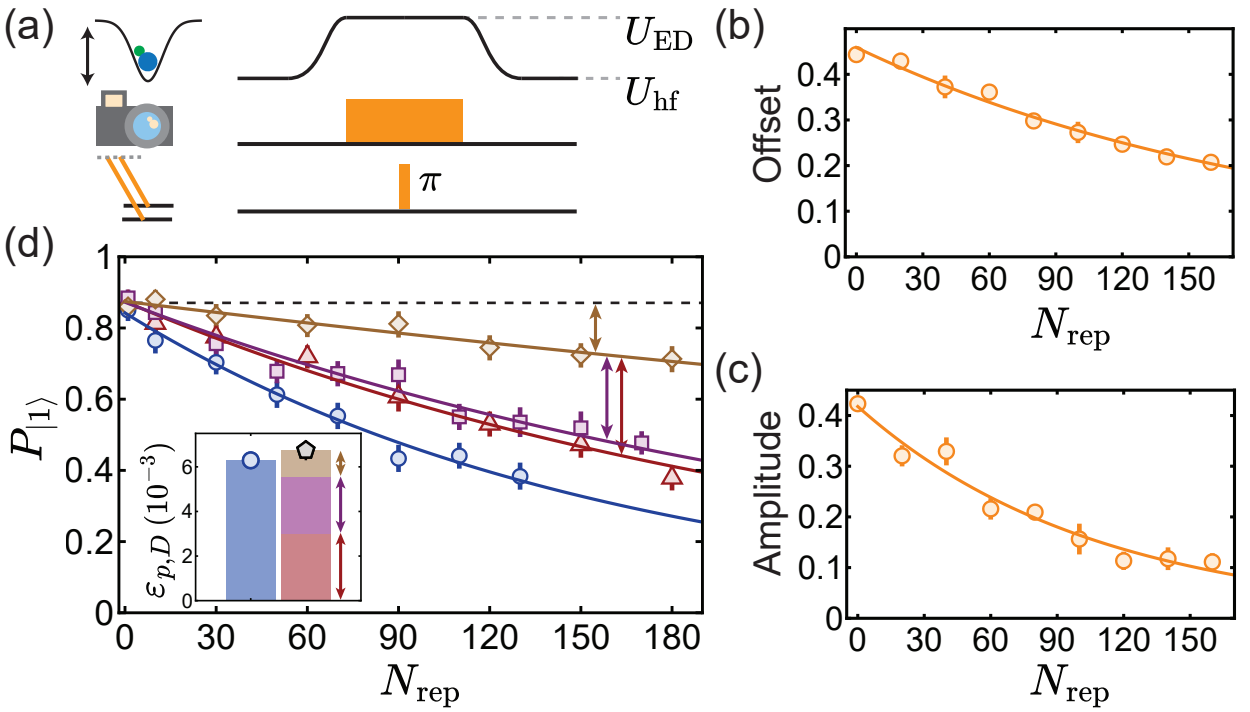


Figure 9.5: Composite Erasure Detection. (a) The composite erasure detection sequence consists of a tweezer depth increase followed by a rapid resonant image and a tweezer depth decrease. A Raman π-pulse is applied mid-sequence. (b) Ramsey fringe offset versus number of composite erasure detections N_{rep}. (c) Ramsey fringe amplitude versus N_{rep}. (d) Population loss measurements with various combinations of tweezer ramp (T), error detection light (E), and $v = 1$ repumping light (V). The surviving population $P_{|1\rangle}$ versus N_{rep} cycles of TEV (blue circles), EV (red triangles), and T (purple squares) is shown. Brown diamonds show measurements at a shallow tweezer depth without TEV. The brown, purple, and red arrows indicate contributions from background vacuum and blackbody loss, tweezer ramp, and erasure detection. Inset shows the population loss per detection image $\varepsilon_{p,D}$. The sum of each source of loss is consistent with the total loss (blue bar and circle).

9.6 Composite Erasure Detection

Having established long coherence times and coherent control of our new hyperfine qubit that is suitable for a quantum memory, we next investigate how to image population in bright states without affecting qubit population and coherence. This is a much more stringent requirement than simply preserving population.

We base our new detection scheme off of the rapid imaging procedure described in Section 9.3. To achieve high detection fidelities of bright state population, a tweezer depth of $U_{\mathrm{ED}} = k_B \times 930(20)\,\mu\mathrm{K}$ is needed, which is $\sim$ 20 times higher than that used to ob-

tain long hyperfine coherence times. At the imaging depth, the qubit frequency shifts by $2\pi \times 0.40(6)$ kHz, leading a ≈ 1 rad phase shift during the 3 ms image. Inhomogeneous tweezer depths also cause the qubit to dephase during the image. To counteract this dephasing, we devise a new "composite erasure detection" scheme that incorporates an echo pulse halfway through the image. As shown in Fig. 9.5(a), our scheme involves 4 steps:

1. The tweezer depth is ramped from U_{hf} to U_{ED}.

2. Local errors are detected using rapid resonant imaging.

3. A π-pulse is applied to the hyperfine qubit halfway through the image.

4. The tweezer depth is returned to U_{hf}.

To determine how well this procedure preserves qubit population and coherence, we perform Ramsey measurements with a variable number of composite erasure detections between the two Ramsey $\pi/2$ pulses. Fig. 9.5(b,c) shows the offset (amplitude) of the resulting Ramsey fringe versus the number of erasure images, which is proportional to the qubit population (coherence). Fitting to an exponential decay curve, we find that the population and coherence errors per image are $\varepsilon_p = 5.1(3) \times 10^{-3}$ and $\varepsilon_c = 9.3(8) \times 10^{-3}$, respectively.

To understand whether these errors are fundamental, we next investigate their origins. We independently measure population loss for each step of the composite erasure detection sequence. These include losses due to: (1) off-resonant scattering of the Raman π-pulse light, (2) off-resonant scattering of imaging light, (3) tweezer depth ramps (Fig. 9.5(d)). Our measurements indicate that the Raman π-pulse contributes a loss rate of $4.1(3) \times 10^{-5}$ per image and is therefore negligible. Off-resonant scattering of imaging light and tweezer ramps contribute $3.0(3) \times 10^{-3}$ and $2.6(3) \times 10^{-3}$, respectively. In addition, we measure a background loss rate of $1.2(1) \times 10^{-3}$ per imaging duration, consistent with the estimated leakage rate to higher vibrational states due to blackbody radiation at room temperature [3, 181]. Since leakage due to blackbody radiation can in principle be suppressed in a cryogenic setup and

loss during the tweezer ramps can likely be reduced with colder molecular temperatures, our scheme is likely only fundamentally limited by off-resonant scattering of imaging light. Shorter imaging durations could potentially allow one to achieve errors per image at the low 10^{-3} level.

9.7 Correcting Hyperfine Leakage Errors

The second part of this chapter concerns detecting qubit leakage errors. To do so, we utilize the new qubit encoding using two non-interacting hyperfine states in the dark state manifold $\mathcal{T}$ introduced in Section 9.5. We also utilize the new imaging protocols outlined in Section 9.6 ("erasure imaging") to optically detect population in the bright states $\mathcal{F}$ while minimally affecting *both population and coherence* of the dark qubit. Using these developments, we show that a significant source of error for the new qubit - leakage into other molecular states induced by blackbody radiation - can be converted to population in bright states, which can be detected as local errors. These local qubit errors are known as erasures [182, 183], a topic that has attracted much attention in both theoretical [172, 184–186] and experimental work in quantum error correction recently [76, 173–177]. This work constitutes the first demonstration of erasure conversion in molecules.

9.7.1 Leakage Errors Induced by Black-Body Radiation

Having quantified the performance of our composite erasure imaging scheme, we next use this to mitigate a significant error for our hyperfine qubit - leakage into higher vibrational states due to blackbody radiation at room temperature. Specifically, blackbody radiation drives $\Delta v = 1$ vibrational-changing E1 transitions, leading to leakage from the qubit states (encoded in $v = 0$) to the vibrationally excited states $\mathcal{E} = X^2\Sigma(v = 1, N = 1)$. The estimated leakage rate is $\Gamma_{01} \approx 0.3\,\mathrm{s}^{-1}$ [187], which is a slow but significant source of qubit loss. As we will show, these errors can be converted to population in the bright states $\mathcal{F}$

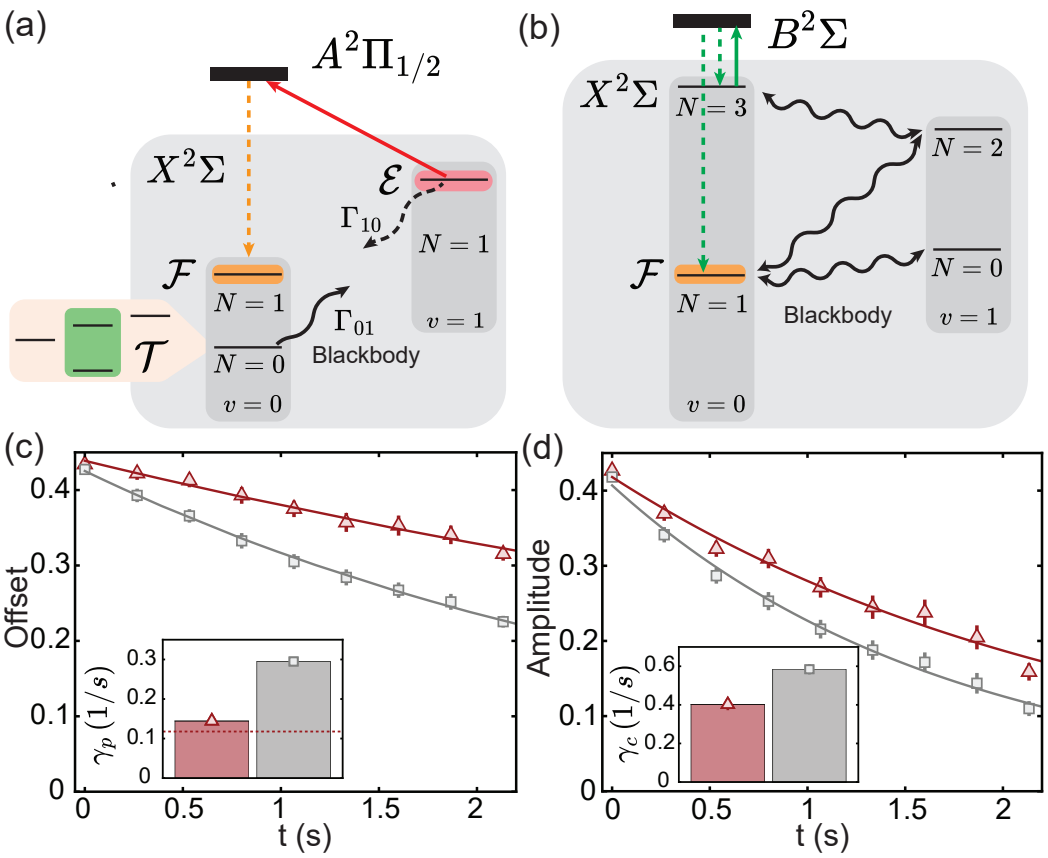


Figure 9.6: Erasure Conversion of Blackbody Errors: (a) Erasure Conversion Scheme. Blackbody radiation (black solid wavy) predominantly excites molecules from $\mathcal{T}$ to $\mathcal{E}$ at a rate Γ_{01}, which radiatively decays (black dashed wavy) back to $v = 0$ at a rate Γ_{10}. We erasure convert to $\mathcal{F}$ using $v = 1$ repumping light (red arrow). (b) Robustness of $\mathcal{F}$ to blackbody leakage errors. Blackbody leakage errors (black wavy) primarily populate $X^2\Sigma(v = 0, N = 3)$ states, which are converted back to $\mathcal{F}$ via the rotational repumping (solid green). (c) Ramsey fringe offset and exponential fit versus hold time t without erasure excision (gray squares) and with a single final error detection image. Inset: fitted $1/e$ loss rates γ_p, with red dashed line showing a prediction outlined in Section 9.7.3). (d) Ramsey fringe amplitude versus hold time with (red triangles) and without (gray squares) error excision. Inset: amplitude loss rate γ_c from the exponential fits.

and detected in a site-resolved manner. In other words, the leakage errors can be converted into erasures and detected.

To perform erasure conversion, we simply apply $v = 1$ vibrational repumping light that repumps molecules into the bright manifold $\mathcal{F}$ with 98% probability (Fig.9.6(a)). There are, however, two subtleties. First, vibrationally excited molecules in $X^2\Sigma(v = 1)$ decay back to the ground vibrational manifold $X^2\Sigma(v = 0)$ at a rate $\Gamma_{10} \approx 5.3\,\mathrm{s}^{-1}$, which is much quicker

than the blackbody excitation rate $\Gamma_{01} \approx 0.3\,\mathrm{s}^{-1}$. Therefore, erasure conversion should occur at a rate much faster than Γ_{10}. It is not necessary, however, to detect the error flags in $\mathcal{F}$ quickly, since they lie in the long-lived ground vibrational manifold. Second, blackbody radiation causes secondary leakage of molecules out of the detectable bright states $\mathcal{F}$ into the undetected dark states $X^2\Sigma(v = 1, N = 0, 2)$(Fig.9.6(b)). These states then decay both back to $\mathcal{F}$ and also to another dark rotational manifold $X^2\Sigma(v = 0, N = 3)$. We close this leakage pathway by applying rotational repumping light ($N = 3$ repumper) that brings $X^2\Sigma(v = 0, N = 3)$ molecules back to the error flag manifold $\mathcal{F}$ (Fig. 9.6(b)).

We first experimentally confirm that secondary blackbody leakage is indeed suppressed by $N = 3$ repumping light. We find indeed that with the extra repumping light, the error flags $\mathcal{F}$ have a population lifetime of $\tau = 13.5(5)\,\mathrm{s}$, well exceeding the blackbody-limited lifetime by a factor of ≈ 4. The residual loss is attributed to background gas collisions and double blackbody excitation events into dark rotational manifolds with $N \geq 5$.

We next experimentally implement our blackbody erasure conversion scheme and investigate whether it extends qubit population lifetimes and coherence times. We measure the offset and amplitude of Ramsey fringes with and without erasure excision. For these measurements, erasure conversion is repeatedly applied mid-circuit, with erasure detection occurring once at the end of the sequence. During the Ramsey hold time, XY8 dynamical decoupling is applied.

Regarding qubit population loss, we measure a bare loss rate of $\gamma_p = 0.30(1)\,\mathrm{s}^{-1}$, consistent with the estimated blackbody excitation rate. Excising erasures, the loss rate decreases to $\gamma_{p,E} = 0.14(1)\,\mathrm{s}^{-1}$ (Fig. 9.6(c)). We find that a loss rate model that incorporates vacuum loss, blackbody excitation, erasure conversion and detection efficiency, and the internal state preparation fidelity agrees well with our measurements (Fig. 9.6(c)). We use this model to infer that $\approx 80\%$ of blackbody errors are erasure-converted and detected correctly (see Section 9.7.3). Regarding qubit coherence, we measure a bare loss rate of $\gamma_c = 0.58(2)\,\mathrm{s}^{-1}$, which decreases to $\gamma_{c,E} = 0.40(2)\,\mathrm{s}^{-1}$ upon excising erasures. This improvement is consistent

with the improvement in population loss, suggesting that blackbody radiation does not lead to additional decoherence beyond population loss. Overall, we find that erasure conversion of blackbody errors allows excision of 51(3)% (31(5)%) of *all* qubit population (coherence) errors, which includes loss due to finite vacuum lifetime.

Looking ahead, because these blackbody erasures can be detected mid-sequence, they can in principle be corrected, as previously demonstrated in molecular ions [181]. For molecular tweezer arrays, blackbody erasures can be removed via reloading a site or by reinitializing the molecular state [83, 188].

9.7.2 Lifetimes Affecting Erasure Conversion and Detection

Loss to Higher-N States due to BBR

Since molecules in $\mathcal{F} = X^2\Sigma(v = 0, N = 1)$ serve as error flags, it is important to quantify their population lifetime, which we measure in the pseudo-magic configuration ($U = k_B \times 39(1)\,\mu\text{K}$, $B = 2.0\,\text{G}$). As discussed in this chapter, molecules in the detection manifold $\mathcal{F}$ that leak to $X^2\Sigma(v = 0, N = 3)$ because of blackbody excitation can be repumped back into $\mathcal{F}$ using a rotational repumper, which is applied during the final destructive image.

We model population loss in $\mathcal{F}$ using a rate equation model that includes $X^2\Sigma(v = 0)$ rotational states with odd N for $N \leq 13$, $X^2\Sigma(v = 1)$ rotational states with even N for $N \leq 13$, and vacuum loss. We further assume that the population is initially distributed uniformly across all hyperfine states in $\mathcal{F}$ and all blackbody excitations and decays keep populations uniformly distributed within each N-manifold.

Fig. 9.7 shows the measured $X^2\Sigma(v = 0, N = 1, 3)$ total population decay and inferred populations in various rovibrational manifolds. Fitting our rate equation model to the data yields a vacuum loss rate of $\gamma_{\text{vac}} = 0.047(3)\,\text{s}^{-1}$. Our model, along with the fitted vacuum loss rate, allows us to infer populations in various rovibrational manifolds (Fig. 9.7) and attribute losses. At the measured lifetime of $\tau = 13.5(5)\,\text{s}$, our model predicts that of the molecules that survive vacuum loss, 32% of population is missed in the final readout image

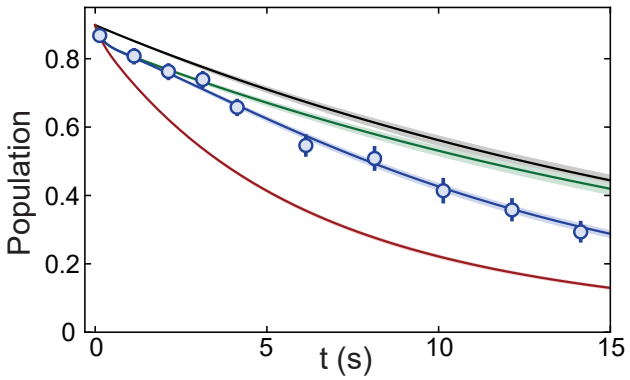


Figure 9.7: Population of $X^2\Sigma(v=0, N=1)$ Molecules Under BBR: Blue circles show the measured total population in $X^2\Sigma(v=0, N=1,3)$ versus hold time t. The blue line shows a fit using our rate equation model, which incorporates blackbody excitation, spontaneous vibrational decay, and vacuum loss. Using our rate equation model and the vacuum loss rate determined from fitting the data, we infer various molecular populations. Simulation results (solid lines) and $\pm 1\sigma$ error bands (shaded bands) are shown for the total population (black), the $X^2\Sigma(v=0, N=1)$ population (red), the $X^2\Sigma(v=0, N=1,3)$ population (blue), and the $X^2\Sigma(v=0)$ population (green).

due to equilibration with states in $v=1$ (5%) and a multi-step excitation and decay chain populating $v=0, N \geq 5$ (27%).

Single-Photon Scattering From the Raman Beam

In this section, we describe the procedures used to measure population errors in our hyperfine qubit when subject to Raman light. We characterize population loss due to single-photon scattering by applying a single Raman frequency component and measuring population loss. We measure a single-photon lifetime per Raman component of $\tau_{1\gamma} = 1.06(5)\,\mathrm{s}$ and a population lifetime of $\tau_d = 4.3(2)\,\mathrm{s}$ in the absence of Raman light. These lifetimes, combined with the π-time of $t_\pi = 29\,\mu\mathrm{s}$ allows estimating a single-photon limited population error per Raman π-pulse of $\varepsilon_p = 4.1(3) \times 10^{-5}$.

To quantify the effect of off-resonant scattering by Raman light, we define the quality factor $Q_\pi = \Omega_R/(\pi\Gamma_{sc})$, which describes the ratio of the two-photon Rabi frequency Ω_R to the off-resonant scattering rate Γ_{sc}. For Raman light detuned near the X-$A^2\Pi_{1/2}$ and X-$A^2\Pi_{3/2}$ transitions, and assuming each Raman leg has equal intensity and σ^+ projections

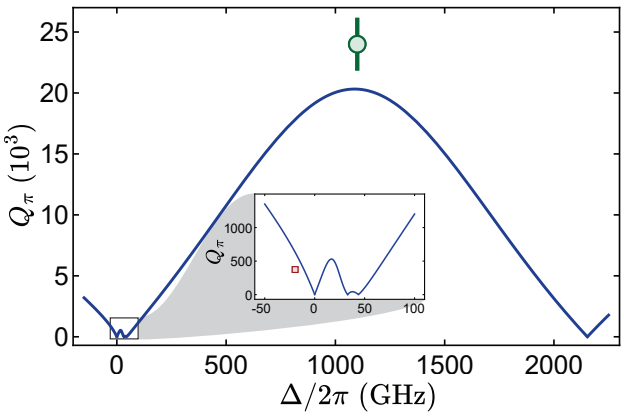


Figure 9.8: Raman π-Pulse Quality Factor: The theoretical Raman π-pulse quality factor $Q_\pi = \Omega_R/(\pi\Gamma_{sc})$ gives an upper-bound on the number of Raman π-pulses that can be applied with $1/e$ of population remaining. The quality factor (blue curve) is plotted vs single-photon detuning $\Delta/2\pi$ from the $X^2\Sigma(N = 0) \rightarrow A^2\Pi_{1/2}(J = 1/2, -)$ transition. Empirically measured quality factor at $\Delta \approx 1.1\,\text{THz}$ (green circle) matches the theoretical upper bound. Inset: quality factor at $\Delta = -2\pi \times 19.6\,\text{GHz}$ (red square) is a factor of 1.7(1) lower than theory.

onto the quantization axis, the π-pulse quality factor Q_π for our choice of states is given by

$$Q_\pi = \frac{1}{\pi\Gamma} \frac{\left|\frac{1}{\Delta}\frac{2}{3} - \frac{1}{\Delta-\delta_{rot}}\frac{1}{6} - \frac{1}{\Delta-\delta_{rot}-\delta_{FS}}\frac{1}{2}\right|}{\left(\frac{1}{\Delta^2}\frac{2}{3} + \frac{1}{(\Delta-\delta_{rot})^2}\frac{1}{3} + \frac{1}{(\Delta-\delta_{rot}-\delta_{FS})^2}\right)}, \tag{9.2}$$

where Δ is the single photon detuning from the $X^2\Sigma(v = 0, N = 0) \rightarrow A^2\Pi_{1/2}(v = 0, J = 1/2, -)$ transition, $\delta_{rot} = 2\pi \times 33\,\text{GHz}$ is the angular frequency difference between $A^2\Pi_{1/2}(v = 0, J = 1/2, -)$ and $A^2\Pi_{1/2}(v = 0, J = 3/2, -)$, and $\delta_{FS} = 2\pi \times 2120\,\text{GHz}$ is the angular frequency difference between $A^2\Pi_{1/2}(v = 0, J = 3/2, -)$ and $A^2\Pi_{3/2}(v = 0, J = 3/2, -)$.

Fig. 9.8 shows Q_π versus the single photon detuning Δ for X-A Raman light. In a near-detuned X-A Raman configuration ($\Delta = -2\pi \times 19.6\,\text{GHz}$), we predict $Q_\pi = 630$. From single-photon scattering rate measurements, we find $Q_\pi = 374(29)$, which is close to but lower than the theoretical value by a factor of 1.7(1). At the optimal single photon detuning, we predict $Q_\pi = 20.3 \times 10^3$, in good agreement with the measured $Q_\pi = 24(2) \times 10^3$.

9.7.3 Modeling BBR Erasure Conversion Efficiencies

In this section, we describe a model that we use to capture population dynamics due to blackbody vibrational excitation and subsequent decay. This model allows us to extract an erasure conversion efficiency from the measured data.

Blackbody errors occur when population $p_{\mathcal{T}}$ from the target qubit manifold ($\mathcal{T} = \{|0\rangle, |1\rangle\}$) is excited to $X^2\Sigma(v = 1, N = 1)$ via absorption of a thermal blackbody photon, which occurs at a rate of γ_{BB}. This population is converted to population $p_{\mathcal{F}}$ in the detectable states ($\mathcal{F} = X^2\Sigma(v = 0, N = 1)$) by the $v = 1$ vibrational repumper that is applied continuously mid-sequence in our blackbody erasure conversion scheme. However, if the rate of vibrational repumping is too slow or if molecules are lost in the repumping process, part of the population can end up in states outside of $\mathcal{T}$, which cannot be detected in our scheme. These decay events reduce the erasure conversion efficiency η.

In the limit where the conversion is much faster than all other timescales, the populations are described by the rate equation model:

$$\begin{aligned} \dot{p}_{\mathcal{T}} &= -(\gamma_{\text{vac}} + \gamma_{\text{BB}})\, p_{\mathcal{T}} \\ \dot{p}_{\mathcal{F}} &= \eta\gamma_{\text{BB}}\, p_{\mathcal{T}} - \gamma_{\text{vac}}\, p_{\mathcal{F}} \end{aligned} \tag{9.3}$$

with initial conditions of $p_{\mathcal{T}}(0) = s$ and $p_{\mathcal{F}}(0) = 0$, because the molecules are initially in the hyperfine qubit manifold.

The population that is successfully pumped to $\mathcal{F} = X^2\Sigma(v = 0, N = 1)$ is subsequently detected via rapid resonant imaging, with a true positive probability of $\bar{\epsilon}_{10} = 1 - \epsilon_{10}$. The erasure-excised probability is then

$$p_{\text{E},\mathcal{T}}(t) = \frac{p_{\mathcal{T}}(t)}{1 - p_{\mathcal{F}}(t)\bar{\epsilon}_{10}}. \tag{9.4}$$

In the experiment, $p_{\mathcal{T}}(t)$ and $p_{\mathcal{F}}(t)$ are directly measured. $p_{E,\mathcal{T}}$ is also available via post-selection. These can be used to extract parameters or be used to provide verification of our loss model. For example, using the measured decay of $p_{\mathcal{T}}(t)$ along with the value of γ_{vac} extracted from the $X^2\Sigma(v=0, N=1,3)$ lifetime data, we obtain a blackbody rate of $\gamma_{\text{BB,exp}} = 4.0(2)\text{s}^{-1}$, comparable to the blackbody theory prediction of $\gamma_{\text{BB,th}} = 3.4\,\text{s}^{-1}$ [187].

Early-Time Dynamics

At short times, the populations evolve linearly versus time, and we obtain

$$\begin{aligned} p_{\mathcal{T}}(t) &= s\left[1-(\gamma_{\text{vac}}+\gamma_{\text{BB}})t\right] \\ p_{\mathcal{F}}(t) &= s\eta\gamma_{\text{BB}}t, \end{aligned} \tag{9.5}$$

where s is the initial non-destructive survival probability. To first order in t, we obtain

$$p_{\text{E},\mathcal{T}}(t) = s\left[1-(\gamma_{\text{vac}}+\gamma_{\text{BB}})t + s\eta\gamma_{\text{BB}}\bar{\epsilon}_{10}t\right], \tag{9.6}$$

giving an erasure-excised population decay rate of

$$\gamma_{\text{p,E}} = -\frac{1}{s}\frac{dp_{\text{E},\mathcal{T}}(t)}{dt} = \gamma_{\text{vac}} + \gamma_{\text{BB}}(1-s\eta\bar{\epsilon}_{10}). \tag{9.7}$$

Note that $\gamma_{\text{p,E}}$, γ_{vac}, γ_{BB}, s, and $\bar{\epsilon}_{10}$ are all separately measured. Additional losses and imperfections can be lumped into η. We can therefore combine all imperfections such as imperfect identification ($\bar{\epsilon}_{10}$), imperfect erasure conversion, and blackbody equilibration into a single parameter η_{eff} and write

$$\gamma_{\text{p,E}} = -\frac{1}{s}\frac{dp_{\text{E},\mathcal{T}}(t)}{dt} = \gamma_{\text{vac}} + \gamma_{\text{BB}}(1-s\eta_{\text{eff}}). \tag{9.8}$$

f_{therm}	γ_{BB}	$\gamma_{\text{p,E}}$
Yes	Th	0.118(4)
Yes	Exp	0.107(5)
No	Th	0.105(4)
No	Exp	0.096(4)

Table 9.1: Erasure-corrected $N = 0$ population lifetime: Predictions for the erasure-corrected $N = 0$ population lifetime are given in the presence (Yes) or absence (No) of immediate blackbody population equilibration between $v = 0$ and $v = 1$ (f_{therm}), and using the theoretical (Th) or experimentally measured (Exp) blackbody excitation rate (γ_{BB}).

Fitting to our measured erasure-excised population decay data, we obtain $\eta_{\text{eff}} = 0.78(8)$ when using our measured value of $\gamma_{\text{BB,exp}} = 4.0(2)\text{s}^{-1}$. Using the theoretical value of $\gamma_{\text{BB,th}} = 3.4\,\text{s}^{-1}$ gives a similar value of $\eta_{\text{eff}} = 0.84(4)$.

Intermediate Time Dynamics

At intermediate times, blackbody vibrational excitations from $X^2\Sigma(v = 0)$ to $X^2\Sigma(v = 1)$ and spontaneous radiative decays back to $X^2\Sigma(v = 0)$ lead to a steady-state $X^2\Sigma(v = 1)$ fraction of

$$f_{\text{term}} = \frac{e^{-\hbar\omega_{01}/k_B T}}{1 + e^{-\hbar\omega_{01}/k_B T}}, \tag{9.9}$$

where $\omega_{01} = 2\pi \times 17.5\,\text{THz}$ is the vibrational splitting between $X^2\Sigma(v = 0)$ and $X^2\Sigma(v = 1)$ and $T = 295\,\text{K}$ is the ambient lab temperature. Numerically, the $v = 1$ fraction is $f_{\text{therm}} = 5.5\%$, and equilibration occurs at a rate of

$$\gamma_{\text{therm}} = 2\gamma_{\text{BB}} + \Gamma_{1,\text{rad}}, \tag{9.10}$$

where $\Gamma_{1,\text{rad}}$ is the $v = 1$ to $v = 0$ decay rate. Together, we obtain $\gamma_{\text{therm}} = 5.3\,\text{s}^{-1}$, corresponding to a characteristic timescale of $\tau_{\text{therm}} = 1/\gamma_{\text{therm}} \approx 190\,\text{ms}$.

Hence, for lifetime measurements that include wait times much longer than τ_{therm}, such as those presented in this chapter out to $t = 2\,\text{s}$, equilibration dynamics could be present. These, however, do not result in a substantial change in the estimated decay rates.

Comparison with Measurements

In this section, we discuss comparisons of our model with the measured population dynamics. Note that $\gamma_{\mathrm{p,E}}$, γ_{vac}, γ_{BB}, s, and $\bar{\epsilon}_{10}$ are all separately measured, and η is assumed to be unity since the vibrational repump is continuously applied.

We perform four estimates of $\gamma_{\mathrm{p,E}}$ that either assumes immediate equilibration of $p_{v=1}$ to $f_{\mathrm{therm}} = 5.5\%$ or no equilibration ($f_{\mathrm{therm}} = 0$) at all, along with either the theoretical value or experimentally extracted value for γ_{BB}. Specifically, we use the measured vacuum lifetime γ_{vac}, erasure identification error $\bar{\epsilon}_{10}$, and initial overall survival s, but use the theoretical value of $\eta = 1$.

The results are summarized in Table 9.1 and range from $0.096\,\mathrm{s}^{-1}$ to $0.118\,\mathrm{s}^{-1}$ with error bars of $\approx 0.05\,\mathrm{s}^{-1}$. These values are in tension with the measured erasure-corrected population lifetime of $\gamma_{\mathrm{p,E}} = 0.14(1)\,\mathrm{s}^{-1}$, suggesting some degree of loss during vibrational repumping. This reduces the overall conversion efficiency to $\eta \approx 85\%$.

Late-Time Dynamics

In this section, we present $N = 0$ population survival results with and without erasure excision out to long hold times ($t \leq 16\,\mathrm{s}$). In this study, we dither the $v = 1$ repump and apply a single erasure detection image at the end of the variable hold time. Although erasure excision improves the population survival at all times, the erasure-corrected population dynamics are no longer described by a simple exponential decay at all times (Fig. 9.9). This deviation from the early-time exponential decay dynamics arises due to population which cannot be repumped to the erasure flag manifold ($v = 0, N = 1$) arising from vacuum loss and multiple black-body excitation and decay processes.

We model the influence of erasure-flag population loss via a simplified loss model of population in $N = 0$ ($p_{|0\rangle}$) and population which can be repumped to the erasure-flag manifold ($p_{1,3}$). This model incorporates the measured loss from $p_{|0\rangle}$ without erasure excision ($\gamma_{m0} = (3.4\,\mathrm{s})^{-1}$), the measured erasure flag loss ($\gamma_{m1,3} = (13.5\,\mathrm{s})^{-1}$), and the extracted

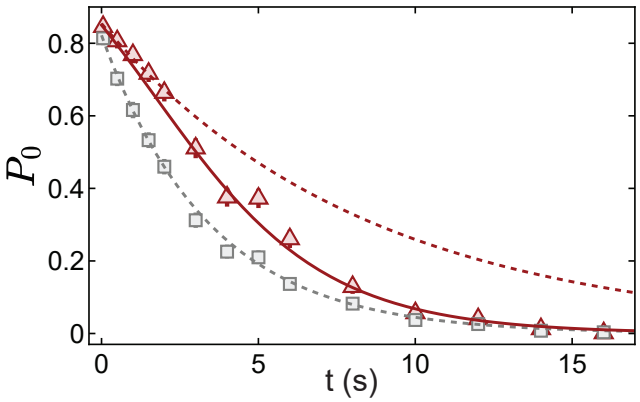


Figure 9.9: Long-time $N = 0$ population survival: Although $N = 0$ population survival improves upon erasure excision (red triangles) compared to without excision (gray squares), erasure-corrected population dynamics is non-exponential at late times. To illustrate this deviation, we fit the (non)erasure-corrected data for $t \leq 2\,\mathrm{s}$ to an exponential decay, shown as the red (gray) dashed curve. Disagreement between the fit and data only appears for the erasure-corrected data, which we attribute to population loss in the erasure flag manifold. A model which incorporates the separately characterized vacuum loss rate and erasure-flag loss rate (red solid curve) captures the erasure-corrected population dynamics to a better extent.

vacuum loss ($\gamma_{\mathrm{vac}} = (21.3\,\mathrm{s})^{-1}$). The population loss prediction is obtained from solutions to the differential equations describing the loss processes

$$\begin{aligned} \dot{p}_{|0\rangle} &= -\,\gamma_{m0}\, p_{|0\rangle} \\ \dot{p}_{1,3} &= (\gamma_{m0} - \gamma_{vac})\, p_{|0\rangle} - \gamma_{m1,3}\, p_{1,3}, \end{aligned} \tag{9.11}$$

which are incorporated into the expression describing erasure conversion and detection

$$p_E = \frac{s\, p_{|0\rangle}}{1 - s\, f_{\mathrm{Er}}\, p_{1,3}}. \tag{9.12}$$

For our prediction, we take $s = 0.85$ and $f_{\mathrm{Er}} = 0.8$.

We see good agreement between our model and the erasure-corrected population loss data (Fig. 9.9), supporting our suspicion that loss from the erasure-flag manifold is the mechanism behind the observed non-exponential erasure-corrected population dynamics.

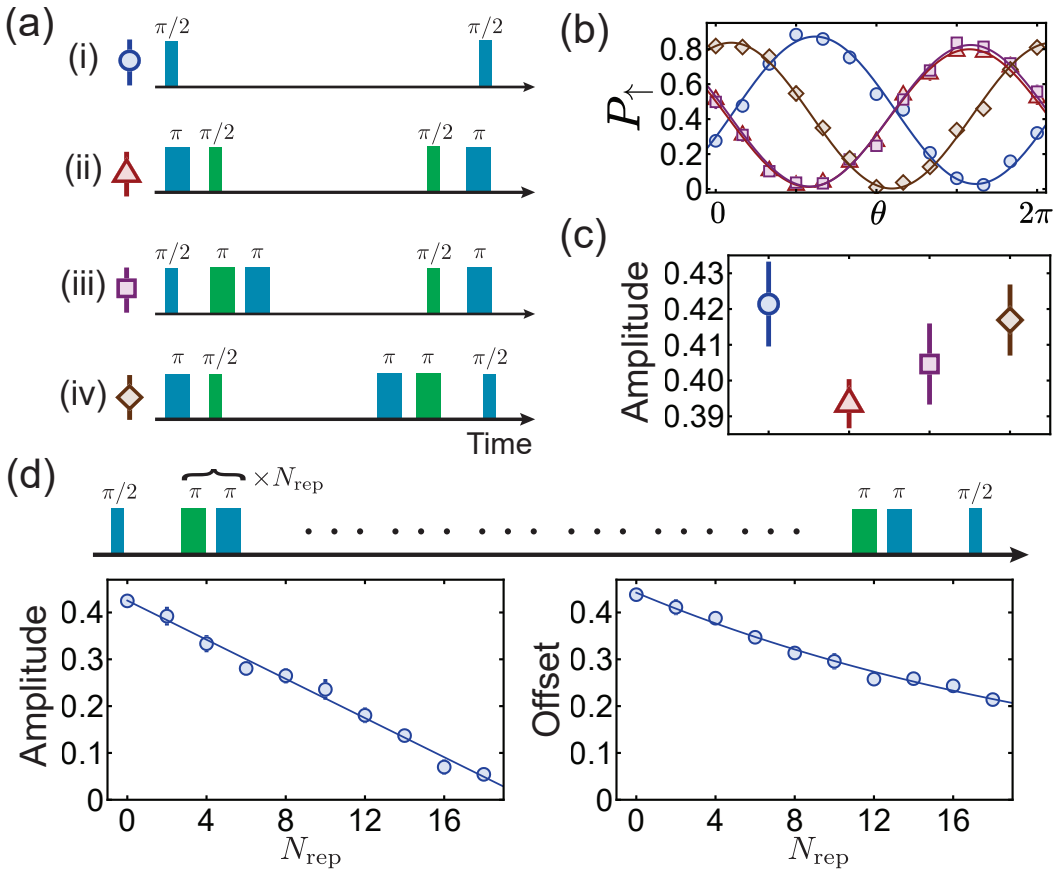


Figure 9.10: Coherent Qubit Transfer Between Rotational and Hyperfine Encodings: (a) The four Ramsey sequences (i-iv) are used to probe various coherences between the three states involved in the two qubit encodings. Blue (green) boxes depict microwave pulses on the rotational encoding $|\uparrow\rangle$-$|\downarrow\rangle$ (hyperfine encoding $|1\rangle$-$|0\rangle$). The sequences (i-ii) probe rotational coherence and hyperfine coherence, respectively. Sequence (iii, iv) verify the ability to transduce a quantum state between the two encodings. (b) $P_\uparrow$ versus the phase θ of the final $\pi/2$ pulse for the four Ramsey sequences. The corresponding markers are indicated in (a). (c) Amplitude of $P_\uparrow$ Ramsey fringes for the four Ramsey sequences. The corresponding markers are indicated in (a). (d) Characterizing efficiency of transduction. A superposition initially created in the rotational encoding is repeatedly transferred to and from the hyperfine encoding using a Raman and microwave π-pulse. Amplitude and offset of Ramsey fringes versus the number of transfers $N_{\rm rep}$.

9.8 Coherent Transduction Between Qubit Encodings

Although it was not explicitly used in the context of this work, coherent transduction between the rotational qubit and hyperfine qubit was also realized and characterized during our erasure investigations. In this section, we provide supplemental information and data

showing how the quantum information can be coherently transferred between the rotational encoding, where long-range electric dipolar interaction are present, and the new hyperfine qubit, where interactions are extinguished and long coherence times can be maintained.

The building blocks for transferring a qubit between the rotational encoding and the hyperfine encoding are π-pulses along the Raman and microwave transitions (Fig. 9.10(a)). For this data, due to technical limitations, Raman light detuned from the X-B transition was used. Specifically, the Raman light is detuned halfway between the $X^2\Sigma(N=0) \rightarrow B^2\Sigma(N=1, J=1/2)$ and $X^2\Sigma(N=0) \rightarrow B^2\Sigma(N=1, J=3/2)$ transitions. This results in a single-photon detuning of 500 MHz for optical transitions resonant with the hyperfine qubit states. Q_π for this scheme is measured to be 37(3).

We characterize the ability to transfer arbitrary states between the rotational ($|\uparrow\rangle$-$|\downarrow\rangle$) and hyperfine encoding ($|\downarrow\rangle$-$|0\rangle$) by comparing single-particle coherence after four different Ramsey sequences: two in which no transfer occurs, and two in which a single transfer occurs (Fig. 9.10(a)). We find that the decrease in single-particle coherence is consistent with zero after one round of transfer (Fig. 9.10(b,c)). To more precisely estimate the transfer efficiency, we measure single-particle coherence as a function of repeated transfers between the two qubit encodings (Fig. 9.10(d)). From these measurements, we find a transfer fidelity of $f = 0.951(2)$, limited by off-resonant scattering of the Raman light. We find that off-resonant scattering accounts for 89(9)% of the infidelity, with the remaining amount consistent with the separately measured microwave transfer infidelity. We therefore expect the transfer fidelity to improve to $f \approx 0.995$ when using optimally detuned Raman light on the X-A transition.

9.9 Measurement-Enhanced Cooling Protocols

In this section, we extend measurement-enhanced preparation protocols to decrease thermal excitations of tweezer-trapped molecules. These investigations build on techniques developed

during our Raman Sideband Cooling (RSC) investigation (see Ref. [5] and Yukai's Thesis [90] for specific details of the setup), and a tweezer light generation upgrade employing two independent 2D-AODs, which is detailed in Section 3.4.

In the first investigation, we utilize the techniques developed during our RSC investigation to selectively transfer thermally excited molecules to a state that is bright during rapid imaging. The cold molecules not transferred to this states are shelved into $|-\rangle$. By post-selecting away hot molecules detected during the rapid image, the remaining should be colder.

In the second investigation, we utilize two independent AODs to transfer thermally excited molecules from the main tweezer array to an auxiliary empty array. At an appropriate separation between the loaded and empty tweezer, only hot molecules have sufficient kinetic energy to hop into the empty tweezer. After locally shelving the initially loaded main tweezer to a dark state in $N = 0$, a rapid image detects population in the auxilary tweezer. After post-selecting on tweezer pairs where the molecule did not tunnel (ie, an empty auxiliary tweezer), we maintain comparable single-particle state preparation fidelities and observe that the molecules are substantially less likely to thermally hop.

9.9.1 Measurement-Enhanced Sideband Cooling

The investigation presented in this section was motivated in part by the discussion and implementation of measurement-assisted cooling reported in Refs. [173, 174]. In our implementation of Raman sideband cooling (RSC) in Ref. [5], a dominant source of heating arises from the repeated scattering of photons during the optical pumping step used to reinitialize molecules into the starting state of the cooling cycle. Notably, this initial state, $|D'\rangle$, is also the first state involved in the measurement-enhanced state preparation protocol developed in this chapter. This overlap suggests a natural pathway to reduce heating by avoiding unnecessary optical pumping for molecules that are already near the ground motional state.

Building on this idea, we explored a protocol where population in all but the motional ground state along one tweezer axis is selectively transferred to a second internal state used in RSC, which is conveniently bright to resonant imaging. In this scheme, molecules remaining in $|D'\rangle$ correspond to a colder sub-ensemble, which are transferred to $|-\rangle$ via a MW pulse. The hotter molecules, having been transferred to the bright state, can then be identified and post-selected. In this way, the cold fraction of the ensemble is preserved while eliminating the primary source of heating associated with repeated optical pumping cycles.

Preliminary investigations of this protocol revealed qualitative signatures consistent with cooling. However, quantitative thermometry proved challenging in our apparatus. In particular, long magnetic field settling times led to the accumulation of a background molecular signal, complicating the extraction of reliable temperature estimates. After subtracting this background contribution, sideband thermometry indicated a reduction in temperature along one axis from $\bar{n}_x = 1.5(7)$ to $\bar{n}_x = 0.7(3)$. While these results suggest that some degree of cooling was achieved, there was substantial room for improvement in both cooling performance and thermometry.

Ultimately, this line of investigation was not pursued further. A practical implementation of this protocol would ideally begin with an already cold ensemble ($\bar{n} \sim 1$) and apply measurement-enhanced cooling sequentially along all three tweezer axes, requiring intermediate imaging steps for each direction.

9.9.2 Measurement-Enhanced Suppression of Thermal Tunneling

After installing two independent 2D-AODs (see Section 3.4.1 for details), we explored whether we could observe stronger dipolar interactions. This main + interlaced array configuration should enable exploring smaller frequency separations between tweezers without the effects of intermodulation loss. However, early measurements revealed an unexpected degradation in performance. When comparing state preparation fidelities with and without reducing the separation between tweezer pairs generated by the two AODs, we observed a

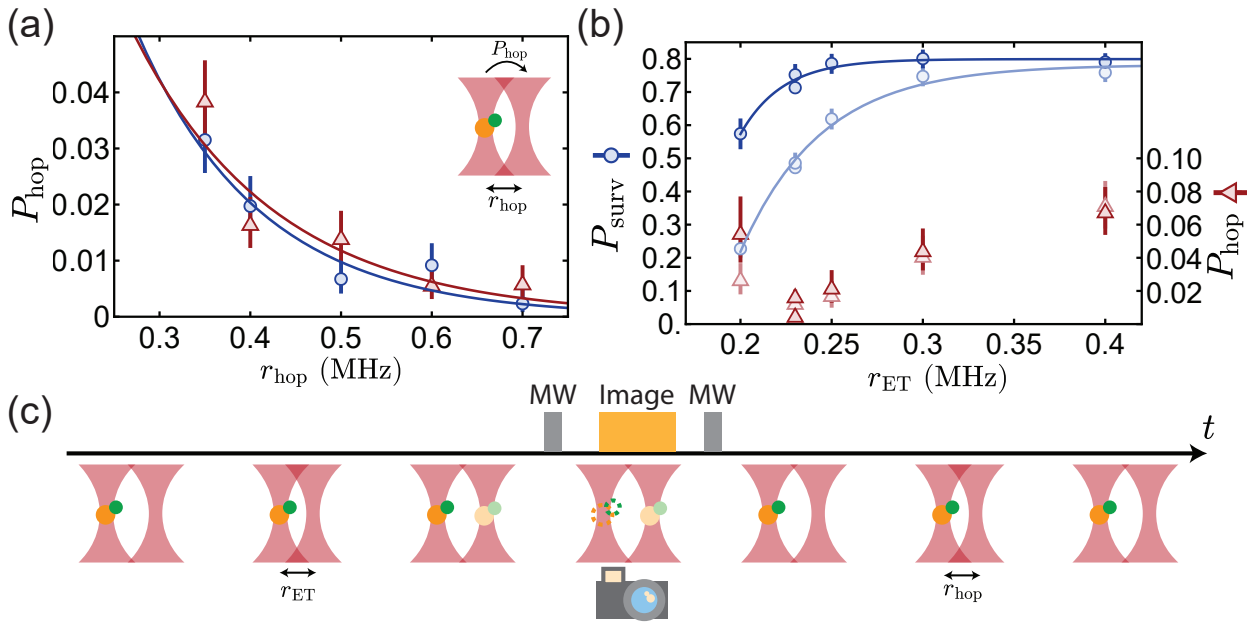


Figure 9.11: Suppressing Thermal Tunneling via Mid-Sequence Measurement: (a) The probability of a molecule hopping from a loaded tweezer to an empty tweezer (P_{hop}) is probed as a function of tweezer pair separation (r_{hop}). The hopping probability does not depend on whether both tweezers are generated using the main array (blue circles) or one from each array (red triangles). Solid lines (exponential fits) are guides to the eye. (b) The probability for a molecule to remain in the initially loaded tweezer (P_{surv}) decreases with r_{ET}. P_{surv} with (without) post-selecting on thermal tunneling is shown by dark (light) blue circles, with lines as guides to the eye. The hopping probability (red triangles) decreases with r_{ET}, indicating successful elimination of the hottest molecules during the r_{ET} step. (c) Detailed sequence for the investigation in (b), which is described in the text.

pronounced drop in population survival at small separations. This behavior was initially puzzling, as the removal of inter-modulation should have mitigated population loss.

The origin of this effect became clear through a more controlled diagnostic measurement. Specifically, we repeated the experimental sequence with only a single tweezer from each pair loaded. As shown in Fig. 9.11(a), the probability for a molecule to hop from the initially occupied tweezer into the neighboring empty site becomes appreciable when the frequency spacing between the pair is reduced below approximately 0.4 MHz (spatial separation goes as ~ 4.2 μm/MHz). Notably, this hopping probability is independent of whether the two tweezers are generated by the same AOD or the main + interlaced configuration, pointing

towards a mechanism in which thermally excited molecules are able to hop between the two tweezers; that is, the molecule's classical trajectory allows for both traps to be explored.

This thermal hopping process presents a significant challenge, particularly for experiments in one-dimensional chains and two-dimensional lattice geometries. When a molecule hops into a neighboring site that is already occupied, there is a high probability of light-assisted or inelastic collisions, resulting in pairwise loss. As the lattice coordination number increases, the thermal hopping likelihood grows. Minimizing these hopping processes is therefore essential for preserving high filling fractions in many-body molecular tweezer array experiments.

A straightforward strategy to reduce thermal hopping is to breifly reduce the depth of the optical tweezers during state preparation, thereby preferentially spilling hot molecules. The tweezer depth would then returned to the magic depth for the quantum simulation part of the experiment. While this strategy is effective at suppressing tunneling, the tweezer spilling process is inherently stochastic and hence randomly introduces holes to the system. Consequently, this spilling protocol is only suitable in scenarios where the underlying physics is robust to randomly distributed holes.

A more controlled approach leverages the measurement and feedback framework developed in this chapter. In particular, we aim to selectively transfer hot molecules into an auxiliary array for detection. Then, either the remaining cold tweezer arrays sites can be rearranged into the targeted defect-free pattern, or the hot molecules can be re-cooled.

To implement a proof-of-principle demonstration of the ingredients for this protocol, we follow the sequence illustrated in Fig. 9.11(c). A tweezer from the main array is first loaded with a molecule prepared in $|\uparrow\rangle$, while the interlaced array remains empty. The separation between the tweezer pairs is reduced to r_{ET}, enabling preferential hopping of hot molecules into the interlaced array. The arrays are subsequently separated, and a site-selective microwave transfers the molecule in the main array (if it didn't tunnel) into $|\downarrow\rangle$, which is dark to resonant imaging. Imaging is then performed to detect if the molecule has

hopped into the interlaced array, as well as any imperfections in site-selective MW transfer. Finally, molecules successfully transferred to $|\downarrow\rangle$ are returned to $|\uparrow\rangle$ via a MW pulse.

To verify the effectiveness of this protocol, we then apply the hopping measurement used in Fig. 9.11(a), fixing the probe separation at $r_{\mathrm{tun}} = 0.3$ MHz. Fig. 9.11(b) shows the survival and tunneling probabilities as a function of the initial pair separation r_{ET} used to remove hot molecules. Two key features emerge from the data. First, the survival probability of molecules in the main array returns close to the initial state preparation fidelity (P_{surv} at large r_{ET}) after post-selecting on tunneling evens. Second, the hopping probability is substantially reduced for $r_{\mathrm{ET}} \approx 0.25$ MHz. The increase in hopping at the closest measured separation likely arises from non-adiabatic heating of the molecule during the hot-molecule transfer step.

Together, these results constitute a proof-of-principle demonstration that thermal hopping can be suppressed using a measurement-based protocol. Importantly, this approach should be able to reduce hopping-induced loss while introducing few defects, making it well-suited for applications in quantum simulation experiments where thermal hopping is undesired but high filling fractions are desired.

We also note that the thermally excited molecules removed during this protocol are typically difficult to cool via RSC protocols in the first place, as they explore non-harmonic regions of the tweezer. Thus, this protocol could assist in producing colder ensembles that are easier to cool using RSC. Additionally, this protocol only relies on site-selective population transfer between a bright and dark state, enabling cooling tweezer-trapped atoms or molecules which do not posses the properties or internal states necessary to implement RSC.

9.10 Discussion and Outlook

Our error mitigation work opens several possibilities. First, state preparation fidelities of $\approx 95\%$ open the door to quantum simulation of many-body Hamiltonians with low defect

rates. In particular, for mesoscopic systems of $\mathcal{O}(10)$ particles, we can post-select on perfectly prepared arrays with a tolerable level of data reduction.

Second, our work lays the foundations for exploring erasure conversion in the context of quantum error correction with molecular qubits. For quantum error correction, erasure conversion is useful when the dominant errors - often from 2-qubit gates - are converted and detected [172]. Our current work concerns erasure conversion of a significant source of leakage errors in non-interacting hyperfine qubits. For quantum memories stored in these qubits, our work could thus substantially mitigate *idling errors*. Beyond idling errors, our erasure conversion approach could be extended to mitigate 2-qubit gate errors in specific regimes. To date, entangling 2-qubit gates in molecular tweezer arrays have all relied on the electric dipolar interaction, whose strength depends sensitively on molecular separation. In several experiments including ours [4, 87, 164], 2-qubit gate fidelities were limited by thermal motion within tweezers, which led to variations in the interaction strength and consequently gate errors. Work from Ref. [163] substantially reduces this source of gate errors by placing molecules far apart, where interaction strength variations due to motion becomes small. However, at these far separations, gate times became significantly increased, which led to significant leakage errors ($\sim 5\%$) arising from off-resonant scattering of trapping light. In this far-separated regime, leakage was the dominant source of gate infidelity. Because leakage errors are erasure-convertible, molecular 2-qubit gates in the far separated regime are a clear use case where gate fidelities could be improved using erasure conversion.

Third, the composite erasure detection scheme used in our erasure conversion work could open the door to mid-circuit measurements in molecular tweezer arrays, a powerful tool for quantum error correction and exploring exotic many-body phases of matter. Specifically, our composite erasure detection shows that site-resolved measurements of bright state populations can be made without affecting quantum information encoded in dark states. By combining this readout capability with site-selective transfer from the hyperfine qubit

encoding into bright states implementable via local light shifts, site-selective mid-circuit measurements with crosstalk errors at the 10^{-3} level could be achieved.

In addition to the above possibilities opened by our error mitigation results, the new technical capabilities developed in our work also open additional possibilities. First, our new non-interacting hyperfine qubit encoding can be integrated with the previously used interacting rotational encoding, directly enabling applications using 3-level systems that include quantum information processing with qutrits, simulation of $S = 1$ quantum spin models, bosonic t-J models [189], and lattice gauge theory models [190]. Second, our work on detecting blackbody excitations is directly relevant to investigations of molecule-based temperature standards [191]. Third, our work on enhanced tweezer preparation and catching blackbody errors could aid molecular tweezer-based precision measurement experiments [54, 88, 192], both through reducing spatial disorder in molecular arrays and through using metrologically useful entangled states such as spin-squeezed states [167, 193] that can be naturally generated in interacting defect-free arrays of many molecules [194, 195].

Chapter 10

Generating Metrologically Useful Spin-Squeezed States

A diatomic molecule is 3dB atoms too many.

– Arthur Shawlow, adapted

The developments presented in Chapter 9 – in particular, the ability to generate defect-free and internally pure arrays with high fidelity – position our molecular tweezer arrays squarely within the many-body regime. While the precise boundary between few-body and many-body physics is somewhat subjective, a useful and geometry-dependent definition is based on the relative size of the system's bulk compared to its boundary. In one dimension, the boundary consists of only two sites (the ends of the chain). Under this generous definition, an array of five molecules is many-body. The experiments presented in this chapter employ arrays of eight molecules, placing the system well within this many-body regime.

A natural starting point for investigating many-body physics in this platform is the native long-range spin-exchange Hamiltonian, which we characterized in our investigations from Chapter 8. For the geometry used in this work, this takes the form of a ferromagnetic

XX model with couplings that decay as $1/r^3$. Explicitly, the Hamiltonian can be written as

$$H_{XX} = \sum_{i<j} \frac{J}{|i-j|^3} \left(S_i^x S_j^x + S_i^y S_j^y \right), \tag{10.1}$$

where S_i^α are spin-1/2 operators acting on site i. Building upon this native interaction, we employ Floquet Hamiltonian engineering techniques, outlined in Ref. [162] and discussed in Section 10.2, to access a broader class of spin models. In particular, we realize XXZ Hamiltonians of the form

$$H_{XXZ} = \sum_{i<j} \frac{J}{|i-j|^3} \left(S_i^x S_j^x + S_i^y S_j^y + \Delta S_i^z S_j^z \right), \tag{10.2}$$

with tunable anisotropy Δ. More generally, this Floquet Hamiltonian engineering approach enables XYZ spin models to be generated, which host rich dynamical phenomena such as quantum walks of spins, magnon bound states, and coherent creation and annihilation of spin pairs. The investigations of the XYZ model are not the focus of this chapter; see Ref. [8] and Ref. [90] for more details.

In this chapter, we instead focus on the generation of entangled states useful for quantum-enhanced metrology. In breif, entanglement provides a route to surpass a fundamental limit of quantum sensing with uncorrelated sensors. A particular class of entangled states, so-called spin-squeezed states, utilize entanglement to reduce variance along one collective spin quadrature at the expense of increasing variance in a conjugate quadrature, all while maintaining a large total spin length. The reduced variance along one quadrature enhances sensitivity to global fields in a Ramsey-type measurement sequence.

A key development enabling our investigations of quantum-enhanced metrology with molecules is spin-resolved imaging (SRI), which significantly enhances the readout capabilities of our molecular tweezer array (see Section 10.3). By exploiting the rich internal rotational structure of our molecules, this protocol allows us to distinguish between the two spin states as well as empty tweezers.

Using these tools, in Section 10.4 we demonstrate that, beginning with a product state of eight molecules, evolution under the XX Hamiltonian generates a spin-squeezed state with 3.0(3) dB of metrological gain. This level of squeezing corresponds to a sensitivity comparable to that of an unentangled ensemble of $\sim$ 16 molecules. We also investigate the role of finite-range interactions in shaping the structure of the generated entanglement, probed via spatially resolved spin-spin correlations of the spin-squeezes states. In contrast to all-to-all interacting models, which produce spatially uniform correlation maps, the $1/r^3$ XX model generates squeezed states with short-range spin-spin correlations.

The consequences of the spatial structure of these correlations are explored in Section 10.5. By partitioning the system into two sub-ensembles, we show that the state is capable of differential sensing with precision below the standard quantum limit. We also find that the partition into two sub-ensembles is non-separable, revealing entanglement between spatially separated regions of the system. We further show that a stronger form of quantum correlations are present, which are capable of EPR steering between the two sub-ensembles. A detailed discussion of these measurements and their interpretation is provided in Section 10.5.1.

We then extend our investigation beyond the XX model by introducing non-zero Ising anisotropy (Δ). As discussed in Section 10.6, Floquet engineering allows us to tune Δ up to and beyond the Heisenberg point ($\Delta = 1$). In several theoretical works, it was shown that approaching the Heisenberg point is expected to improve spin squeezing and drive the system toward a regime with effective all-to-all interactions. Experimentally, while we can still generate squeezed states for all Δ explored, we do not observe an improvement in metrological gain as $\Delta \to 1$. We attribute this to imperfections in the Floquet sequence and to the longer evolution times required to generate squeezing. Nevertheless, we do observe a clear transition from short-range correlated squeezed states near $\Delta = 0$ to states exhibiting nearly all-to-all correlations as $\Delta \to 1$.

Finally, in Section 10.7, we demonstrate coherent transduction of the squeezed state from a rotational qubit encoding, where interactions are present, to a hyperfine encoding, where interactions are extinguished. We find that the state retains metrological advantage following transduction, and remains squeezed for approximately 50 ms. Furthermore, this state maintains a relative advantage over an unentangled state for over 100 ms. This capability highlights the potential of combining controllable interactions to generate useful quantum entanglement in a many-body system with long-lived and non-interacting encodings useful for quantum-enhanced sensing.

The work presented in this thesis will be published in a forthcoming manuscript.

10.1 Introduction to Quantum-Enhanced Metrology

The central task in quantum sensing is to estimate the strength of a weak external perturbation acting on a quantum system. For sufficiently small perturbations, the sensitivity of a given protocol is determined by how strongly the quantum state responds to the perturbation, as well as the level of noise in the measurement. Intuitively, one seeks to prepare quantum states whose evolution under the perturbation produces a large and measurable change in an observable, while simultaneously minimizing noise (both technical and fundamental) incurred while measuring this observable.

A canonical sensing protocol can be illustrated using a single two-level system with basis states $|\uparrow\rangle$ and $|\downarrow\rangle$. The sensing task is to measure a small energy shift corresponding to a perturbation of the form δS_z. The optimal single-qubit protocol takes the form of a Ramsey interferometer. Starting from the state $|\downarrow\rangle$, a $\pi/2$ pulse about $\hat{x}$ prepares a coherent superposition oriented along the $\hat{y}$-axis of the Bloch sphere,

$$\frac{1}{\sqrt{2}}\left(|\downarrow\rangle - i|\uparrow\rangle\right).$$

The system then evolves for a time t under the perturbation, acquiring a relative phase,

$$\frac{1}{\sqrt{2}}\left(|\downarrow\rangle - ie^{-i\delta t}|\uparrow\rangle\right).$$

A second $\pi/2$ pulse maps this phase onto population, yielding a measurable signal in S_z:

$$\langle S_z\rangle = \frac{1}{2}\cos(\delta t).$$

Thus, the perturbation strength is converted into a population difference. For a static perturbation strength, the sensitivity of this protocol can always be increased by extending the measurement time t, assuming a perfect quantum system with no decoherence or depolarization.

This protocol generalizes to an ensemble of N non-interacting qubits by initializing the spins in $|\downarrow\rangle^{\otimes N}$ and applying the Ramsey sequence in parallel. Defining collective spin operators $S_\alpha = \sum_{i=1}^{N} S_i^\alpha$, the measured signal becomes

$$\langle S_z\rangle = \frac{N}{2}\cos(\delta t).$$

At this point, it is important to note that, for small perturbations $\delta \ll 1$, the measurement signal is given by the derivative of the observable with respect to the perturbation strength. Thus, for this example, we have $\frac{\partial}{\partial\delta}\langle S_z\rangle = N/2$. However, a good sensor must not only maximize signal, but also minimize noise. In this case, noise arises from quantum projection noise (QPN), reflecting the probabilistic outcome of measuring each spin in the S_z basis. For uncorrelated particles, each spin contributes a variance of $1/4$, leading to a total variance

$$\mathrm{Var}(S_z) = \frac{N}{4}.$$

As a result, the signal-to-noise ratio scales as $\sqrt{N}$, and the uncertainty in estimating δ scales as $1/\sqrt{N}$. This scaling defines the standard quantum limit (SQL), which represents the best achievable sensitivity using unentangled particles.

To quantify metrological performance independent of particle number, one introduces the Wineland spin squeezing parameter,

$$\xi^2 = \frac{N \, \min_\theta \mathrm{Var}(S_\theta)}{|\langle S_y \rangle|^2}, \tag{10.3}$$

where $S_\theta = S_z \cos\theta + S_x \sin\theta$ defines a rotated measurement axis. Product states saturate the SQL with $\xi^2 = 1$, while states with $\xi^2 < 1$ exhibit enhanced metrological sensitivity. One class of metrologically useful states, so-called spin-squeezed states, achieve $\xi^2 < 1$ by reducing quantum projection noise along one collective spin quadrature while maintaining a large mean spin length. The reduction in noise along one quadrature is necessarily accompanied by increased fluctuations in the conjugate quadrature, consistent with the Heisenberg uncertainty principle.

While spin-squeezed states provide a practical route to quantum-enhanced sensing, they do not exhaust the set of useful entangled states. For example, Greenberger–Horne–Zeilinger (GHZ) states,

$$|\mathrm{GHZ}\rangle = \frac{1}{\sqrt{2}} \left(|\downarrow\rangle^{\otimes N} + |\uparrow\rangle^{\otimes N} \right),$$

achieve a phase sensitivity scaling as $1/N$, known as the Heisenberg limit. However, this enhanced sensitivity is revealed through measurements of the parity of S_z, rather than simply $\langle S_z \rangle$. As a result, the Wineland squeezing parameter does not fully capture the metrological usefulness of GHZ states.

A more general framework for quantifying sensitivity is provided by the quantum Fisher information (QFI). For a pure state $|\psi\rangle$ subjected to unitary evolution generated by $\hat{\mathcal{O}}$, the QFI is given by

$$F_Q[\hat{\mathcal{O}}] = 4 \, \mathrm{Var}(\hat{\mathcal{O}}). \tag{10.4}$$

The QFI characterizes the sensitivity of the quantum state to $\hat{\mathcal{O}}$ by quantifying how rapidly the state evolves under an infinitesimal application of $\hat{\mathcal{O}}$. More precisely, it determines the statistical distinguishability between nearby quantum states $|\psi\rangle$ and $e^{-i\hat{\mathcal{O}}\delta}|\psi\rangle$, optimized over all possible measurements. In this sense, a larger QFI implies that the application of $e^{-i\delta\hat{\mathcal{O}}}$ produce mores distinguishable measurement outcomes, and therefore $\hat{\mathcal{O}}$ can be estimated with higher precision.

The QFI sets a fundamental limit on parameter estimation via the quantum Cramér–Rao bound,

$$\Delta\theta \geq \frac{1}{\sqrt{F_Q[\hat{\mathcal{O}}]}}. \tag{10.5}$$

Within this framework, and applied to sensing S_z perturbations ($\hat{\mathcal{O}} = S_z$), product states are characterized by $F_Q \propto N$, while maximally entangled states such as GHZ states achieve $F_Q \propto N^2$. The QFI therefore provides a unified framework to evaluate the best-possible performance of sensing S_z. Notably, although the FQI can indicate that a certain measurement sensitivity can be attained with a given state, QFI provides no indication on how that measurement should be done. Thus, from a practical point of view, the QFI helps evaluate how far away from optimal a given sensing protocol is.

The quantum Fisher information can be directly related to the Wineland spin squeezing parameter, providing a useful bridge between these two metrological figures of merit. Applied to a spin-squeezed state, the Heisenberg uncertainty relationship gives

$$\mathrm{Var}[S_\theta]\,\mathrm{Var}[S_{\theta+\pi/2}] \geq |\langle S_y\rangle|^2/4$$

This allows one to bound the QFI as

$$F_Q[S_z] \geq \frac{|\langle S_y\rangle|^2}{\mathrm{Var}(S_\theta)}, \tag{10.6}$$

where θ is chosen to minimize $\mathrm{Var}[S_\theta]$, and hence also maximize $\mathrm{Var}[S_{\theta+\pi/2}]$. Comparing with the definition of ξ^2 yields the bound

$$\frac{F_Q[S_z]}{N} \geq \frac{1}{\xi^2}. \tag{10.7}$$

This inequality shows that any spin-squeezed state with $\xi^2 < 1$ necessarily has $F_Q > N$, and is therefore metrologically useful. More generally, it establishes that spin squeezing provides a sufficient condition for enhanced quantum Fisher information, and thus metrological gain in a quantum sensing application.

An important aspect of quantum-enhanced metrology is its direct connection to entanglement. Both the Wineland squeezing parameter and the quantum Fisher information serve as witnesses of multipartite entanglement. In particular, states with $\xi^2 < 1$ are necessarily entangled, while bounds on the quantum Fisher information can be used to infer the entanglement depth of the system, i.e., the minimum number of particles that are genuinely entangled. For example, a value of $F_Q > kN$ certifies at least $(k+1)$-particle entanglement. In this sense, improved metrological sensitivity is not merely a practical advantage, but also a direct signature of nonclassical correlations within the system.

This connection to entanglement motivates a deeper investigation into the structure of correlations present in spin-squeezed states. Beyond global figures of merit such as ξ^2 or F_Q, one can probe how entanglement is distributed spatially and whether the system can be partitioned into separable or non-separable subsystems. Such considerations naturally lead to questions of entanglement depth, the spreading of correlations, and stronger forms of quantum correlations such as Einstein–Podolsky–Rosen (EPR) steering. These concepts, which are often associated with many-body physics and quantum information science, are directly relevant in the context of quantum sensing. Indeed, the generation of spin-squeezed states provides a platform not only for enhanced metrology, but also for exploring the rich in-

terplay between entanglement, correlations, and collective quantum dynamics in interacting many-body systems.

10.2 Floquet Engineering XXZ Models

In this section, we briefly outline how XXZ spin models are generated via Floquet Hamiltonian engineering, and our procedures to validate the generation of the targeted Hamiltonian. Full details can be found in Ref. [8, 90].

10.2.1 Pulse Sequence to Engineer XYZ Models

For our investigations of spin squeezing in the XXZ model, as well as our investigations into coherent dynamics in the XYZ model reported in Ref. [8], we employ Floquet Hamiltonian engineering to transform the native XX interactions into a more general anisotropic spin model. Specifically, we can realize an effective Hamiltonian of the form

$$H_{XXZ} = \sum_{i<j} \frac{1}{|i-j|^3} \left(J_x S_i^x S_j^x + J_y S_i^y S_j^y + J_z S_i^z S_j^z \right), \tag{10.8}$$

where the relative strengths of the spin couplings along different axes can be tuned by adjusting pulse sequence parameters. This Hamiltonian can equivalently be written as

$$H_{XYZ} = \sum_{i<j} \frac{J}{|i-j|^3} \left[\frac{1}{2}(S_i^+ S_j^- + S_i^- S_j^+) + \frac{\gamma}{2}(S_i^+ S_j^+ + S_i^- S_j^-) + \Delta S_i^z S_j^z \right], \tag{10.9}$$

with parameters defined as $J = (J_x + J_y)/2$, $\Delta = 2J_z/(J_x + J_y)$, and $\gamma = (J_x - J_y)/(J_x + J_y)$.

The accessible parameter space of this engineered Hamiltonian is constrained by the underlying native XX interaction strength J_0. In particular, the Floquet protocol enforces $J_x + J_y + J_z = 2J_0$ with $0 \leq J_\alpha \leq J_0$, which translates to the bounds $0 \leq \Delta \leq 2$ and $|\gamma| \leq \Delta/2$. In this chapter, we focus on the case $\gamma = 0$, corresponding to the XXZ model. In practice, the MW pulse durations slightly restrict the range of accessible Δ to $0 \leq \Delta \lesssim 1.8$.

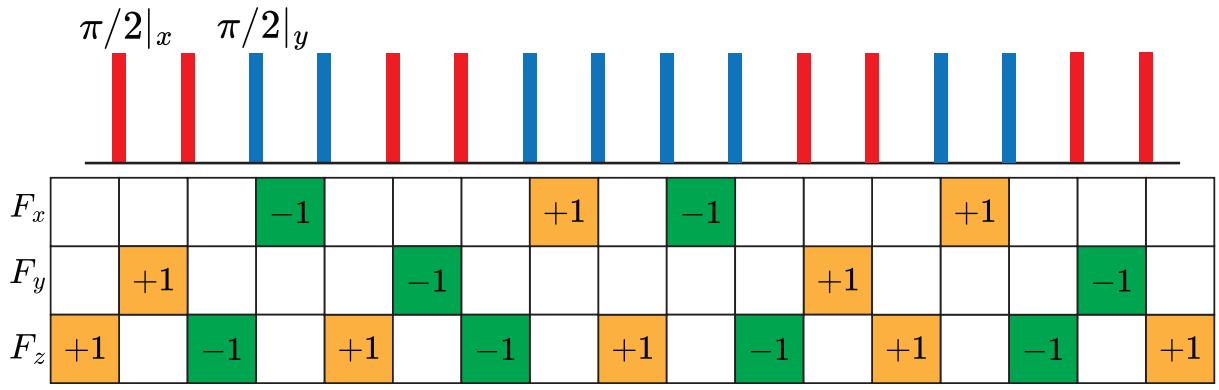


Figure 10.1: XY8-XYZ Floquet-engineering sequence is obtained from XY8 by splitting each π into two $\pi/2$ pulses. The symmetric duration of time spent in the ± 1 frames illustrates that this sequence is robust to static detuning errors.

Our Floquet engineering protocol is implemented by periodically repeating a sequence of $\pi/2$ pulses applied along the $\hat{x}$ and $\hat{y}$ axes of the Bloch sphere. The sequence is inspired by the well-known XY8 dynamical decoupling protocol; starting from the XY8 sequence, each π pulse is decomposed into two $\pi/2$ pulses. We refer to this sequence as XY8-XYZ. In its most general form, the sequence contains 16 free-evolution intervals between pulses. However, to preserve robustness against fluctuating background fields and pulse-area errors, we restrict the protocol to a symmetric form characterized by only three independent parameters.

Conceptually, the pulse sequence can be understood as periodically toggling between three distinct interaction frames. These frames are defined by which axis of the original Bloch sphere is mapped onto the effective $\hat{z}$ axis during a given segment of the evolution. While the sign of this mapping plays a role in robustness to fluctuations in S_z, the sign of the frame does not affect the engineered Hamiltonian for native XX interactions. From this perspective, the sequence effectively relabels the axes of the interaction: starting in the original frame, the Hamiltonian has the form $XX + YY$. A $\pi/2$ rotation about $\hat{x}$ maps $\hat{y} \to \hat{z}$ and $\hat{z} \to -\hat{y}$, yielding an $XX + ZZ$ Hamiltonian. Similarly, a $\pi/2$ pulse about $\hat{y}$ maps $\hat{z} \to \hat{x}$ and $\hat{x} \to -\hat{z}$, resulting in a $YY + ZZ$ Hamiltonian.

For experimental simplicity and robustness, we parameterize the sequence using three durations, τ_x, τ_y, and τ_z, corresponding to the time spent in each of the three frames (defined from pulse center to pulse center). This reduced parameterization retains the essential tunability of the Hamiltonian while suppressing sensitivity to miscalibrations and low-frequency noise. As illustrated in Fig. 10.1 using the visualization introduced in Ref. [162], the sequence symmetrically samples positive and negative realizations of each frame. As a result, it is first-order insensitive to global S_z fields arising from slowly varying magnetic fields or microwave detuning errors. This robustness is particularly important for generating spin-squeezed states with sub-SQL performance, since globally correlated rotations introduce collective noise that scales unfavorably with system size.

10.2.2 Characterizing Floquet-Engineered XXZ Models

Using the protocol outlined in Ref. [8], we initialize pairs of molecules in a variety of product states and monitor their population dynamics as a function of evolution time. These dynamics provide a sensitive probe of the underlying interaction Hamiltonian. In particular, by fitting the observed oscillations, we extract the effective Ising anisotropy Δ, finding good agreement with the values predicted from the ideal Floquet engineering model for each realized experimental sequence.

In addition to verifying the engineered interaction parameters, we benchmark the coherence properties of the system for each targeted value of Δ. We observe long coherence times and find no evidence for significant spurious global fields introduced by the Floquet sequence. To quantify this, we probe T_1 and T_2 coherence times. T_1 is probed by measuring the difference in $|\uparrow\rangle$ and $|\downarrow\rangle$ population as a function of Floquet cycles. T_2 is measured by tracking the contrast of a Ramsey fringe as a function of Floquet cycles. The results, shown in Fig. 10.2(a,b) for $\Delta = 0.67$, demonstrate coherence times much longer than predicted optimal squeezing durations.

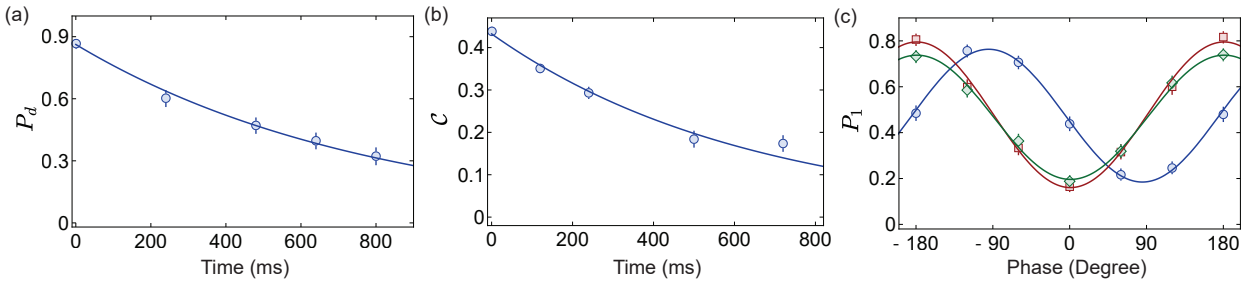


Figure 10.2: XY8-XYZ Coherence Times and Global Fields: Single-particle characterization of the sequence used to engineer the $\Delta = 0.67$ XXZ Hamiltonian. (a) $P_d = P_\uparrow - P_\downarrow$ as a function of time, yielding $T_1 = 0.80(4)$ s. (b) Decay of the coherence $\mathcal{C}$, yielding $T_2 = 0.64(5)$ s. (c) Ramsey fringes after 300 Floquet cycles (240 ms). Blue circles, red squares, and green diamonds correspond to measurements (i), (ii), and (iii) described in the text, indicating negligible $\vec{B}_{\text{eff}}$.

We further probe the presence of effective global magnetic fields $\vec{B} = \{B_x, B_y, B_z\}$ using Ramsey-type interferometry. The B_z component is measured using a standard Ramsey sequence, while the transverse components are accessed by appropriate frame rotations of this protocol. Concretely, we implement the following three sequences. For each, molecules are initialized in $|\uparrow\rangle$

(i) to measure B_y, we apply XY8-XYZ $- \frac{\pi}{2}\big|_x - \frac{\pi}{2}\big|_\phi$

(ii) to measure B_x, we apply XY8-XYZ $- \frac{\pi}{2}\big|_y - \frac{\pi}{2}\big|_\phi$

(iii) to measure B_z, we apply $\frac{\pi}{2}\big|_x$ – XY8-XYZ $- \frac{\pi}{2}\big|_\phi$

Here, the subscripts denote the rotation axes of the $\pi/2$ pulses. Representative Ramsey fringes for these three sequences (Fig. 10.2(c)), measured for the Floquet sequence producing $\Delta = 0.67$ show, no evidence of significant global fields after 300 Floquet cycles (240 ms).

10.3 Spin-Resolved Imaging

In this section, we describe our implementation of spin-resolved imaging (SRI). This protocol enables distinguishing between the three possible occupations of a tweezer: loaded with a molecule in $|\uparrow\rangle$, loaded with a molecule in $|\downarrow\rangle$, and unoccupied $|\emptyset\rangle$. We characterize SRI

performance, outline a model-free protocol to correct for loss and cross-talk during SRI, and describe a consistent post-selection procedure in the presence of population loss, cross-talk, and imaging identification errors.

10.3.1 Implementation of SRI

Our implementation of SRI relies on the ability to rapidly and efficiently optically pump population between rotational manifolds that are bright and dark to the imaging light. While we have previously demonstrated shelving into a dark state in Chapter 9, pumping to $N = 3$ offers several advantages over shelving into $N = 0$.

First, using $N = 0$ as a dark manifold would require coherent transfer into a specific hyperfine state. The efficiency of such a transfer can be degraded by microwave power fluctuations and the technical subtleties of operating under pseudomagic trapping conditions. Moreover, storage in a single hyperfine state of $N = 0$ is not robust to off-resonant scattering events. After scattering even a single imaging photon, population can leak into other hyperfine states in $N = 0$ or into $N = 2$, making repumping back to $N = 1$ technically demanding.

In contrast, optical pumping into $N = 3$ via the $X(N = 1) \rightarrow B(N = 2)$ transition (denoted $N12$) is comparatively straightforward. By adding sidebands to the laser, rapid scattering rates can be achieved. The efficiency of this process is also robust to variations in tweezer depth and magnetic field configuration. We note, however, that the line center exhibits a weak dependence on tweezer depth (see Chapter 6). Once population is transferred to $N = 3$, scattering events that return population to $N = 3$ manifold can all be repumped back to $N = 1$. Those that return to $N = 1$ lead to cross-talk and those that go to $N = 5$ will be lost (in principle, even these can be repumped using an $N54$ laser). Repumping from $N = 3$ back to $N = 1$ is achieved via the $X(N = 3) \rightarrow B(N = 2)$ transition (denoted $N32$).

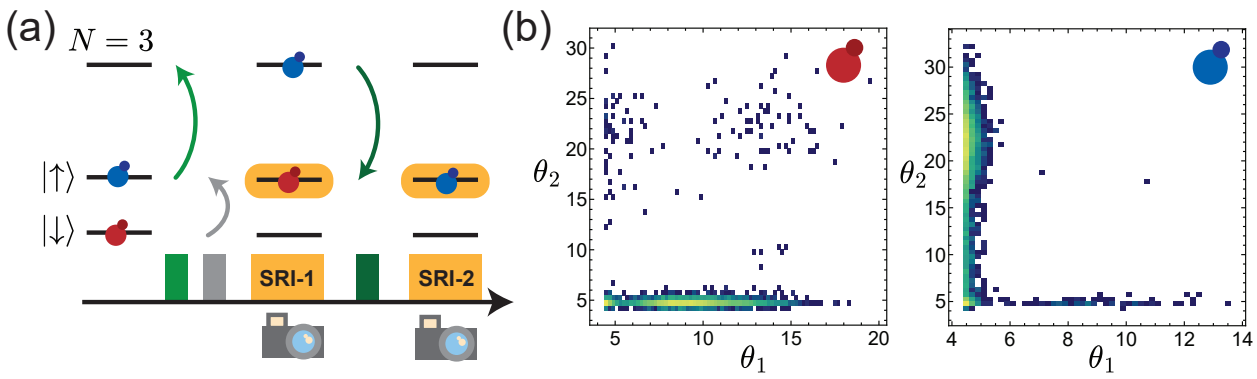


Figure 10.3: SRI Sequence and Histograms: (a) SRI begins with molecules in the rotational encoding. Application of $N32$ and a MW π-pulse transfers $|\uparrow\rangle \rightarrow N = 3$ and $|\downarrow\rangle \rightarrow |\uparrow\rangle$. SRI-1 is applied to identify molecules originally in $|\downarrow\rangle$. Next, $N12$ is applied to return $N = 3 \rightarrow N = 1$ before the SRI-2 image, which identifies molecules originally in $|\uparrow\rangle$ (b) Fluoresence histograms from the two images with molecules primarily initialized in either $|\downarrow\rangle$ (left) or $|\uparrow\rangle$ (right). This data set is used to extract the SRI process fidelity matrix, as elaborated in the text.

Experimentally, prior to each SRI sequence, molecules are prepared in the $|\uparrow\rangle$–$|\downarrow\rangle$ encoding at science tweezer depth. The full SRI protocol consists of the following steps (see Fig. 10.3(a)):

1. The tweezer depth is increased to 7× science depth to improve survival during rotational shelving.

2. $N12$ light is applied for 0.2 ms, transferring $|\uparrow\rangle$ population to $N = 3$. This duration is much longer than the measured $\sim 20\,\mu$s $1/e$ pumping timescale.

3. The tweezer depth is returned to science depth.

4. A microwave π-pulse transfers population from $|\downarrow\rangle$ to $|\uparrow\rangle$.

5. The tweezer depth is increased to full imaging depth and the magnetic field is set to zero.

6. The first of two images is taken, consisting of a 4 ms of 5-beam Λ-imaging followed by 7 ms of resonant 5-beam imaging (SRI-1). Tweezers that fluoresce during this image predominantly correspond to population initially in $|\downarrow\rangle$.

7. During the $\sim$ 10 ms camera readout, $N32$ light is applied to pump the dark state population in $N = 3$ back to $N = 1$.

8. The second of two images is taken using a 30 ms 5-beam Λ-image (SRI-2). Tweezers that fluoresce during this image primarily correspond to population initially in $|\uparrow\rangle$.

The fluorescence counts from the two images are binarized using two thresholds (θ_1, θ_2). In the absence of loss and cross-talk, the possible outcomes $\{(00), (01), (10)\}$ correspond to initial states $\{|\emptyset\rangle, |\uparrow\rangle, |\downarrow\rangle\}$. Additionally, we observe that $\sim 4\%$ of population survives the SRI-1 image, leading to the additional outcome (11), which would be assigned to $|\downarrow\rangle$. Fig. 10.3(b) shows fluoresence histograms initializing molecules in $|\uparrow\rangle$ or $|\downarrow\rangle$.

10.3.2 Correcting for Errors During SRI

This section outlines the characterization and correction of errors arising from SRI. The errors can be separated into two categories: 1) image classification errors and 2) SRI process errors.

Image classification errors are characterized using the same procedure described in Section 6.3.2. Briefly, molecules are first identified using non-destructive imaging, after which either SRI-1 or SRI-2 is applied. This allows extraction of $\epsilon_{10}(\theta)$ and $\epsilon_{01}(\theta)$ for each image. From these, we construct the matrix

$$C_{4\times4} = \underbrace{\begin{pmatrix} 1-\varepsilon_{01}^{(1)} & \varepsilon_{01}^{(1)} \\ \varepsilon_{10}^{(1)} & 1-\varepsilon_{10}^{(1)} \end{pmatrix}}_{\text{SRI-1}} \otimes \underbrace{\begin{pmatrix} 1-\varepsilon_{01}^{(2)} & \varepsilon_{01}^{(2)} \\ \varepsilon_{10}^{(2)} & 1-\varepsilon_{10}^{(2)} \end{pmatrix}}_{\text{SRI-2}}. \tag{10.10}$$

which quantifies imaging identification errors. This matrix transforms the true occupation probability during the two images (p_{img}) into measured outcome probabilities after binarization (p_{m}). Explicitly, we have $p_{\text{m}} = C_{4\times4} \cdot p_{\text{img}}$.

Regarding SRI process errors, we treat the full process—including loss and cross-talk—without attempting to isolate individual contributions. We first determine the state-preparation fidelity for $|\downarrow\rangle$ by preparing this state, transferring it to $|\uparrow\rangle$, and detecting population with a 30 ms Λ-image. The true preparation probability is obtained via

$$\begin{pmatrix} p_{\mathrm{SP}}^{\mathrm{true}} \\ 1 - p_{\mathrm{SP}}^{\mathrm{true}} \end{pmatrix} = \begin{pmatrix} 1 - \varepsilon_{10} & \varepsilon_{01} \\ \varepsilon_{10} & 1 - \varepsilon_{01} \end{pmatrix}^{-1} \begin{pmatrix} p_{\mathrm{SP}}^{\mathrm{raw}} \\ 1 - p_{\mathrm{SP}}^{\mathrm{raw}} \end{pmatrix}. \tag{10.11}$$

This is then used to construct the state-preparation matrix

$$M_{\mathrm{SP}} = \begin{pmatrix} p_{\mathrm{SP}}^{\mathrm{true}} & 0 & 0 \\ 0 & p_{\mathrm{SP}}^{\mathrm{true}} & 0 \\ 1 - p_{\mathrm{SP}}^{\mathrm{true}} & 1 - p_{\mathrm{SP}}^{\mathrm{true}} & 1 \end{pmatrix}. \tag{10.12}$$

The rows of this matrix quantify how well we can prepare a molecule in $|\uparrow\rangle$, $|\downarrow\rangle$, or $|\emptyset\rangle$, where we assume a perfect π-pulse fidelity.

Next, we apply SRI to tweezers prepared in $|\uparrow\rangle$, $|\downarrow\rangle$, or $|\emptyset\rangle$. We compile the measurement outcomes as a function of SRI imaging thresholds into the matrix

$$P_{\mathrm{out}}(\theta_1, \theta_2) = \begin{pmatrix} P_{11}^{(N=0)} & P_{11}^{(N=1)} & P_{11}^{(\mathrm{dark})} \\ P_{10}^{(N=0)} & P_{10}^{(N=1)} & P_{10}^{(\mathrm{dark})} \\ P_{01}^{(N=0)} & P_{01}^{(N=1)} & P_{01}^{(\mathrm{dark})} \\ P_{00}^{(N=0)} & P_{00}^{(N=1)} & P_{00}^{(\mathrm{dark})} \end{pmatrix}. \tag{10.13}$$

Finally, we introduce the projection matrix,

$$\Pi = \begin{pmatrix} 1 & 1 & 0 & 0 \\ 0 & 0 & 1 & 0 \\ 0 & 0 & 0 & 1 \end{pmatrix}, \tag{10.14}$$

which conveys that, after correcting for identification errors, (11) and (10) arise from a molecule in $N = 1$ during the SRI-1 image.

From here, we can relate the inferred occupation of the tweezers following SRI to the true state preparation probabilities M_{SP} subjection to the SRI process matrix ($\mathcal{M}$):

$$\Pi \cdot C_{4\times4}^{-1} \cdot P_{\mathrm{out}} = \mathcal{M} \cdot M_{\mathrm{SP}} \tag{10.15}$$

Solving for the process matrix we obtain

$$\mathcal{M} = \Pi \cdot C_{4\times4}^{-1} \cdot P_{\mathrm{out}} \cdot M_{\mathrm{SP}}^{-1}. \tag{10.16}$$

Finally, the full correction matrix $\mathcal{R}$, relating a true distribution p_{t} to a measured distribution p_{m}, is

$$p_{\mathrm{t}} = \underbrace{\mathcal{M}^{-1} \cdot \Pi \cdot C_{4\times4}^{-1}}_{\mathcal{R}} \cdot p_{\mathrm{m}}. \tag{10.17}$$

Written in full, we have

$$\mathcal{R} = M_{\mathrm{SP}} \cdot [\Pi \cdot C_{4\times4}^{-1} \cdot P_{\mathrm{out}}]^{-1} \cdot \Pi \cdot C_{4\times4}^{-1} \tag{10.18}$$

where M_{SP} is the 3×3 state-preparation matrix (Eq. 10.12), Π is the 3×4 projection matrix (Eq. 10.14), $C_{4\times4}^{-1}$ is the inverse image-identification error matrix (Eq. 10.10), and P_{out} is the 4×3 measured probability matrix (Eq. 10.13).

10.3.3 Post-selection and Expectation Values

The single-tweezer correction matrix generalizes to an array of N tweezers as $\mathcal{R}_N = \mathcal{R}^{\otimes N}$. While this matrix becomes large (for $N = 8$, $\mathcal{R}^{\otimes N}$ is $3^8 \times 4^8$), it only needs to be stored temporarily during the correction step.

To perform measurement correction and post-selection:

1. Apply $\mathcal{R}^{\otimes N}$ to the measured outcome vector P_{meas} (dimension 4^N), yielding the occupation probability vector P_{occ} (dimension 3^N).

2. Post-select by setting all entries of P_{occ} corresponding to hole configurations to zero

3. Normalize the resulting vector so all entries sum to 1

Before normalization, this vector can be written as

$$P_{\text{occ,PS}} = \text{diag}\{1,1,0\}^{\otimes N} \cdot \mathcal{R}^{\otimes N} \cdot P_{\text{meas}} = [\text{diag}\{1,1,0\} \cdot \mathcal{R}]^{\otimes N} \cdot P_{\text{meas}}. \tag{10.19}$$

Since $\text{diag}\{1,1,0\} \cdot \mathcal{R}$ contains a row of zeros, the correction matrix reduces to dimension 2×4, significantly reducing computational overhead.

Expectation values and uncertainties are computed via bootstrap resampling. Starting from the binarized measurement outcomes, we generate resampled datasets, apply correction and post-selection, and compute expectation values $\{\langle \mathcal{O} \rangle\}_i$. Reported values correspond to the mean and standard deviation over bootstrap samples.[1]

Unless otherwise stated, all results in this chapter include both measurement correction and post-selection for defect-free arrays. Notably, however, no post-selection was applied for the transduction investigation in Section 10.7. In some cases, we also report uncorrected results with post-selection applied; in this case, post-selection corresponds to requiring at least one bright image per tweezer during SRI.

10.4 Realizing Spin-Squeezing with XX Interactions

Pioneering theoretical work [194, 195] established that short-range XXZ models can generate one-axis-twisting-like (OAT-like) dynamics, closely resembling the canonical OAT evolution found in all-to-all interacting systems. In this regime, a coherent spin state (CSS) initialized

[1] This procedure can be parallelized by stacking resampled P_{meas} vectors into a matrix and applying the correction simultaneously.

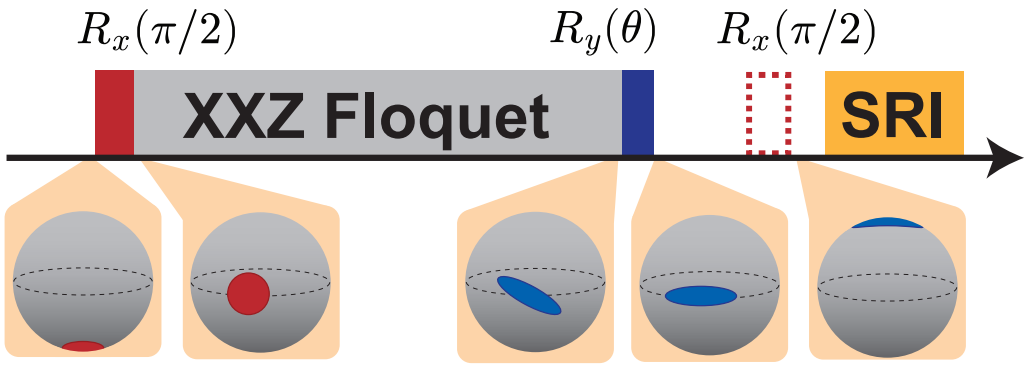


Figure 10.4: Spin Squeezing Protocol: For all squeezing investigations, molecules are initialized along the y axis of the collective Bloch sphere via a $\pi/2$ pulse. OAT-like dynamics shear the quantum state's projection noise. The state is re-oriented via a θ-pulse, enabling measurements of $\mathrm{Var}[S_\theta]$. An optional final $\pi/2$ pulse probes S_y.

on the equator of the Bloch sphere develops an anisotropic, sheared uncertainty distribution. This shearing reduces quantum projection noise along an appropriately chosen measurement axis, while preserving the large collective spin length required for high-contrast Ramsey interferometry.

Experimentally, we probe these squeezing dynamics using the pulse sequence depicted in Fig.10.4. Molecules are first initialized in a CSS aligned along the $\hat{y}$ axis of the collective Bloch sphere via a $\pi/2$ pulse. The system then undergoes coherent evolution, after which the collective spin is rotated by a variable angle θ. This θ rotation allows measuring $\mathrm{Var}[S_\theta]$. Optionally, a final $\pi/2$ pulse enables measurement of S_y.

We begin by investigating squeezing generated by the native molecular spin-exchange Hamiltonian, corresponding to the XXZ model at $\Delta = 0$. To characterize the resulting state, we measure $\mathrm{Var}[S_z]$ as a function of the readout angle θ near the optimal squeezing time (Fig. 10.5(a)). The observed sinusoidal dependence of the variance on θ is a direct signature of the elliptical noise distribution produced by OAT-like dynamics. Quantitatively, the measured variances show good agreement with a disorder-free simulation of the XX Hamiltonian.

We next characterize the dynamics of XX spin squeezing. For this and all future measurements where θ is a free parameter to be minimized over, θ is determined via a disorder-free

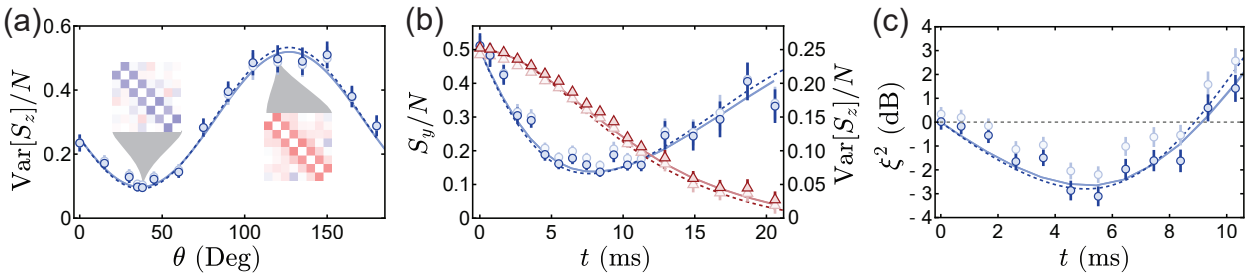


Figure 10.5: XX Squeezing Dynamics: a) Variance of S_z after 4.55 ms of XX squeezing is sinusoidal with respect to the readout axis θ. $\langle S_z^i S_z^j \rangle_c$ at $\theta = 38°$ (left) and $\theta = 120°$ (right) show predominatly short-ranged correlations. b) Variance (red) and spin length (blue) as a function of squeezing duration, showing good agreement with a noiseless diorder-free theory (dashed) and and our full noise theory (bands). c) Weinland parameter ξ^2 as a function of squeezing duration shows the generation of metrologically useful states, achieving the highest metrological gain of 3.0(3) dB at $t = 5.51$ ms.

XXZ model simulation. Strikingly, we find excellent agreement between the measured variance and spin length compared to predictions from a disorder-free XX model, indicating unitary OAT-like squeezing dynamics (Fig. 10.5(b)). We combine the variance and spin length measurements to probe the Weinland squeezing parameter, and find a lowest Weinland squeezing parameter of $-3.0(3)$ dB ($-2.2(3)$ dB without MC), in agreement with the best possible performance from unitary dipolar XX squeezing (Fig. 10.5(c)).

10.5 Probing Spatial Structure of XX Squeezed States

So far, our investigations have focused exclusively on collective observables, which fully describe spatially uniform squeezed states generated via all-to-all interacting Hamiltonians. However, the short-range nature of dipolar interactions is expected to imprint spatially inhomogeneous patterns onto the many-body squeezed state. To probe this structure, we examine two-point connected spin-spin correlators

$$\langle S_z^i S_z^j \rangle_c = \langle S_z^i S_z^j \rangle - \langle S_z^i \rangle \langle S_z^j \rangle, \tag{10.20}$$

which are closely related to the variance of the collective S_z via

$$\mathrm{Var}(S_z) = \sum_{i \neq j} \langle S_z^i S_z^j \rangle_c + \sum_i \mathrm{Var}(S_z^i). \tag{10.21}$$

From this perspective, the reduction in QPN enabling metrological advantage arises from negative connected spin-spin correlators. When examining the connected correlations of the squeezed state from Fig. 10.5(a) (see insets), we see strongly inhomogeneous correlations, dominated primarily by negative nearest-neighbor correlators.

We also investigate the measurement direction orthogonal to the S_z variance minimum. This direction maximizes the variance, which is physically meaningful via its relationship to bounding optimal quantum phase sensitivity via its relationship to the quantum Fisher information and Cramers-Rao bound (see Section 10.1). Inspection of the connected correlators along this maximum-variance direction again shows dominant nearest neighbor correlations, this time primarily positive. This spatial structure motivates constructing an observable with low QPN by flipping the sign of spins on every-other site. We investigate the variance of this antisymmetric observable

$$S_z^{\mathrm{A}} = \sum_i (-1)^i S_z^i, \tag{10.22}$$

and find that $\mathrm{Var}[S_z^{\mathrm{A}}]$ attains a minimum roughly where $\mathrm{Var}[S_z]$ attains its maximum (Fig. 10.6(a)).

To probe for metrological advantage, we evaluate the Wineland squeezing parameter for sensing both spatially uniform and spatially staggered fields as a function of measurement orientation. Remarkably, the squeezed state exhibits metrological advantage for sensing both types of fields (Fig. 10.6(b)). This simultaneous sensitivity to uniform and staggered perturbations is a distinctive feature of the state and arises from the predominantly nearest-neighbor correlations generated by XX squeezing dynamics.

This observation admits a complementary interpretation in terms of spatial structure. The staggered observable S_z^{A} naturally partitions the system into two sub-ensembles: sub-

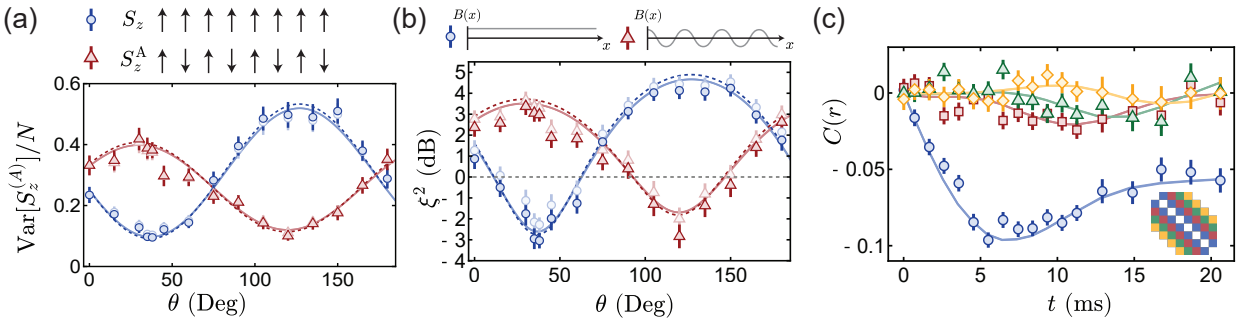


Figure 10.6: Spatial Structure of XX Squeezed State: a) The variance of S_z and S_z^{A} reach a minimum roughly 90° away from each other. b) Both the conventional (blue) and staggered (red) Wineland parameters attain $\xi^2 < 1$, highlighting how spatial structure of the squeezed state impacts sensing capabilities c) The dynamics of spin-spin correlations are dominated by $C(r = 1)$, pointing to predominantly local buildup of correlations in the XX squeezing protocol.

lattice A (odd sites) and sublattice B (even sites). Notably, contributions from these two partitions enter into a separability witness probing whether the joint quantum state can be written as a separable product of density matrices for the two subsystems.

Following criteria used in earlier work with spin-squeezed Bose–Einstein condensates [196–198], a separable bipartite system described by subsystems A and B must satisfy

$$\mathcal{E}_{\mathrm{Ent}} = \frac{4\,\mathrm{Var}\left(g_z S_z^A + S_z^B\right)\,\mathrm{Var}\left(g_x S_x^A + S_x^B\right)}{\left(|g_z g_x|\,\left(|\langle S_y^A\rangle| + |\langle S_y^B\rangle|\right)\right)^2} \geq 1, \tag{10.23}$$

where g_z and g_x are real-valued parameters. Violation of this inequality certifies that the state is non-separable along the A-B bi-partition. By setting $g_z = 1$ and $g_x = -1$, we find that $\mathcal{E}_{\mathrm{Ent}} = 4\mathrm{Var}[S_z]\,\mathrm{Var}[S_x^{\mathrm{A}}]/|S_y|^2$. Thus, we see that the small variance in these two combinations of S_z measured in orthogonal bases directly hints at the non-separability of the quantum state.

At the optimal squeezing duration, we measure $\mathcal{E}_{\mathrm{Ent}} = 0.22(2)$ (setting $g_z = 1$, $g_x = -1$), clearly violating the separability bound and certifying entanglement between the A and B sub-ensembles. This investigation explicitly probes the spatially inhomogeneous distribution of entanglement in the XX spin-squeezed state. In Section 10.5.1, we extend this investigation by probing for a stronger form of quantum correlations and entanglement structure.

Lastly, we probe the temporal dynamics of squeezing correlations via the mean distance-r connected correlator

$$C(r) = \frac{1}{N-r} \sum_{|i-j|=r} \langle S_z^i S_z^j \rangle_c. \tag{10.24}$$

Although $C(r \geq 2)$ do contain some dynamics, the correlations are dominated by $C(r = 1)$ before and well beyond the optimal squeezing duration (Fig. 10.6(c)). These observations suggest that squeezing in the short-range XX model arises from a buildup of spatially localized many-body correlations rather than from purely collective all-to-all mechanisms.

10.5.1 EPR Steering and Many-Body Entanglement

As a follow-up to our probe of inseparability, we investigate a more intricate entanglement structure capable of Einstein–Podolsky–Rosen (EPR) steering between two spatial sub-ensembles. EPR steering represents a stronger form of quantum correlation than simple inseparability, lying intermediate between entanglement and Bell nonlocality. Operationally, EPR steering describes a scenario in which measurements performed on one subsystem (e.g., subsystem A) can nonlocally influence, or "steer" the state of another subsystem (subsystem B) in a way that cannot be explained by a local hidden variable model assigned to subsystem B. Equivalently, EPR steering implies that measurement outcomes on subsystem A can be used to predict the outcomes of non-commuting observables on subsystem B with a precision surpassing the Heisenberg uncertainty relation applied to subsystem B alone.

States for which sub-ensemble A cannot steer sub-ensemble B satisfy the inequality

$$\mathcal{E}_{\mathrm{EPR}}^{A\to B} = \frac{\mathrm{Var}\left[\left(\sum_{i\in A} g_z^i S_z^i\right) + S_z^B\right] \mathrm{Var}\left[\left(\sum_{i\in A} g_x^i S_x^i\right) + S_x^B\right]}{\left|\left\langle S_y^B \right\rangle\right|^2 / 4} \geq 1\,. \tag{10.25}$$

Here, $\{g_z^i, g_x^i\}$ are real-valued parameters that can be optimized to minimize the witness. Violation of this inequality, $\mathcal{E}_{\mathrm{EPR}}^{A\to B} < 1$, certifies that subsystem A can steer subsystem B.

Δ	g_1^z	g_3^z	g_5^z	g_7^z	g_1^x	g_3^x	g_5^x	g_7^x
0	0.445	0.727	0.733	0.831	-0.414	-0.751	-0.717	-0.898
0.33	0.450	0.632	0.663	0.744	-0.414	-0.637	-0.659	-0.844
0.5	0.499	0.595	0.658	0.696	-0.471	-0.539	-0.734	-0.850
0.67	0.586	0.607	0.653	0.669	-0.528	-0.593	-0.667	-0.919
0.8	0.668	0.636	0.621	0.682	-0.692	-0.601	-0.641	-0.857
1.33	0.446	0.516	0.604	0.518	-0.337	-0.500	-0.649	-0.688
1.8	0.374	0.506	0.567	0.568	-0.341	-0.453	-0.589	-0.637

Table 10.1: EPR Witness Parameters vs Δ: The g_α^i that minimize $\mathcal{E}_{\text{EPR}}^{A\to B}$ are obtained from noiseless disorder-free simulations of XXZ models at the optimal squeezing durations. All values are rounded to 3 significant figures. The mirror-symmetry of the eight molecule chain implies that optimal parameter for $\mathcal{E}_{\text{EPR}}^{B\to A}$ come from simply substituting spatial indices $\{1,3,5,7\} \to \{8,6,4,2\}$ in this table.

It is instructive to build intuition for this witness. The quantities $\sum_{i\in A} g_z^i S_z^i$ and $\sum_{i\in A} g_x^i S_x^i$ can be viewed as estimators for the collective observables $-S_z^B$ and $-S_y^B$, respectively. If these estimators are highly correlated with the corresponding observables in subsystem B (that is, if they are good estimators), the variances in the numerator will be small. In this sense, the witness quantifies how well measurements on subsystem A can predict measurement outcomes in subsystem B. The role of the denominator becomes apparent if we set all $g = 0$ and multiply both sides of the inequality by $\left|\langle S_y^B\rangle\right|^2/4$; doing so recovers the Heisenberg uncertainty relation for subsystem B. A violation of the inequality therefore implies that information obtained from measurements of subsystem A allows one to predict measurement outcomes of non-commuting observables in subsystem B with a precision exceeding the Heisenberg limit applied to those same observables in subsystem B.

We evaluate this EPR-steering witness for the spin-squeezed states generated under XX squeezing dynamics. The coefficients $\{g_z^i, g_x^i\}$ are chosen to minimize the witness for a noiseless and disorder-free $1/r^3$ XX model. The optimized values used in this analysis are provided in Table 10.1; the measured EPR witnesses across all XXZ anisotropies Δ is presented in Section 10.6. For the XX model, we measure $\mathcal{E}_{\text{EPR}}^{A\to B} = 0.55(5)$ and $\mathcal{E}_{\text{EPR}}^{B\to A} = 0.57(6)$, demonstrating bi-directional EPR steering between the two sub-ensembles.

More generally, EPR steering occupies an intermediate position in the hierarchy of quantum correlations, with Bell nonlocality representing an even stronger form. Bell inequalities place constraints on correlations that cannot be explained by any local hidden variable model for either subsystem. Violations of Bell inequalities have been observed in related atomic systems, including Bose–Einstein condensates, and represent an intriguing target for future investigations in molecular tweezer arrays. Accessing this regime would require measurements in a broader set of bases than those explored here. As discussed in Section 10.8, a natural extension of this work is to investigate spin squeezing in higher-dimensional geometries and under more general Hamiltonians, such as XYZ models exhibiting two-axis counter-twisting (TACT) dynamics. These systems may provide new opportunities to explore how geometry and interaction structure influence the emergence of EPR steering and potentially Bell-nonlocal correlations.

10.6 Spin Squeezing Towards the Heisenberg Point

We next investigate spin squeezing in the XXZ model as a function of Ising anisotropy (Δ). Pioneering theoretical works predicted that improved metrological advantage could be attained near the Heisenberg point, albeit at the cost of longer coherent spin-squeezing duration [194, 195]. Near the Heisenberg point, the XXZ Hamiltonian can be well-approximated by an effective all-to-all interacting model, which is capable of generating scalable spin squeezing. While spin squeezing has been explored in 2D dipolar systems at the XX point [199] and in systems with contact interactions at fixed Ising anisotropy in 1D and 3D geometries [200], the specific prediction of emergent all-to-all correlations as $\Delta \to 1$ has not yet been empirically tested.

To investigate these predictions, we measure the variance, spin length, and squeezing parameter at $\Delta = 0.67$, shown in Fig. 10.7(a,b) ($\Delta = 0.8$, shown in Fig. 10.7(d,e)). Due to a combination of shorter coherence times and longer squeezing durations, no state surpasses

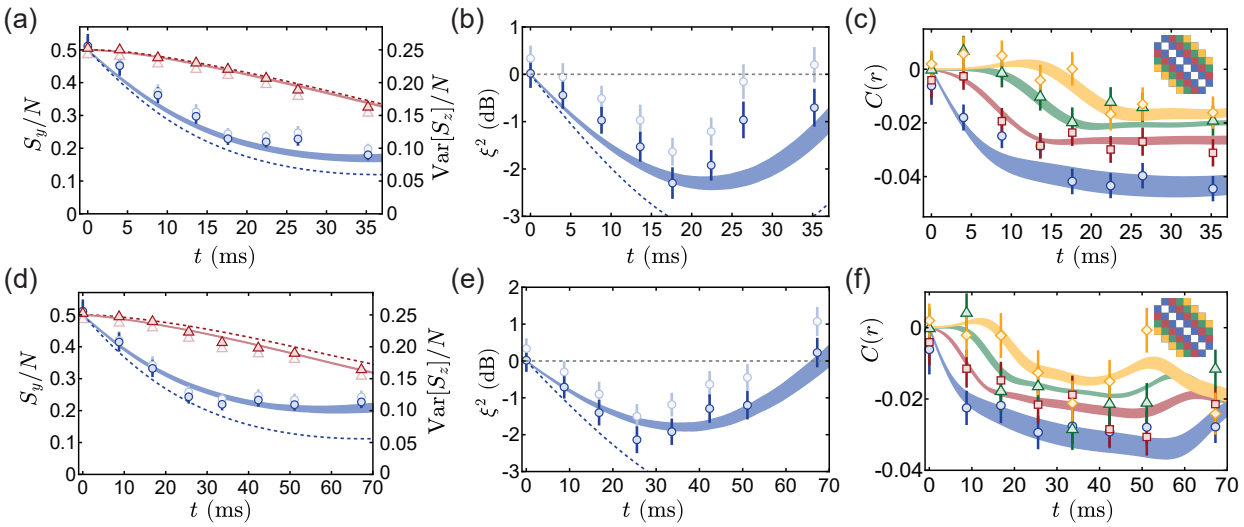


Figure 10.7: Temporal Dynamics of Squeezing at $\Delta \neq 0$ a) Dynamics of $\mathrm{Var}[S_z]/N$ (blue), S_y/N (red), b) ξ^2, and c) $C(r)$ as a function of squeezing duration t at $\Delta = 0.67$. (d,e,f) Dynamics at $\Delta = 0.8$. In contrast to $\Delta = 0$, there are clear deviations from unitary dynamics (dashed), which are well described by our noise model (shaded bands). Even under the influence of noise and decoherence, metrological enhancement is still observed. (c,f) also indicate that correlations spread well beyond nearest neighbor.

the metrological advantage of the $\Delta = 0$ state. Nonetheless, we observe $\xi^2(t) < 1$ over all probed interaction durations, reaching a minimum of $-2.3(3)$ dB for $\Delta = 0.67$ ($-2.1(3)$ dB for $\Delta = 0.8$).

Strikingly, the spatial structure of the squeezing correlations at $\Delta = 0.67$ and $\Delta = 0.8$ are qualitatively distinct from that of the XX model. Significant correlations extend out to $C(r = 4)$, hinting at the emergence of an extended effective interaction range as $\Delta \to 1$. The temporal dynamics of $C(r)$ are in good qualitative agreement with disorder-free theoretical predictions and are in excellent agreement with our full-disorder model (Fig. 10.7(c,f)). Thus, despite the absence of a quantitative improvement in ξ^2, many qualitative features of the XXZ squeezed states persist near the Heisenberg point.

We next probe whether any metrological improvement over the XX point can be realized by measuring ξ^2 at the no-noise optimal parameters predicted for six anisotropies, $\Delta = \{0.33, 0.5, 0.67, 0.8, 1.33, 1.8\}$. As shown in Fig. 10.8(a), no enhancement in metrological gain is observed relative to $\Delta = 0$. Our noise model quantitatively accounts for the observed

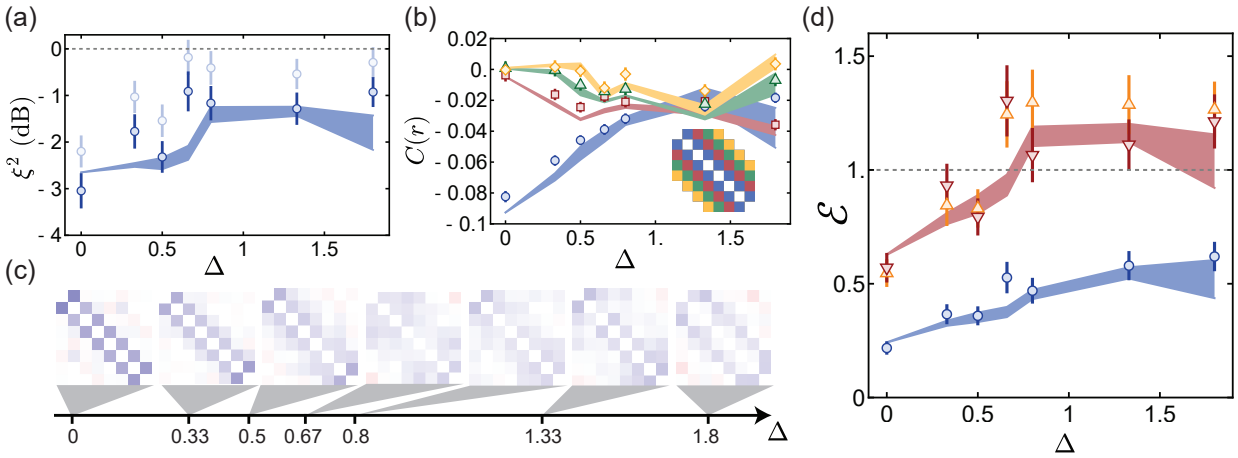


Figure 10.8: Squeezing, Correlations, and Witnesses vs Δ: a) Across all Δ, metrologically useful states can be produced, albeit with worse metrological gain compared to $\Delta = 0$. Shaded bands indicate full-noise simulations at the experimentally probed Δ. b) The spatial structure of correlations grow increasingly uniform as $\Delta \to 1$, evidenced by C(r) becoming more uniform. g) Under an even/odd site partition, all Δ generate non-separable states (blue), while only $\Delta = 0$ produces states significantly capable of EPR steering (red; orange $\mathcal{E}_{\mathrm{EPR}}^{A\to B}$; $\mathcal{E}_{\mathrm{EPR}}^{B\to A}$).

degradation in squeezing performance across this range, suggesting that improved control over decoherence and pulse imperfections could enable the predicted advantages to emerge.

Despite no improvement in squeezing parameter compared to $\Delta = 0$, the spatial structure of squeezing correlators change substantially as a function Δ. In contrast to $C(r = 1)$ dominating correlations at $\Delta = 0$, $C(r)$ becomes increasingly uniform as $\Delta \to 1$ (Fig. 10.8(b)). This increase in uniformity is also directly visible from $\langle S_z^i S_z^j \rangle_c$, which show the transition from localized to spatially extended correlations near $\Delta = 1$ (Fig. 10.8(c)). The emergence of these spatially uniform correlations provide indirect evidence of the emergent all-to-all effective Hamiltonian description near the Heisenberg point.

Lastly, we extend our investigations of separability and EPR steering to non-zero Δ. Under the same even/odd site partition, we find that the squeezed states across all anisotropies are significantly separable, with the $\Delta = 0$ state attaining the highest separability. Following a similar trend, EPR steering is strongest at $\Delta = 0$; the states produced at $\Delta = 0.33$ and $\Delta = 0.5$ are still steered, but with some significances not exceeding 1σ (Fig. 10.8(d)). Al-

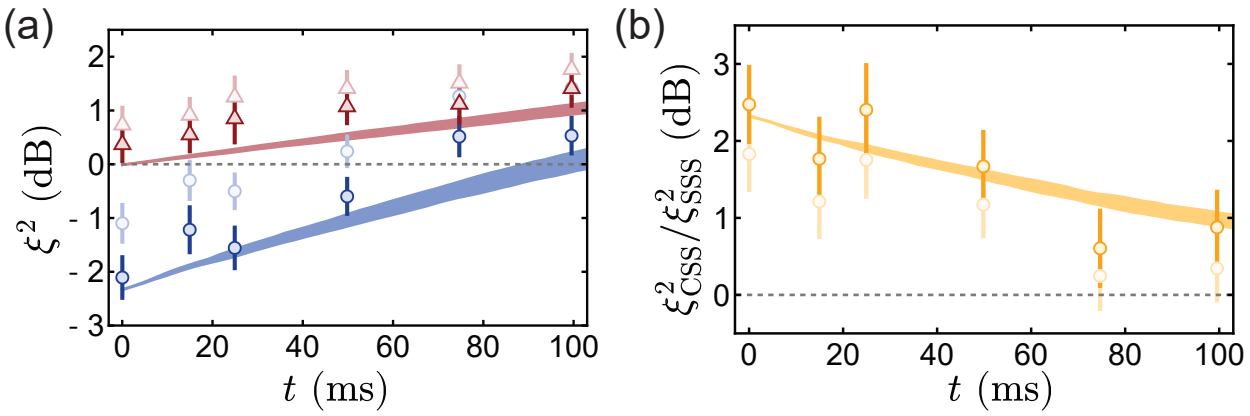


Figure 10.9: Transduction of Spin-Squeezed States: a) We demonstrate transduction of the XX spin squeezed state (SSS) (blue) and an unentangled CSS (red). Dark (light) data points correspond to (no) measurement correction. Shaded bands show simulation results assuming a hole fraction $p = 0.1$ and 10% uncertainty in the measured coherence times. Data at $\xi^2(t = 0)$ indicates that metrological advantage can be maintained following transduction. The SSS maintains metrological advantage out to storage times exceeding $t = 50\,\mathrm{ms}$. b) Practical metrological advantage of the SSS compared to the CSS ($\xi^2_{\mathrm{CSS}}/\xi^2_{\mathrm{SSS}}$) exceeds $t = 100\,\mathrm{ms}$. Shaded band is obtained from the simulations in (a).

though the ideal XXZ squeezing protocol produces states capable of EPR steering for all Δ, the delicate entanglement structure enabling EPR steering is easily degraded by decoherence and imperfections in Floquet engineering.

10.7 Transduction to Non-Interacting States

Once a spin-squeezed state is generated, it is desirable to extinguish interactions during the phase-accumulation interval of a Ramsey interferometer. In previous work [7], we developed a coherent transduction protocol to transfer population from the rotational encoding, where dipolar interactions are present, to a hyperfine encoding, where interactions are extinguished. Here, we employ this transduction technique to store both the optimal XX spin-squeezed state (SSS) and a coherent spin state (CSS) in the non-interacting hyperfine manifold.

In the present experiment, the optical tweezers depths are deeper that those used in the investigations from Chapter 9, leading to a modest reduction in hyperfine coherence times to $T_1 = T_2 \approx 700\,\mathrm{ms}$. Nevertheless, these timescales are still much longer than those of the

squeezing dynamics. For all measurements, the squeezed state is stored with its minimum-variance quadrature aligned along $\hat{z}$. Although optimal sensing of S_z fields in the hyperfine manifold would require the state to be rotated by 90°, the relative decay of metrological advantage is expected to be independent of the state's orientation since we measure $T_1 = T_2$.

Following transduction and a variable storage duration, we characterize the stored states by measuring their spin length and variance. This is accomplished by applying coherent global rotations within the hyperfine manifold, followed by hyperfine-SRI. The hyperfine-SRI protocol involves first transferring population from the hyperfine to rotational qubit encoding, and then applying SRI. Independent process fidelities are measured for this hyperfine-SRI protocol using the procedure outlined in Section 10.3, which is used for measurement correction. For these investigations, we do not post-select for defect-free arrays. We find a hole fraction of $p_h \sim 10\%$.

First and foremost, we find that the optimal squeezed state retains significant metrological advantage following transduction. The modest degradation in the squeezing parameter is attributable to technical noise introduced during the transfer process. The squeezed state maintains metrological advantage ($\xi^2 < 1$) for over 50 ms of storage, but eventually both the SSS and CSS rise significantly above $\xi^2 = 1$ (Fig. 10.9(a)).

To assess practical metrological advantage, we track the ratio $\xi^2_{\mathrm{CSS}}/\xi^2_{\mathrm{SSS}}$ as a function of storage duration. The squeezed state maintains a relative advantage over the CSS for approximately 100 ms (Fig. 10.9(b)), defining an effective measurement bandwidth over which the non-classical state provides enhanced sensitivity. These results demonstrate that interaction-generated spin squeezing can be coherently stored in a non-interacting manifold where they remain metrologically useful.

10.8 Outlook

The techniques developed in this work are broadly applicable to systems exhibiting spin-squeezing dynamics. In particular, our investigations of the practical limitations imposed by noise and interaction disorder provide a roadmap for incorporating metrologically useful entangled states into molecular precision-measurement platforms. These insights could prove critical to achieving practical gains in sensitivity and bandwidth in probes for BSM physics using trapped polar molecules [201].

Even in 1D geometries, substantial improvements in metrological gain remain achievable as technical sources of decoherence are reduced. In particular, suppressing magnetic field noise and implementing truly magic trapping conditions for the interacting qubit states would provide access to unitary spin-squeezing dynamics across a wider range of XXZ anisotropies. Operating under such conditions could allow the enhanced metrological gain predicted near the Heisenberg point to be achieved.

As demonstrated here, tuning the anisotropy near the Heisenberg point influences the spatial structure of squeezing correlations. The ability to engineer the spatial extent of connected correlators suggests new opportunities for designing tailored entangled states optimized for specific sensing tasks. When combined with coherent mid-circuit rearrangement [170], these capabilities could allow generating custom squeezing correlation maps, opening the door to new classes of differential sensing protocols and multi-parameter metrology schemes exploiting spatially structured entanglement.

On the geometry frontier, 2D dipolar arrays offer distinct advantages for generating strongly squeezed states. In particular, two-axis counter-twisting (TACT) dynamics, which have been realized in our platform through XYZ spin models, permit scalable spin squeezing in 2D dipolar systems. Moreover, the nature of TACT dynamics provides intrinsic robustness to interaction inhomogeneity and filling disorder [202], making 2D dipolar TACT an especially attractive protocol for generating large metrologically useful states.

Beyond quantum-enhanced metrology, these capabilities may enable systematic studies of families of Hamiltonians that share similar dynamical behavior while differing in their underlying microscopic interaction structure. Such flexibility may allow probing regimes exhibiting unusual transport and correlation dynamics in long-range interacting systems. Together, these capabilities position dipolar molecular arrays as a versatile platform for investigating both practical quantum technologies and fundamental many-body physics.

Chapter 11

Outlook

I stopped paying attention as soon as they said "molecule".

– Overhead at DAMOP

Although I am admittedly biased, ultracold molecules appear well positioned for a bright and successful future. In particular, only a small portion of the accessible physics in Floquet-engineered spin models has been explored to date. While our current work has focused on one-dimensional systems, extending these studies to ladder geometries and fully two-dimensional arrays promises access to a broader range of many-body phenomena. Optical tweezer platforms, with their inherent geometric flexibility, are especially well suited to realizing such configurations.

At present, the number of molecules in tweezer arrays remains relatively limited. However, several promising approaches to enhanced loading have been proposed [188, 203], suggesting a path toward larger system sizes with little to no technical upgrades of experimental hardware. In parallel, a more systematic understanding of loss mechanisms during non-destructive imaging is lacking. Improvements in trapping geometries and wavelengths that push survival probabilities toward the 0.99 level would open up preparation of low-defect arrays of $\mathcal{O}(50)$ molecules in the near term. Separately, the interplay of geometry and the defects themselves are an interesting research direction to explore [202].

Another particularly exciting direction is the exploration of multilevel Hamiltonians which can be realized via hyperfine and rotational state encodings [7, 204, 205]. Both directly cooled and bialkali molecules offer access to a rich set of internal states that can be coherently manipulated. Importantly, both platforms allow for state-resolved detection across multiple internal levels [33], addressing a limitation in current implementations of multilevel encodings using Rydberg states in atomic systems.

Beyond applications in quantum information and simulation, the level of control and detection in molecular tweezer arrays opens new opportunities in ultracold chemistry. The ability to initialize, manipulate, and read out molecular states with hyperfine-level resolution provides a powerful toolset for studying collisions and reaction dynamics [206]. Such measurements in systems like CaF may offer insights that extend to other molecular species.

Looking further ahead, interfacing molecules with platforms that enable strong light-matter interactions presents an intriguing and largely unexplored direction. In particular, the integration of molecular systems with optical cavities could provide new avenues for control, detection, and the study of collective effects, and is beginning to attract attention from several research groups.

On the technical side, mitigating loss due to blackbody radiation will likely be essential for continued progress. For molecules such as CaF, this may require operating at reduced trap spacings, cryogenic temperatures, or a combination of both. While blackbody-induced transitions can sometimes be converted into erasure errors, the associated loss rates impose a fundamental limitation on achievable fidelities in room-temperature environments. Moving to more closely spaced arrays will, in turn, necessitate improved cooling strategies to suppress thermal motion and interaction inhomogeneities. Additionally, truly magic trapping conditions, similar to recent demonstrations in bialkali molecules [67], could significantly extend coherence times and enable studies of quantum dynamics over much longer timescales.

Bibliography

[1] C. M. Holland, Y. Lu, and L. W. Cheuk. "Synthesizing optical spectra using computer-generated holography techniques". *New Journal of Physics* **23**, 033028 (2021).

[2] Y. Lu, C. M. Holland, and L. W. Cheuk. "Molecular Laser Cooling in a Dynamically Tunable Repulsive Optical Trap". *Phys. Rev. Lett.* **128**, 213201 (2022).

[3] C. M. Holland, Y. Lu, and L. W. Cheuk. "Bichromatic Imaging of Single Molecules in an Optical Tweezer Array". *Phys. Rev. Lett.* **131**, 053202 (2023).

[4] C. M. Holland, Y. Lu, and L. W. Cheuk. "On-demand entanglement of molecules in a reconfigurable optical tweezer array". *Science* **382**, 1143–1147 (2023).

[5] Y. Lu, S. J. Li, C. M. Holland, and L. W. Cheuk. "Raman sideband cooling of molecules in an optical tweezer array". *Nature Physics* **20**, 389–394 (2024).

[6] S. J. Li, C. M. Holland, Y. Lu, and L. W. Cheuk. "Blue-Detuned Magneto-optical Trap of CaF Molecules". *Phys. Rev. Lett.* **132**, 233402 (2024).

[7] C. M. Holland, Y. Lu, S. J. Li, C. L. Welsh, and L. W. Cheuk. "Demonstration of Measurement-Enhanced State Preparation and Erasure Conversion in a Molecular Tweezer Array". *Phys. Rev. X* **15**, 031018 (2025).

[8] Y. Lu, C. M. Holland, C. L. Welsh, X.-Y. Chen, and L. W. Cheuk. "Probing Coherent Many-Body Spin Dynamics in a Molecular Tweezer Array Quantum Simulator". *arXiv preprint arXiv:2603.19090* (2026).

[9] I. I. Rabi, S. Millman, P. Kusch, and J. R. Zacharias. "The Molecular Beam Resonance Method for Measuring Nuclear Magnetic Moments. The Magnetic Moments of $_3\mathrm{Li}^6$, $_3\mathrm{Li}^7$ and $_9\mathrm{F}^{19}$". *Phys. Rev.* **55**, 526–535 (1939).

[10] H. Lyons. *The Atomic Clock: An Atomic Standard of Frequency and Time*. 1949.

[11] D. DeMille. "Quantum Computation with Trapped Polar Molecules". *Phys. Rev. Lett.* **88**, 067901 (2002).

[12] A. Micheli, G. K. Brennen, and P. Zoller. "A toolbox for lattice-spin models with polar molecules". *Nature Physics* **2**, 341–347 (2006).

[13] L. D. Carr, D. DeMille, R. V. Krems, and J. Ye. "Cold and ultracold molecules: science, technology and applications". *New Journal of Physics* **11**, 55049 (2009).

[14] J. L. Bohn, A. M. Rey, and J. Ye. "Cold molecules: Progress in quantum engineering of chemistry and quantum matter". *Science* **357**, 1002–1010 (2017).

[15] V. Andreev, D. G. Ang, D. DeMille, J. M. Doyle, G. Gabrielse, J. Haefner, N. R. Hutzler, Z. Lasner, C. Meisenhelder, B. R. O'Leary, C. D. Panda, A. D. West, E. P. West, X. Wu, and A. Collaboration. "Improved limit on the electric dipole moment of the electron". *Nature* **562**, 355–360 (2018).

[16] T. S. Roussy, L. Caldwell, T. Wright, W. B. Cairncross, Y. Shagam, K. B. Ng, N. Schlossberger, S. Y. Park, A. Wang, J. Ye, and E. A. Cornell. "An improved bound on the electron's electric dipole moment". *Science* **381**, 46–50 (2023).

[17] S. Ospelkaus, K.-K. Ni, D. Wang, M. H. G. de Miranda, B. Neyenhuis, G. Quéméner, P. S. Julienne, J. L. Bohn, D. S. Jin, and J. Ye. "Quantum-State Controlled Chemical Reactions of Ultracold Potassium-Rubidium Molecules". *Science* **327**, 853–857 (2010).

[18] Y.-X. Liu, L. Zhu, J. Luke, J. J. A. Houwman, M. C. Babin, M.-G. Hu, and K.-K. Ni. "Quantum interference in atom-exchange reactions". *Science* **384**, 1117–1121 (2024).

[19] B. Capogrosso-Sansone, C. Trefzger, M. Lewenstein, P. Zoller, and G. Pupillo. "Quantum Phases of Cold Polar Molecules in 2D Optical Lattices". *Phys. Rev. Lett.* **104**, 125301 (2010).

[20] K.-K. Ni, T. Rosenband, and D. D. Grimes. "Dipolar exchange quantum logic gate with polar molecules". *Chem. Sci.* **9**, 6830–6838 (2018).

[21] K.-K. Ni, S. Ospelkaus, M. H. G. de Miranda, A. Pe'er, B. Neyenhuis, J. J. Zirbel, S. Kotochigova, P. S. Julienne, D. S. Jin, and J. Ye. "A High Phase-Space-Density Gas of Polar Molecules". *Science* **322**, 231–235 (2008).

[22] T. Takekoshi, L. Reichsöllner, A. Schindewolf, J. M. Hutson, C. R. Le Sueur, O. Dulieu, F. Ferlaino, R. Grimm, and H.-C. Nägerl. "Ultracold Dense Samples of Dipolar RbCs Molecules in the Rovibrational and Hyperfine Ground State". *Phys. Rev. Lett.* **113**, 205301 (2014).

[23] P. K. Molony, P. D. Gregory, Z. Ji, B. Lu, M. P. Köppinger, C. R. Le Sueur, C. L. Blackley, J. M. Hutson, and S. L. Cornish. "Creation of Ultracold ^{87}Rb^{133}Cs Molecules in the Rovibrational Ground State". *Phys. Rev. Lett.* **113**, 255301 (2014).

[24] J. W. Park, S. A. Will, and M. W. Zwierlein. "Ultracold Dipolar Gas of Fermionic ^{23}Na^{40}K Molecules in Their Absolute Ground State". *Phys. Rev. Lett.* **114**, 205302 (2015).

[25] F. Seeßelberg, N. Buchheim, Z.-K. Lu, T. Schneider, X.-Y. Luo, E. Tiemann, I. Bloch, and C. Gohle. "Modeling the adiabatic creation of ultracold polar ^{23}Na^{40}K molecules". *Phys. Rev. A* **97**, 013405 (2018).

[26] M. Guo, B. Zhu, B. Lu, X. Ye, F. Wang, R. Vexiau, N. Bouloufa-Maafa, G. Quéméner, O. Dulieu, and D. Wang. "Creation of an Ultracold Gas of Ground-State Dipolar ^{23}Na^{87}Rb Molecules". *Phys. Rev. Lett.* **116**, 205303 (2016).

[27] T. M. Rvachov, H. Son, A. T. Sommer, S. Ebadi, J. J. Park, M. W. Zwierlein, W. Ketterle, and A. O. Jamison. "Long-Lived Ultracold Molecules with Electric and Magnetic Dipole Moments". *Phys. Rev. Lett.* **119**, 143001 (2017).

[28] I. Stevenson, A. Z. Lam, N. Bigagli, C. Warner, W. Yuan, S. Zhang, and S. Will. "Ultracold Gas of Dipolar NaCs Ground State Molecules". *Phys. Rev. Lett.* **130**, 113002 (2023).

[29] A. Schindewolf, R. Bause, X.-Y. Chen, M. Duda, T. Karman, I. Bloch, and X.-Y. Luo. "Evaporation of microwave-shielded polar molecules to quantum degeneracy". *Nature* **607**, 677–681 (2022).

[30] N. Bigagli, W. Yuan, S. Zhang, B. Bulatovic, T. Karman, I. Stevenson, and S. Will. "Observation of Bose–Einstein condensation of dipolar molecules". *Nature* **631**, 289–293 (2024).

[31] L. Christakis, J. S. Rosenberg, R. Raj, S. Chi, A. Morningstar, D. A. Huse, Z. Z. Yan, and W. S. Bakr. "Probing site-resolved correlations in a spin system of ultracold molecules". *Nature* **614**, 64–69 (2023).

[32] J. T. Zhang, L. R. B. Picard, W. B. Cairncross, K. Wang, Y. Yu, F. Fang, and K.-K. Ni. "An optical tweezer array of ground-state polar molecules". *Quantum Science and Technology* **7**, 035006 (2022).

[33] D. K. Ruttley, A. Guttridge, T. R. Hepworth, and S. L. Cornish. "Enhanced Quantum Control of Individual Ultracold Molecules Using Optical Tweezer Arrays". *PRX Quantum* **5**, 020333 (2024).

[34] N. R. Hutzler, H.-I. Lu, and J. M. Doyle. "The Buffer Gas Beam: An Intense, Cold, and Slow Source for Atoms and Molecules". *Chemical Reviews* **112**, 4803–4827 (2012).

[35] E. S. Shuman, J. F. Barry, and D. DeMille. "Laser cooling of a diatomic molecule". *Nature* **467**, 820–823 (2010).

[36] J. F. Barry, E. S. Shuman, E. B. Norrgard, and D. DeMille. "Laser Radiation Pressure Slowing of a Molecular Beam". *Phys. Rev. Lett.* **108**, 103002 (2012).

[37] V. Zhelyazkova, A. Cournol, T. E. Wall, A. Matsushima, J. J. Hudson, E. A. Hinds, M. R. Tarbutt, and B. E. Sauer. "Laser cooling and slowing of CaF molecules". *Phys. Rev. A* **89**, 053416 (2014).

[38] B. Hemmerling, E. Chae, A. Ravi, L. Anderegg, G. K. Drayna, N. R. Hutzler, A. L. Collopy, J. Ye, W. Ketterle, and J. M. Doyle. "Laser slowing of CaF molecules to near the capture velocity of a molecular MOT". *Journal of Physics B: Atomic, Molecular and Optical Physics* **49**, 174001 (2016).

[39] J. F. Barry, D. J. McCarron, E. B. Norrgard, M. H. Steinecker, and D. DeMille. "Magneto-optical trapping of a diatomic molecule". *Nature* **512**, 286–289 (2014).

[40] S. Truppe, H. J. Williams, M. Hambach, L. Caldwell, N. J. Fitch, E. A. Hinds, B. E. Sauer, and M. R. Tarbutt. "Molecules cooled below the Doppler limit". *Nature Physics* **13**, 1173–1176 (2017).

[41] L. Anderegg, B. L. Augenbraun, E. Chae, B. Hemmerling, N. R. Hutzler, A. Ravi, A. Collopy, J. Ye, W. Ketterle, and J. M. Doyle. "Radio Frequency Magneto-Optical Trapping of CaF with High Density". *Phys. Rev. Lett.* **119**, 103201 (2017).

[42] A. L. Collopy, S. Ding, Y. Wu, I. A. Finneran, L. Anderegg, B. L. Augenbraun, J. M. Doyle, and J. Ye. "3D Magneto-Optical Trap of Yttrium Monoxide". *Phys. Rev. Lett.* **121**, 213201 (2018).

[43] L. W. Cheuk, L. Anderegg, B. L. Augenbraun, Y. Bao, S. Burchesky, W. Ketterle, and J. M. Doyle. "Λ-Enhanced Imaging of Molecules in an Optical Trap". *Phys. Rev. Lett.* **121**, 083201 (2018).

[44] S. Ding, Y. Wu, I. A. Finneran, J. J. Burau, and J. Ye. "Sub-Doppler Cooling and Compressed Trapping of YO Molecules at μK Temperatures". *Phys. Rev. X* **10**, 021049 (2020).

[45] T. K. Langin, V. Jorapur, Y. Zhu, Q. Wang, and D. DeMille. "Polarization Enhanced Deep Optical Dipole Trapping of Λ-Cooled Polar Molecules". *Phys. Rev. Lett.* **127**, 163201 (2021).

[46] L. Anderegg, B. L. Augenbraun, Y. Bao, S. Burchesky, L. W. Cheuk, W. Ketterle, and J. M. Doyle. "Laser cooling of optically trapped molecules". *Nature Physics* **14**, 890–893 (2018).

[47] H. J. Williams, L. Caldwell, N. J. Fitch, S. Truppe, J. Rodewald, E. A. Hinds, B. E. Sauer, and M. R. Tarbutt. "Magnetic Trapping and Coherent Control of Laser-Cooled Molecules". *Phys. Rev. Lett.* **120**, 163201 (2018).

[48] Y. Wu, J. J. Burau, K. Mehling, J. Ye, and S. Ding. "High Phase-Space Density of Laser-Cooled Molecules in an Optical Lattice". *Phys. Rev. Lett.* **127**, 263201 (2021).

[49] J. Lim, J. R. Almond, M. A. Trigatzis, J. A. Devlin, N. J. Fitch, B. E. Sauer, M. R. Tarbutt, and E. A. Hinds. "Laser Cooled YbF Molecules for Measuring the Electron's Electric Dipole Moment". *Phys. Rev. Lett.* **120**, 123201 (2018).

[50] J. Dai, Q. Sun, B. C. Riley, D. Mitra, and T. Zelevinsky. "Laser cooling of a fermionic molecule". *Phys. Rev. Res.* **6**, 033135 (2024).

[51] Z. Zeng, S. Deng, S. Yang, and B. Yan. "Three-Dimensional Magneto-Optical Trapping of Barium Monofluoride". *Phys. Rev. Lett.* **133**, 143404 (2024).

[52] J. E. Padilla-Castillo, J. Cai, P. Agarwal, P. Kukreja, R. Thomas, B. G. Sartakov, S. Truppe, G. Meijer, and S. C. Wright. "Magneto-Optical Trapping of Aluminum Monofluoride". *Phys. Rev. Lett.* **135**, 243401 (2025).

[53] J. Dai, B. Riley, Q. Sun, D. Mitra, and T. Zelevinsky. "Magneto-Optical Trapping of a Metal Hydride Molecule". *arXiv preprint arXiv:2512.22350* (2025).

[54] I. Kozyryev, L. Baum, K. Matsuda, B. L. Augenbraun, L. Anderegg, A. P. Sedlack, and J. M. Doyle. "Sisyphus Laser Cooling of a Polyatomic Molecule". *Phys. Rev. Lett.* **118**, 173201 (2017).

[55] L. Baum, N. B. Vilas, C. Hallas, B. L. Augenbraun, S. Raval, D. Mitra, and J. M. Doyle. "1D Magneto-Optical Trap of Polyatomic Molecules". *Phys. Rev. Lett.* **124**, 133201 (2020).

[56] D. Mitra, N. B. Vilas, C. Hallas, L. Anderegg, B. L. Augenbraun, L. Baum, C. Miller, S. Raval, and J. M. Doyle. "Direct laser cooling of a symmetric top molecule". *Science* **369**, 1366–1369 (2020).

[57] N. B. Vilas, C. Hallas, L. Anderegg, P. Robichaud, A. Winnicki, D. Mitra, and J. M. Doyle. "Magneto-optical trapping and sub-Doppler cooling of a polyatomic molecule". *Nature* **606**, 70–74 (2022).

[58] Z. D. Lasner, A. Frenett, H. Sawaoka, L. Anderegg, B. Augenbraun, H. Lampson, M. Li, A. Lunstad, J. Mango, A. Nasir, T. Ono, T. Sakamoto, and J. M. Doyle. "Magneto-Optical Trapping of a Heavy Polyatomic Molecule for Precision Measurement". *Phys. Rev. Lett.* **134**, 083401 (2025).

[59] B. L. Augenbraun, Z. D. Lasner, A. Frenett, H. Sawaoka, C. Miller, T. C. Steimle, and J. M. Doyle. "Laser-cooled polyatomic molecules for improved electron electric dipole moment searches". *New Journal of Physics* **22**, 022003 (2020).

[60] L. Anderegg, N. B. Vilas, C. Hallas, P. Robichaud, A. Jadbabaie, J. M. Doyle, and N. R. Hutzler. "Quantum control of trapped polyatomic molecules for eEDM searches". *Science* **382**, 665–668 (2023).

[61] B. Neyenhuis, B. Yan, S. A. Moses, J. P. Covey, A. Chotia, A. Petrov, S. Kotochigova, J. Ye, and D. S. Jin. "Anisotropic Polarizability of Ultracold Polar ^{40}K^{87}Rb Molecules". *Phys. Rev. Lett.* **109**, 230403 (2012).

[62] J. W. Park, Z. Z. Yan, H. Loh, S. A. Will, and M. W. Zwierlein. "Second-scale nuclear spin coherence time of ultracold ^{23}Na^{40}K molecules". *Science* **357**, 372–375 (2017).

[63] F. Seeßelberg, X.-Y. Luo, M. Li, R. Bause, S. Kotochigova, I. Bloch, and C. Gohle. "Extending Rotational Coherence of Interacting Polar Molecules in a Spin-Decoupled Magic Trap". *Phys. Rev. Lett.* **121**, 253401 (2018).

[64] J. Lin, J. He, X. Ye, and D. Wang. "Anisotropic polarizability of ultracold ground-state ^{23}Na^{87}Rb molecules". *Phys. Rev. A* **103**, 023332 (2021).

[65] S. Burchesky, L. Anderegg, Y. Bao, S. S. Yu, E. Chae, W. Ketterle, K.-K. Ni, and J. M. Doyle. "Rotational Coherence Times of Polar Molecules in Optical Tweezers". *Phys. Rev. Lett.* **127**, 123202 (2021).

[66] A. J. Park, L. R. B. Picard, G. E. Patenotte, J. T. Zhang, T. Rosenband, and K.-K. Ni. "Extended Rotational Coherence of Polar Molecules in an Elliptically Polarized Trap". *Phys. Rev. Lett.* **131**, 183401 (2023).

[67] P. D. Gregory, L. M. Fernley, A. L. Tao, S. L. Bromley, J. Stepp, Z. Zhang, S. Kotochigova, K. R. A. Hazzard, and S. L. Cornish. "Second-scale rotational coherence and dipolar interactions in a gas of ultracold polar molecules". *Nature Physics* **20**, 415–421 (2024).

[68] B. Yan, S. A. Moses, B. Gadway, J. P. Covey, K. R. A. Hazzard, A. M. Rey, D. S. Jin, and J. Ye. "Observation of dipolar spin-exchange interactions with lattice-confined polar molecules". *Nature* **501**, 521–525 (2013).

[69] J.-R. Li, K. Matsuda, C. Miller, A. N. Carroll, W. G. Tobias, J. S. Higgins, and J. Ye. "Tunable itinerant spin dynamics with polar molecules". *Nature* **614**, 70–74 (2023).

[70] M. Endres, H. Bernien, A. Keesling, H. Levine, E. R. Anschuetz, A. Krajenbrink, C. Senko, V. Vuletic, M. Greiner, and M. D. Lukin. "Atom-by-atom assembly of defect-free one-dimensional cold atom arrays". *Science* **354**, 1024–1027 (2016).

[71] D. Barredo, S. de Léséleuc, V. Lienhard, T. Lahaye, and A. Browaeys. "An atom-by-atom assembler of defect-free arbitrary two-dimensional atomic arrays". *Science* **354**, 1021–1023 (2016).

[72] G. Semeghini, H. Levine, A. Keesling, S. Ebadi, T. T. Wang, D. Bluvstein, R. Verresen, H. Pichler, M. Kalinowski, R. Samajdar, A. Omran, S. Sachdev, A. Vishwanath, M. Greiner, V. Vuletić, and M. D. Lukin. "Probing topological spin liquids on a programmable quantum simulator". *Science* **374**, 1242–1247 (2021).

[73] D. Bluvstein, H. Levine, G. Semeghini, T. T. Wang, S. Ebadi, M. Kalinowski, A. Keesling, N. Maskara, H. Pichler, M. Greiner, V. Vuletić, and M. D. Lukin. "A quantum processor based on coherent transport of entangled atom arrays". *Nature* **604**, 451–456 (2022).

[74] H. Bernien, S. Schwartz, A. Keesling, H. Levine, A. Omran, H. Pichler, S. Choi, A. S. Zibrov, M. Endres, M. Greiner, V. Vuletić, and M. D. Lukin. "Probing many-body dynamics on a 51-atom quantum simulator". *Nature* **551**, 579–584 (2017).

[75] P. Scholl, M. Schuler, H. J. Williams, A. A. Eberharter, D. Barredo, K.-N. Schymik, V. Lienhard, L.-P. Henry, T. C. Lang, T. Lahaye, A. M. Läuchli, and A. Browaeys. "Quantum simulation of 2D antiferromagnets with hundreds of Rydberg atoms". *Nature* **595**, 233–238 (2021).

[76] S. Ma, G. Liu, P. Peng, B. Zhang, S. Jandura, J. Claes, A. P. Burgers, G. Pupillo, S. Puri, and J. D. Thompson. "High-fidelity gates and mid-circuit erasure conversion in an atomic qubit". *Nature* **622**, 279–284 (2023).

[77] D. Bluvstein, S. J. Evered, A. A. Geim, S. H. Li, H. Zhou, T. Manovitz, S. Ebadi, M. Cain, M. Kalinowski, D. Hangleiter, J. P. B. Ataides, N. Maskara, I. Cong, X. Gao, P. S. Rodriguez, T. Karolyshyn, G. Semeghini, M. J. Gullans, M. Greiner, V. Vuletić, and M. D. Lukin. "Logical quantum processor based on reconfigurable atom arrays". *Nature* **626**, 58–65 (2024).

[78] A. Cao, W. J. Eckner, T. L. Yelin, A. W. Young, S. Jandura, L. Yan, K. Kim, G. Pupillo, J. Ye, N. D. Oppong, and A. M. Kaufman. "Multi-qubit gates and Schrödinger cat states in an optical clock". *Nature* **634**, 315–320 (2024).

[79] R. Finkelstein, R. B.-S. Tsai, X. Sun, P. Scholl, S. Direkci, T. Gefen, J. Choi, A. L. Shaw, and M. Endres. "Universal quantum operations and ancilla-based read-out for tweezer clocks". *Nature* **634**, 321–327 (2024).

[80] A. Cooper, J. P. Covey, I. S. Madjarov, S. G. Porsev, M. S. Safronova, and M. Endres. "Alkaline-Earth Atoms in Optical Tweezers". *Phys. Rev. X* **8**, 041055 (2018).

[81] M. A. Norcia, A. W. Young, and A. M. Kaufman. "Microscopic Control and Detection of Ultracold Strontium in Optical-Tweezer Arrays". *Phys. Rev. X* **8**, 041054 (2018).

[82] S. Saskin, J. T. Wilson, B. Grinkemeyer, and J. D. Thompson. "Narrow-Line Cooling and Imaging of Ytterbium Atoms in an Optical Tweezer Array". *Phys. Rev. Lett.* **122**, 143002 (2019).

[83] K. Singh, S. Anand, A. Pocklington, J. T. Kemp, and H. Bernien. "Dual-Element, Two-Dimensional Atom Array with Continuous-Mode Operation". *Phys. Rev. X* **12**, 011040 (2022).

[84] D. Bloch, B. Hofer, S. R. Cohen, A. Browaeys, and I. Ferrier-Barbut. "Trapping and Imaging Single Dysprosium Atoms in Optical Tweezer Arrays". *Phys. Rev. Lett.* **131**, 203401 (2023).

[85] D. S. Grün, S. J. M. White, A. Ortu, A. Di Carli, H. Edri, M. Lepers, M. J. Mark, and F. Ferlaino. "Optical Tweezer Arrays of Erbium Atoms". *Phys. Rev. Lett.* **133**, 223402 (2024).

[86] L. Anderegg, L. W. Cheuk, Y. Bao, S. Burchesky, W. Ketterle, K.-K. Ni, and J. M. Doyle. "An optical tweezer array of ultracold molecules". *Science* **365**, 1156–1158 (2019).

[87] Y. Bao, S. S. Yu, L. Anderegg, E. Chae, W. Ketterle, K.-K. Ni, and J. M. Doyle. "Dipolar spin-exchange and entanglement between molecules in an optical tweezer array". *Science* **382**, 1138–1143 (2023).

[88] N. B. Vilas, P. Robichaud, C. Hallas, G. K. Li, L. Anderegg, and J. M. Doyle. "An optical tweezer array of ultracold polyatomic molecules". *Nature* **628**, 282–286 (2024).

[89] J. M. Brown and A. Carrington. *Rotational spectroscopy of diatomic molecules*. Cambridge university press, 2003.

[90] Y. Lu. "Reconfigurable Optical Tweezer Arrays of Ultracold Molecules for Quantum Science". PhD thesis. Princeton University, 2025.

[91] M. Di Rosa. "Laser-cooling molecules: Concept, candidates, and supporting hyperfine-resolved measurements of rotational lines in the AX (0, 0) band of CaH". *The European Physical Journal D-Atomic, Molecular, Optical and Plasma Physics* **31**, 395–402 (2004).

[92] L. Caldwell and M. R. Tarbutt. "Sideband cooling of molecules in optical traps". *Phys. Rev. Res.* **2**, 013251 (2020).

[93] S. de Léséleuc, V. Lienhard, P. Scholl, D. Barredo, S. Weber, N. Lang, H. P. Büchler, T. Lahaye, and A. Browaeys. "Observation of a symmetry-protected topological phase of interacting bosons with Rydberg atoms". *Science* **365**, 775–780 (2019).

[94] A. Browaeys and T. Lahaye. "Many-body physics with individually controlled Rydberg atoms". *Nature Physics* **16**, 132–142 (2020).

[95] S. Baier, M. J. Mark, D. Petter, K. Aikawa, L. Chomaz, Z. Cai, M. Baranov, P. Zoller, and F. Ferlaino. "Extended Bose-Hubbard models with ultracold magnetic atoms". *Science* **352**, 201–205 (2016).

[96] L. Su, A. Douglas, M. Szurek, R. Groth, S. F. Ozturk, A. Krahn, A. H. Hébert, G. A. Phelps, S. Ebadi, S. Dickerson, F. Ferlaino, O. Marković, and M. Greiner. "Dipolar quantum solids emerging in a Hubbard quantum simulator". *Nature* **622**, 724–729 (2023).

[97] L. Anderegg. "Ultracold molecules in optical arrays: from laser cooling to molecular collisions". PhD thesis. Harvard University, 2020.

[98] A. Keshet and W. Ketterle. "A distributed, graphical user interface based, computer control system for atomic physics experiments". *Review of Scientific Instruments* **84**, 015105 (2013).

[99] E. B. Norrgard, D. J. McCarron, M. H. Steinecker, M. R. Tarbutt, and D. DeMille. "Submillikelvin Dipolar Molecules in a Radio-Frequency Magneto-Optical Trap". *Phys. Rev. Lett.* **116**, 063004 (2016).

[100] M. R. Tarbutt and T. C. Steimle. "Modeling magneto-optical trapping of CaF molecules". *Phys. Rev. A* **92**, 053401 (2015).

[101] M. Tarbutt. "Magneto-optical trapping forces for atoms and molecules with complex level structures". *New Journal of Physics* **17**, 015007 (2015).

[102] J. L. Hall, L. Hollberg, T. Baer, and H. G. Robinson. "Optical heterodyne saturation spectroscopy". *Applied Physics Letters* **39**, 680–682 (1981).

[103] S. Chu, L. Hollberg, J. E. Bjorkholm, A. Cable, and A. Ashkin. "Three-dimensional viscous confinement and cooling of atoms by resonance radiation pressure". *Phys. Rev. Lett.* **55**, 48–51 (1985).

[104] M. Lu, S. H. Youn, and B. L. Lev. "Trapping ultracold dysprosium: a highly magnetic gas for dipolar physics". *Phys. Rev. Lett.* **104**, 063001 (2010).

[105] N. Leefer, A. Cingöz, B. Gerber-Siff, A. Sharma, J. Torgerson, and D. Budker. "Transverse laser cooling of a thermal atomic beam of dysprosium". *Physical Review A* **81**, 043427 (2010).

[106] J. J. McClelland and J. L. Hanssen. "Laser cooling without repumping: a magneto-optical trap for erbium atoms". *Phys. Rev. Lett.* **96**, 143005 (2006).

[107] D. Sukachev, A. Sokolov, K. Chebakov, A. Akimov, S. Kanorsky, N. Kolachevsky, and V. Sorokin. "Magneto-optical trap for thulium atoms". *Phys. Rev. A* **82**, 011405 (2010).

[108] R. W. Gerchberg and W. O. Saxton. "A practical algorithm for the determination of phase from image and diffraction plane pictures." *Optik (Stuttgart)* **35**, 237–250 (1972).

[109] T. D. Milster. "The Gerchberg-Saxton Phase Retrieval Algorithm and Related Variations". In: *Optical Holography-Materials, Theory and Applications*. Elsevier, 2020, 61–72.

[110] J. R. Fienup. "Phase retrieval algorithms: a comparison". *Appl. Opt.* **21**, 2758–2769 (1982).

[111] J. R. Fienup and C. C. Wackerman. "Phase-retrieval stagnation problems and solutions". *Journal of the Optical Society of America A* **3**, 1897 (1986).

[112] H. Wang, W. Yue, Q. Song, J. Liu, and G. Situ. "A hybrid Gerchberg–Saxton-like algorithm for DOE and CGH calculation". *Optics and Lasers in Engineering* **89**, 109–115 (2017).

[113] R. C. Cumming. "The Serrodyne Frequency Translator". *Proceedings of the IRE* **45**, 175–186 (1957).

[114] K. K. Wong, R. M. D. L. Rue, and S. Wright. "Electro-optic-waveguide frequency translator in LiNbO3 fabricated by proton exchange". *Opt. Lett.* **7**, 546–548 (1982).

[115] D. M. S. Johnson, J. M. Hogan, S.-w. Chiow, and M. A. Kasevich. "Broadband optical serrodyne frequency shifting". *Opt. Lett.* **35**, 745–747 (2010).

[116] C. E. Rogers, J. L. Carini, J. A. Pechkis, and P. L. Gould. "Creation of arbitrary time-sequenced line spectra with an electro-optic phase modulator". *Review of Scientific Instruments* **82**, 73107 (2011).

[117] V. Flambaum, I. Khriplovich, and O. Sushkov. *Zh. Eksp. Teor. Fiz.* **87**, 1521 (1984).

[118] V. V. Flambaum, D. DeMille, and M. G. Kozlov. "Time-Reversal Symmetry Violation in Molecules Induced by Nuclear Magnetic Quadrupole Moments". *Phys. Rev. Lett.* **113**, 103003 (2014).

[119] I. Kozyryev and N. R. Hutzler. "Precision Measurement of Time-Reversal Symmetry Violation with Laser-Cooled Polyatomic Molecules". *Phys. Rev. Lett.* **119** (2017).

[120] M. Petzold, P. Kaebert, P. Gersema, M. Siercke, and S. Ospelkaus. "A Zeeman slower for diatomic molecules". *New Journal of Physics* **20**, 042001 (2018).

[121] F. Kogel, T. Garg, M. Rockenhäuser, S. A. Morales-Ramírez, and T. Langen. "Molecular laser cooling using serrodynes: implementation, characterization and prospects". *New Journal of Physics* **27**, 055001 (2025).

[122] F. Kogel, M. Rockenhäuser, R. Albrecht, and T. Langen. "A laser cooling scheme for precision measurements using fermionic barium monofluoride (137Ba19F) molecules". *New Journal of Physics* **23**, 095003 (2021).

[123] F. Kogel, T. Garg, M. Rockenhäuser, S. A. Morales-Ramírez, and T. Langen. "Isotopologue-selective laser cooling of molecules". *New Journal of Physics* **27**, 013001 (2025).

[124] M. Rockenhäuser, F. Kogel, T. Garg, S. A. Morales-Ramírez, and T. Langen. "Laser cooling of barium monofluoride molecules using synthesized optical spectra". *Phys. Rev. Res.* **6**, 043161 (2024).

[125] F. Kogel, T. Garg, M. Rockenhäuser, and T. Langen. "Laser-cooled ^{137}BaF molecules for measuring nuclear-spin-dependent parity violation". *Phys. Rev. Res.* **7**, L022041 (2025).

[126] Y. Zeng, A. Jadbabaie, A. N. Patel, P. Yu, T. C. Steimle, and N. R. Hutzler. "Optical cycling in polyatomic molecules with complex hyperfine structure". *Phys. Rev. A* **108**, 012813 (2023).

[127] X. Wei, Z. Li, A. V. Karve, A. L. Shaw, D. I. Schuster, and J. Simon. "A 10 Megahertz Spatial Light Modulator". *arXiv preprint arXiv:2601.08906* (2026).

[128] H. Swan, A. Torchylo, M. J. Van de Graaff, J. Rudolph, and J. M. Hogan. "High-fidelity holographic beam shaping with optimal transport and phase diversity". *Optics Express* **33**, 6290–6303 (2025).

[129] R. Lin, H.-S. Zhong, Y. Li, Z.-R. Zhao, L.-T. Zheng, T.-R. Hu, H.-M. Wu, Z. Wu, W.-J. Ma, Y. Gao, et al. "AI-enabled parallel assembly of thousands of defect-free neutral atom arrays". *Physical Review Letters* **135**, 060602 (2025).

[130] S. S. Phatak, K. N. Blodgett, D. Peana, M. R. Chen, and J. D. Hood. "Generalized theory for optical cooling of a trapped atom with spin". *Phys. Rev. A* **110**, 043116 (2024).

[131] A. Cooper, J. P. Covey, I. S. Madjarov, S. G. Porsev, M. S. Safronova, and M. Endres. "Alkaline-Earth Atoms in Optical Tweezers". *Phys. Rev. X* **8**, 041055 (2018).

[132] M. Rockenhäuser, F. Kogel, E. Pultinevicius, and T. Langen. "Absorption spectroscopy for laser cooling and high-fidelity detection of barium monofluoride molecules". *Phys. Rev. A* **108**, 062812 (2023).

[133] L. W. Cheuk, L. Anderegg, Y. Bao, S. Burchesky, S. S. Yu, W. Ketterle, K.-K. Ni, and J. M. Doyle. "Observation of Collisions between Two Ultracold Ground-State CaF Molecules". *Phys. Rev. Lett.* **125**, 043401 (2020).

[134] T. M. Graham, M. Kwon, B. Grinkemeyer, Z. Marra, X. Jiang, M. T. Lichtman, Y. Sun, M. Ebert, and M. Saffman. "Rydberg-Mediated Entanglement in a Two-Dimensional Neutral Atom Qubit Array". *Phys. Rev. Lett.* **123**, 230501 (2019).

[135] Y. Hao, L. F. Pašteka, L. Visscher, P. Aggarwal, H. L. Bethlem, A. Boeschoten, A. Borschevsky, M. Denis, K. Esajas, S. Hoekstra, K. Jungmann, V. R. Marshall, T. B. Meijknecht, M. C. Mooij, R. G. E. Timmermans, A. Touwen, W. Ubachs, L. Willmann, Y. Yin, and A. Zapara. "High accuracy theoretical investigations of CaF, SrF, and BaF and implications for laser-cooling". *J. Chem. Phys.* **151**, 034302 (2019).

[136] S. Truppe, H. J. Williams, N. J. Fitch, M. Hambach, T. E. Wall, E. A. Hinds, B. E. Sauer, and M. R. Tarbutt. "An intense, cold, velocity-controlled molecular beam by frequency-chirped laser slowing". *New Journal of Physics* **19**, 022001 (2017).

[137] S. Raouafi, G.-H. Jeung, and C. Jungen. "Permanent and transition dipole moments in CaF and CaCl". *The Journal of Chemical Physics* **115**, 7450–7459 (2001).

[138] L. A. Kaledin, J. C. Bloch, M. C. McCarthy, and R. W. Field. "Analysis and Deperturbation of the A2Π and B2Σ+ States of CaF". *Journal of Molecular Spectroscopy* **197**, 289–296 (1999).

[139] C. M. Gittins, N. A. Harris, R. W. Field, J. Verges, C. Effantin, A. Bernard, J. Dincan, W. E. Ernst, P. Bundgen, and B. Engels. "Analysis and Deperturbation of the C2Π and D2Σ+ States of CaF". *Journal of Molecular Spectroscopy* **161**, 303–311 (1993).

[140] S. F. Rice, H. Martin, and R. W. Field. "The electronic structure of the calcium monohalides. A ligand field approach". *J. Chem. Phys.* **82**, 5023–5034 (1985).

[141] N. R. Hutzler, L. R. Liu, Y. Yu, and K.-K. Ni. "Eliminating light shifts for single atom trapping". *New Journal of Physics* **19**, 023007 (2017).

[142] I. Kozyryev, T. C. Steimle, P. Yu, D.-T. Nguyen, and J. M. Doyle. "Determination of CaOH and CaOCH3 vibrational branching ratios for direct laser cooling and trapping". *New Journal of Physics* **21**, 052002 (2019).

[143] G. Lao, G.-Z. Zhu, C. E. Dickerson, B. L. Augenbraun, A. N. Alexandrova, J. R. Caram, E. R. Hudson, and W. C. Campbell. "Laser spectroscopy of aromatic molecules with optical cycling centers: strontium (I) phenoxides". *The Journal of Physical Chemistry Letters* **13**, 11029–11035 (2022).

[144] D. Mitra, Z. D. Lasner, G.-Z. Zhu, C. E. Dickerson, B. L. Augenbraun, A. D. Bailey, A. N. Alexandrova, W. C. Campbell, J. R. Caram, E. R. Hudson, et al. "Pathway toward optical cycling and laser cooling of functionalized arenes". *The Journal of Physical Chemistry Letters* **13**, 7029–7035 (2022).

[145] G.-Z. Zhu, D. Mitra, B. L. Augenbraun, C. E. Dickerson, M. J. Frim, G. Lao, Z. D. Lasner, A. N. Alexandrova, W. C. Campbell, J. R. Caram, J. M. Doyle, and E. R. Hudson. "Functionalizing aromatic compounds with optical cycling centres". *Nature Chemistry* (2022).

[146] B. K. Stuhl, B. C. Sawyer, D. Wang, and J. Ye. "Magneto-optical Trap for Polar Molecules". *Phys. Rev. Lett.* **101**, 243002 (2008).

[147] J. A. Devlin and M. R. Tarbutt. "Three-dimensional Doppler, polarization-gradient, and magneto-optical forces for atoms and molecules with dark states". *New Journal of Physics* **18**, 123017 (2016).

[148] S. Ding, Y. Wu, I. A. Finneran, J. J. Burau, and J. Ye. "Sub-Doppler Cooling and Compressed Trapping of YO Molecules at μK Temperatures". *Phys. Rev. X* **10**, 021049 (2020).

[149] T. K. Langin, V. Jorapur, Y. Zhu, Q. Wang, and D. DeMille. "Polarization Enhanced Deep Optical Dipole Trapping of Λ-Cooled Polar Molecules". *Phys. Rev. Lett.* **127**, 163201 (2021).

[150] K. N. Jarvis, J. A. Devlin, T. E. Wall, B. E. Sauer, and M. R. Tarbutt. "Blue-Detuned Magneto-Optical Trap". *Phys. Rev. Lett.* **120**, 083201 (2018).

[151] T. K. Langin and D. DeMille. "Toward improved loading, cooling, and trapping of molecules in magneto-optical traps". *New Journal of Physics* **25**, 043005 (2023).

[152] S. Xu, P. Kaebert, M. Stepanova, T. Poll, M. Siercke, and S. Ospelkaus. "Engineering the sub-Doppler force in magneto-optical traps". *Phys. Rev. Res.* **4**, L042036 (2022).

[153] J. J. Burau, P. Aggarwal, K. Mehling, and J. Ye. "Blue-Detuned Magneto-optical Trap of Molecules". *Phys. Rev. Lett.* **130**, 193401 (2023).

[154] V. Jorapur, T. K. Langin, Q. Wang, G. Zheng, and D. DeMille. "High Density Loading and Collisional Loss of Laser-Cooled Molecules in an Optical Trap". *Phys. Rev. Lett.* **132**, 163403 (2024).

[155] H. J. Williams, L. Caldwell, N. J. Fitch, S. Truppe, J. Rodewald, E. A. Hinds, B. E. Sauer, and M. R. Tarbutt. "Magnetic Trapping and Coherent Control of Laser-Cooled Molecules". *Phys. Rev. Lett.* **120**, 163201 (2018).

[156] H. J. Williams, S. Truppe, M. Hambach, L. Caldwell, N. J. Fitch, E. A. Hinds, B. E. Sauer, and M. R. Tarbutt. "Characteristics of a magneto-optical trap of molecules". *New J. Phys.* **19**, 113035 (2017).

[157] D. McCarron, E. Norrgard, M. Steinecker, and D. DeMille. "Improved magneto-optical trapping of a diatomic molecule". *New Journal of Physics* **17**, 035014 (2015).

[158] E. L. Raab, M. Prentiss, A. Cable, S. Chu, and D. E. Pritchard. "Trapping of Neutral Sodium Atoms with Radiation Pressure". *Phys. Rev. Lett.* **59**, 2631–2634 (1987).

[159] C. Hallas, G. K. Li, N. B. Vilas, P. Robichaud, L. Anderegg, and J. M. Doyle. "High Compression Blue-Detuned Magneto-Optical Trap of Polyatomic Molecules". *Phys. Rev. Lett.* **136**, 133402 (2026).

[160] S. S. Yu, J. You, Y. Bao, L. Anderegg, C. Hallas, G. K. Li, D. Lim, E. Chae, W. Ketterle, K.-K. Ni, et al. "A conveyor-belt magneto-optical trap of CaF". *Nature Communications* **17**, 1175 (2026).

[161] G. Zheng, J. Wang, M. Verma, Q. Wang, T. K. Langin, and D. DeMille. "Simulated laser cooling and magneto-optical trapping of group-IV atoms". *Phys. Rev. A* **113**, 043115 (2026).

[162] J. Choi, H. Zhou, H. S. Knowles, R. Landig, S. Choi, and M. D. Lukin. "Robust Dynamic Hamiltonian Engineering of Many-Body Spin Systems". *Phys. Rev. X* **10**, 031002 (2020).

[163] D. K. Ruttley, T. R. Hepworth, A. Guttridge, and S. L. Cornish. "Long-lived entanglement of molecules in magic-wavelength optical tweezers". *Nature* **637**, 827–832 (2025).

[164] L. R. B. Picard, A. J. Park, G. E. Patenotte, S. Gebretsadkan, D. Wellnitz, A. M. Rey, and K.-K. Ni. "Entanglement and iSWAP gate between molecular qubits". *Nature* **637**, 821–826 (2025).

[165] C. A. Sackett, D. Kielpinski, B. E. King, C. Langer, V. Meyer, C. J. Myatt, M. Rowe, Q. A. Turchette, W. M. Itano, D. J. Wineland, and C. Monroe. "Experimental entanglement of four particles". *Nature* **404**, 256–259 (2000).

[166] Q. A. Turchette, C. S. Wood, B. E. King, C. J. Myatt, D. Leibfried, W. M. Itano, C. Monroe, and D. J. Wineland. "Deterministic Entanglement of Two Trapped Ions". *Phys. Rev. Lett.* **81**, 3631–3634 (1998).

[167] L. Pezzè, A. Smerzi, M. K. Oberthaler, R. Schmied, and P. Treutlein. "Quantum metrology with nonclassical states of atomic ensembles". *Rev. Mod. Phys.* **90**, 035005 (2018).

[168] N. Schine, A. W. Young, W. J. Eckner, M. J. Martin, and A. M. Kaufman. "Long-lived Bell states in an array of optical clock qubits". *Nature Physics* **18**, 1067–1073 (2022).

[169] M. Bergonzoni, S. Jandura, and G. Pupillo. "iSWAP gate with polar molecules: Robustness criteria for entangling operations". *Physical Review A* **112**, 032621 (2025).

[170] J. You, J. M. Doyle, Z. Liu, S. S. Yu, and A. Periwal. "Control of Dipolar Dynamics by Geometrical Programming". *Physical Review Letters* **135**, 253002 (2025).

[171] M. Hughes, M. D. Frye, R. Sawant, G. Bhole, J. A. Jones, S. L. Cornish, M. R. Tarbutt, J. M. Hutson, D. Jaksch, and J. Mur-Petit. "Robust entangling gate for polar molecules using magnetic and microwave fields". *Phys. Rev. A* **101**, 062308 (2020).

[172] Y. Wu, S. Kolkowitz, S. Puri, and J. D. Thompson. "Erasure conversion for fault-tolerant quantum computing in alkaline earth Rydberg atom arrays". *Nature communications* **13**, 4657 (2022).

[173] P. Scholl, A. L. Shaw, R. B.-S. Tsai, R. Finkelstein, J. Choi, and M. Endres. "Erasure conversion in a high-fidelity Rydberg quantum simulator". *Nature* **622**, 273–278 (2023).

[174] A. L. Shaw, P. Scholl, R. Finkelstein, R. B.-S. Tsai, J. Choi, and M. Endres. "Erasure cooling, control, and hyperentanglement of motion in optical tweezers". *Science* **388**, 845–849 (2025).

[175] M. N. Chow, V. Buchemmavari, S. Omanakuttan, B. J. Little, S. Pandey, I. H. Deutsch, and Y.-Y. Jau. "Circuit-based leakage-to-erasure conversion in a neutral-atom quantum processor". *PRX Quantum* **5**, 040343 (2024).

[176] H. Levine et al. "Demonstrating a Long-Coherence Dual-Rail Erasure Qubit Using Tunable Transmons". *Phys. Rev. X* **14**, 011051 (2024).

[177] A. Koottandavida, I. Tsioutsios, A. Kargioti, C. R. Smith, V. R. Joshi, W. Dai, J. D. Teoh, J. C. Curtis, L. Frunzio, R. J. Schoelkopf, and M. H. Devoret. "Erasure Detection of a Dual-Rail Qubit Encoded in a Double-Post Superconducting Cavity". *Phys. Rev. Lett.* **132**, 180601 (2024).

[178] Y. Bao, S. S. Yu, J. You, L. Anderegg, E. Chae, W. Ketterle, K.-K. Ni, and J. M. Doyle. "Raman Sideband Cooling of Molecules in an Optical Tweezer Array to the 3D Motional Ground State". *Phys. Rev. X* **14**, 031002 (2024).

[179] P. D. Gregory, J. A. Blackmore, S. L. Bromley, J. M. Hutson, and S. L. Cornish. "Robust storage qubits in ultracold polar molecules". *Nature Physics* **17**, 1149–1153 (2021).

[180] J. Lin, J. He, M. Jin, G. Chen, and D. Wang. "Seconds-Scale Coherence on Nuclear Spin Transitions of Ultracold Polar Molecules in 3D Optical Lattices". *Phys. Rev. Lett.* **128**, 223201 (2022).

[181] Y. Liu, J. Schmidt, Z. Liu, D. R. Leibrandt, D. Leibfried, and C.-w. Chou. "Quantum state tracking and control of a single molecular ion in a thermal environment". *Science* **385**, 790–795 (2024).

[182] M. Grassl, T. Beth, and T. Pellizzari. "Codes for the quantum erasure channel". *Phys. Rev. A* **56**, 33–38 (1997).

[183] C. H. Bennett, D. P. DiVincenzo, and J. A. Smolin. "Capacities of Quantum Erasure Channels". *Phys. Rev. Lett.* **78**, 3217–3220 (1997).

[184] A. Kubica, A. Haim, Y. Vaknin, H. Levine, F. Brandão, and A. Retzker. "Erasure Qubits: Overcoming the T_1 Limit in Superconducting Circuits". *Phys. Rev. X* **13**, 041022 (2023).

[185] M. Kang, W. C. Campbell, and K. R. Brown. "Quantum Error Correction with Metastable States of Trapped Ions Using Erasure Conversion". *PRX Quantum* **4**, 020358 (2023).

[186] J. D. Teoh, P. Winkel, H. K. Babla, B. J. Chapman, J. Claes, S. J. de Graaf, J. W. O. Garmon, W. D. Kalfus, Y. Lu, A. Maiti, K. Sahay, N. Thakur, T. Tsunoda, S. H. Xue, L. Frunzio, S. M. Girvin, S. Puri, and R. J. Schoelkopf. "Dual-rail encoding with superconducting cavities". *Proceedings of the National Academy of Sciences* **120**, e2221736120 (2023).

[187] S. Hou and P. F. Bernath. "Line list for the ground state of CaF". *Journal of Quantitative Spectroscopy and Radiative Transfer* **210**, 44–51 (2018).

[188] A. L. Shaw, P. Scholl, R. Finklestein, I. S. Madjarov, B. Grinkemeyer, and M. Endres. "Dark-State Enhanced Loading of an Optical Tweezer Array". *Phys. Rev. Lett.* **130**, 193402 (2023).

[189] L. Homeier, T. J. Harris, T. Blatz, S. Geier, S. Hollerith, U. Schollwöck, F. Grusdt, and A. Bohrdt. "Antiferromagnetic Bosonic $t-J$ Models and Their Quantum Simulation in Tweezer Arrays". *Phys. Rev. Lett.* **132**, 230401 (2024).

[190] J. C. Halimeh, L. Homeier, A. Bohrdt, and F. Grusdt. "Spin Exchange-Enabled Quantum Simulator for Large-Scale Non-Abelian Gauge Theories". *PRX Quantum* **5**, 030358 (2024).

[191] E. B. Norrgard, S. P. Eckel, C. L. Holloway, and E. L. Shirley. "Quantum blackbody thermometry". *New Journal of Physics* **23**, 033037 (2021).

[192] C. Hallas, N. B. Vilas, L. Anderegg, P. Robichaud, A. Winnicki, C. Zhang, L. Cheng, and J. M. Doyle. "Optical Trapping of a Polyatomic Molecule in an ℓ-Type Parity Doublet State". *Phys. Rev. Lett.* **130**, 153202 (2023).

[193] M. Kitagawa and M. Ueda. "Squeezed spin states". *Physical Review A* **47**, 5138 (1993).

[194] M. A. Perlin, C. Qu, and A. M. Rey. "Spin squeezing with short-range spin-exchange interactions". *Physical Review Letters* **125**, 223401 (2020).

[195] M. Block, B. Ye, B. Roberts, S. Chern, W. Wu, Z. Wang, L. Pollet, E. J. Davis, B. I. Halperin, and N. Y. Yao. "Scalable spin squeezing from finite-temperature easy-plane magnetism". *Nature Physics* **20**, 1575–1581 (2024).

[196] P. Kunkel, M. Prüfer, H. Strobel, D. Linnemann, A. Frölian, T. Gasenzer, M. Gärttner, and M. K. Oberthaler. "Spatially distributed multipartite entanglement enables EPR steering of atomic clouds". *Science* **360**, 413–416 (2018).

[197] M. Fadel, T. Zibold, B. Décamps, and P. Treutlein. "Spatial entanglement patterns and Einstein-Podolsky-Rosen steering in Bose-Einstein condensates". *Science* **360**, 409–413 (2018).

[198] K. Lange, J. Peise, B. Lücke, I. Kruse, G. Vitagliano, I. Apellaniz, M. Kleinmann, G. Tóth, and C. Klempt. "Entanglement between two spatially separated atomic modes". *Science* **360**, 416–418 (2018).

[199] G. Bornet, G. Emperauger, C. Chen, B. Ye, M. Block, M. Bintz, J. A. Boyd, D. Barredo, T. Comparin, F. Mezzacapo, T. Roscilde, T. Lahaye, N. Y. Yao, and A. Browaeys. "Scalable spin squeezing in a dipolar Rydberg atom array". *Nature* **621**, 728–733 (2023).

[200] Y. K. Lee, M. Block, H. Lin, V. Fedoseev, P. J. D. Crowley, N. Y. Yao, and W. Ketterle. "Observation of Spin Squeezing with Contact Interactions in One- and Three-Dimensional Easy-Plane Magnets". *Phys. Rev. Lett.* **135**, 023402 (2025).

[201] D. DeMille, N. R. Hutzler, A. M. Rey, and T. Zelevinsky. "Quantum sensing and metrology for fundamental physics with molecules". *Nature Physics* **20**, 741–749 (2024).

[202] N. U. Koyluoglu, S. V. Rajagopal, G. L. Moreau, J. A. Hines, O. Marković, and M. Schleier-Smith. "Squeezing towards the Heisenberg limit with locally interacting spins". *arXiv preprint arXiv:2506.16973* (2025).

[203] E. F. Walraven, M. R. Tarbutt, and T. Karman. "Scheme for Deterministic Loading of Laser-Cooled Molecules into Optical Tweezers". *Phys. Rev. Lett.* **132**, 183401 (2024).

[204] T. R. Hepworth, D. K. Ruttley, F. von Gierke, P. D. Gregory, A. Guttridge, and S. L. Cornish. "Long-lived multilevel coherences and spin-1 dynamics encoded in the rotational states of ultracold molecules". *Nature Communications* **16**, 7131 (2025).

[205] A. P. Raghuram, F. M. Blondell, J. M. Mortlock, B. P. Maddox, S. Dasgupta, H. A. Middleton-Spencer, K. R. Hazzard, H. M. Price, P. D. Gregory, and S. L. Cornish. "Probing topological edge states in a molecular synthetic dimension". *arXiv preprint arXiv:2604.00745* (2026).

[206] E. F. Walraven and T. Karman. "Hyperfine van der Waals repulsion between open-shell polar molecules". *Phys. Rev. A* **112**, 032810 (2025).